Measurements of the W boson resonance at LEP2

Jorgen D'Hondt

Promotor : Prof. Dr. Catherine De Clercq

CERN-THESIS-2004-009
20/03/2003

Maart 20, 2003

Vakgroep Natuurkunde
Faculteit van de Wetenschappen
Vrije Universiteit Brussel

Proefschrift ingediend met het oog op het behalen
van de Wettelijke Graad van Doctor in de Wetenschappen

Promotor	:	dr. Catherine De Clercq
Members of the jury	:	dr. Jean Van Craen (president)
		dr. Robert Roosen (secretary)
		dr. Martin W. Grünewald (University College Dublin)
		dr. Niels J. Kjær (CERN/NIKHEF)
		dr. Jacques Lemonne (Vrije Universiteit Brussel)
		dr. Pascal Vanlaer (Université Libre de Bruxelles)

The author of this thesis was financially supported by the IWT-Vlaanderen, the ’Instituut voor de aanmoediging van Innovatie door Wetenschap en Technologie in Vlaanderen’ or ’Flanders Institute to encourage scientific and technological research in the industry’.

Contents

Introduction **1**

Acknowledgements **3**

1 Standard Model **5**
1.1 Particle physics 5
1.2 Structure and framework of the Standard Model 6
1.3 Electroweak symmetry breaking 9
1.4 Radiative corrections to $\mathbf{m_W}$ within the Standard Model 10
1.5 Measurements and constraints within the Standard Model 12
1.6 Shortcomings of the Standard Model 14
1.7 Possible extensions of the Standard Model 14

2 Experimental setup **17**
2.1 The LEP collider 17
2.2 Determination of the LEP beam energy characteristics 21
2.2.1 Average beam energy 21
2.2.2 Spread of beam energy 26
2.3 The DELPHI detector 27
2.4 Track reconstruction and momentum measurement 27
2.5 Calorimetry 31
2.6 Collection of data 31

3 Theory and phenomenology of $\mathrm{e^+e^-} \to \mathrm{W^+W^-}$ events **33**
3.1 Monte Carlo simulation 34
3.2 Electroweak properties of the hard event 35
3.2.1 On-shell W pair production 35
3.2.2 Off-shell W pair production 36
3.2.3 Radiative corrections 38
3.2.4 Background for the $\mathrm{e^+e^-} \to \mathrm{W^+W^-}$ process 42
3.3 Perturbative QCD and gluon radiation 43
3.4 Phenomenological modelization in the confined region 45
3.5 Possible non-factorization of both W decays 47
3.5.1 Bose-Einstein Correlations 48
3.5.2 Colour Reconnection 51

3.6 Monte Carlo tuning of relevant model parameters with Z^0 LEP1 data 54
3.6.1 Definition of observables 55
3.6.2 Data distributions 57
3.6.3 Tuning procedure 57
3.6.4 Tuned parameters 61
3.6.5 Systematic cross-checks 61
3.6.6 Comparison with the standard DELPHI tuned parameters 64
3.6.7 Comments and conclusions 67
3.7 Overview of W^+W^- phenomenology 69

4 Experimental event reconstruction techniques 71
4.1 Energy flow reconstruction and particle selection 71
4.2 Identification of b quark-jets or 'b-tagging' 76
4.3 Particle clustering algorithms or jet finders 76
4.4 Kinematic constraints between initial and final state 80

5 The 2D ideogram analysis 87
5.1 Event selection 87
5.1.1 Sequential cut selection of fully hadronic $\mathbf{W^-W^+}$ events 87
5.1.2 Monte Carlo parametrized purity of the event 91
5.1.3 Properties of the event selection 93
5.2 Event-by-event reconstruction of the kinematic properties 96
5.3 Construction of the event-by-event 2D ideogram 98
5.3.1 Monte Carlo parametrized weight for possible jet pairings 100
5.3.2 Use of different clustering algorithms 104
5.3.3 Hypothesis about Initial State Radiation 105
5.3.4 Weighted sum of all possible ideograms 106
5.4 Maximum likelihood inference of the W boson resonance parameters . . . 106
5.4.1 Bayesian construction of the event-by-event likelihood via 2D convolution 106
5.4.2 The 2D inference of $\mathbf{m_W}$ and $\mathbf{\Gamma_W}$ 108
5.5 Monte Carlo calibration of the inference method 109
5.6 Consistency checks of the estimator with the bootstrap method 115
5.7 Alternative $\mathbf{m_W}$ estimators 118
5.8 Inferred results from the data 121

6 Systematic uncertainties 125
6.1 Hypothesis of factorisable systematic uncertainties 125
6.2 Monte Carlo calibration 126
6.3 Detector effects 126
6.3.1 Energy flow and jet reconstruction 127
6.3.2 Mixed Lorentz Boosted Z^0's 131
6.3.3 Aspect ratio 137
6.3.4 Non-linearity of energy scale 140
6.4 Background description 140

6.5 The LEP beam . . . 141
6.6 Uncertainties on the hard process . . . 141
6.7 Fragmentation of primary quarks into colour singlet particles . . . 144
6.7.1 Fragmentation models . . . 144
6.7.2 Uncertainty on Monte Carlo tuned model parameters . . . 145
6.7.3 Bose-Einstein Correlations . . . 148
6.8 Summary . . . 152
6.9 Correlation between systematic uncertainties . . . 152

7 Colour Reconnection **153**
7.1 The parametrized Colour Reconnection effect on the $\mathbf{m_W}$ and $\mathbf{\Gamma_W}$ determination . . . 153
7.2 Inferred likelihood information about the Colour Reconnection effect . . . 158
7.2.1 Direct information from geometrical energy flow observables . . . 159
7.2.2 Indirect information from the different $\mathbf{m_W}$ measurements . . . 164
7.3 Optimal convolution . . . 177
7.4 Structure of final analysis . . . 178

8 Results on W boson resonance properties **181**
8.1 Individual data samples . . . 181
8.2 Combination . . . 181
8.2.1 Combination procedure . . . 182
8.2.2 Combination of all data points . . . 184
8.2.3 Combination with the semi-leptonic channel . . . 186
8.3 Combination with other LEP experiments . . . 186
8.3.1 Most general result . . . 187
8.3.2 Colour Reconnection scenario I : 'full SK1 calibration' . . . 188
8.3.3 Colour Reconnection scenario II : 'half ARIADNE calibration' . . . 189
8.3.4 Systematic uncertainty due to radiative corrections . . . 189
8.3.5 Comparison between LEP experiments . . . 190
8.4 Discussion and conclusions . . . 192

9 Interpretation of the results **193**
9.1 Comparison of W boson resonance properties obtained from different WW decay channels at LEP2 . . . 193
9.2 World average for W boson properties . . . 194
9.3 Compatibility within the Standard Model . . . 195
9.4 Compatibility with models beyond the Standard Model . . . 199
9.5 Outlook . . . 200

Summary **203**

Appendices **205**

A The Jackknife method **205**

B Update of ALEPH results **207**

Bibliography **211**

Introduction

The Standard Model of elementary particles arose from a fruitful collaboration between experimental and theoretical scientific researchers over the last century. During the late '60s and early '70s it was formulated into his final framework, with the prediction of at that time yet undiscovered particles. Among them the W boson, which is one of the most essential particles for electroweak interactions and its mass was predicted to be around 80 GeV/c^2. Mainly due to this relative heavy mass, the W boson was not observed until the epoch of the Underground Area (UA) experiments at the $\mathrm{Sp\bar{p}S}$ collider at CERN. It were the UA1 and UA2 Collaborations who discovered this particle first in 1983. The mass of the W boson occupies a crucial role in the Standard Model, because with its prior knowledge one can evaluate other important parameters of the model. With this concept it becomes possible to verify the relations predicted by the Standard Model or theories beyond it.

This thesis presents measurements of the W boson resonance, which is mainly characterized by its pole mass and width. The data accumulated by the DELPHI experiment in e^+e^- collisions at the LEP machine was used. The W boson parameters were inferred from the W^+W^- events where both W bosons decay hadronically, W$\rightarrow q\bar{q}'$. This data set contains about $\sqrt{1/8} \simeq 35\%$ of the full statistical information available in the world on these quantities in e^+e^- collisions. During the research performed to accomplish a precise measurement, many other interesting physical phenomena had to be studied.

The thesis is structured to aim for a thorough and complete overview of these W boson measurements, including all relevant phenomena related to them. The first chapter introduces the mathematical framework of the Standard Model and discusses its electroweak relations. The experimental setup consisted out of an accelerator and a high performance detector, both of which are shortly discussed in chapter two. An important part in the study was to understand the phenomenological aspects of W^+W^- events produced at the LEP collider. Therefore a complete chapter is devoted to it, including some original studies on the topic of Monte Carlo parameter tuning. The techniques applied in the experimental reconstruction of these W^+W^- events are explained and studied in chapter four. In the fifth chapter, the estimators for the W mass and width are constructed and their statistical properties are studied thoroughly. The systematic uncertainties on these estimators arising from several effects are evaluated in chapter six, while a separate chapter is subsequently devoted to the evaluation of the systematic uncertainties arising from possible Colour Reconnection effects. Chapter eight discusses internal combinations of all obtained results in the thesis, but also with similar results from other LEP experiments or other W^+W^- decay channels. In the last chapter, the results are interpreted within the Standard Model or theories beyond it.

Acknowledgements

Since the start of my doctoral studies in the fall of 1999, I've met several interesting people at the IIHE in Brussels, at CERN nearby Geneva and at many scientific conferences and workshops in which I have participated. Among them some names should be highlighted as they had a great impact on this thesis.

First, I would like to thank the head of the IIHE-VUB, Prof. Jacques Lemonne, and my promotor, Prof. Catherine De Clercq, as they accepted me as a doctoral student. They created a scientific freedom around me in which I could manifest myself as an independent researcher. In this environment I profited from an education into the many qualifications needed for a future career in the domain of scientific research. Also the experience of both professors, was helpful for the redaction of this thesis.

In particular I enjoyed the close collaboration with Niels Kjær. From the first day onwards I've been learning from this productive collaboration at an incredible speed. Most of the knowledge on data analysis I've accumulated during the last 3,5 years I owe to him. His endless list of new ideas is a great resource for many young researchers, although it takes some time to create a personal trigger on this continuous flow of inspiration. But Niels would probably claim (correctly) that this is part of the scientific evolution one has to follow. Fortunately I was quickly poisoned with his tremendous workspirit which motivated me to investigate many of these triggered brainstorming flashes. Thanks Niels for the education !! And hopefully, you succeeded in making me a little bit less 'brain-death' as you call it and that you get the chance to do the same thing for many other young researchers.

During the first year, I appreciated the help from Martijn Mulders, another pupil of Niels Kjær. He introduced me into the tricky concepts of the W mass analysis which I continued afterwards. Thanks for the effort you put into answering all my questions.

Within the WW community at LEP I should thank many people, especially those within the DELPHI Collaboration. I profited from the constructive discussions with amongst others Fabio Cossutti, Chris Parkes and Ahmimed Ouraou.

Pascal Vanlaer I thank for the support on the topic of my annex thesis.

At the IIHE in Brussels I had the pleasure to meet many young colleagues : Olivier, Ann, Roel, Gilles, Caroline, Xavier, Pascal, Lionel,... and I encourage those who are working on their PhD for the moment : Philip, Steven, Daan. I also thank Bob and Jean-Paul who prevented me of blowing up the Muon Chambers within DELPHI. Another person which should be highlighted on this page is the secretary of the IIHE, Rosine. Her perfect organization and quick response on many requests facilitated my work enormously.

For all the fun, experienced on the Belgian apartment in St.Genis and within the Belgian DELPHI office at CERN, I thank Nick and Thomas.

Last but certainly not least, I thank my parents and Annelies for their unconditional support during these years. This thesis wouldn't have been possible without their patience and understanding.

Chapter 1

Standard Model

Since more than 2000 years philosophers have been speculating about the smallest constituents of matter. It was not until the 19th century in the age of J. Dalton that experiments could verify the many hypotheses. During the last century scientists have accumulated a large database of precise information about the nature of these fundamental quanta (section 1.1) and theoretical interpretations have been formulated in a more rigorous framework. Currently it is the Standard Model that provides the best formalism of our knowledge of particle physics (section 1.2), by defining the elementary constituents of matter and their interactions. One of the yet unresolved questions in this framework concerns the origin of mass of these particles (section 1.3), as for example the mass of the W boson measured in this thesis. When confronting the predictions of the Standard Model with the present experimental verifications one observes a remarkable agreement (section 1.5). Nevertheless there are some natural features or questions which are left unanswered by the model (section 1.6) and therefore extensions are formulated to partially incorporate those weak points (section 1.7).

1.1 Particle physics

Our understanding of particle physics, the science of the ultimate constituents of universal matter and the interactions among them, has undergone a remarkable development during the last decades. At present the Standard Model (together with Einstein's theory of gravity) summarizes the elementary particles in two categories according to their spin.

The first group are the half-integer spin fermions, which are further divided into quarks and leptons according to their specific interactions and each fall into three generations. All quarks and leptons have an anti-particle with opposite quantum numbers and each quark comes in three colour charges of the strong interactions.

The second group consists of integer spin gauge bosons, the photon γ, the W^+, W^- and Z^0 bosons and 8 gluons. They mediate the force between the fermions.

This is all adding up to a large number of elementary particles : 12 leptons, 36 quarks and 12 mediators, all of which are discovered. As we shall see the Standard Model calls for at least one so-called Higgs particle, however this has not been observed directly due to its indirect expected large mass of 81^{+52}_{-33} GeV/c^2 [1] and the experimental limitations which

can only exclude its existence below 114.4 GeV/c^2 at 95% CL [2]. All these particles are summarized in Table 1.1 and 1.2.

Fermions	Generation 1	2	3	Q	I_3 (left-handed)	Y
Leptons	ν_e	ν_μ	ν_τ	0	1/2	-1
	e^-	μ^-	τ^-	-1	-1/2	-1
Quarks	u^i	c^i	t^i	2/3	1/2	1/3
	d^i	s^i	b^i	-1/3	-1/2	1/3

Table 1.1: *The three families of left-handed fermions in the Standard Model with some of their quantum numbers like the electric charge Q, the third component of weak isospin I_3 and the hypercharge Y related by Q=I_3+Y/2. Each of them has a corresponding anti-fermion particle and the index i refers to the three possible colour charges of the quarks.*

Vector bosons	Interaction	Spin	Mass (GeV/c^2)
γ	Electromagnetic	1	0
W^+ and W^-	Charged current Weak	1	$\simeq 80$
Z^0	Neutral current Weak	1	$\simeq 91$
g	Strong	1	0
graviton	Gravity	2	0
Higgs	Yukawa coupling	0	> 114

Table 1.2: *The bosons of the Standard Model and gravity interactions with their spin properties and an indication of their mass value.*

1.2 Structure and framework of the Standard Model

Mathematically the particles mentioned above are described in a quantum field theory [1], which is the best framework currently available for the description of the fundamental theories of matter and force. These theories are based on Hamilton's principle of least action $S = \int L dt$, where the action is defined in terms of a Lagrangian L. This Lagrangian is a functional of a set of generic fields and their time-derivatives, and is the space-integral of a scalar function known as the Lagrangian density $\mathcal{L}$. The field equations or Euler-Lagrange equations are obtained from the postulate that the action S should be stationary $\delta S = 0$ when the fields, described in a Hilbert space, are varied. Whenever $\mathcal{L}$ is a scalar then these equations are Lorentz-invariant. This Lagrangian formalism provides a natural framework for the

[1] For an extensive overview, reference [3] is recommended.

quantum mechanical implementation of symmetry principles, which refer by the theorem of Noether to a conservation law.

The non-Abelian formalism of the Standard Model proposed by S.L.Glashow [4], A.Salam [5] and S.Weinberg [6], describes the interactions between elementary particles via the symmetry group $SU(3)_c \otimes SU(2)_L \otimes U(1)_Y$. This group defines a set of symmetry transformations that will not change the result of our experiment, which can always be expressed in terms of probabilities. The principle of gauge invariance under local phase transformations of this symmetry group will entail the introduction of gauge boson fields, as many as the dimensionality of the Lie algebra of the group:

- $SU(3)_c$: non-Abelian colour symmetry group of the strong force with 8 massless gauge boson fields G^a_μ called Yang-Mills gluon fields each having two colour charges and a coupling constant g_s related to α_s by $\alpha_s = g_s^2/4\pi$ (a $\in \{1,...,8\}$) ;
- $SU(2)_L$: non-Abelian symmetry group of left handed chirality states with 3 massless boson fields and coupling constant g ;
- $U(1)_Y$: Abelian hypercharge symmetry group with one neutral massless boson field and coupling constant g'.

The first part of the symmetry, $SU(3)_c$, describes the strong force with the theory of Quantum Chromodynamics (QCD), where gluon fields G^a_μ interact with the 4-component Dirac spinors ψ^i_q associated with each quark field of colour i and flavour q. Electroweak interactions are uniformly described by the gauge group U(2) which reduces to the algebras of $SU(2)_L$ and $U(1)_Y$. If T_0 denotes the generator of the Abelian factor $U(1)_Y$ and $\{T_i | i = 1,2,3\}$ the generators of $SU(2)_L$, one can write the Lie algebra of these operators as:

$$\begin{aligned} [T_0, T_\alpha] &= 0 \qquad \text{with } \alpha = 0,1,2,3 \\ [T_i, T_j] &= i \sum_{k=1}^{3} \epsilon_{ijk} T_k \end{aligned} \tag{1.1}$$

where ϵ_{ijk} are the $SU(2)_L$ group structure constants denoted by the totally anti-symmetric Levi-Civita tensor in 3 real dimensions. The generators T_i are related to the three Pauli matrices τ_i (defined in Equation 1.8) by the relation $T_i = \frac{(1+\gamma_5)}{4}\tau_i$. The four gauge fields A^α_μ corresponding to these four generators form the adjoint representation of the group and must be combined to obtain real physical fields:

$$A_\mu = ie \sum_{\alpha=0}^{3} T_\alpha A^\alpha_\mu \tag{1.2}$$

where A^0_μ is a singlet, while the fields $\{A^i_\mu | i = 1,2,3\}$ form a triplet with respect to $SU(2)_L$. Because the gauge field carries both an internal symmetry index α and a Lorentz vector index μ, the object A_μ transforms like a Lorentz vector field and takes its values in the Lie algebra of the structure group because it is an operator in this group. The two physical W boson fields are conjugate of each other, and must be linear combinations of two of the triplet fields:

$$W_\mu^\pm = \mp\frac{1}{\sqrt{2}}(A_\mu^1 \pm iA_\mu^2) \tag{1.3}$$

These W boson fields couple only with left-handed chirality states. The physical photon and Z^0 boson fields, A_μ and Z_μ, must be linear combinations of the third triplet field A_μ^3 and the singlet field A_μ^0:

$$\begin{aligned} A_\mu &= \sin\theta_W A_\mu^3 + \cos\theta_W A_\mu^0 = \frac{1}{\sqrt{g^2+g'^2}}\left(g'A_\mu^3 + gA_\mu^0\right) \\ Z_\mu &= \cos\theta_W A_\mu^3 - \sin\theta_W A_\mu^0 = \frac{1}{\sqrt{g^2+g'^2}}\left(gA_\mu^3 - g'A_\mu^0\right) \end{aligned} \tag{1.4}$$

where θ_W is the Weinberg mixing angle which is related to the coupling constants in the following way:

$$g = -e/\sin\theta_W \qquad\qquad g' = -e/\cos\theta_W. \tag{1.5}$$

They couple both with left-handed (LH) and right-handed (RH) fermions. The left-handed fermion fields ψ_i of the ith fermion family transform as doublets under SU(2)$_L$, while the right-handed fields are SU(2)$_L$ singlets. Also it is assumed that there is no direct coupling between lepton families, or between quark and lepton families and that the neutrinos do not interact with photons. If the model has to incorporate the well known QED theory the fermion coupling to the photon field must be parity conserving and the coupling constant must reflect the charge of the fermion q_f. In the hypothesis of lepton universality one can write an effective Lagrangian density as:

$$\mathcal{L} = \mathcal{L}_{gauge} + \mathcal{L}_{Higgs} + \mathcal{L}_{Yukawa} \tag{1.6}$$

where

$$\begin{aligned} \mathcal{L}_{gauge} \;=\; & -\tfrac{1}{4}\, G^{a\ \mu\nu} G^a_{\ \mu\nu} - \tfrac{1}{4}\, A^{i\ \mu\nu} A^i_{\ \mu\nu} - \tfrac{1}{4}\, A^{0\ \mu\nu} A^0_{\ \mu\nu} \\ & -i\,\overline{L}_\alpha \gamma^\mu\, \mathcal{D}_\mu L_\alpha - i\,\overline{R}_\alpha \gamma^\mu\, \mathcal{D}_\mu R_\alpha \\ & -i\,\overline{Q}_{\alpha\ i}\ \gamma^\mu\ (\mathcal{D}_\mu)^i_j\ Q^j_{\ \alpha} - i\,\overline{U}_{\alpha\ i}\ \gamma^\mu\ (\mathcal{D}_\mu)^i_j\ U^j_{\ \alpha} - i\,\overline{D}_{\alpha\ i}\ \gamma^\mu\ (\mathcal{D}_\mu)^i_j\ D^j_{\ \alpha} \end{aligned}$$

with

$$\begin{aligned} G^a_{\ \mu\nu} &= \partial_\mu G^a_\nu - \partial_\nu G^a_\mu - g_s f^{abc} G^b_\mu G^c_\nu, \\ A^i_{\ \mu\nu} &= \partial_\mu A^i_{\ \nu} - \partial_\nu A^i_{\ \mu} - g\epsilon^{ijk} A^j_{\ \mu} A^k_{\ \nu}, \\ A^0_{\ \mu\nu} &= \partial_\mu A^0_{\ \nu} - \partial_\nu A^0_{\ \mu}, \\ \mathcal{D}_\mu L_\alpha \text{ (LH leptons)} &= (\partial_\mu + i\tfrac{g}{2}\vec{\tau}\cdot\vec{A}_\mu - i\tfrac{g'}{2}A^0_{\ \mu})L_\alpha, \\ \mathcal{D}_\mu R_\alpha \text{ (RH leptons)} &= (\partial_\mu - ig'A^0_{\ \mu})R_\alpha, \\ (\mathcal{D}_\mu)^i_j Q^j_\alpha \text{ (LH quarks)} &= (\delta^i_j\partial_\mu + \delta^i_j i\tfrac{g}{2}\vec{\tau}\cdot\vec{A}_\mu + \delta^i_j i\tfrac{g'}{6}A^0_{\ \mu} - i\tfrac{g_s}{2}(\lambda^a)^i_j G^a_\mu)Q^j_\alpha, \\ (\mathcal{D}_\mu)^i_j U^j_\alpha \text{ (RH quarks u,c,t)} &= (\delta^i_j\partial_\mu + \delta^i_j i\tfrac{2}{3}g'A^0_{\ \mu} - i\tfrac{g_s}{2}(\lambda^a)^i_j G^a_\mu)U^j_\alpha, \\ (\mathcal{D}_\mu)^i_j D^j_\alpha \text{ (RH quarks d,s,b)} &= (\delta^i_j\partial_\mu - \delta^i_j i\tfrac{1}{3}g'A^0_{\ \mu} - i\tfrac{g_s}{2}(\lambda^a)^i_j G^a_\mu)D^j_\alpha, \end{aligned}$$

where the f^{abc} stand for the $SU(3)$ group structure constants, the τ^i are the three Pauli matrices and the $(\lambda^a)^i_j$ are the components of the 8 linear independent Gell-Mann matrices with

a,b,$c = \{1,...,8\}$ and i,j,$k = \{1,2,3\}$. The Dirac spinors of the particle fields ψ_i are represented by L, R, Q, U and D. The $\frac{\lambda^a}{2}$ matrices are representations of the SU(3)$_c$ generators which obey a Lie algebra in a similar way than the T_α obey Equation 1.1. The γ_μ matrices can be represented as function of the Pauli matrices:

$$\gamma_\mu = \begin{pmatrix} 0 & \tau_\mu \\ \bar{\tau}_\mu & 0 \end{pmatrix}; \qquad \gamma_5 \equiv i\gamma^0\gamma^1\gamma^2\gamma^3 = \begin{pmatrix} 1 & 0 \\ 0 & -1 \end{pmatrix}, \tag{1.7}$$

where

$$\begin{aligned} \tau_0 = \bar{\tau}_0 &= \begin{pmatrix} 1 & 0 \\ 0 & 1 \end{pmatrix}; \qquad \tau_1 = -\bar{\tau}_1 = \begin{pmatrix} 0 & 1 \\ 1 & 0 \end{pmatrix}; \\ \tau_2 = -\bar{\tau}_2 &= \begin{pmatrix} 0 & -i \\ i & 0 \end{pmatrix}; \qquad \tau_3 = -\bar{\tau}_3 = \begin{pmatrix} 1 & 0 \\ 0 & -1 \end{pmatrix}. \end{aligned} \tag{1.8}$$

The terms $\mathcal{L}_{Higgs}$ and $\mathcal{L}_{Yukawa}$ generate mass for the particle fields and will be explained in the next section.

1.3 Electroweak symmetry breaking

The unified theory as developed up to this point, is gauge invariant with respect to the symmetry group SU(3)$_c$⊗SU(2)$_L$⊗U(1)$_Y$ of local gauge transformations. However the theory is also invariant under this group considered as a global symmetry. As a consequence, the particles of the theory are massless. To introduce masses for the vector bosons, the internal symmetry should be broken in such a way that the gauge invariance of the theory is preserved and the theory remains renormalizable. Breaking the global symmetry gives rise to massless spin zero Goldstone bosons, which are not observed in Nature, but when the symmetry is broken local, rather than global, these Goldstone bosons are absent. Instead, these degrees of freedom show up as helicity zero states of the vector particles associated with the broken local symmetries, which thereby acquire a mass. This fundamental observation was first made, in the relativistic context, by R.Brout, F.Englert [7] and P.W.Higgs [8].

Gauge invariant terms must be added in $\mathcal{L}$ involving scalar and gauge fields. The most general form consistent with SU(2)$_L$⊗U(1)$_Y$ gauge invariance, Lorentz invariance and renormalizability is:

$$\begin{cases} \mathcal{L}_{Higgs} &= -(\mathcal{D}_\mu\Phi)^\dagger(\mathcal{D}^\mu\Phi) - V(\Phi) \\ V(\Phi) &= \mu^2\Phi^\dagger\Phi + \lambda(\Phi^\dagger\Phi)^2 \end{cases} \tag{1.9}$$

with

$$\mathcal{D}_\mu\Phi = (\partial_\mu + i\,\frac{g}{2}\,\vec{\tau}\cdot\vec{A}_\mu + i\,\frac{g'}{2}\,A^0{}_\mu)\Phi. \tag{1.10}$$

where λ and μ^2 are real constants. The scalar iso-doublet field Φ is defined as:

$$\Phi = \begin{pmatrix} \phi^+ \\ \phi^o \end{pmatrix} \longrightarrow \begin{cases} \phi^+ = \frac{\phi_1 + i\phi_2}{\sqrt{2}} \\ \phi^o = \frac{\phi_3 + i\phi_4}{\sqrt{2}} \end{cases} \tag{1.11}$$

where the ϕ are the real fields. For $\mu^2 < 0$, there is a non-vanishing vacuum expectation value v:

$$\langle \Phi^\dagger \, \Phi \rangle \;=\; v^2 \;=\; \frac{|\mu^2|}{\lambda} \;>\; 0. \tag{1.12}$$

As we know, the bilinear non-derivative terms correspond to vector mass terms which reflect the masses of the fields. From Equation 1.9 one obtains that the photon is massless, thereby confirming the U(1)$_Y$ gauge invariance of the vacuum, while:

$$m_W = \frac{1}{2}\, v\, |g| \qquad\qquad m_Z = \frac{1}{2}\, v\, \sqrt{g^2 + g'^2} \tag{1.13}$$

or at tree level

$$m_W = \cos\theta_W \; m_Z. \tag{1.14}$$

This symmetry breaking mechanism predicts the existence of an additional neutral massive boson, usually called the scalar Higgs boson H, with mass $m_H = \sqrt{-2\mu^2}$. Because μ is unknown, the Standard Model is not predicting m_H and only via radiative corrections on physical quantities (like m_W) information can be obtained (see section 1.4).

The mass of the fermion fields is generated by adding gauge invariant Yukawa couplings in the Lagrangian density:

$$\mathcal{L}_{Yukawa} = -G^L_{\alpha\beta} \overline{L}_\alpha R_\beta \Phi - G^D_{\alpha\beta} \overline{Q}_\alpha D_\beta \Phi - G^U_{\alpha\beta} \overline{Q}_\alpha U_\beta \; \tilde{\Phi} + \; h.c. \tag{1.15}$$

where the $G^{L,U,D}_{\alpha\beta}$ are the unknown Yukawa matrices (for example $m_e = G^e v$) which can be related to the Cabibbo-Kobayashi-Maskawa matrix and $\tilde{\Phi}$ is defined as $i\tau^2\Phi^\dagger$.

1.4 Radiative corrections to m_W within the Standard Model

The very precise measurement of the Z^0 boson mass, m_Z, has changed the way that electroweak data is analyzed. Instead of comparing predictions of m_W and m_Z with the observed values, the pole mass m_Z is taken as an experimental input, along with the Fermi coupling constant G_F, related to the muon life-time, and the fine structure constant $\alpha(m_Z)$. These parameters have been measured independently with high precision and form a solid choice of renormalization scheme, which has no natural or physical preference among all other possibilities. In this way for example the weak mixing angle θ_W becomes a derived quantity. With these inputs, the electroweak theory can be used to make predictions of other quantities, like m_W, with sufficient precision (when m_t and m_H are given) that it becomes necessary to take electroweak radiative corrections into account [9]. The tree level Equation 1.14 can be rewritten as a function these three parameters:

$$\Delta r = 1 - \frac{\pi\alpha(m_Z)}{\sqrt{2}G_F m_W^2 \left(1 - (\frac{m_W}{m_Z})^2\right)} \tag{1.16}$$

where Δr absorbs all radiative corrections due to higher order diagrams, and is equal to zero at tree level. In one-loop order these radiative corrections involve the masses of the top quark, m_t, and the scalar Higgs boson, m_H. Since the Standard Model is a normalizable theory [10], higher order corrections can be reliably computed. The quantity Δr can be decomposed into different contributions:

$$\Delta r = \Delta\alpha - \frac{\cos^2\theta_W}{\sin^2\theta_W}\Delta\rho + \Delta r_{Higgs} + \Delta r_{vertex,box} + \Delta r_{others} \tag{1.17}$$

where $\Delta\alpha$ represents the contribution of the fermions to the vacuum polarization, or the radiative corrections on the photon propagator and is induced by the change in the running coupling constant α from soft to hard scale:

$$\alpha(Q^2 = m_Z^2) = \frac{\alpha(Q^2 = 0)}{1 - \Delta\alpha}. \tag{1.18}$$

The uncertainty on the determination of $\Delta\alpha$ is dominated by the contributions from light quarks $\Delta\alpha_{had}^{(5)}$ (all except the top quark), which dominates also the uncertainty on Δr. The term $\Delta\rho$ is a correction to the parameter ρ [11] which is the ratio between the amplitudes of the neutral and the charged current at zero momentum transfer:

$$\rho = \frac{\mathcal{M}_{NC}(0)}{\mathcal{M}_{CC}(0)} = \frac{m_W^2}{m_Z^2\cos^2\theta_W} \tag{1.19}$$

which equals unity at tree level if the masses m_W and m_Z are induced by a Higgs doublet. This $\Delta\rho$ term includes radiative corrections to the self-energy of the weak vector bosons via fermionic loops. The largest corrections are induced by the SU(2) quark doublet (b,t), shown in Figure 1.1. The most important radiative contributions to $\Delta\rho$ are quadratically related to m_t by:

$$\Delta\rho_t = \frac{3G_F}{8\sqrt{2}\pi^2} m_t^2 \left(1 + \delta_{QCD}\right) + \mathcal{O}(m_t^4) \tag{1.20}$$

and are the dominant contributions to the value of Δr.

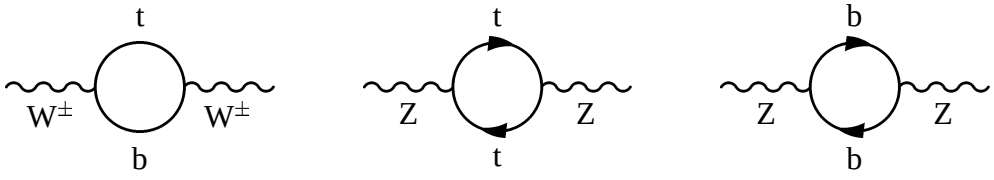

Figure 1.1: *Diagrams of the largest radiative self-energy corrections to the W propagator (left) and Z propagator (center and right) via di-fermion loops.*

Also bosonic loops, as shown in Figure 1.2, affect the self-energy of the vector bosons. The leading correction from a Higgs boson is however logarithmic in m_H:

$$\Delta r_{Higgs} = \frac{\sqrt{2} G_F m_W^2}{16\pi^2} \cdot \frac{11}{3} \left(ln \frac{m_H^2}{m_W^2} - \frac{5}{6} \right) + ... \tag{1.21}$$

which becomes small if $m_H \simeq m_W$. The remaining terms $\Delta_{vertex,box}$ related to vertex and box higher order corrections and Δ_{others}, reflect radiative corrections which are about one order of magnitude smaller than those presented.

Figure 1.2: *Bosonic radiative correction loops to the W and Z propagators involving the Higgs boson.*

Currently the value of Δr obtained from fits within the framework of the Standard Model using all data is given by [12]:

$$\Delta r = 0.0355 \pm 0.0019 \, . \tag{1.22}$$

These radiative correction formula will be used in chapter 9 to interpret the results obtained in this thesis as a function of the expected Higgs boson mass and the measured top quark mass.

1.5 Measurements and constraints within the Standard Model

The electroweak and QED radiative corrections on Standard Model observables and the large database of precision measurements make it possible to test the consistency of the model. Each parameter or pseudo-observable related to these parameters is calculated as a function of $\alpha(m_Z)$, $\alpha_s(m_Z)$, m_Z, G_F, m_{top} and m_H using the programs TOPAZ0 [13] and ZFITTER [14]. The value m_{top} is measured at the Tevatron collider [15], while the interval for m_H is defined by its lower limit obtained from the direct search of the scalar Higgs boson at LEP2 [2]. The obtained indirect constraints on the parameters or pseudo-observables are compared to their experimental measurements, see Figure 1.3 [1]. The so-called pull reflects the number of standard deviations that the measured value deviates from the calculated one. In order to obtain a statistical correct analysis of the Standard Model, the distribution of this pull over all quantities should reflect a normal Gaussian.

Most measured values agree with their expectations, nevertheless from the χ^2 of the Standard Model fit divided by its number of degrees of freedom one determines a probability of 1.3 % for these results to occur in the hypothesis that the model is correct. A probability

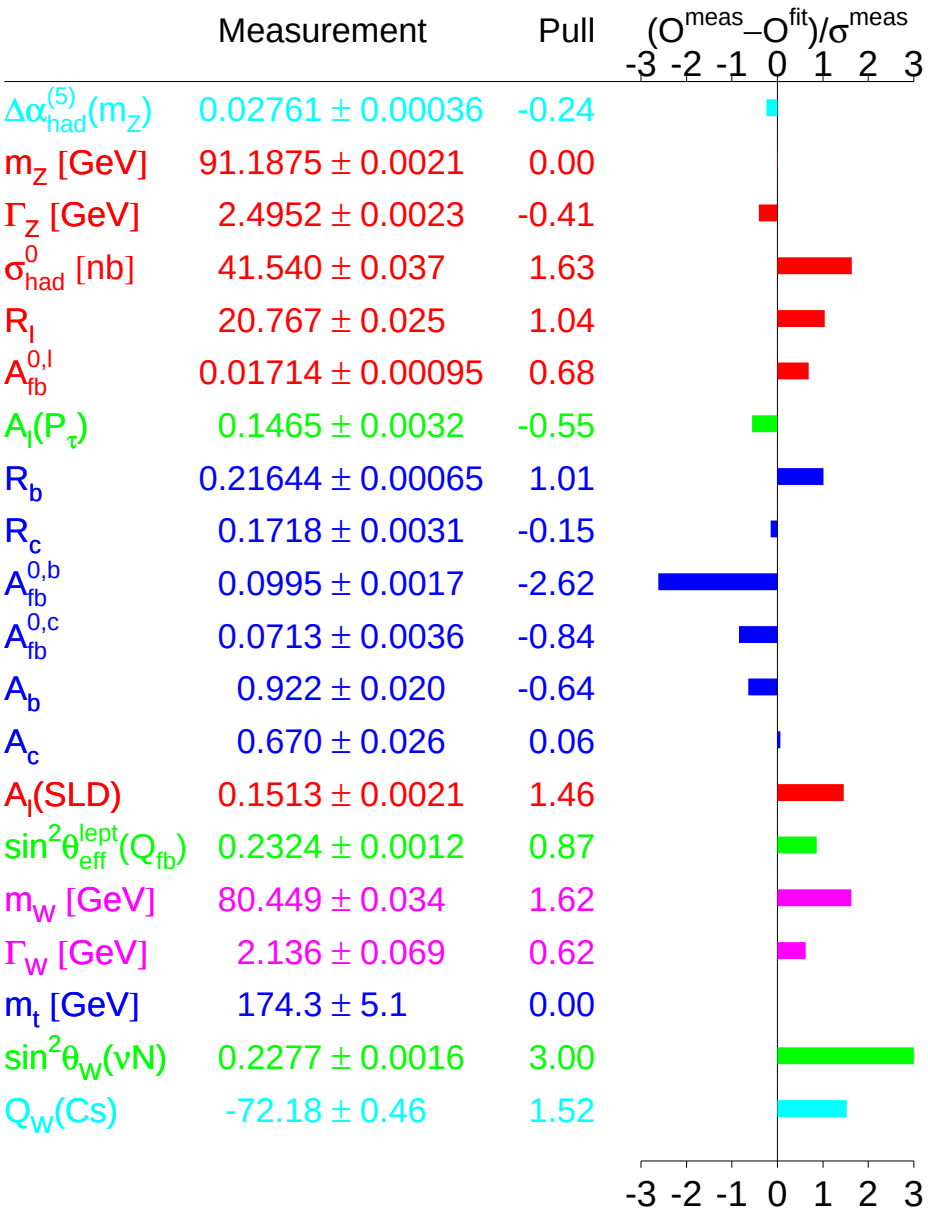

Figure 1.3: *Global Standard Model fit of all relevant measured electroweak observables, defined in [1], to their predictions using radiative corrections up to second order (QED to third order).*

which is still reasonable taking into account the difficulty of most of these precise measurements. The largest contribution to the χ^2 is the result from the NuTeV experiment [16] concerning $\sin^2\theta_W$. Without this result the probability would increase to 11.3%. The results obtained in this thesis will be interpreted in the same way in chapter 9.

1.6 Shortcomings of the Standard Model

Beyond the striking success of the Standard Model there are strong conceptual indications for new physics to appear at higher energies. The model is consistent with almost all present data, but it is found to be totally inadequate as a final theory. The structure of the Standard Model can not naturally explain the relative smallness of the weak scale of vector boson masses or Fermi scale $\Lambda \sim 1/\sqrt{G_F} \sim 250$ GeV, set by the Higgs mechanism, compared to either the quantum gravity or Planck scale $M_{Pl} = 1/\sqrt{8\pi G_N} \sim 2.4\,10^{18}$ GeV where gravity could be unified with the other forces or either the GUT [2] scale $M_{GUT} \sim 10^{14} - 10^{16}$ GeV where electroweak and strong force couplings unify [17].

The electroweak symmetry is broken if the mass parameter m_H^2 of the Higgs field, after renormalization, is positive. This parameter receives additive radiative corrections which are quadratically divergent with energy and therefore infinite. They can be made finite by a cut-off at some energy M, hence m_H^2 can only be much less than M^2 if the corrections are finely tuned to cancel. If M is taken to be the Planck scale, these corrections must cancel in the first 30 decimal places. This gauge hierarchy problem is a symptom of the fact that the Standard Model is only a parametrization, and not an explanation, of the electroweak symmetry breaking.

Besides these hard conceptual problems of the Standard Model, there are many others. The theory does not explain why there are exactly three generations of fermions, neither does it explain the mass hierarchy observed in this fermion sector. While the masses of the neutrinos are close or equal to zero, the top quark mass scale is around $m_t \sim 175$ GeV/c^2. Again these fermion masses are not predicted by the theory, therefore up to 19 free parameters are embedded in the theory.

1.7 Possible extensions of the Standard Model

It could be that the Standard Model is correct up to a mass scale above 10^{16} GeV, and that the only new physics below that scale is one Standard Model Higgs boson. This conclusion would be extremely embarrassing, because it would imply that the spontaneous breaking of the electroweak symmetry and the values of the quark and lepton masses could not be understood as a matter of principle.

Generally it is considered to be highly implausible that these features can be explained by the Standard Model, without accompanying new phenomena. There are several possibilities

[2] Grand Unified Theories propose to embed the $SU(3)_c \otimes SU(2)_L \otimes U(1)_Y$ gauge group in various simple Lie groups, like SU(5) or SO(10), which would depend only on one single coupling constant. The unification of the three coupling constants is however only exact in supersymmetric extensions of the Standard Model.

to solve these handicaps, of which two are discussed below and all of them are extensions of the existing theory.

A popular hypothesis is a generalization of the Standard Model by a supersymmetry [3] between bosons and fermions. It would downgrade the bosonic degree of divergence from quadratic to logarithmic, by introducing for each fermion a related supersymmetric boson and vice-versa. It provides a natural solution which is well defined, computable and that preserves all the virtues of the Standard Model. The Minimal Supersymmetric Standard Model (MSSM) [20] is the most traditional approach where supersymmetry is broken in a hidden sector at a mass scale of $\Lambda \sim \sqrt{M_{Pl}/\sqrt{G_F}}$. Since the hidden sector only communicates with the visible sector through for example gravitational interactions (SUGRA), the splitting of the supersymmetric multiplets is much smaller than this scale and one therefore expects supersymmetric particles at the TeV scale. In the MSSM there are two Higgs doublets, which implies three neutral physical Higgs particles and a pair of charged Higgses. The lightest neutral Higgs (h) should be lighter than m_Z at tree-level approximation, but can become heavier due to radiative corrections proportional to m_t^4 and $log(m_{\tilde{t}}^2)$, where the stop $\tilde{t}$ particle is the supersymmetric partner of the top quark. For all values of tan(β) [4] and for $m_t = 174$ GeV/c^2 one finds a limit $m_h \leq 130$ GeV/c^2. With no discovery of the Higgs bosons nor supersymmetric particles at LEP, the case for the MSSM certainly becomes less natural, and even less natural become the gauge mediated (GMSB) and anomaly mediated (AMSB) models of supersymmetry breaking. The precise LEP measurements on $\alpha_s(m_Z)$ and $\sin^2\theta_W$ confirm however that the standard GUT's fail in predicting $\sin^2\theta_W$ given $\alpha_s(m_Z)$ and $\alpha(m_Z)$, while supersymmetric GUT's are in agreement with the present experimental results.

Another suggestion to solve the Standard Model problems includes dynamical models with new gauge interactions [21], leading to a strongly coupled theory at TeV energies. In these composite theories the Higgs boson is not elementary but either a bound state of fermions or a condensate due to this new force. The most realistic examples are Technicolor theories, which introduce new heavy techniquarks at a nearby scale of about three times Λ_{QCD}. These predictions clash with the electroweak precision observations.

Some of the above models are severely constrained, however none of them can be ruled out, neither can they be confirmed by experimental data. Maybe the data from the Tevatron collider at Fermilab, but certainly those from the Large Hadron Collider (LHC) at CERN will be conclusive about the possible hypotheses to solve the Standard Model diseases.

The measurement of the W$^\pm$ boson mass is probing the most essential relations of the electroweak theory on which all above mentioned models are based. Via the radiative corrections its value is directly related with the spontaneous symmetry breaking mechanism and the top quark mass. Its precise evaluation is therefore a milestone test in the history of particle physics. Today, the direct estimation of the parameter m_W is dominated by the LEP2 data. This thesis describes, among other studies, the results on m_W obtained by the DELPHI Collaboration in the channel $e^+e^- \rightarrow W^+W^- \rightarrow q\bar{q}'Q'\bar{Q}$. Taking into account the Standard Model branching ratio of the W$^\pm$ bosons decaying into quarks, this represents about $\sqrt{1/8}$ or 35% of the full statistical information we have about the world combined value of m_W in e^+e^- collisions.

[3] For an extensive overview, references [18] and [19] are recommended.

[4] The parameter tan(β) is defined as the ratio of the vacuum expectation values of the Higgs fields.

Chapter 2

Experimental setup

2.1 The LEP collider

The Large Electron Positron or LEP collider at the European Organization for Nuclear Research (CERN) is geographically located on the Swiss-French border near Geneva. The circular synchrotron has a circumference of 26.7 km and lies on average 100m below the surface. It extends from the foothills of the Jura mountains to the Geneva airport as shown in Figure 2.1. LEP consists of eight arcs and eight straight sections where the e^+e^- interaction points are situated, four of which were surrounded by general purpose detectors ALEPH, DELPHI, L3 and OPAL.

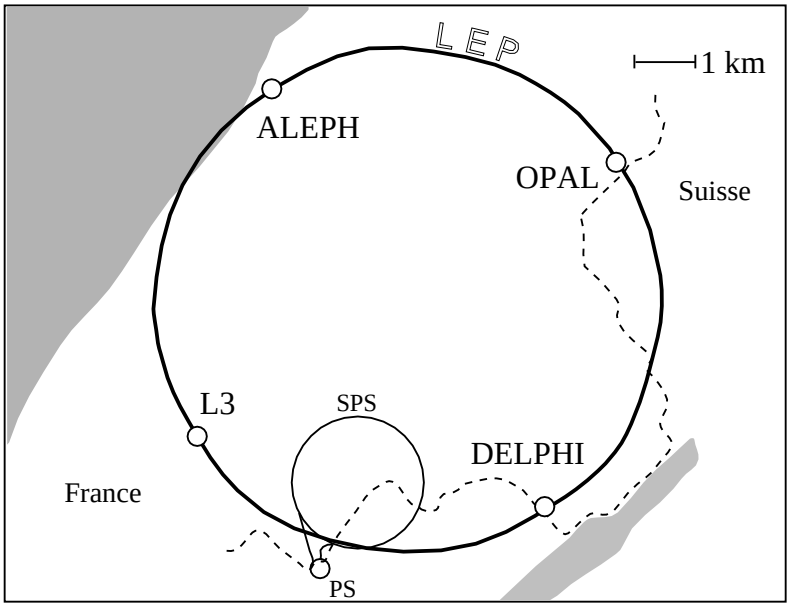

Figure 2.1: *Schematic view of the CERN site at the border between Switzerland and France, situated between the Jura mountains and the Geneva airport (shaded).*

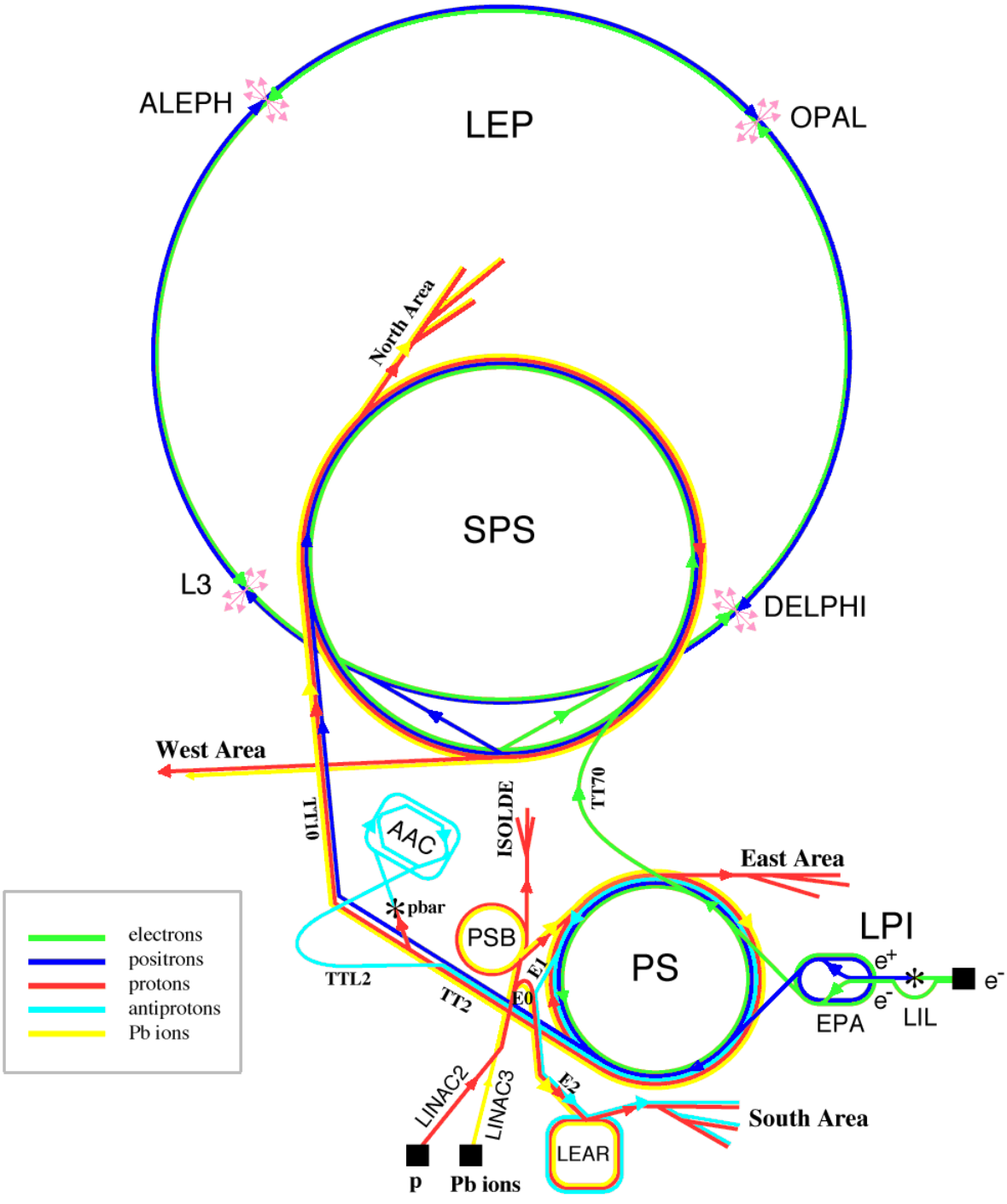

Figure 2.2: *Schematic drawing of the LEP e^+e^- injection and accelerator set-up.*

The LEP collider was used to produce e^+e^- collisions at high energy and with high luminosity. From 1989 to 1995, LEP was operating at the centre-of-mass energy of the Z^0 resonance, corresponding to about 91.2 GeV (LEP1 phase). Since November 1995 until December 2000, the accelerating power was increased progressively with the addition of superconducting radio-frequency (RF) cavities (LEP2 phase).

Before the electrons and positrons were injected in the LEP collider, they traveled through a chain of pre-accelerators, shown in Figure 2.2.

- A high intensity electron source followed by a linear accelerator (LIL1 [1]) produced a beam of 200 MeV electrons. Positrons were produced by bombarding a tungsten target with this electron beam;
- The LIL2, a second LINAC, accelerated the electrons and positrons (injected with a mean energy of 10 MeV) up to 600 MeV;
- The Electron Positron Accumulator (EPA) collected the particles in bunches;
- The Proton Synchrotron (PS) and the Super Proton Synchrotron (SPS) increased the energy up to 3.5 GeV and 20 GeV respectively, before final injection into LEP.

The LEP accelerator was a synchrotron operated as a storage ring. The acceleration was done in the straight sections of the tunnel using RF cavities, while 3336 dipole magnets guide the beams through the curved sections. Several systems of quadrupole magnets were used to focus the beams. Due to the well known betatron oscillations in the transverse plane on the beam direction, optical resonances exist up to third order when the particles circulate. Therefore a proper LEP working point of the magnetic fields was used in order not to reach certain resonant motions which would result in a partial loss of the beam current. The natural momentum spread of the beam and the so-called chromaticity effect can become so large that some part of the beam unavoidably hits dangerous resonance lines. Sextupoles with quadratic magnetic fields were installed to correct for this.

The longitudinal particle motion is determined by the RF system and the energy loss of the particles. The oscillations of the RF fields must be synchronous to the revolution frequency of the reference particle, which is 11.249 kHz. In the assumption of eight bunches per beam, this leads to a beam crossing each 11 μs. Radiation damping occurs due to continuous energy loss into synchrotron radiation :

$$E_{\text{loss}} = 8.85 \times 10^{-5} \frac{E_{\text{beam}}^4}{\rho} \text{ MeV (per turn)} \tag{2.1}$$

where E_{beam} is given in GeV and ρ is the radius of the curvature in km. This corresponds to around 2 GeV per turn at $\sqrt{s} = 200$ GeV. Damping of energy deviations originates from an energy dependence of the radiation. This constant exponential damping of betatron and synchrotron oscillation amplitudes determines the energy spread of the beam.

A central parameter of an accelerator is its delivered luminosity $\mathcal{L}$ which relates the event rate $\dot{N}$ of a given physical process to its cross-section σ by

[1] In Figure 2.2 the linear accelerators LIL1 and LIL2 are together denoted by LIL.

$$\dot{N} = \frac{dN}{dt} = \mathcal{L} \cdot \sigma \quad . \tag{2.2}$$

At all four interaction points dedicated detectors (the STIC for the DELPHI experiment) were installed to measure almost on-line the luminosity. This was provided from the measurement of the rate of Bhabha scattered e^+e^- pairs for scattering angles between 2 and 5 mrad. The cross-section of Bhabha scattering is well known and can be calculated precisely from QED theory. Typical numbers for luminosity at LEP2 are around $10^{31}\text{cm}^{-2}\text{s}^{-1}$, which produced a total integrated luminosity ($\int \mathcal{L}\text{dt}$) around 660 pb^{-1} for the LEP2 period for each experiment. Its breakdown into the relevant periods can be found in Table 2.2.

Normally data was taken at fixed beam energy points, ranging from $\sqrt{s} = 161$ up to almost 209 GeV. The LEP operation during the year 2000 was significantly different with respect to previous years [22]. This was motivated by the aim of delivering luminosity at the highest possible energies to exploit the search for the yet undiscovered scalar Higgs boson. The luminosity collected in a single experiment as a function of $\sqrt{s}$ for the year 2000 is shown in Figure 2.3, excluding the Z^0 calibration fills and some very limited running at 200 GeV. The mean energy was 205.9 GeV.

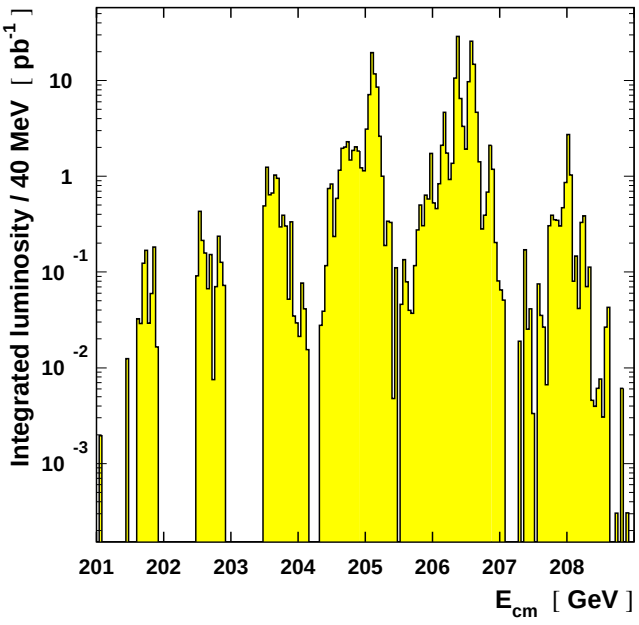

Figure 2.3: *The integrated luminosity in bins of $\sqrt{s}$ for a single LEP experiment in 2000.*

2.2 Determination of the LEP beam energy characteristics

2.2.1 Average beam energy

The direct measurement of the W boson mass at LEP2 requires a determination of the beam energy with the highest possible accuracy. The relative uncertainty on the beam energy translates into the same uncertainty on the measured m_{W} since the beam energy is used as a kinematic constraint to improve the mass resolution (see section 4.4). The energy scale calibration is based on the principle of resonant depolarization which is possible at beam energies ranging between 41 to 61 GeV. A magnetic extrapolation method is used to extract E_{beam} at LEP2 energies. Due to the significant systematic uncertainties of this extrapolation, independent alternative methods were developed by the LEP Energy Working Group to cross-check this technique. One approach was to install a dedicated beam spectrometer, a second one is the energy determination based on measurements of the energy loss and a third one uses radiative return events to the Z^0 pole to reconstruct directly the Z^0 resonance which is known to high precision.

Resonant depolarization

The knowledge of the LEP beam energy is provided by a measurement of the electron spin precession frequency. It uses the principle that the classical spin vector $\vec{S}$ of a relativistic electron moving perpendicular to a constant magnetic field $\vec{B}_0$ is conserved in the direction of the field ($\vec{1}_y$ in LEP coordinates, illustrated in Figure 2.4). The spin precession frequency around this field direction is constant. Due to synchrotron radiation of the circulating parti-

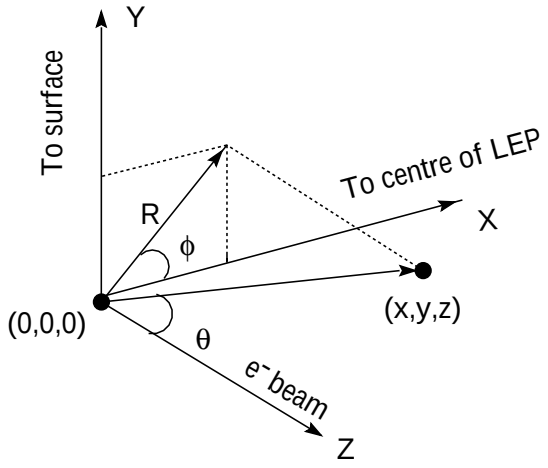

Figure 2.4: *Illustration of the Cartesian and polar coordinate systems used at LEP, the origin is the nominal interaction point or the geometrical center of the four LEP detectors. The z axis is along the electron flight direction, the x axis points toward the center of LEP, and the y axis points upwards.*

cles at LEP, a small probability to flip the direction of the spin of the particle radiating the photon does exist. Because this probability depends on the initial direction of the particles spin relative to the magnetic dipole field $\vec{B}_0$ a transverse polarization [2] ($\vec{1}_y$) is created. This transverse polarization can however be perturbed by applying a small magnetic field perpendicular to the main dipole bending field ($\vec{1}_x$). When this perturbation, generated by an RF-magnet, is oscillating in phase with the nominal spin precession frequency, we create a resonant transverse depolarization (RDP) effect. The spin rotations about the $\vec{1}_x$ direction add up coherently from turn to turn. This tilts the polarization vector away from its stable transverse direction $\vec{1}_y$. About 10^4 turns ($\approx$ 1 second) are needed to bring the polarization vector into the xz plane, or twice as much to flip its sign $\vec{1}_y \rightarrow -\vec{1}_y$. Small angle Compton scattering of circularly polarized laser light on the electron or positron beam was used to measure the polarization. The angular distribution of the back scattered photons depends on the known laser and the unknown electron beam polarization. Dedicated detectors were installed about 230 m from the interaction points to measure this distribution. When reversing the helicity of the circular polarization of the laser beam the center-of-gravity position of the showers induced by the back scattered photons is shifted proportionally to the polarization level of the beam.

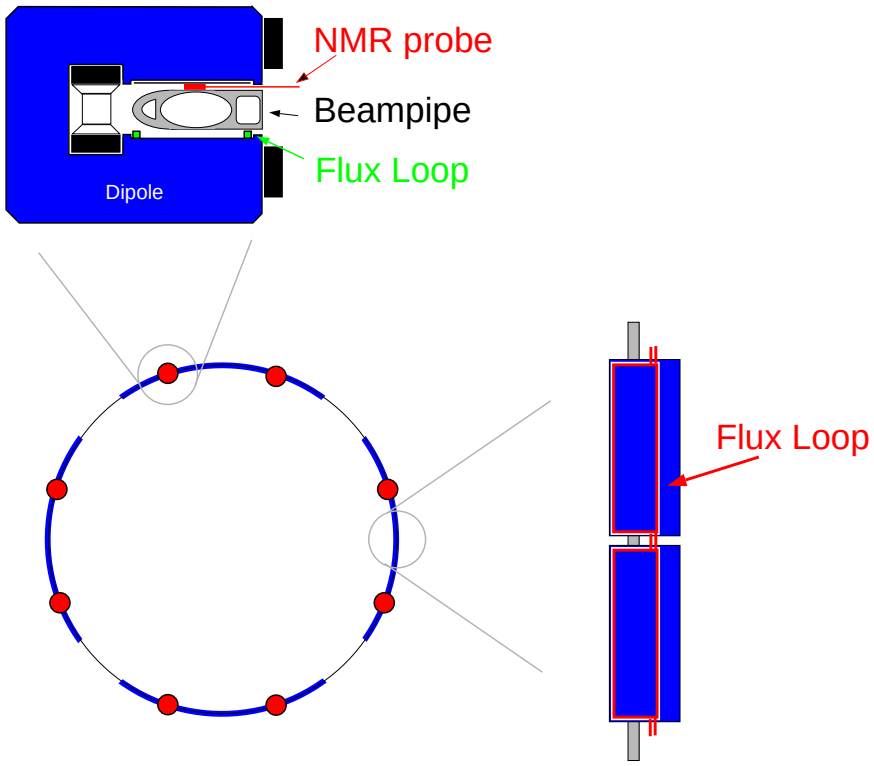

Figure 2.5: *Location of magnetic measurement devices in the LEP dipole magnets, with a cross-section of a dipole indicating the position of the NMR probes and flux loop cables.*

[2] The polarization vector is defined as the ensemble average of all spin vectors.

By changing the frequency of the RF-magnet and measuring the beam polarization, several RDP conditions can be found. From two subsequent RDP conditions the spin precession frequency ν can be inferred and the beam energy can be calculated from the relation :

$$\nu = \frac{g_e - 2}{2} \frac{E_{\rm beam}}{m_e c^2} \tag{2.3}$$

where $(g_e - 2)/2$ is the electron anomalous magnetic moment and m_e is its mass. The obtained uncertainty on the LEP beam energy was measured with a precision of better than 1 MeV, in a beam energy range from 41 to 61 GeV.

Unfortunately no significant spin polarization is naturally build up above 61 GeV, this due to incoherent depolarization effects caused by bremsstrahlung and which increase rapidly with the beam energy. Hence for the LEP2 phase extrapolation methods have to be used to obtain the beam energy. Nuclear Magnetic Resonance (NMR) probes were installed to measure continuously the local field inside the LEP bending structure, see Figure 2.5. The energy of a particle $E_{\rm beam}$ with charge e in a storage ring is proportional to this bending field B integrated along the ring l, in a good approximation we can define $E_{\rm beam}$ as :

$$E_{\rm beam} = \frac{ec}{2\pi} \oint_l B(s) ds \; . \tag{2.4}$$

The measured bending field is calibrated in each of the NMR probes with the energy measured by the RDP method in the $E_{\rm beam}$ range between 41 and 61 GeV to take local field

Source	Uncertainty [MeV]				Correlation
	1997	1998	1999	2000	
Extrapolation from NMR–polarization:					
NMR rms/$\sqrt{N}$ at physics energy	10	8	11	13	100%
Variations from calibration procedure	5	4	3	3	0%
Flux-loop test of extrapolation:					
NMR flux-loop difference at physics energy	20	15	15	15	100%
Field not measured by flux loop	5	5	5	5	100%
Polarization systematic	1	1	1	1	100%
e^+e^- energy difference	2	2	2	2	100%
Optics difference	4	6	4	4	50%
Corrector effects	3	4	2	13	50%
Tide	1	1	1	1	100%
Initial dipole energy	2	1	1	2	0%
Dipole rise modeling	1	1	1	1	100%
IP specific corrections ($\delta E_{\rm CM}/2$):					
RF model	4	4	5	5	100%
Dispersion	1	1	1	1	50%
Total	25	20	21	25	82%

Table 2.1: *List of contributions to the uncertainty on the LEP beam energy calibration including the correlation coeffi cients between 1999 and 2000 [22].*

variations outside the dipoles into account. By means of an extrapolation of the linear relation between the RDP measured beam energy and the NMR measured integrated bending field, the beam energy was determined during LEP2 running at higher energies.

To check the linearity of the NMR calibration, in each of the LEP main dipoles the bending field was measured with a flux loop. The induced voltage on the wire is proportional to the time derivative of the magnetic flux penetrating the area of the loop. Table 2.1 shows the evaluated systematic uncertainties on the LEP2 beam energy, not taking into account deviations from the alternative methods.

The LEP spectrometer

The concept of the spectrometer, which replaced one of the standard LEP dipoles, is based on the measurement of the bending angle of a particle beam passing through a magnetic dipole field. The beam energy is calculated from the dependence of the bending angle on the integral over the magnetic field and on the beam energy :

$$\theta \propto \frac{\int Bds}{E_{\mathrm{beam}}} \quad . \tag{2.5}$$

The bending angle of the beam is estimated by measuring the beam trajectories on both sides of the analyzing magnet in the field free parts of the spectrometer where 6 high precision beam position monitors or BPM's are placed. Magnetic field B and bending angle θ have to be measured with the needed accuracy for a high precision energy measurement. To obtain a relative uncertainty of $\Delta E/E = 1 \cdot 10^{-4}$ the beam position in the monitors has to be measured to 1 μm and the uncertainty on the magnetic field must not exceed $\Delta B/B = 3 \cdot 10^{-5}$. Figure 2.6 shows the layout of the LEP spectrometer. The comparison with NMR and polarization measurements have shown that the beam energy uncertainty of the spectrometer measurements was of the order of 15 MeV at LEP2 energies [23].

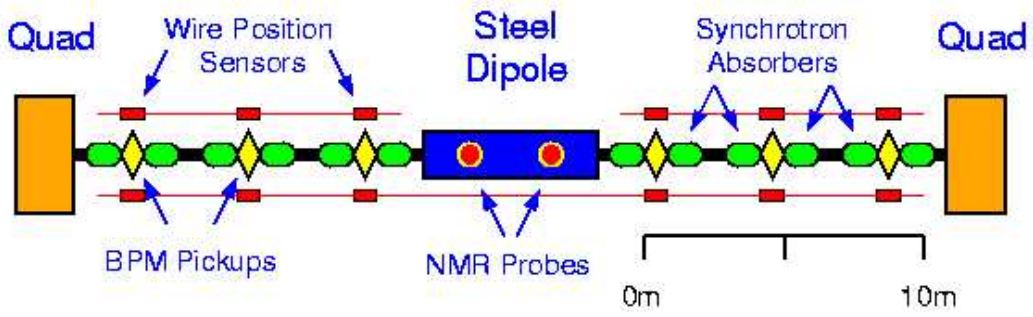

Figure 2.6: *The layout of the LEP spectrometer. The change in bending angle in the steel injection type dipole magnet is measured with three beam position monitors (BPM's) on both sides of the magnet. Each BPM is protected against synchrotron radiation from nearby dipoles by copper absorbers.*

Energy loss methods

This method exploits the energy dependence of well known synchrotron radiation, Equation 2.1. Whenever an observable x is sensitive ($\frac{\partial x}{\partial E_{\text{loss}}} \neq 0$) to the average beam energy loss per turn, E_{loss}, the beam energy itself can be inferred from it. A synchrotron tune Q_s is a machine working point obtained when the beam energy loss is exactly compensated by the accelerating field of the RF cavities. Particles with a momentum lower than the beam reference particle, will experience a stronger deflection in the dipole bending fields resulting in a shorter path length. Therefore they arrive earlier in the RF cavities positioned after the bending magnets and experience a higher voltage, which results in a momentum increase higher than the reference particle. This effect leads to a synchrotron oscillation around the phase ϕ_s of the synchronous reference particle, where the particle gains an energy equal to the energy loss per turn. Hence the synchrotron oscillation frequency Ω which depends in first order on the maximum amplitude V_0 of the voltage supply to an RF cavity, together with the revolution frequency ω_{rev} of particles can be used to estimate the beam energy. A quantitative definition of the synchrotron tune is

$$Q_s^2 = \left(\frac{\Omega}{\omega_{\text{rev}}}\right)^2 \propto \left(\frac{1}{E_{\text{beam}}}\right)\sqrt{e^2V_0^2 - E_{\text{loss}}^2} \ . \tag{2.6}$$

The beam energy was extracted by fitting this function to the measured values of Q_s at different setting for V_0. This method is again limited by systematical uncertainties up to the level of 15 MeV.

Radiative Return events

In this last method the beam energy was not determined indirectly via extrapolation techniques, but rather directly via the reconstruction of the effective centre-of-mass energy in radiative Z^0 production in the LEP2 energy range. In LEP2 events with fermion pair production $Z^0 \to f\bar{f}\gamma$, the photon radiated in the initial state reduces $\sqrt{s}$ to an effective centre-of-mass energy $\sqrt{s'}$. Through energy and momentum constraints, used in kinematic fits (similar to the one described in section 4.4), the distribution of $\sqrt{s'}$ is sensitive to the beam energy. It is peaked around $\sqrt{s'} \sim m_Z$ because the photon tends to reduce the energy scale $\sqrt{s}$ to m_Z due to the large on-shell cross-section of the non-radiative two fermion process $Z^0 \to f\bar{f}$. Fitting this pseudo Z^0-peak resulted in a value for the Z^0 boson mass, m_Z^{fit}, or an equivalent value for the beam energy, $E_{\text{beam}}^{\text{fit}}$. Any deviation of this inferred value from the precise measurement of m_Z at LEP1 was attributed to a discrepancy in the measurement of the beam energy via indirect methods, $E_{\text{beam}}^{\text{LEP}}$. Averaged over all data the following value was obtained [24]

$$\Delta E_{\text{beam}} = E_{\text{beam}}^{\text{fit}} - E_{\text{beam}}^{\text{LEP}} = -10 \pm 27 \pm 26 \text{ MeV} \tag{2.7}$$

where the first uncertainty is statistical and the second systematical. For the hadronic $q\bar{q}\gamma$ final states the dominant systematic uncertainties were the description of jet fragmentation and the reconstructed jet energy scale. In the leptonic channels the angular scale was the most important effect contributing to the systematic uncertainty.

Comparison of beam energy measurements

All results of the different beam energy measurements are still preliminary, nevertheless a comparison can be made. The extrapolation of the energy scale provided by the RDP method using the NMR measurements was tested by four complementary methods with different systematic uncertainties : the flux loop, the LEP spectrometer, the synchrotron tune Q_s and the indirect m_Z measurement via radiative return events. All of them are consistent with each other and with the NMR extrapolation [25], hence a combination of all this information will be performed in the near future. This will reduce the uncertainty on the beam energy and therefore also the systematic uncertainty it induces on the W mass measurement.

Year	Nominal $\sqrt{s}$ [GeV]	Spread on $\sqrt{s}$ [MeV]	Uncertainty on E_{beam} [MeV]	Integrated Luminosity pb^{-1}
1996	161.31	144 ± 7	27	9.93
1996	172.14	165 ± 8	30	9.98
1997	182.65	219 ± 11	25	54.07
1998	188.63	237 ± 12	20	157.64
1999	191.58	254 ± 13	21	25.85
1999	195.52	266 ± 13	21	76.41
1999	199.52	265 ± 13	21	83.37
1999	201.64	253 ± 13	21	40.64
2000	205.9	236 ± 12	25	223.89

Table 2.2: *The luminosity weighted centre-of-mass energy, its spread, the total uncertainty on the measured beam energy and the integrated luminosity estimated by DELPHI for the high-energy LEP2 data [22].*

2.2.2 Spread of beam energy

The spread in centre-of-mass energy is relevant in the evaluation of the width of the W boson. The natural momentum spread of the particles (cfr. synchrotron oscillations) in a bunch induces a statistical random variation on the centre-of-mass energy $\sqrt{s}$ of particle collisions. The beam energy spread can be predicted for particular settings of beam optics, beam energy and RF frequency shift. Weighting the prediction with the DELPHI integrated luminosity gives the average predicted values in Table 2.2 for each nominal centre-of-mass energy. The beam energy spread can also be derived from the longitudinal bunch size σ_z measured by the experiments via the relation

$$\sigma_{E_{\mathrm{beam}}} = \frac{\sqrt{2}E_{\mathrm{beam}}}{\alpha R_{\mathrm{LEP}}} Q_s \sigma_z \tag{2.8}$$

where α is the momentum compaction factor related to the synchrotron oscillation effect, R_{LEP} is the average radius of the LEP accelerator and Q_s the incoherent synchrotron tune [22]. The beam energy spread must be multiplied by $\sqrt{2}$ to give the centre-of-mass energy spread.

2.3 The DELPHI detector

The **DE**tector with **L**epton, **P**hoton and **H**adron **I**dentification or DELPHI is a general purpose detector for e^+e^- physics, designed to provide high granularity over a 4π solid angle. The detector consists of a cylindrical section covering the 'barrel' region (typically in a θ range between 40^o and 140^o) and two endcaps covering the 'forward' regions. The general layout is schematically shown in Figure 2.7. The overall length and diameter are over 10 m and the total weight is about 3500 tons. The components or subdetectors used in DELPHI are described and commented in [26]. They can be subdivided into detectors used for track reconstruction or momentum measurement, calorimetry or energy measurement, particle identification and detectors for triggering purposes.

2.4 Track reconstruction and momentum measurement

Particles are mainly detected via their electromagnetic interaction with matter. Relativistic charged particles, other than electrons, lose energy in matter through the Coulomb interaction with the atomic electrons of the material. The energy transferred to the electrons causes them either to be ejected from the parent atom (ionization) or to be excited to a higher level (excitation). These ionizations and de-excitations were detected by the various tracking devices within the DELPHI detector. The momentum of the charged particle was measured by reconstructing its trajectory in a uniform solenoidal magnetic field. The curvature of the particle, ρ, is related to its transverse momentum p_t and to the magnetic field $\vec{B}$:

$$p_t[\mathrm{GeV/c}] = 0.3\ |\vec{B}[\mathrm{T}]| \cdot \rho[\mathrm{m}]\ . \tag{2.9}$$

Obviously the better you measure the curvature, the better the resolution on the particles momentum. The relative resolution will typically be, for N equidistant measuring points [27]:

$$\frac{\sigma(p_t)}{p_t} = \frac{\sigma(x)p_t}{0.3|\vec{B}|L^2}\sqrt{\frac{720}{N+4}} \tag{2.10}$$

where L is the radial distance between the first and last measuring point in the detector. The relative uncertainty on the momentum of a charged particle is increasing with its momentum. For low momentum particles ($|\vec{p}| \leq 1$ GeV/c) the effect of multiple scattering becomes important and dominates the relative uncertainty.

Within DELPHI the superconducting solenoid had a length of 7.4 m and an inner diameter of 5.2 m. It produced an axial magnetic field of 1.23 T by a single conductor layer carrying a current of 5000 A. Only in the 35 cm long end sections a second layer with optimized currents was used to increase the azimuthal field homogeneity in the range $z \in \{-2\mathrm{m}; 2\mathrm{m}\}$ to the level of 0.1%. The residual radial component of the magnetic field was smaller than 5 Gauss, which is negligible compared to the axial component of 12334^{+1}_{-10} Gauss (indicating a weak axial asymmetry). This magnetic field bended the trajectory of each charged particle into a spiral whose radius is proportional to the momentum of the particle (Equation 2.9).

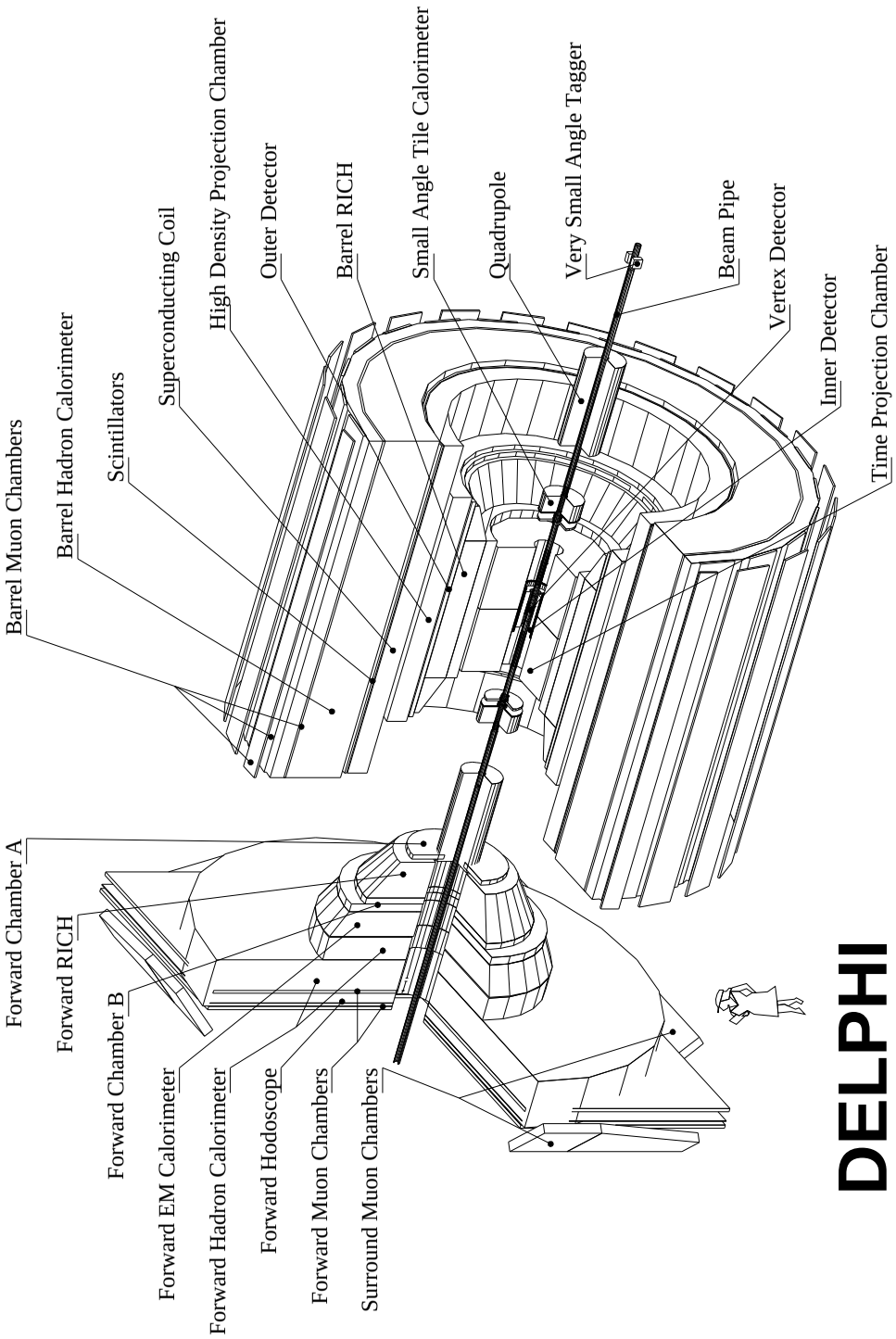

Figure 2.7: *Schematic overview of the DELPHI detector.*

In the barrel part of the detector the Vertex Detector (VD), the Inner Detector (ID), the Time Projection Chamber (TPC), the Outer Detector (OD) and the Barrel Muon Chambers (MUB) and in the forward part the Forward Chambers A and B (FCA and FCB), the Very Forward Tracker (VFT), the Forward Muon Chambers (MUF) and the Surround Muon Chambers (SMC) were devoted to a precise measurement of these trajectories, and hence to the precise determination of the directions and momenta of the charged particles. More specifications about these tracking chambers can be found in Table 2.3. The space between the TPC and OD was used by the RICH particle identification detector and limits the size of our TPC compared with other LEP experiments.

In a first stage, the DELPHI reconstruction program called DELANA [28] decoded the raw data from each subdetector, applied calibrations and where possible performed a local pattern recognition. The global track search algorithm used in the barrel region continues with these track segments seen in the TPC and extrapolates inwards and outwards to form candidate strings of track elements with the ID and OD. During the last 2 months of data taking (from September 1st 2000 onwards) one of the azimuthal sectors of the TPC covering 1/12 of the 4π solid angle ceased operation, hence tracking started from the information of the VD and ID during that period [29]. In the forward region two additional algorithms were used. One based on the transformation of the helical track trajectory in the plane perpendicular to the magnetic field into a straight line, and another one based on the information provided by the FCB and the beamspot.

Within this global track search the alignment of the tracking detectors was of major importance. Within DELPHI the OD was chosen as reference because of its Rϕ resolution and its good time stability. The position of the VD with respect to the OD was determined assuming that the two muons in $Z^0 \rightarrow \mu^+\mu^-$ events form single tracks. This was one of the reasons to collect each year data at the well known Z^0 peak, during the so-called calibration runs. The ID and TPC were aligned according to the reference tracks formed by the VD and OD, imposing a fixed momentum but relaxing the collinearity constraint. After fixing the barrel alignment, the muon tracks reconstructed in the TPC were extrapolated to the forward region to align the forward tracking chambers FCA and FCB.

All strings of track elements found by the above global search techniques were passed through the full track fitting processor based on Kalman filter techniques and accounts for multiple scattering and energy loss in the material between the measurements. The information from the calorimeters will associate clusters of energy to the reconstructed charged particle tracks and create so-called neutral tracks from the remaining clusters.

The obtained momentum resolution was measured from the inverse momentum spectrum of muons from $Z^0 \rightarrow \mu^+\mu^-$ events in which the acollinearity of the two muons was below 15^o (to remove radiative Z^0 decays) and whose tracks contain information from all the barrel detectors (VD, ID, TPC, OD). The precise knowledge of the beam energy was taken as the exact value of the momentum expected for those muons, hence the variance on the $\frac{1}{p}$ observable gave a direct measure for the tracking resolution. A width of

$$\sigma\left(\frac{1}{p}\right) = 0.57 \cdot 10^{-3} \frac{\mathrm{c}}{\mathrm{GeV}} \tag{2.11}$$

was obtained for the tracks in the barrel region [26]. In the forward region the resolution was worse, obtaining a value of

$$\sigma\left(\frac{1}{p}\right) = 2.7 \cdot 10^{-3} \frac{\mathrm{c}}{\mathrm{GeV}} \tag{2.12}$$

for the most forward region $\theta \leq 25^o$. The momentum resolution depended on the momentum itself (Equation 2.10), therefore the precision obtained on the track parameters at other momenta than $\frac{m_{Z^0}}{2}$ can only be estimated by comparing the simulated and reconstructed parameters in a sample of generated Z^0 hadronic decays.

Tracking detectors					
	Position		Coverage	No.points along track	Resolution per point
	R [cm]	|z| [cm]	θ [deg]		[mm]
VD	6.3,9.0,10.9	≤ 24	25 - 155	3	$R\phi$: 0.0076
				2	z : (6 + $\|cotg(\theta)\|$·16) 10^{-3}
ID-j	11.8 - 22.3	≤ 40	17 - 163	24	$R\phi$: 0.09
ID-t	23 - 28	≤ 50	30 - 150	5	$z(\theta)$: ≤ 1
TPC	29 - 122	≤ 134	20 - 160	16	$R\phi$: 0.25
				192	z : 0.88
OD	197 - 206	≤ 232	42 - 138	5 ·$R\phi$	$R\phi$: 0.11
				3 · z	z : 44
MUB	445,485	≤ 385	53 - 88.8 ; 91.5 - 127	2 (+2)	$R\phi$: 1.
					z : 10
VFT			10 - 26 ; 155 - 170	4	x, y :
FCA	30 - 103	155 - 165	11 - 32 ; 148 - 169	2 ·(x, u, v)	x, u, v : 0.3
FCB	53 - 195	267 - 283	11 - 36 ; 144 - 169	4 ·(x, u, v)	x, u, v : 0.25
MUF	70 - 460	463,500	20 - 42 ; 138 - 160	(2+2) ·(x, y)	x, y : 5.0
SMC	550	487	42 - 53	2	10.0 x 10.0

Calorimeters					
	Position		Coverage	Granularity	Shower Resolution
	R [cm]	|z| [cm]	θ [deg]		(σ_E/E) [%]
HPC	208 - 260	≤ 254	43 - 137	$\phi \sim 1^o$,z : 4 mm	1.1 $\oplus \frac{23}{\sqrt{E}}$
FEMC	46 - 240	284 - 340	10 - 36.5	ϕ : 1^o,θ : 1^o	0.35 $\oplus \frac{5}{\sqrt{E}} \oplus \frac{6}{E}$
HCAL	(B) 320-479	≤ 380	10 - 170	ϕ : 3.75^o,θ : 3.0^o	0.21 $\oplus \frac{1.12}{\sqrt{E}}$
	(FW) 65-460	340 - 489		ϕ : 3.75^o,θ : 2.6^o	

Table 2.3: *In the upper part of the table the specifications and performances of the tracking detectors [26] are quoted, where ID-j denotes the jet-chamber part of the Inner Detector and ID-t the sense wire part used by the trigger. The specifications and performances of the calorimeters are found in the bottom part. The different parts of the shower resolution are defined in Equation 2.13 and the coordinate system is defined in Figure 2.4.*

2.5 Calorimetry

Different from the momentum measurement, the energy measurement or calorimetry is a destructive method based on the total absorption of the particles energy in a block of material, combined with spatial reconstruction. The deposited energy of the charged or neutral particles is rendered measurable by ionization or excitation of the atoms of the matter in the active medium. The measurable energy or detector response is usually linearly proportional to the incident energy. This approximation could introduce systematic uncertainties in the measurement performed in this thesis and is discussed in section 6.3.4.

A distinction can be made between electromagnetic calorimeters, detecting cascades initiated by leptons or photons, and hadronic calorimeters, detecting cascades initiated by charged or neutral hadrons. Hadronic showers are much longer and broader than electromagnetic ones, hence their spatial separation resolutions are worse. The energy resolution of calorimeters is generally parametrized as :

$$\frac{\sigma(E)}{E} = \frac{a}{\sqrt{E}} \oplus \frac{b}{E} \oplus c \tag{2.13}$$

where one should take the square root of the quadratic sum of the three terms. The first term is the stochastic term and accounts for statistical fluctuations in the number of primary and independent signal generating processes. The second term includes electronic noise and fluctuations in energy carried by particles other than the one of interest entering the measurement area (so-called pile up). The last constant term is a quality term reflecting for example the uncertainty in the calibration of the calorimeter.

The electromagnetic calorimetry system within the DELPHI detector is composed of the High-density Projection Chamber (HPC) in the barrel, the Forward ElectroMagnetic Calorimeter (FEMC) in the forward region and two very forward calorimeters, the Small angle TIle Calorimeter (STIC) and the Very Small Angle Tagger (VSAT). The latter two are used mainly for luminosity measurements. In order to achieve complete hermeticity for high energy photon detection, additional scintillators have been installed in the cable duct region between barrel and each endcap and between the HPC modules.

Only one Hadron CALorimeter (HCAL) was installed within the DELPHI detector. It was primarily used to measure the energies of jets and hence the most important quantities that characterize them are the jet energy resolution, energy linearity and missing transverse energy resolution (cfr. section 4.4).

2.6 Collection of data

With eight bunches of electrons and positrons circulating at equal distances in the machine, the LEP bunch-crossing interval is 11 μs. Therefore every 11 μs there is the potential to create an interesting detectable event which has a typical readout time of 3 ms. In order to cope with high luminosities and large background rates, a trigger system [30] is applied which is composed out of four successive levels (T1, T2, T3 and T4) of increasing selectivity.

In addition to the above mentioned detectors, two scintillator counters, the Time Of Flight

(TOF) in the barrel and the HOrizontal Flight tagger (HOF) in the forward part of the detector, were installed. They were used for a fast trigger of beam events and cosmic radiation.

The first trigger level T1 is based on the fastest tracking detectors and the scintillators, which are making a loose pre-decision within 3.5 μs. The T2 trigger decision is available 39 μs after the bunch-crossing and uses apart from complementary information from major detectors as the TPC, HPC and the MUF, also combinations of signals from different sub-detectors. The T3 and T4 levels are software filters performed asynchronously with respect to the bunch-crossing. Together they reduce the residual background left after the T2 level by a factor four. The final event rate after the T4 trigger level was a few Hz. The dead-time introduced by T1 and T2 is typically 3% and is an important quantity when estimating the integrated luminosity via Bhabha events, but will not introduce any systematic uncertainty on the results presented in this thesis.

For all events passing this trigger configuration, the raw data from each sub-detector is collected by the DELPHI data acquisition system and together with the parameters reflecting the detectors' status it was stored. The off-line reconstruction program DELANA performs the tracking and energy cluster reconstruction as described in previous sections and writes its output on Data Summary Tapes (DST) available for physics analysis. The common DELPHI software packages PHDST [31] interfaced with the SKELANA framework [32], are the primary tools used when starting a data analysis. The DELPHI simulation program DELSIM [33] produces Monte Carlo generated events in the same format as the real data, taking into account the response functions of the complicated detector.

Chapter 3

Theory and phenomenology of $e^+e^- \to W^+W^-$ events

The description of the production of a multi-particle final state in collisions between elementary particles can be subdivided chronologically into four different parts (Figure 3.1): the electroweak elementary process, the parton shower in the perturbative phase-space, the probabilistic fragmentation process in the confined phase-space and the decays of long or short lived resonances. A brief discussion of each of these production steps is discussed in this chapter. Section 3.6 describes a Monte Carlo tuning of the most important model parameters in JETSET including the effect of Bose-Einstein Correlations modeled by the LUBOEI algorithm.

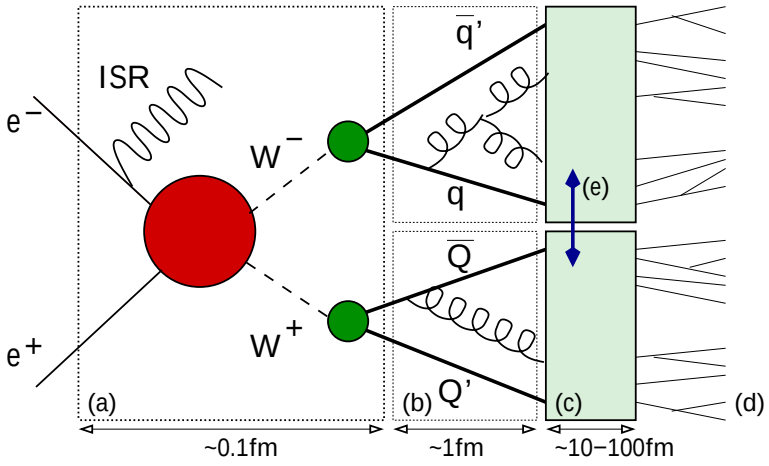

Figure 3.1: *Illustration of the factorization properties of the evolution of the $e^+e^- \to W^+W^- \to q\bar{q}Q\bar{Q}$ process. The primary partons are created in the electroweak hard process (a) and fragment according to perturbative theory (b). In the confined region (c) colour singlets are formed which can be long lived resonances decaying later in the process (d). The possible existence of cross-talk effects like inter-W Bose-Einstein Correlations and Colour Reconnection between both W systems is denoted by (e).*

3.1 Monte Carlo simulation

The hypothetical population of a set of observables, $\vec{\Omega}$, is extracted from a theory about the physical process under investigation and its physical unknown parameters $\vec{\alpha}$ by means of a probability density function (p.d.f.) which is the square of the matrix elements $|\mathcal{M}(\vec{\Omega};\vec{\alpha})|^2$ in our case. These matrix elements generated by the perturbative theory are masked by the response function $R(\vec{\Omega},\vec{\Omega}';\vec{\alpha}\,')$ depending on different parameters $\vec{\alpha}\,'$ most of the time non-physical and factorisable from the real physics parameters of interest $\vec{\alpha}$. With this information one can analytically calculate the average of an event quantity, for example its mean energy E :

$$< E(\vec{\alpha}) > = \frac{\int d\vec{\Omega} E(\vec{\Omega}) \int d\vec{\Omega}' R(\vec{\Omega},\vec{\Omega}';\vec{\alpha}\,') \cdot |\mathcal{M}(\vec{\Omega}';\vec{\alpha})|^2}{\int d\vec{\Omega} \int d\vec{\Omega}' R(\vec{\Omega},\vec{\Omega}';\vec{\alpha}\,') \cdot |\mathcal{M}(\vec{\Omega}';\vec{\alpha})|^2} \quad . \tag{3.1}$$

Where the energies E($\vec{\Omega}$) of an infinite number of hypothetical events are weighted according to their matrix elements with unknown but fixed parameters $\vec{\alpha}$ convoluted with the response function $R(\vec{\Omega},\vec{\Omega}';\vec{\alpha}\,')$. This, one can repeat for each value of the parameters $\vec{\alpha}$ and compare the results with the mean event energy E measured from the data. The main problem of this method is that the analytic expression of E($\vec{\Omega}$) for each value of $\vec{\Omega}$ must be calculable. This is often not the case.

The term Monte Carlo collects all calculation techniques which make use of random numbers. These random numbers are used as sampling points in the parameter space $\vec{\alpha}\,'$ to create a finite sample of events $\vec{\Omega}_i$ with i $\in$ {1,...,n} according to a hypothetical population $\int d\vec{\Omega}' R(\vec{\Omega},\vec{\Omega}';\vec{\alpha}\,') \cdot |\mathcal{M}(\vec{\Omega}';\vec{\alpha})|^2$ depending on the fixed physical parameters $\vec{\alpha}$. From these random samples the probability distribution and its moments, like for example the mean value of the events energy E, can be inferred and a random or so-called statistical uncertainty can be obtained on their values :

$$< E(\vec{\alpha}) > = \frac{1}{n} \sum_{i=1}^{n} E(\vec{\Omega}_i;\vec{\alpha}) \quad . \tag{3.2}$$

Again these values can be compared with the one measured from data and information can be inferred about the physical parameters $\vec{\alpha}$.

In the case of the $e^+e^- \to W^+W^- \to q\bar{q}'Q'\bar{Q}$ events of interest the response function can be factorized in a chain of convolutions, for example the parameters describing the Initial State Radiation, the Parton Shower, the hadronization, the decay of the resonances and the detector response can be integrated separately. An important consequence of this factorization into f pieces is that also systematic uncertainties on the measurement due to uncertainties on the parameters $\vec{\alpha}\,' = (\vec{\alpha}\,'^{\,1},...,\vec{\alpha}\,'^{\,f})$ or the functions $R_k(\vec{\Omega}^k,\vec{\Omega}^{k+1};\vec{\alpha}\,'^{\,k})$ with k $\in$ {1,...,f} factorize.

In the rest of this chapter the factorized parts in this chain will be discussed and where needed the important parameters $\vec{\alpha}\,'$ will be indicated. In section 3.6 it will be shown that this factorization hypothesis is only an approximation to simplify the Monte Carlo production of $e^+e^- \to W^+W^- \to q\bar{q}'Q'\bar{Q}$ events and the study of systematic uncertainties on the measurement of $\vec{\alpha}$.

3.2 Electroweak properties of the hard event

The nature of the hard $e^+e^- \to W^+W^-$ process will determine the main topology of the event. Differential cross-sections and quantum-mechanical amplitudes of several processes can be determined by use of perturbative Feynman calculus in quantum field theory. However a full perturbative calculation including all higher orders is nowadays not possible. A short overview of the state-of-the-art is presented, starting with on-shell or stable W pair production in lowest order. A logical next step beyond the on-shell limit is to treat the W bosons as resonances with a finite width. Finally, attempts to include higher order radiative corrections are described.

3.2.1 On-shell W pair production

At Born level or in lowest order perturbation only three diagrams, shown in Figure 3.2, contribute to the Charged Current or CC03 cross-section for W^+W^- production. The infrared divergent t-channel diagram involves a ν_e exchange and therefore contributes only for left-handed electrons. The two s-channel diagrams contain the non-Abelian triple gauge-boson couplings and contribute for both helicities of the electron. The Higgs-exchange diagram is suppressed by a factor m_e/M_W and is thus completely negligible. Since this CC03 cross-section is based on a subset of diagrams it is gauge-dependent and therefore not an observable. The 6 interference terms between the various graphs show all the cancellation properties of a renormalizable gauge theory. The combined amplitude or matrix-element $\mathcal{M}$, which represents the actual interactions dynamics among the particles in the S-matrix scattering formalism, is therefore infra-red safe and usually defined in the 't Hooft gauge. They can be organized into two gauge-invariant subsets [34] :

$$\mathcal{M}_{Born}(\kappa,\lambda_+,\lambda_-,\vec{p}\,) = \frac{e^2}{2sin^2\theta_W}\mathcal{M}_I(\kappa,\lambda_+,\lambda_-,\vec{p}\,)\delta_{\kappa-} + e^2\mathcal{M}_Q(\kappa,\lambda_+,\lambda_-,\vec{p}\,) \qquad (3.3)$$

where the arguments indicate the momenta and helicities of the incoming fermions and outgoing bosons ($\kappa_i = \pm\frac{1}{2}$, $\lambda_i = 1,0,-1$). The Weinberg mixing angle θ_W was introduced in section 1.2. The Kronecker $\delta_{\kappa-}$ function is 1 for left-handed electrons and 0 for right-handed electrons. The gauge invariant contributions $\mathcal{M}_I$ and $\mathcal{M}_Q$

$$\mathcal{M}_I(\kappa,\lambda_+,\lambda_-,\vec{p}\,) = \frac{1}{t}\mathcal{M}_1^\kappa(\lambda_+,\lambda_-,\vec{p}\,) + \frac{1}{s-M_Z^2}2\left[\mathcal{M}_3^\kappa(\lambda_+,\lambda_-,\vec{p}\,) - \mathcal{M}_2^\kappa(\lambda_+,\lambda_-,\vec{p}\,)\right]$$

$$\mathcal{M}_Q(\kappa,\lambda_+,\lambda_-,\vec{p}\,) = \left[\frac{1}{s} - \frac{1}{s-M_Z^2}\right]2\left[\mathcal{M}_3^\kappa(\lambda_+,\lambda_-,\vec{p}\,) - \mathcal{M}_2^\kappa(\lambda_+,\lambda_-,\vec{p}\,)\right] \qquad (3.4)$$

are accompanied by different coupling constants, one of which involving the electromagnetic coupling constant e, the other the charged current coupling constant $e/(\sqrt{2}\sin\theta_W)$. Whereas $\mathcal{M}_I$ corresponds to the pure $SU(2)$ isospin contribution, the parity conserving or electromagnetic contribution $\mathcal{M}_Q$ is a result of the symmetry-breaking mechanism. The term $\mathcal{M}_1^\kappa$ corresponds to the t-channel, while the terms $\mathcal{M}_2^\kappa$ and $\mathcal{M}_3^\kappa$ correspond respectively to the

s-channel γ and Z^0 annihilation. The cross-sections for the s-channel processes are proportional to β_W^3, where $\beta_W = \sqrt{1 - \frac{4m_W^2}{s}}$ is the boost of the W boson, while the t-channel is proportional to β_W making it the dominant diagram at energies close to threshold.

The asymmetric behavior of the differential cross-section as a function of the W production angle θ is an important property to probe the Yang-Mills form of the triple gauge boson couplings. It will be used to differentiate between the reconstructed W^+ and W^- in chapter 5.

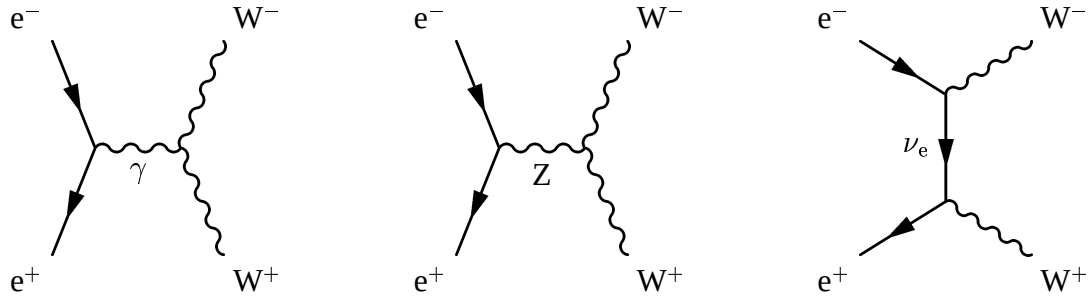

Figure 3.2: *Dominant lowest order diagrams for on-shell $e^+e^- \to W^+W^-$ production.*

3.2.2 Off-shell W pair production

Four-fermion production as the one studied in this thesis involves fermions in the initial and final state and unstable gauge bosons as intermediate particles (neglecting photons in the final state for the moment). If complete sets of Feynman diagrams contributing to a given process are taken into account, the associated matrix elements are gauge-invariant. This is however not the case when we only consider the CC03 doubly resonant diagrams shown in Figure 3.3. One has to include all double and single resonant (some of them are shown in Figure 3.4) and finally all non-resonant diagrams in order to obtain a manifestly gauge-independent result for the W pair production cross-section.

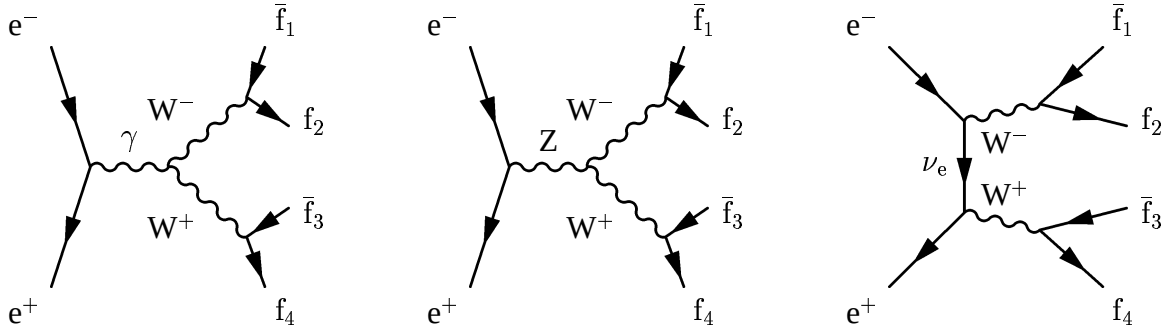

Figure 3.3: *Dominant lowest order diagrams for the process $e^+e^- \to W^+W^- \to \bar{f}_1 f_2 \bar{f}_3 f_4$.*

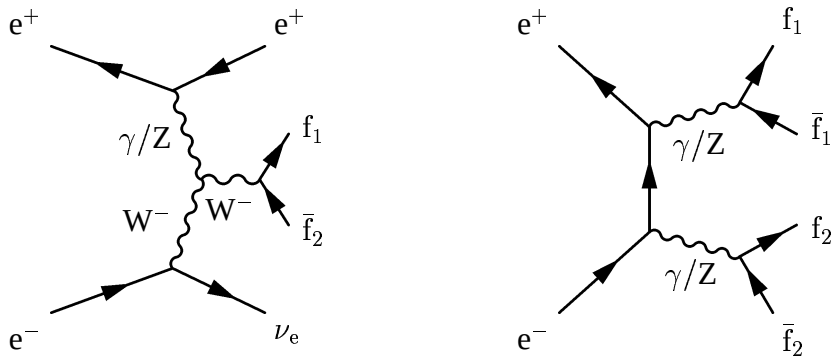

Figure 3.4: *Example of a single W production diagram (left) and a neutral current doubly-resonant ZZ process (right). These diagrams interfere with WW diagrams as they are leading to the same 4-fermion final states.*

In addition the unstable gauge bosons that appear as intermediate particles can give rise to poles $1/(p^2 - M^2)$ in physical observables if they are treated as stable particles. This can be cured by introducing a finite width Γ for these resonances. The on-shell CC03 cross-section must be convoluted over the available phase-space with the Breit-Wigner densities ρ_W in order to obtain the leading-order off-shell cross-section

$$\sigma(s) = \int_0^s ds_- \rho_W(s_-) \int_0^{(\sqrt{s}-\sqrt{s_-})^2} ds_+ \rho_W(s_+) \sigma_0(s; s_-, s_+) \tag{3.5}$$

where $s_\pm$ are the virtualities or invariant mass squared $k^\mu k_\mu$ of the internal $W^\pm$ bosons and σ_0 is the on-shell cross-section at hypothetical values of the W masses fixed by $\sqrt{s_-}$ and $\sqrt{s_+}$. The relativistic Breit-Wigner densities $\rho_W(s_\pm)$ contain the finite width of the W boson. Although not being theoretically justified, two intuitive schemes of introducing the finite W width are used. In the fixed width scheme one approximates $\Gamma_W(s_\pm)$ in the W propagator as being constant $\Gamma_W(s_\pm) \equiv \overline{\Gamma}_W \overline{m}_W$

$$\rho_W(s_\pm) = \frac{1}{\pi} \frac{\overline{\Gamma}_W \overline{m}_W}{(s_\pm - \overline{m}_W^2)^2 + \overline{m}_W^2 \overline{\Gamma}_W^2} \tag{3.6}$$

hence violating unitarity. In the running width scheme, the one used for this thesis, an energy dependent width $\Gamma_W(s_\pm) \equiv \frac{s_\pm}{m_W^2} \Gamma_W(m_W^2)$ where $\Gamma_W(m_W^2) \equiv \Gamma_W$ is used

$$\rho_W(s_\pm) = \frac{1}{\pi} \frac{\Gamma_W}{m_W} \frac{s_\pm}{(s_\pm - m_W^2)^2 + m_W^2 \Gamma_W^2(s_\pm)} \tag{3.7}$$

which does not violate unitarity but still is not gauge invariant. At LEP1 the Z^0 lineshape was fitted according to this definition and the same convention is used for the presentation of LEP2 W mass results. Both Breit-Wigner shapes are equivalent, provided that the mass and the width parameters satisfy the following transformation:

$$\overline{m}_W = m_W / \sqrt{1 + \frac{\Gamma_W^2}{m_W^2}} \approx m_W \left(1 - \frac{1}{2}\frac{\Gamma_W^2}{m_W^2}\right) \approx m_W - 26.9\,\mathrm{MeV}/c^2 \qquad (3.8)$$

$$\overline{\Gamma}_W = \Gamma_W / \sqrt{1 + \frac{\Gamma_W^2}{m_W^2}} \approx \Gamma_W \left(1 - \frac{1}{2}\frac{\Gamma_W^2}{m_W^2}\right) \approx \Gamma_W - 0.7\,\mathrm{MeV}/c^2 \ . \qquad (3.9)$$

After introducing the finite W width, the off-shell differential cross-section of $e^+e^- \to W^+W^- \to f_1\bar{f}_2 f_3 \bar{f}_4$ production as a function of the invariant masses of both W bosons has a double resonant shape. This shape is truncated due to the limited phase-space allowed by the collision energy $\sqrt{s}$ in the centre-of-mass system:

$$\forall\{m_{W^+}, m_{W^-}\} : m_{W^+} + m_{W^-} \leq \sqrt{s} \ . \qquad (3.10)$$

The infinite set of matrix elements in the parameter space reflect therefore the absolute probabilities which generate this truncated two-dimensional Breit-Wigner probability density function.

Knowing the decay properties of the W boson, we can separate the production of $W^+W^- \to f_1\bar{f}_2 f_3 \bar{f}_4$ final states into three channels and estimate their energy independent branching ratios :

- The $q\bar{q}'Q'\bar{Q}$ or fully hadronic final state with BR $\simeq$ 45.6 % ;
- The $q\bar{q}l\nu_l$ or semi-leptonic final state with BR $\simeq$ 43.9 % ;
- The $l\nu_l l\nu_l$ or fully leptonic final state with BR $\simeq$ 10.5 %.

Because the neutrino cannot be detected directly, the events which decay according to the fully hadronic channel contain in principle the most kinematic information. This thesis presents a reconstruction technique together with its systematic uncertainties for a measurement of m_W and Γ_W from fully hadronic decaying W^+W^- events.

3.2.3 Radiative corrections

To improve the theoretical predictions of the four fermion processes in the phase-space regions accessible at LEP2 energies one needs to include radiative corrections on these processes [1]. This is rather complex due to the number of Feynman diagrams involved, but it is important as it affects the W mass analysis due to for example radiated photons. The calculation of $\mathcal{O}(\alpha)$ electroweak corrections for four fermion processes is at present only available for the W^+W^- signal in Double Pole Approximation (DPA) and is only implemented in the Monte Carlo generators RacoonWW [36] and YFSWW [37] . The DPA approximation of the lowest-order cross-section emerges from the CC03 diagrams upon projecting the W boson momenta in the matrix elements to their on-shell values. One usually retains only

[1] A complete overview can be found in the report of the LEP2 Monte Carlo Workshop held at CERN from 1999 to 2000 [35].

those terms with the highest degree of double resonance. The radiative corrections to the four fermion processes consist of virtual corrections, resulting from loop diagrams, as well as of real corrections. Real photon radiation originates from the process :

$$e^+e^- \to W^+W^-[\gamma] \to \bar{f}_1 f_2 \bar{f}_3 f_4 \gamma \tag{3.11}$$

where in the intermediate state there may or may not be a photon. For this process there are two types of contributions to both corrections, the factorisable (Figure 3.5) and the non-factorisable (Figure 3.6) ones. The former are the ones where the one-loop corrections can be associated either to the production of the W boson pair or to the decay subprocesses. The latter are the ones that connect these subprocesses and therefore do not have two separate W propagators as factors in their matrix elements.

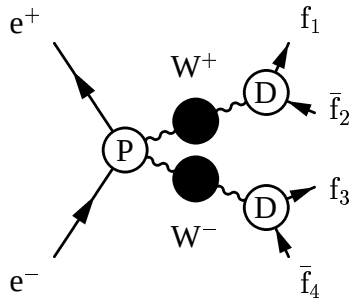

Figure 3.5: *The generic structure of the virtual factorisable corrections to W pair production. The shaded circles indicate the Breit-Wigner resonances, whereas the open circles denote the Green functions for the on-shell production (P) and on-shell decay (D) subprocesses up to $\mathcal{O}(\alpha)$ precision.*

- RacoonWW : The full DPA method is used to estimate the virtual $\mathcal{O}(\alpha)$ corrections to the four fermion process, hence without any further approximations. The real photonic corrections are calculated in the full matrix element of the process 3.11, while the higher order Initial State Radiation corrections are treated via the structure function approach.

- YFSWW : Full $\mathcal{O}(\alpha)$ electroweak radiative corrections of real photons to the on-shell W^+W^- production stage are included with the Yennie-Frautschi-Suura (YFS) exponentiation to leading-logarithmic approximation. In this YFS framework a master formula is used to calculate the cross-section. The Initial State Radiation corrections are calculated to $\mathcal{O}(\alpha^3)$. The Final State Radiation is externally generated by the dedicated program PHOTOS [38] up to $\mathcal{O}(\alpha^2)$ again in the leading-logarithmic approximation and normalized to the W branching ratios.

The resulting cross-section using the DPA method, which has uncertainties around 0.5%, is found to be 2.5 to 3% smaller than the CC03 one. This is a significant effect since the combined LEP accuracy on the measured cross-section is around 1 %. The combined LEP data

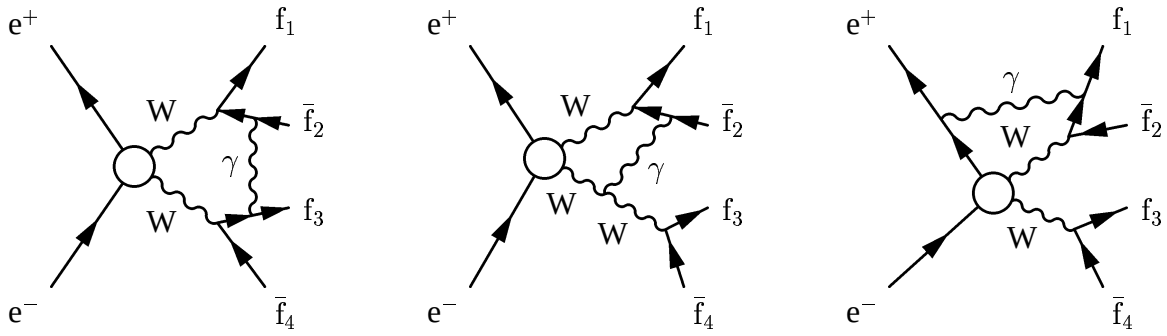

Figure 3.6: *Examples of virtual non-factorisable corrections to W pair production. The open circles denote the lowest-order Green functions generating the virtual W boson pair.*

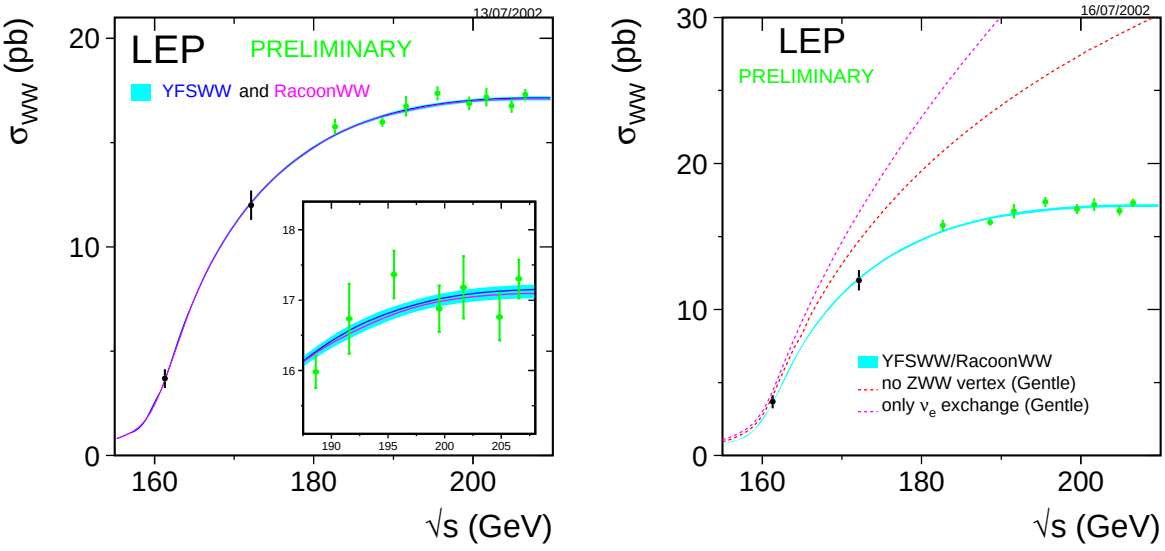

(a) (b)

Figure 3.7: *In plot (a) the measurements of the CC03 W-pair production cross-section are compared to the predictions of RacoonWW and YFSWW. The shaded area represents the uncertainty on the estimated theoretical predictions, amounting $\pm 2\%$ for $\sqrt{s} < 170$ GeV and ranging from 0.7 to 0.4% above 170 GeV. Plot (b) illustrates the cross-section behaviour if some Standard Model vector boson couplings would be absent.*

seem to agree well with this DPA calculation, see Figures 3.7(a) and 3.7(b). The difference between RacoonWW and YFSWW is estimated to be 0.4 %.

Within the DELPHI experiment the WPHACT Monte Carlo generator [39] for massive four fermion physics was chosen as unweighted 4-fermion event generator on top of which

the YFSWW reweighting has been implemented [40]. The generation of large samples of fully simulated events is best performed if all processes or specific sub-classes can be generated simultaneously. This option is not available within the RacoonWW framework. Therefore we generate the whole 4-fermion phase-space with only one generator which produces unweighted events, then reweight events according to the YFS formalism to account for the DPA corrections. This weight can be evaluated [39, 40] as a ratio of matrix elements squared $w = |4f|^2_{DPA}/|4f|^2$, where $|4f|^2_{DPA}$ is the 4-fermion matrix element squared in the DPA approximation and can be decomposed in the following way:

$$|4f|^2_{DPA} = |4f|^2 - |CC03|^2 + |CC03_{DPA}|^2 = |4f - CC03|^2 + Int. + |CC03_{DPA}|^2 \quad (3.12)$$

where $Int.$ is the interference term between the CC03 part and the rest. In this reweighting procedure the interference term is included, although computed using CC03 as given by the Improved Born Approximation (IBA) [2]. The weight can be rewritten in a more concise form as:

$$|4f|^2_{DPA} = |CC03|^2 \cdot (1 + \delta_{4f} + \delta_{DPA}) \quad (3.13)$$

where

$$\delta_{4f} = \frac{|4f|^2}{|CC03|^2} - 1\ , \quad \delta_{DPA} = \frac{|CC03_{DPA}|^2}{|CC03|^2} - 1\ . \quad (3.14)$$

The advantage of using this additive approach is that it depends only upon two ratios (Equation 3.14), where the first one can be calculated event-by-event with an IBA 4-fermion generator, while the second can be determined from the YFSWW output. The YFSWW generator returns the value $|CC03_{DPA}|^2/|CC03_{K-C}|^2$, i.e. the DPA squared matrix element with respect to the CC03 one which already includes the Coulomb screening via the Khoze-Chapovsky (K-C) correction [41]. This K-C ansatz is a way to implement non-factorisable corrections. The desired ratio can be determined by multiplying this output by $|CC03_{K-C}|^2/|CC03|^2$. To take the DPA into account in the interference term, $Int.$, it was multiplied by:

$$Int. \ \to \ Int. \cdot \sqrt{\frac{|CC03_{DPA}|^2}{|CC03|^2}}\ . \quad (3.15)$$

The full CKM matrix is taken into account, which provides a more accurate description of the flavour content of hadronic final states. For events in the non-double resonant phase-space, the p_t of the Initial State Radiated photons are generated via QEDPS [42] which can be used as an alternative for the structure function approach. This QEDPS program is based on the parton shower algorithm in QED, which solves the DGLAP equations in the leading logarithmic approximation. The transverse momentum of emitted photons can have sizable effects on the absolute cross-section and might modify the shape of differential distributions. Different treatments of the radiative corrections will be studied in chapter 6.

[2] The coupling constants are replaced by effective constants valid at the q^2 scale of the events of interest rather than in the Thomson limit $q^2 = 0$.

3.2.4 Background for the $e^+e^- \to W^+W^-$ process

In e^+e^- collisions, processes other than those governed by the double resonant WW diagrams of interest, could produce a final state similar to that expected from $e^+e^- \to W^+W^- \to q\bar{q}'Q'\bar{Q}$ and therefore dilute the signal. In the analyses to be discussed in this thesis the measurement estimators are designed with Monte Carlo simulation reflecting the selected data event sample. The background events contain no intrinsic information about the measured quantity, nevertheless they could perturb the properties of the estimators, for example their statistical bias. To avoid major systematic uncertainties or even errors on these estimators, we have to model also these background events with an optimal accuracy.

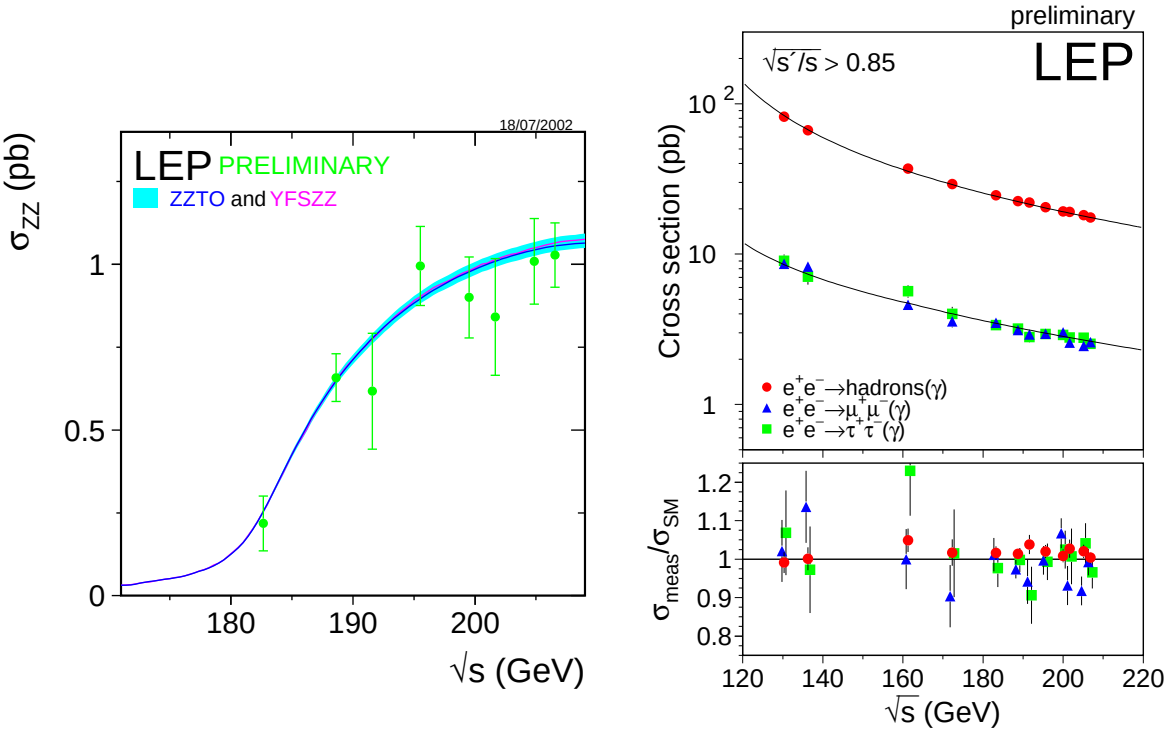

(a) (b)

Figure 3.8: *In plot (a) the measurements of the Z-pair production cross-section are compared to the predictions of YFSZZ [43] and ZZTO [44]. The shaded area represents the ±2% uncertainty on the theoretical predictions. Plot (b) represents the preliminary combined LEP results on the cross-section for $q\bar{q}$, $\mu^+\mu^-$ and $\tau^+\tau^-$ final states, as a function of the centre-of-mass energy. The expectations of the Standard Model calculated with ZFITTER [14] are shown as curves. The lower plot shows the ratio of the data divided by the Standard Model.*

It will be confirmed in section 5.1 that the most important backgrounds after the event selection, are those arising from the processes $e^+e^- \to Z^0Z^0 \to q\bar{q}Q'\bar{Q}'$ and $e^+e^- \to q\bar{q}$ where both primary quarks radiate hard gluons.

For the first process, the cross-section in the relevant LEP2 energy range is about one

order of magnitude smaller than the hadronic WW cross-section, see Figure 3.8(a). It is however very difficult to differentiate its detected kinematic structure from that expected in $W^+W^- \to q\bar{q}'Q'\bar{Q}$ events. The double resonant $Z^0Z^0 \to q\bar{q}Q'\bar{Q}'$ final states are generated with the WPHACT generator at the same time as the WW events, this to include the interference between both sets of Feynman diagrams. As one observes in the Figure 3.8(a), the combined production cross-section of the 4 LEP experiments is in good agreement with the calculations.

Due to a radiative return $e^+e^- \to Z^0\gamma$ from centre-of-mass energies reached at LEP2 back to the Z^0 peak, the second process benefits from the high on-peak cross-section dominated by the annihilation to an almost on-shell Z^0 boson in the s-channel. Therefore its cross-section in the relevant LEP2 energy range is about one order of magnitude larger than the hadronic WW cross-section, see Figure 3.8(b). This di-quark production is generated with a separate generator called KK2f [45]. Radiative effects on the matrix elements of the $e^+e^- \to f\bar{f} + n\gamma$ process, due to photon emission from the initial beams and outgoing fermions are included up to second order $\mathcal{O}(\alpha^2)$ as well as the interference effects between both. The electroweak corrections are included up to first order $\mathcal{O}(\alpha)$.

In summary, the centre-of-mass energy dependent cross-section for CC03 W^+W^- production is about 16.5 pb^{-1}, for Z^0Z^0 production it is about 1.5 pb^{-1} and for the $Z^0 \to q\bar{q}$ process it is about 80 pb^{-1}.

3.3 Perturbative QCD and gluon radiation

The parton shower represents an approximate perturbative treatment of QCD dynamics at scales of momentum transfer-squared t greater than some infra-red cut-off value t_0, typically taken to be of the order of 1 GeV^2. Due to this relative high momentum transfer scale this part in the formation of the visible $q\bar{q}'Q'\bar{Q}$ final state will define the main event topology. The branching process of a parton a with virtual mass m_a into partons b and c is based on the leading logarithm approximation (LLA) according to the Altarelli-Parisi (DGLAP) [46] equations. They describe the evolution of the parton distribution functions:

$$\frac{d\mathcal{P}_{a\to bc}}{dt} = \int dz \frac{\alpha_s(Q^2)}{2\pi} P_{a\to bc}(z) \tag{3.16}$$

where the evolution parameter t can be related to the parent's virtual mass and to the QCD scale parameter Λ_{QCD} by

$$t = ln\left(\frac{Q^2}{\Lambda^2_{QCD}}\right) = ln\left(\frac{m_a^2}{\Lambda^2_{QCD}}\right) \tag{3.17}$$

and the running strong coupling constant $\alpha_s(Q^2)$ is evaluated at Q^2 equal to the transverse momentum squared of the branching. The Altarelli-Parisi splitting function is denoted by $P_{a\to bc}(z)$ and is used to generate the $(E + p_z)$ fractions carried by the daughters, z and $1 - z$, in the CM frame of the event:

$$\begin{aligned}(E + p_z)_b &= z(E + p_z)_a \\ (E + p_z)_c &= (1 - z)(E + p_z)_a \ .\end{aligned} \tag{3.18}$$

Once formed, these daughters b and c may branch again to a lower virtual scale Q^2.

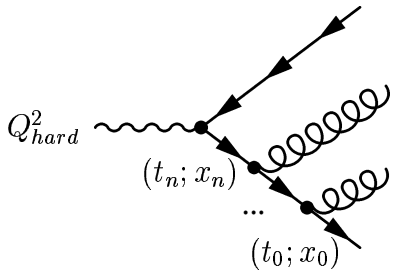

Figure 3.9: *Illustration of the consecutive parton shower branchings starting at the scale of the virtual hard process Q^2_{hard}. The notations in the (t,x)-space refer to the text.*

A Monte Carlo branching algorithm consists of consecutive fundamental steps, illustrated in Figure 3.9. It starts with parton a having initial conditions (t_i, x_i) at a given virtual mass scale t_i and with a fraction $x_i = 2E_i/\sqrt{s_{q\bar{q}}}$ of the total energy available in the $q\bar{q}$ system. The algorithm subsequently generates the values (t_{i-1}, x_{i-1}) according to the above described DGLAP model, where $t_j \in [t_0, t_{j+1}]$ and $x_j \in [0, x_{j+1}]$. The mass scale t evolves downwards from the hard process scale Q^2_{hard} towards the cut-off value t_0. Often the time-like Sudakov form factors $\Delta(t)$ are introduced in the DGLAP equation

$$\Delta_{a\to bc}(t) \equiv \exp\left[-\int_t^{t_{max}} \frac{dt'}{t'} \int dz \frac{\alpha_s}{2\pi} P_{a\to bc}(z)\right] \tag{3.19}$$

where the exponential factor reflects the decay properties of the parton. The factor $\Delta(t_{i-1})/\Delta(t_i)$ represents the probability for parton a to evolve from mass scale t_i to t_{i-1} without any resolvable branching $a \to bc$. In this formalism t_{i-1} can be generated by solving the equation

$$\frac{\Delta(t_{i-1})}{\Delta(t_i)} = \mathcal{R} \in [0, 1] \tag{3.20}$$

where $\mathcal{R}$ is a random number. The momentum fractions $z_i = x_i/x_{i+1}$ are randomly generated according to a probability distribution proportional to $\frac{\alpha_s}{2\pi} P_{a\to bc}(z)$.

Each emitted parton with time-like four-momentum squared [3] in the shower can itself undergo further branching. The parton shower ends at a given energy cut-off scale Q_0, hence a parton a can only branch if $m_a \geq Q_0$. This value defines the allowed phase-space for the parton shower and tells you where the non-perturbative fragmentation takes over. The main model parameters [4] in the parton shower are therefore Q_0 and Λ_{QCD}.

The choice of Q^2 in Equation 3.17 is not unique. Within this thesis three different cascade implementations are studied, in each of them a different ordering scheme is used for the coherent emission of gluons.

[3] All virtualities $m^2 = E^2 - \mathbf{p}^2$ are positive.

[4] The model parameters quoted have the following definitions within the PYTHIA [47] algorithm : $Q_0 \to PARJ(82)$ and $\Lambda_{QCD} \to PARJ(81)$.

- **JETSET [47]** : The JETSET parton shower algorithm consists of an evolution in decreasing squared mass of a radiating parton $Q^2 = m_a^2$, where the partons obey energy and momentum conservation at each step of the shower. Angular ordering is imposed as an additional constraint to recover the coherence property of the branchings. The first parton branching is forced to conform to the exact $\mathcal{O}(\alpha_s)$ matrix element, which approximates the hard gluon emission better than the LLA and is given by

$$\frac{d^2\sigma_{ME}}{dx_1 dx_2} = \frac{2\alpha_s}{3\pi} \frac{x_1^2 + x_2^2}{(1-x_1)(1-x_2)} \tag{3.21}$$

  where x_1 and x_2 are the energy or momentum fractions of the original quark and antiquark after gluon emission.

- **HERWIG [48]** : In HERWIG the ordering is explicit in decreasing opening angle and one uses therefore $Q^2 = \theta^2 \simeq m^2/(2z(1-z))$, hence coherence of soft gluon emission is a natural consequence. As in JETSET Equation 3.21 is used for the first gluon branch.

- **ARIADNE [49]** : An alternative formulation of parton showers in terms of the colour dipole model is implemented in ARIADNE where a gluon emitted from a $q\bar{q}$ pair is treated as being radiated from the colour dipole between the q and $\bar{q}$ (as Equation 3.21 is reflecting). The emission of a second softer gluon can be treated as radiation from two independent dipoles, one between q and g and one between g and $\bar{q}$. A transverse momentum ordering $Q^2 = p_\perp^2 \simeq z(1-z)m^2$ is used.

These three descriptions are consistent with perturbative QCD and it has not been possible to say that one is better than another.

3.4 Phenomenological modelization in the confined region

After the perturbative parton shower has terminated, at the virtual scale t_0, we enter the low-momentum transfer regime. In this confined phase-space the strong coupling constant α_s becomes so large that non-perturbative effects cannot be neglected. The hadronization stage is assumed to be energy independent and local in nature. This local parton-hadron duality supposes that the flow of momentum and quantum numbers at the hadron level tends to follow the flow established at the parton level.

The hadronization process is not yet understood from first principles, starting from the QCD Lagrangian and resulting in an amplitude based quantum-mechanical description. However many phenomenological attempts were made, all of them formulated in a probabilistic language.

The so-called string hadronization is performed via an iterative string break-up scheme where one converts the colour singlet partons into colour neutral objects. In the assumption

of linear confinement [5], the virtual quark-antiquark pair can be interpreted as a flux-tube, which is a string stretched between both opposite colour charge objects via a number of intermediate gluons. Breaking of this string will generate more quarks or gluons, until only on-shell hadrons remain.

A second equally well motivated hadronization model is the cluster model, where colour singlet clusters are formed from the partons after the perturbative fragmentation phase. Gluons are split non-perturbatively into $q\bar{q}$ pairs, thereafter neighboring quarks and anti-quarks can combine into singlets. Most clusters have masses of up to a few GeV/c^2, hence these clusters can be looked upon as superpositions of meson resonances and therefore branching ratios of the isotropic decaying clusters can be determined via the density of the states. No additional hadronization functions have to be implemented within this model. It is known that cluster models have more difficulties compared to string fragmentation models in dealing with the decay of very massive clusters and in describing the baryon and heavy quark production rate.

- **JETSET** : A stochastic hadronization scheme based on the Lund string model [50] is implemented following the equations of motion of a classical, relativistic, constant tension string with no transverse excitations. An exponential area suppression law is used to emulate the matrix elements and links the model to field theories via a quantum mechanical tunneling process for the $q\bar{q}$ production in the string. To supply the energy for a $q\bar{q}$ pair of transverse mass $m_\perp^2 = m^2 + p_\perp^2$, it is necessary to consume a finite length of the string $2m_\perp/\kappa$. The transverse momenta $p_\perp$ of the hadrons are generated according to a flavour independent Gaussian probability density function of width σ_q, predicted to be $\sqrt{\kappa/2\pi} \simeq 0.3$ GeV. Longitudinal hadron momenta are determined by means of the symmetric Lund functions based upon general principles such as causality, Lorentz covariance and confinement. These functions express the probability that a hadron consumes a given fraction z of the available energy-momentum and are described by parameters a and b for light quarks (u,d,s):

$$f(z) = \frac{(1-z)^a}{z} \cdot exp\left(-\frac{bm_\perp^2}{z}\right) \tag{3.22}$$

  where $m_\perp^2 = m^2 + p_\perp^2$ is the transverse mass squared of the hadron. The function $f(z)$ is symmetric because the hadronization process starting at the $\bar{q}$ side of the system and fragmenting towards the q end must be the same as the process starting at the q side. There is a strong anti-correlation between the Lund model parameters a and b. For heavy quarks (c,b) the Peterson function is used:

$$f(z) = \frac{1}{z(1 - \frac{1}{z} - \frac{\epsilon_q}{1-z})^2} \tag{3.23}$$

[5] A linearly rising potential with the separation distance between the colour charge and anti-charge. That is, the string has a uniform rest energy density or constant tension, estimated to be $\kappa \simeq 1$ GeV/fm. This linear confined potential is expected from Regge phenomenology, bag model calculations, lattice studies and quarkonium spectroscopy. This picture of a collapsed field is analogous to a chain of magnets and the behavior of magnetic fields in type I and II superconductors.

with parameters ϵ_b and ϵ_c which gives a better description of heavy quark fragmentation. They are related to the quark mass as $\epsilon_q \sim 1/m_q^2$. In the Monte Carlo tuning described in section 3.6 no difference was made between quark flavours, hence our main string hadronization model parameters [6] for $W^+W^- \to q\bar{q}Q\bar{Q}$ events are : Lund a, Lund b and σ_q.

- **HERWIG** : The hadronization in HERWIG is modeled with a cluster mechanism. Baryons are produced from cluster decays into baryon-antibaryon pairs, therefore the clusters themselves always have baryon number zero. The hadron flavour composition is mainly determined by the available phase-space in cluster decay and, by the cluster mass spectrum. This model has few parameters and a natural mechanism for generating the transverse momenta of hadrons.

- **ARIADNE** : Uses the JETSET scheme for hadronization.

Many particles produced by the hadronization process will not be observed in the detector, because they are unstable and subsequently decay into the observable stable (or metastable) ones. The decay properties of all particles are stored in tables including branching ratios and decay modes into hadrons, leptons and photons. This list is provided and updated by the experiment itself and therefore the decay of long lived particles factorizes with the rest of the fragmentation process.

Schematically the factorisable fragmentation function can be written as a convolution of the perturbative QCD part (pQCD), the confined part and the subsequent decay of resonances:

$$D_h^a(x,Q^2) = (pQCD : Q^2 \to Q_0^2) \otimes (model : a \to H)_{Q_0^2} \otimes (tables : H \to h, h', ...) \quad (3.24)$$

where $D_h^a(x,Q^2)$ is the probability to find a hadron of type h carrying a fraction x of the parton's momentum, in a jet initiated by parton a, whose maximum virtuality is Q^2 and where H represents the possible intermediate hadrons.

3.5 Possible non-factorization of both W decays

When simulating $W^+W^- \to q\bar{q}'Q'\bar{Q}$ events one works in the hypothesis that both W systems fragment independently. With the exception of Coulomb interactions [7] no other information exchange or interference between the partons coming from different W decays is allowed. Some phenomenological effects however could break this factorization hypothesis and change significantly the W boson properties of the event measured via the method of direct reconstruction.

Interconnection or cross-talk effects between or inside the W systems are interesting on their own and studying their phenomenology can give us important insights into the physics

[6] The model parameters quoted have the following definitions within the PYTHIA algorithm : Lund $a \to PARJ(41)$, Lund $b \to PARJ(42)$ and $\sigma_q \to PARJ(21)$.

[7] Photon exchange between both W bosons in the hard process.

of jet fragmentation. Different modelizations of the effects exist, although none of them claim to be correct and therefore all of them should be compared with the data before using prior knowledge when assessing systematic uncertainties on measurants from $W^+W^- \to q\bar{q}'Q'\bar{Q}$ events. Two main interconnection effects are considered at LEP2 : Bose-Einstein Correlations and Colour Reconnection. The systematic shift of both effects on the estimated W mass and width will be discussed in chapters 6 and 7.

3.5.1 Bose-Einstein Correlations

Particles of integer spin obey Bose-Einstein statistics (ladder operators in QFT obey the commutation relation), while particles of half-integer spin obey Fermi-Dirac statistics (ladder operators obey the anti-commutation relation). Hence if particles **p** and **q** obey Bose-Einstein statistics, then their creation operators in momentum eigenstates, $a^\dagger_{\mathbf{p}}$ and $a^\dagger_{\mathbf{q}}$, commute

$$[a^\dagger_{\mathbf{q}}, a^\dagger_{\mathbf{p}}] = 0 \tag{3.25}$$

and the operator $a^\dagger_{\mathbf{p}} a^\dagger_{\mathbf{q}}$ will create the same state when acting on the vacuum $|0>$ as the operator $a^\dagger_{\mathbf{q}} a^\dagger_{\mathbf{p}}$ in which the two particles are interchanged. Assuming the concept of QCD factorization [8], Bose-Einstein Correlations will not influence the parton shower. Hence only minor direct changes are expected in global event shape observables. Since most of the observed particles in a hadronic final state $W^+W^- \to q\bar{q}'Q'\bar{Q}$ event are pions, Bose-Einstein effects occur and the production amplitude of the events should be symmetrized for the exchange of identical bosons. The omission of these correlations between particles from different W bosons in our standard simulation could lead to a systematic uncertainty on the W mass and width measurement from those events. A clear picture has yet to emerge from the experimental study of this phenomenon. The existing phenomenological models can be classified according to the way they restore the energy-momentum conservation in the event after introducing Bose-Einstein Correlations by an algorithm.

Local reweighting models

In the LUBOEI BE_0 model [51] (subscript '0' denotes the original LUBOEI version) the effect of Bose-Einstein Correlations is introduced as a perturbation on the momenta of the particles. The particle production vertices have a Gaussian distribution in space-time, which motivates the choice of the form of the enhancement function for two-particle correlations as:

$$R_0(Q) = 1 + \lambda_{\mathrm{BE}} \cdot exp\left(-Q^2 r^2_{\mathrm{BE}}\right) \tag{3.26}$$

where λ_{BE} defines the strength of the correlation, r_{BE} the radius of the source and the observable Q the four-momentum difference between the two particles. All LUBOEI algorithms [9] are based on a local shifting (reweighting) procedure of the final state momenta of identical

[8] Separation between perturbative and confinement phase-space: the non-perturbative physics cannot influence the perturbative phase as a consequence of the large time-distance scales.

[9] The model parameters quoted have the following definitions within the PYTHIA/LUBOEI algorithm : $\lambda_{\mathrm{BE}} \to PARJ(92)$ and $r_{\mathrm{BE}} \to PARJ(93)$.

bosons according to this enhancement function $R_0(Q)$ such that the Q distribution is enhanced by a factor $R_0(Q)$. The main effect in the Q distribution is expected in the region where Q is smaller than 1 GeV/c^2. This function is slightly modified in more recent LUBOEI versions (for example BE_3 and BE_{32}). Additional shifts are introduced for energy conservation, this by an extra global rescaling of all final state hadron momenta in BE_0 or by a local one in the more recent versions. By construction the LUBOEI implementation of the Bose-Einstein effect cannot change the multiplicity or the particle content of the events.

The enhancement function $R_0(Q)$ was obtained by integration of the symmetrical weight function $1+cos(\Delta x \cdot \Delta p)$ over a Gaussian source. We know that when using a non-Gaussian source, an oscillatory behavior appears which should damp rather quickly. Therefore in the LUBOEI version BE_3 [52] the standard enhancement function $R_0(Q)$ is multiplied with a factor $(1 + \alpha\lambda_{\rm BE} exp(-Q^2 r_{\rm BE}^2/9))$:

$$R_3(Q) = \left(1 + \lambda_{\rm BE} exp(-Q^2 r_{\rm BE}^2)\right) \cdot \left(1 + \alpha\lambda_{\rm BE} exp(-Q^2 r_{\rm BE}^2/9)\right) \tag{3.27}$$

It turns out that the average α needed is $\bar{\alpha} \approx -0.2$. For $Q = 0$ the enhancement function becomes $R_3(0) \simeq 1.6$ for $\lambda_{\rm BE} = 1$, rather than $R_3(0) = (1 + \lambda_{\rm BE})(1 + \alpha\lambda_{\rm BE}) = 2$. In LUBOEI version BE_{32} [52] this shortcoming is solved by introducing an extra term:

$$R_{32}(Q) = \left(1 + \lambda_{\rm BE} exp(-Q^2 r_{\rm BE}^2)\right) \cdot \left\{1 + \alpha\lambda_{\rm BE} exp(-Q^2 r_{\rm BE}^2/9)\left(1 - exp(-Q^2 r_{\rm BE}^2/4)\right)\right\} . \tag{3.28}$$

In this case $\bar{\alpha} \approx -0.25$. More recent LUBOEI versions take back the original enhancement function $R_0(Q)$ but differ from each other in the way energy is conserved.

Instead of a Gaussian two-particle enhancement function, an exponential parametrization can be used:

$$R_0(Q) = 1 + \lambda_{\rm BE} \cdot exp\left(-Q r_{\rm BE}\right) \tag{3.29}$$

for the BE_0 model (same kind of changes for the BE_3 and the BE_{32} models). Both parametrizations, Gaussian and exponential, are studied in this thesis.

Within DELPHI the LUBOEI algorithm (version BE_{32} with the Gaussian enhancement function Equation 3.28) was studied in the JETSET fragmentation scheme. The fragmentation model parameters were taken from the standard DELPHI tuning of JETSET comparing simulated distributions with those obtained from the Z^0 peak data of the LEP1 running [**?**]. This tuning neglects the existence of Bose-Einstein Correlations, therefore the LUBOEI model parameters were tuned separately. Six sets of fully simulated $Z^0 \rightarrow q\bar{q}$ events at $\sqrt{s} = m_Z$ were generated in a range of values for the correlation strength (λ) and source radius (r). The four-momentum difference, Q, between all selected same charge particle pairs was calculated. An interpolation was performed on the basis of the Q distribution to obtain λ = 1.35 and r = 0.6 fm [10] which provide the optimal description of the DELPHI Z^0 peak data taken during the 1998 calibration runs. The two-dimensional $\chi^2(\lambda, r)$ mapping of this comparison of Q distributions between data and simulation is shown in Figure 3.10.

[10] Within the JETSET algorithm this refers to parameter PARJ(93) = 0.34 GeV.

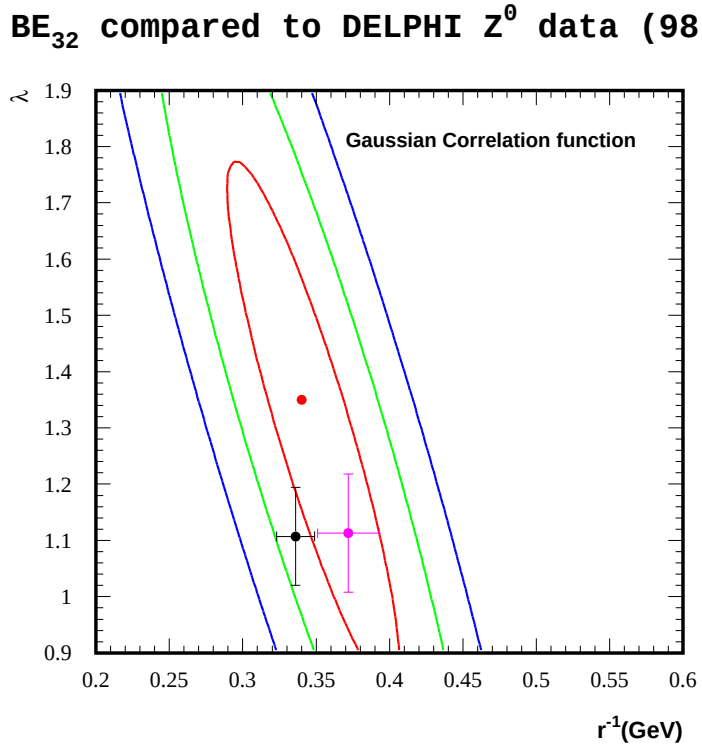

Figure 3.10: *Results from the tuning as described in the text of the relevant LUBOEI (version BE_{32}, Gaussian enhancement function) parameters λ and r are shown as 1-2-3 σ confidence level limits. The black cross indicates the result when more differential information was used (cfr. section 3.6). A comparison is shown with the results obtained from the more evolved global tuning (cfr. section 3.6) by the purple cross. The one standard deviation statistical uncertainties are shown on the markers.*

Global reweighting models

These models aim to reproduce the enhancement of identical bosons close in phase-space by giving weights to events. This procedure does ensure energy and momentum conservation, but may adversely affect other event or particle distributions. It was shown that when using the Kartvelishvili-Kvatadze-Moller (KKM) reweighting scheme [54], no significant effects were observed on the W mass. Therefore no further studies were performed with these global reweighting models.

Measurement of the Bose-Einstein Correlations at LEP

The LEP experiments have measured [1] the strength of Bose-Einstein Correlations between particles from different W bosons in the fully hadronic $W^+W^- \to q\bar{q}'Q'\bar{Q}$ events. The model independent mixing method was used for the measurement. This by a direct comparison of the two-particle spectra of genuine hadronic W^+W^- events and those from a

reference sample of mixed W^+W^- events constructed by mixing the hadronic parts of two semi-leptonic decaying W^+W^- data events. Only the subtraction of the background events, mainly $Z^0 \to q\bar{q}$ with intrinsic Bose-Einstein Correlations between the final state particles, introduces a dependency on a model. Generally PYTHIA was used together with the LUBOEI algorithm. This method reduces most of the systematic uncertainties related to the fragmentation and detector description, and deals in a correct way with the intrinsic Bose-Einstein Correlations between particles produced in the same W decay. A simple χ^2 combination procedure of the numerical results from each experiment with respect to a specific Bose-Einstein model was applied. The combined fraction of the strength of the correlations between particles from different W bosons, predicted by the tuned LUBOEI model, has a data preferred value of $3 \pm 18\%$. A new DELPHI result [56] indicates that the data has a 3σ deviation from the hypothesis that no inter-W Bose-Einstein Correlations are present in hadronic W^+W^- events, and prefers a fraction of about 65% of this predicted strength. These measurements of the strength of the Bose-Einstein Correlations were used for the model dependent estimation of the systematic uncertainty on the W mass measurement, also see section 6.7.3.

3.5.2 Colour Reconnection

Colour Reconnection is the term used for strong interactions between colour singlet parton systems of different origin [55]. The effect can influence the evolution of two nearby parton showers. The kinematics of the hadrons coming from both systems can therefore be perturbed. In the reaction $e^+e^- \to W^+W^- \to q_1\bar{q}_2q_3\bar{q}_4$ the colour singlets $q_1\bar{q}_2$ and $q_3\bar{q}_4$ formed by the decay products of both W bosons, could rearrange themselves to new colour singlets $q_1\bar{q}_4$ and $\bar{q}_2q_3$. Because the flow of the colour quantum numbers, reflecting the particle dynamics at short distances, controls the particle distributions in the final state, one could expect a change in these distributions after the colour rearrangement. In these W^+W^- events produced at LEP2, the separation distance between the $W^\pm$ decay vertices is around $\tau_W \sim 1/\Gamma_W \simeq 0.1$ fm, while the fragmentation scale of the W bosons is around 1 fm. Hence there is a significant space-time overlap of both W hadronization regions where Colour Reconnection could occur. The resulting kinematic structure of a W^+W^- event will be different from the situation without this reconnection. The presence of similar effects was found in hadronic B meson decays $B \to J/\psi + X$ where the colour interference between the two original colour singlets ($\bar{c} + s$ and c+spectator) suppresses this decay [55].

The mass of the dipoles $q_1\bar{q}_2$ and $q_3\bar{q}_4$ sets the scale for the amount of energetic gluon radiation and multiple soft particle production to be expected in the final state of the W^+W^- event. Therefore event properties like the charged particle multiplicity may change a lot if the original dipoles are instantaneously replaced by the rearranged ones. This extreme model is experimentally disfavored by the measurements at LEP2.

The probability to rearrange can be enhanced by gluon exchange between both W decay systems. Within the perturbative parton shower model it was shown that the Colour Reconnection or interference probability is negligible [57]. Colour transmutations between partons from different W bosons can only occur from the interference of at least two emitted gluons. This interference piece is suppressed by the effective number of colours as $1/N_c^2 = 1/9$ compared to the $\mathcal{O}(\alpha_s^2)$ non-reconnection emissions. Also the effects of a finite W width

restrict the energy range of primary gluons generated by the alternative rearranged dipoles, because both W bosons do not necessarily decay at the same time.

When the fragmentation of the primary quarks is entering the confined region, a phenomenological model has to be used which only approximates the physics effect within the event. At this point colour rearrangement or Colour Reconnection is not known from first principles and therefore its effect must be simulated with an appropriate Monte Carlo algorithm. Each of the existing phenomenological hadronization models described in section 3.4 has its own implementation of the effect.

SK models in JETSET [57]

Within the framework of the Lund string fragmentation implemented in JETSET the colour fields of both W boson strings can overlap in space-time. Depending on the type of string which is considered, we can differentiate between two modelizations developed by T. Sjöstrand and V. Khoze :

- **SK1** : The strings are described in their simplest Lorentz invariant way by a linear confinement potential, or as cylindrical bags with a transverse dimension of hadronic size ($\sim$ proton radius $\simeq$ 0.7 fm) and a Gaussian fall of the colour field density in the transverse direction (string tension $\simeq$ 1 GeV/fm). The event probability $\mathcal{P}_i$ to reconnect is related to the volume, $\mathcal{O}_i$, of the string overlap as:

$$\mathcal{P}_i = 1 - e^{-\kappa \cdot \mathcal{O}_i} \quad . \tag{3.30}$$

  The model parameter κ, with a fixed value for each event, is unknown and can only be tuned or measured from experimental data. Based on theoretical assumptions the authors propose a value of κ around 0.66, which gives the same rate of reconnected events as the SK2 scenario described below. An original measurement of this model parameter κ will be presented in chapter 7.

- **SK2** : Vortex lines represent the strings and have a thin core in which all topological information is stored. The core is surrounded by a chromoelectric field with exponential fall in the transverse direction. Colour Reconnection occurs whenever the cores of two strings cross each other in space-time. The free parameter which can be assumed as known in this model is the proper lifetime of the string τ_{frag}, which is taken to be 1.5 fm or about three times the typical hadron radius.

Both models can include multiple reconnections, but for simplicity only one reconnection per event was allowed. This is a good approximation as the probability for a second reconnection is largely reduced.

ARIADNE models [58, 59]

Within ARIADNE the Dipole Cascade Model is also followed by a string fragmentation according to the Lund model. Perturbative QCD prefers string configurations with minimal string potential in Z^0 decays. Partons that are nearby in momentum space are also likely to

be closely related in colour flow. As a criterion for Colour Reconnection one can therefore use the string length Λ defined in the momentum space

$$\Lambda = \sum_{i=1}^{n-1} \frac{ln(p_i + p_{i+1})^2}{m_0^2} \tag{3.31}$$

where the sum covers all $n-1$ string pieces for a string connecting n partons and m_0 is a typical hadronic mass scale (usually Γ_W). Reconnection is allowed when the string length after reconnection is shorter than the original one. In the ARIADNE 2 (AR2) model, reconnection between strings from different W bosons only happens below a fixed energy scale (usually Γ_W), while in the ARIADNE 3 (AR3) version reconnection is allowed at all energy scales which includes the perturbative phase. Within an event multiple inter-string reconnections and self-reconnections inside a single string could occur.

HERWIG models [60]

Before the formation of the clusters in the fragmentation process, reconnection is allowed with a fixed probability ($\simeq$ 1/9) when it reduces the sum of the squared sizes of the formed clusters. The size of a cluster is defined as the space-time separation of the production vertices of the partons forming the cluster. Multiple reconnections and self-reconnections within a single parton shower are allowed.

The models need not be viewed as mutually contradictory. Rather, each may represent some aspect of the true nature of the process.

Measurement of Colour Reconnection via the particle flow

Many observables have been considered in the search for an experimental signature of Colour Reconnection. Most of them are on average invariant when including Colour Reconnection algorithms in the simulation, therefore reflecting a limited sensitivity. The string effect however predicts a higher particle production rate in the region between jets originating from the same $W \to q\bar{q}$ decay ('intra' region), compared to the regions between jets from different W decays ('inter' region). When Colour Reconnection is present, particles tent to migrate from the intra-W to the inter-W region. Therefore an observable which counts the particles in these different regions could be sensitive to the different Colour Reconnection algorithms. The ratio r of the integrated particle density or particle flow in the intra region to the integrated density in the inter region quantifies this behavior.

The value obtained from the LEP combined data [1] is compared to the different models in Figure 3.11. In the SK1 interpretation of Colour Reconnection the data prefers a value of κ = 1.18, and the 68% confidence level lower and upper limits are 0.39 and 2.13 respectively. This corresponds to a reconnection probability of 49% in this model at $\sqrt{s}$ = 189 GeV. More likelihood information about this parameter will be inferred in chapter 7. All four experiments have observed a very weak sensitivity to the ARIADNE and HERWIG colour reconnection models, which does not coincides with the SK1 prediction of the effect. The expected value of r from those fragmentation models in the hypothesis that no colour reconnection is present, differs from the measured LEP combined data value by 3.1 and 3.7

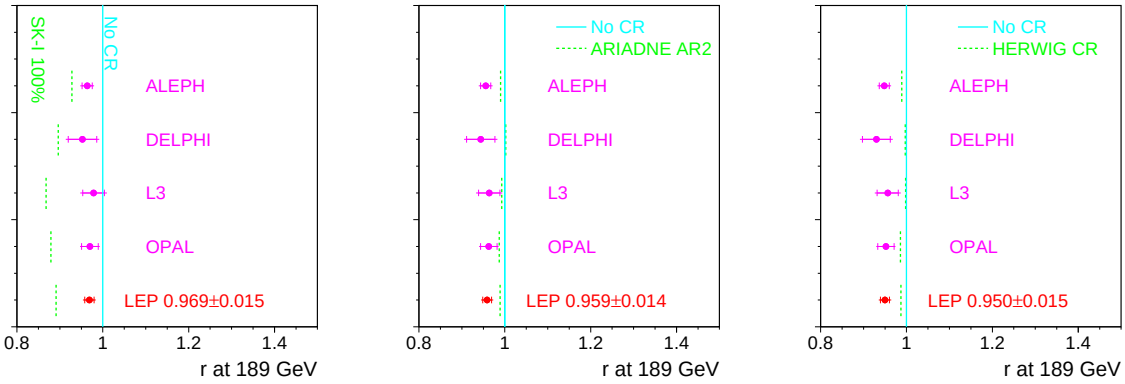

(a) (b) (c)

Figure 3.11: *Preliminary particle flow results using all LEP data [1]. In plot (a) both hypotheses without and with full (100%) SK1 Colour Reconnection are shown, in plot (b) and (c) the ARIADNE and HERWIG Colour Reconnection models are tested, based on the predicted sensitivity. The dashed lines indicate the predicted values of R_N for the analysis of each experiment. For comparison all values are interpolated to a centre-of-mass energy of 189 GeV and the LEP combined values are shown on the bottom of each plot.*

σ for respectively the ARIADNE and HERWIG model. This may indicate a clear underestimation of the systematic uncertainties in these particle flow analyses, the underestimation of the total uncertainty could be as large as a factor 2 which would drastically decrease the sensitivity of this observable.

An alternative and original measurement was initiated in [61] and will be presented in chapter 7. It was shown [62] that within DELPHI this method has a much higher sensitivity to the Colour Reconnection effect compared to the particle flow method and it does not suffer from large fragmentation systematic uncertainties.

3.6 Monte Carlo tuning of relevant model parameters with Z^0 LEP1 data

When studying the effects of Bose-Einstein Correlations in W^+W^- events at LEP2 it was always assumed that the factorization of the Bose-Einstein modelization and the rest of the fragmentation process holds. Therefore in this thesis the influence on the measured W mass and width from W^+W^- events was estimated when breaking this factorization hypothesis.

In this section the correlation between some JETSET model parameters, describing the fragmentation of the partons into hadrons, and the LUBOEI model parameters, emulating the effect of Bose-Einstein Correlations, is estimated from hadronic Z^0 events at LEP1. These correlations were found to be non-negligible and should be taken into account when estimating the values of the JETSET model parameters to be used in the Monte Carlo simulation

of W^+W^- events at LEP2. Many inclusive observable distributions determined from the hadronic Z^0 events at LEP1 were exploited to obtain a new tuning of the relevant JETSET and LUBOEI model parameters. Compared to the standard DELPHI tuning [53] which does not break the factorization hypothesis, the resulting Monte Carlo distributions generated with these so-called globally tuned model parameters have a better agreement with the distributions obtained from the Z^0 data taken during LEP1 running.

3.6.1 Definition of observables

The observable distributions considered in this section are only the most fundamental ones. Apart from the average charged particle multiplicity they can be classified into event shape, single particle and two particle observables. All distributions, either from simulation or from data, are constructed with charged particles only.

- **Thrust T, Major M, Minor m :** The Thrust T and Thrust-axis are defined by

$$T = \max_{\vec{n}_{Thrust}} \frac{\sum_{i=1}^{N_{particle}} |\vec{p}_i \cdot \vec{n}_{Thrust}|}{\sum_{i=1}^{N_{particle}} |\vec{p}_i|} \tag{3.32}$$

  where $\vec{p}_i$ is the 3-momentum of a particle and $\vec{n}_{Thrust}$ is a unit-vector along the Thrust-axis. Major and Minor are defined in a similar way, where $\vec{n}_{Major}$ is perpendicular on $\vec{n}_{Thrust}$ and $\vec{n}_{Minor} = \vec{n}_{Major} \times \vec{n}_{Thrust}$ respectively. In the direction of the Major the total transverse momentum to the Thrust axis of the event is maximal.

- **Sphericity S, Aplanarity A, Planarity P :** When ordering the eigenvalues λ_i of the quadratic momentum tensor

$$M_{\alpha\beta} = \sum_{i=1}^{N_{particle}} p_i^\alpha p_i^\beta \qquad \text{with} \qquad \alpha, \beta = 1, 2, 3 \tag{3.33}$$

  as

$$\lambda_1 \geq \lambda_2 \geq \lambda_3 \tag{3.34}$$

$$\lambda_1 + \lambda_2 + \lambda_3 = 1 \ , \tag{3.35}$$

  the Sphericity is $S = \frac{3}{2}(\lambda_2 + \lambda_3)$, the Aplanarity $A = \frac{3}{2}\lambda_3$ and the Planarity $P = \frac{2}{3}(S - 2A)$. The Sphericity-axis is parallel to the eigenvector corresponding to λ_1. As the momenta enter quadratically the Sphericity-axis is influenced more strongly by large momentum particles than the Thrust-axis.

- **Differential Jet Rates $\mathbf{D_i(y)}$:** Jets are reconstructed using cluster finding algorithms of the JADE type [63]. For each event and each pair of particles i and j the scaled invariant mass or transverse momentum y_{ij} for respectively the JADE or DURHAM algorithm [64] are evaluated as:

$$y_{ij}^{\mathrm{JADE}} = 2 \cdot \frac{E_i E_j}{E_{vis}^2} \cdot (1 - \cos\theta_{ij}) \tag{3.36}$$

$$y_{ij}^{\mathrm{DURHAM}} = 2 \cdot \frac{\min(E_i^2, E_j^2)}{E_{vis}^2} \cdot (1 - \cos\theta_{ij}) \tag{3.37}$$

where E_i, E_j are the energies, θ_{ij} the angle between the momentum vectors of the two particles and E_{vis} the visible energy of the event. The particle pair with the lowest value y_{ij} is selected and replaced by a pseudo-particle with four-momentum $(p_i + p_j)$, hence reducing the multiplicity by one. In successive steps the procedure is repeated until the scaled invariant masses of all pairs of (pseudo-) particles are larger than a given resolution y. The remaining (pseudo-) particles are called jets. The differential 2-jet rate D_2 is derived from the 2-jet rate $R_2 = \frac{N_{2-jets}}{N}$ as:

$$D_2(y) = \lim_{\Delta y \to 0} \frac{R_2(y + \Delta y) - R_2(y)}{\Delta y} \ . \tag{3.38}$$

The differential n-jet rates follow the recursion :

$$D_n(y) = \lim_{\Delta y \to 0} \frac{R_n(y + \Delta y) - R_n(y)}{\Delta y} + D_{n-1}(y) \ . \tag{3.39}$$

- **Scaled momentum $\mathrm{x_p}$:** The scaled momentum x_p is the absolute momentum $|\vec{p}|$ of a particle scaled to the beam momentum.

- **Transverse momenta $\mathrm{p_t^{in}}$ and $\mathrm{p_t^{out}}$:** One can distinguish the transverse momentum (perpendicular to the Thrust axis) of a particle in the event plane $p_t^{in} = \vec{p} \cdot \vec{n}_{Major}$ and out of the event plane $p_t^{out} = \vec{p} \cdot \vec{n}_{Minor}$. Similar definitions are used for the transverse momenta according to the Sphericity axis.

- **Two-particle Q distributions :** The Lorentz invariant four-momentum difference Q can be calculated for each particle pair in the event:

$$Q = \sqrt{(\vec{p}_1 - \vec{p}_2)^2 - (E_1 - E_2)^2} \ . \tag{3.40}$$

We can separate those pairs in two classes, pairs of particles with equal signed electric charge and pairs with opposite charge. The like-sign $Q_{++,--}$ and unlike-sign Q_{+-} distributions reflect the partial density functions of those quantities.

The default JETSET setting of *mstj(22)* [11] was used, therefore the decay products of all long lived resonances are ignored when constructing these distributions.

[11] Cut-off on decay length for a particle that is allowed to decay, by default all particles declared unstable are forced to decay.

3.6.2 Data distributions

The differential distributions of the event shape and charged particle observables mentioned above were determined from the LEP1 data measured with the DELPHI detector. From the full data sample around 750000 hadronic Z^0 events were selected, the track and event selection applied was copied from [53]. The systematic uncertainty which dominates the statistical one in those distributions was reduced by applying cuts on the event kinematics to assure that the major components of the events were measured with optimal detector efficiency and resolution. The observed data distributions were corrected for kinematic cuts, limited acceptance and resolution of the detector as well as effects due to reinteractions of particles inside the detector material. The distributions were bin-by-bin unfolded by use of JETSET simulation as explained in [53].

The two-particle data distribution $Q_{++,--}$ was obtained from the Z^0 peak data taken by DELPHI during the 1998 calibration runs. It was first corrected for single track efficiencies as a function of their azimuthal angle, polar angle and momentum. Residual discrepancies in the two-particle distribution of the opening angle between particles were corrected afterwards. Particle pairs with an opening angle smaller than 2.5 degrees were rejected to reduce the systematic uncertainty. Although the knowledge about the existence of non-negligible bin-to-bin correlations in the $Q_{++,--}$ distribution, their effect was neglected but rather introduced as an extra systematic uncertainty. The information in the Q_{+-} distribution is not directly linked with the main physics behind Bose-Einstein Correlations. The like-sign pairs at low Q values will be enhanced according to the pre-defined correlation function in the LUBOEI algorithm, but due to the locality of the shuffling mechanism to restore the energy conservation the unlike-sign pairs will be influenced. However compared to the $Q_{++,--}$ distribution, the Q_{+-} distribution has only a minor impact on the tuned parameter values and is influenced by resonance decays like $\rho(770) \to \pi\pi$ and $\phi(1020) \to K^+K^-$, therefore is was not used in the tuning.

A comparison of the inclusive distributions obtained from the DELPHI data and those obtained by the three other LEP Collaborations is given in [65]. Good agreement for event shape and single particle spectra was observed, therefore most discrepancies in the tuned model parameters from the individual LEP Collaborations arise from the tuning methods themselves.

3.6.3 Tuning procedure

The precise knowledge of these data distributions allows us to confront them with the Monte Carlo models of the hadronization process and to determine the parameters used in those algorithms. In [53] a tuning of relevant JETSET parameters is obtained by fitting the model to the data distributions. The existence of Bose-Einstein Correlations was neglected is this study and therefore the $Q_{++,--}$ and Q_{+-} were not compared with simulation. In the present study, Bose-Einstein Correlations are introduced in the PYTHIA/JETSET version 6.125 by use of the LUBOEI BE_{32} algorithm (cfr. section 3.5.1). Because LUBOEI also changes the jet properties in the events, one needs to retune globally the parameters used in the JETSET and LUBOEI models, rather than only adding a separately tuned LUBOEI version. Within LUBOEI both the Gaussian and exponential enhancement functions (Equation 3.28) were

considered.

To confront data and simulation, the dependency of the physical observables on the model parameters is approximated analytically in each bin of each distribution in a quadratic form:

$$MC(x;\vec{p}_0+\delta\vec{p}_0) \simeq f(x;\vec{p}_0+\delta\vec{p}_0) = a_0^{(1)}(x) + \sum_{i=1}^{n} a_i^{(2)}(x)\delta p_i + \sum_{i,j=1}^{n} a_{ij}^{(3)}(x)\delta p_i \delta p_j \quad (3.41)$$

where $f(x;\vec{p}_0+\delta\vec{p}_0)$ denotes the predicted distribution of a physical observable x, at a deviation $\delta\vec{p}_0$ of the parameters from their central setting $\vec{p}_0$ in the n-dimensional parameter space. The last term includes correlating terms between the model parameters to be tuned, which are Λ_{QCD} and Q_O in the parton shower (cfr. section 3.3), a, b and σ_q in the confined fragmentation (cfr. section 3.4) and $\lambda_{\rm BE}$ and $r_{\rm BE}$ in the LUBOEI model (cfr. section 3.5.1). The optimal coefficients $a^{(k)}$ of the expansion are determined from a fit to model reference distributions obtained from Monte Carlo simulated events with different parameter settings. The optimal parameters p_i, their uncertainties σ_i and correlation coefficients ρ_{ij} are then determined from a standard χ^2-fit using MINUIT of these analytic approximations to the corresponding data. As discussed in [53] the fitting method is unbiased and the uncertainties on the obtained parameters are estimated correctly.

	Lund a	σ_q	Λ_{qcd}	Q_0	Lund b	$\lambda_{\rm BE}$	$r_{\rm BE}$
Lund a	1.00	-	-	-	-	-	-
σ_q	-0.661	1.00	-	-	-	-	-
Λ_{qcd}	0.714	-0.818	1.00	-	-	-	-
Q_0	-0.755	0.773	-0.686	1.00	-	-	-
Lund b	-0.938	0.839	-0.841	0.898	1.00	-	-
$\lambda_{\rm BE}$	-0.624	0.470	-0.592	0.542	0.637	1.00	-
$r_{\rm BE}$	0.587	-0.337	0.551	-0.488	-0.575	-0.947	1.00

Table 3.1: *Symmetric correlation matrix between all tuned PYTHIA 6.125 and LUBOEI BE_{32} model parameters obtained from the Gaussian parametrization of the enhancement function in LUBOEI and all simulated information defined in section 3.6.1 except the Q_{+-} distribution.*

The parameters of a fragmentation model have a well-defined physical meaning. However some parameters are directly coupled like a, b and σ_q in the Lund fragmentation function. Therefore the choice of distributions to tune the model parameters is not always evident. To keep the influence of statistical uncertainties as small as possible it is clear that the model should be fitted to those distributions which show the strongest dependence on the parameter under consideration and least correlations with others. For each distribution $MC(x;\vec{p}_i)$ its sensitivity to a given model parameter was calculated, i.e. the quantity:

$$S_i(x) = \frac{\frac{\delta MC(x;\vec{p}_i)}{MC(x;\vec{p}_i)}|_{p_i}}{\frac{\delta p_i}{p_i}} \simeq \frac{\partial ln MC(x;\vec{p}_i)}{\partial ln p_i}|_{p_i} \quad (3.42)$$

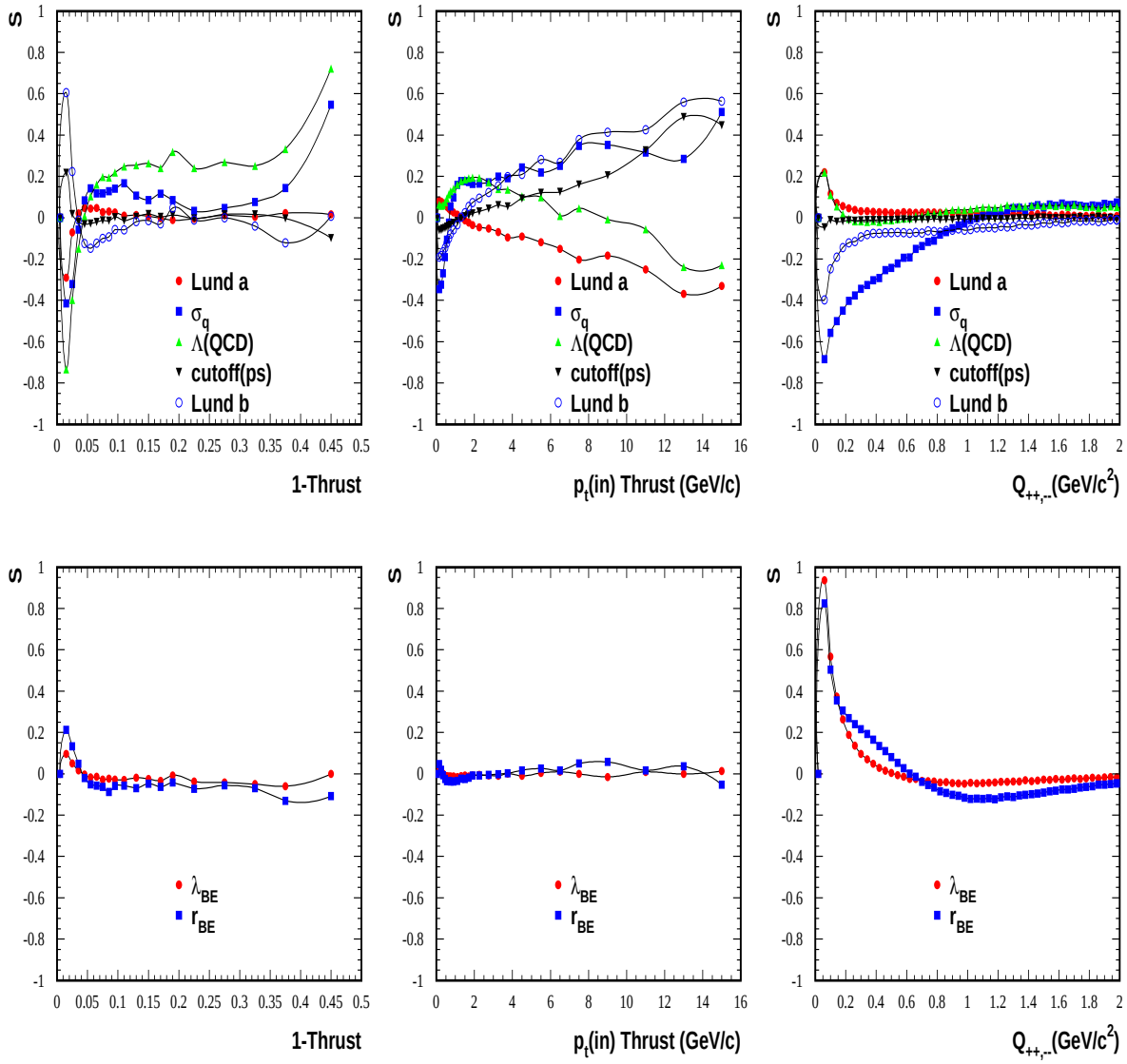

Figure 3.12: *Sensitivity curves for an event shape, a single and double particle distribution. The top plot reflect the sensitivity to the relevant JETSET model parameters, while the bottom plots show the sensitivity to the LUBOEI model parameters.*

where $\delta MC(x;\vec{p}_i)$ is the change of the distribution $MC(x;\vec{p}_i)$ when changing the model parameter i by δp_i around its central value p_i. The fraction $\frac{\delta p_i}{p_i}$ gives all parameters the same normalization. Some sensitivity plots can be found in Figure 3.12 which shows that most of the event shape and single particle distributions are also affected by the LUBOEI model parameters. Likewise the $Q_{++,--}$ and Q_{+-} distributions, typically studied for Bose-Einstein Correlation purposes, are affected by the different JETSET model parameters. This will

introduce correlations between JETSET and LUBOEI model parameters in the MINUIT fit. To take into account these correlations, all distributions were used, rather than using different sets of distributions for different parameters. In section 3.6.5 the stability of this procedure will be discussed.

Positive (or negative) correlations among the model parameters are observed when their sensitivity to the distributions have similar (or opposite) behavior. The estimated correlations using all simulated information mentioned in section 3.6.1 are shown in Table 3.1. The correlations between the most important JETSET fragmentation parameters and the parameters used in the LUBOEI algorithm have the same magnitude as those between the JETSET parameters themselves, mainly because the same distributions were used in the fit for all model parameters. Those correlations cannot be neglected when studying the systematic effect of Bose-Einstein Correlations, simulated with the LUBOEI algorithm, on a measurement based on W^+W^- Monte Carlo at LEP2.

The highly anti-correlated behavior of the sensitivities of the distributions on the parameters Lund a and b can be exploited to determine the correlation function between these parameters. This function was used as a constraint in the MINUIT fit by fixing for example the value of Lund b according to the tuned value of Lund a. The functional dependency between Lund a and b was estimated for both the Gaussian and exponential version of the LUBOEI correlator $R_{32}(Q)$.

	QCD/BE(G)	**BE(G)**	**QCD/BE(E)**	**BE(E)**	DELPHI
Λ_{qcd} (GeV)	0.317±0.003	-	0.329±0.003	-	$0.297^{+0.008}_{-0.009}$
Q_0 (GeV)	2.314±0.050	-	1.826±0.098	-	$1.560^{+0.24}_{-0.19}$
σ_q (GeV)	0.432±0.003	-	0.423±0.003	-	0.408±0.006
a	0.477±0.022	-	0.157±0.032	-	$0.417^{+0.025}_{-0.027}$
b	0.788	-	0.585	-	0.850
$\lambda_{\rm BE}$	1.113±0.105	1.107±0.087	1.735±0.065	1.930±0.122	-
$r_{\rm BE}$ (GeV)	0.372±0.021	0.336±0.013	0.261±0.009	0.240±0.011	-
χ^2	1932	330	1919	324	-
ndf	359	43	359	43	-
χ^2/ndf	5.4	7.7	5.3	7.5	-

Table 3.2: *Values of the JETSET and LUBOEI model parameters obtained from the tuning described in the text. The Gaussian enhancement function in LUBOEI is used in the first and second column, while the exponential one is used in the third and fourth column. The resulting values are compared with the standard set used by the DELPHI Collaboration, shown in column five, omitting the effect of Bose-Einstein Correlations.*

3.6.4 Tuned parameters

The estimates of the values of the JETSET and LUBOEI model parameters obtained by the tuning procedure described above are summarized in Table 3.2. The uncertainty quoted arise from the statistically limited observable distributions (80k events each) which were created with the PYTHIA Monte Carlo generator at 100 different points in the 7 dimensional model parameter space to estimate the coefficients in the analytic prediction functions of Equation 3.41. One should take into account the large χ^2/ndf of the fit when interpreting these uncertainties and remember that the phenomenological model is only a reasonable description of the real physics. When using the Gaussian enhancement function in LUBOEI the first column of results was obtained. The second column reflects the results when fixing the JETSET model parameters to their value mentioned in the last column, the standard values used by the DELPHI Collaboration [53], and tuning the LUBOEI model parameters on the distributions mentioned above. In the third and fourth column similar results are shown when using the exponential enhancement function in the LUBOEI algorithm. Mainly the parton shower cut-off scale Q_0 and both Lund parameters have obtained a different value compared to their standard DELPHI one. The tuned values for the LUBOEI model parameters were found to be different when using the Gaussian or the exponential enhancement function. The χ^2 and the number of degrees of freedom (ndf) of the MINUIT fit indicate that the model does not describe the data perfectly. The distributions simulated with the tuned parameters are compared to the LEP1 data in section 3.6.6.

To illustrate the stability of the fit procedure, the 7 dimensional χ^2 was projected for each tuned model parameter into one dimension, shown in Figures 3.13 and 3.14. When not including the systematic uncertainties on the $Q_{++,--}$ data distribution, or similarly giving this distribution statistically more weight in the fit, a double minimum structure was observed for the model parameters Q_0, a and b.

All the points shown in Figures 3.13 and 3.14 can be fitted locally with a fourth order polynomial. This is a positive control on the applied fitting procedure, which was using a second order prediction function, $MC(x;\vec{p}_i)$, for all simulated observable distributions. The points reflecting the χ^2 of the fit as a function of Q_0 using the Gaussian enhancement function in the LUBOEI model shows a grid point around 1.7 GeV, a feature which does not influence the obtained results as it is observed far from the minimum.

3.6.5 Systematic cross-checks

In the measured data distributions the systematic uncertainties related to the analysis and detector are already included. Therefore no extra systematic effects should be studied except those directly concerning the tuning procedure. In this philosophy the selected set of distributions used by the MINUIT fit becomes crucial. Systematic shifts on the central values of the tuned model parameters can arise from the inclusion or exclusion of certain observable distributions. For this purpose 14 different sets of distributions were defined, and are listed in Table 3.3. Set 1 is the default set using all distributions. To illustrate the stability of the fit towards the used set of distributions, the model parameters were estimated using these alternative sets rather than the default one. The obtained values are compared in Figures 3.15 and 3.16 for the tuning using the Gaussian enhancement function in the LUBOEI model.

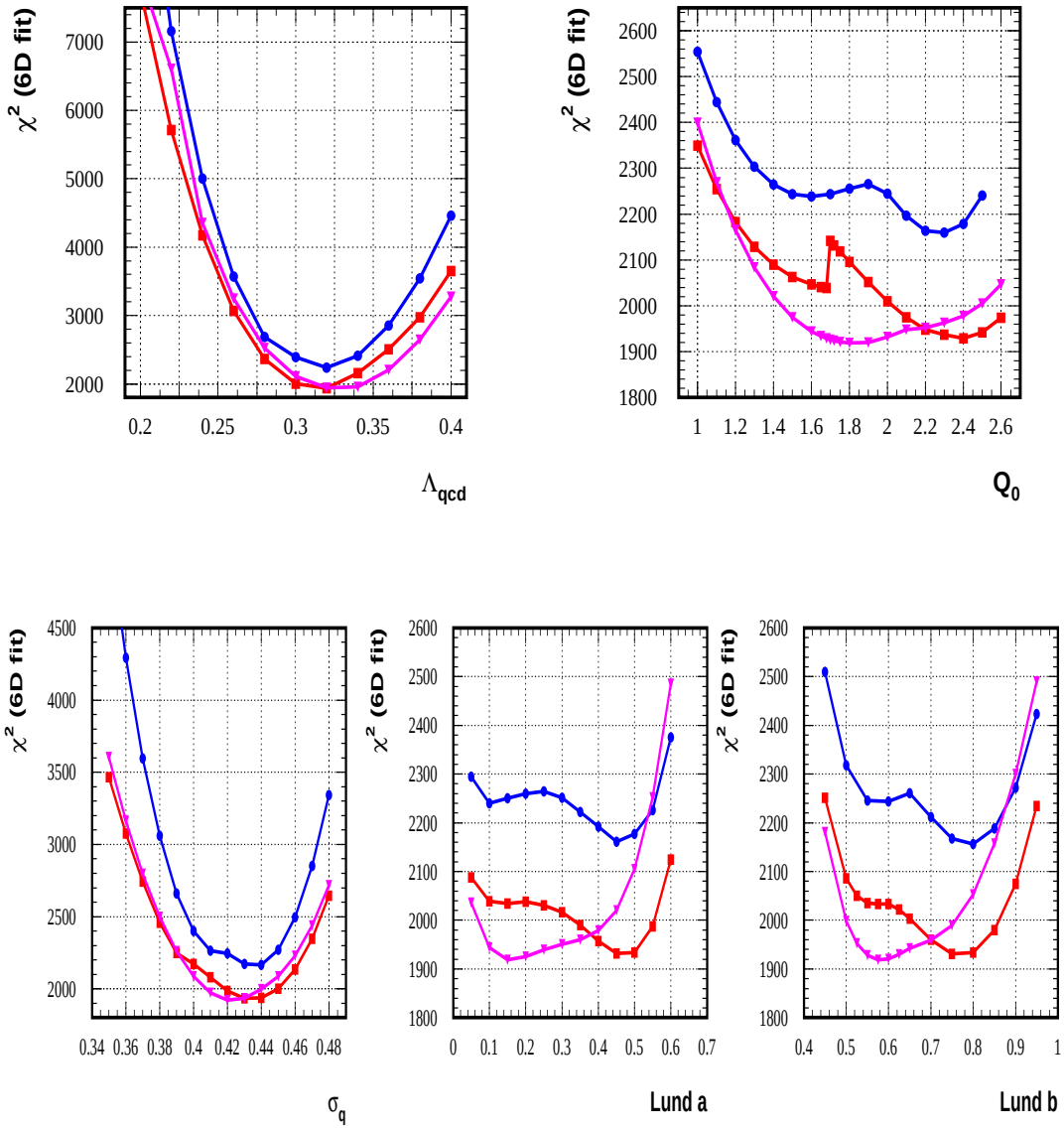

Figure 3.13: *The χ^2 of the fit as a function of one of the seven model parameters is shown (ndf=359). No constraint between Lund a and b was imposed. The χ^2 shown in red reflects the result obtained with the Gaussian parametrization of the enhancement function in the LUBOEI model, similarly the purple curve reflects the results for the exponential parametrization and the blue curve is the χ^2 when the Gaussian parametrization was used but no systematic uncertainties were included in the $Q_{++,--}$ data distribution.*

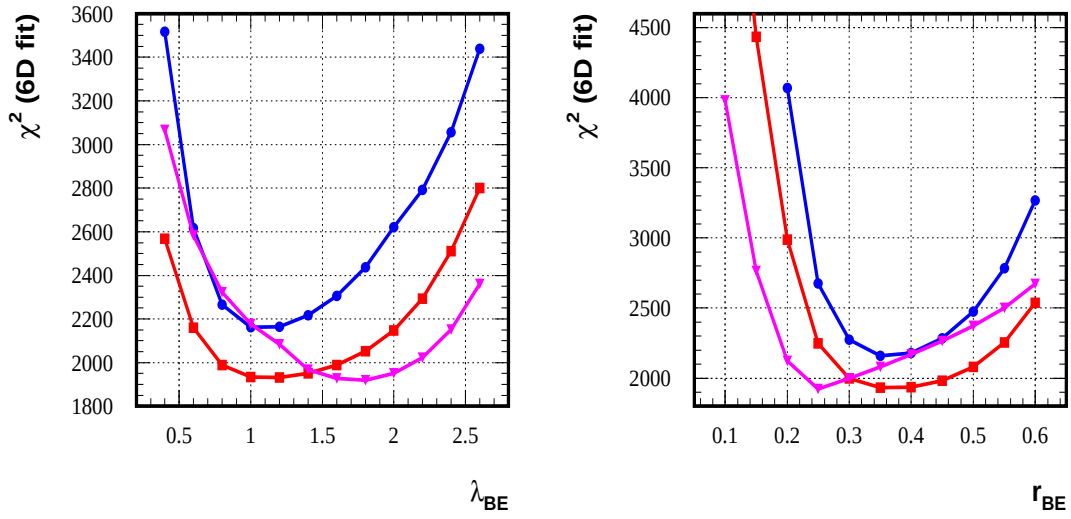

Figure 3.14: *The χ^2 of the fit as a function of one of the seven model parameters is shown (ndf=359). No constraint between Lund a and b was imposed. The χ^2 shown in red reflects the result obtained with the Gaussian parametrization of the enhancement function in the LUBOEI model, similarly the purple curve reflects the results for the exponential parametrization and the blue curve is the χ^2 when the Gaussian parametrization was used but no systematic uncertainties were included in the $Q_{++,--}$ data distribution.*

The observed variation in the result for the parameters Λ_{QCD}, Q_0 and σ_q is much more significant than for the other four parameters, which confirms the importance of this systematic cross-check. The parameter σ_q was for example systematically shifted downwards when including the average charged particle multiplicity in the fit. Sometimes the fit preferred the second minimum in the χ^2, as illustrated in Figure 3.13, which was for example the case for the fit on distribution set 4. For each model parameter the weighted average of its tuned value over all 14 distribution sets is in rather good agreement with the results quoted in Table 3.2, which confirms the stability of the default set.

Some resonance particles have a life-time which is too large to be affected by the Bose-Einstein effect, hence their decay products must be created after applying the LUBOEI algorithm. In JETSET the particles decaying before introducing the LUBOEI algorithm must have a minimum width defined by the input parameter parj(91) which has a default value of 20 MeV/c^2. The particles with a smaller width, hence a longer life-time, will decay after the local reweighting of the particles momenta. In Figure 3.17 the effect of this input parameter is illustrated by comparing the ratio of the simulated $Q_{++,--}$ distribution with the implementation of LUBOEI and the $Q_{++,--}$ distribution simulated by the standard DELPHI tuned version of JETSET which neglects Bose-Einstein Correlations. When increasing the minimum width of the particles affected by LUBOEI the enhancement of particle pairs close in phase-space will become smaller or equivalently the value of the parameter λ_{BE} will

set	1	2	3	4	5	6	7	8	9	10	11	12	13	14
ch.multi.	•							•	•	•	•	•	•	
1-T	•	•	•		•		•	•	•		•		•	
S	•	•		•		•	•	•		•		•	•	
A	•	•		•		•	•	•		•		•	•	
M	•	•	•		•		•	•	•		•		•	
m	•	•	•		•		•	•	•		•		•	
P	•	•		•		•	•	•		•		•	•	
y_{32}(D)	•	•	•		•		•	•	•		•		•	
y_{32}(J)	•	•		•		•	•	•		•		•	•	
y_{43}(D)	•	•			•		•	•			•		•	
y_{43}(J)	•	•				•	•	•				•	•	
y_{54}(D)	•				•		•				•		•	
y_{54}(J)	•					•	•					•	•	
$p_t(in)$ S	•	•		•		•	•	•		•		•	•	
$p_t(out)$ S	•	•		•		•	•	•		•		•	•	
$p_t(in)$ T	•	•	•		•		•	•	•		•		•	
$p_t(out)$ T	•	•	•		•		•	•	•		•		•	
x_p	•	•	•	•	•	•	•	•	•	•	•	•	•	
$Q(++,--)$	•	•	•	•	•	•	•	•	•	•	•	•		•

Table 3.3: *Definition of 14 different sets of distributions used by the MINUIT fit. The distributions indicated with the symbol • are used in the relevant set.*

decrease. In [66] the invariant mass spectrum of the resonance $K^*(892)^0$, which decays for 100% in $K^{\pm}\pi^{\mp}$, was studied with the DELPHI data. Both decay products are bosons and could be influenced by Bose-Einstein Correlations, resulting in a larger resonance width. The data however did not confirm this hypothesis, hence the $K^*(892)^0$ resonance with a width of 50.5 MeV/c^2 lives too long to be influenced by Bose-Einstein Correlations and suggests that the default JETSET value of parj(91), as used in this study, is underestimated. This should be taken into account when interpreting the obtained results.

Systematic comparisons of the simulated observable distributions were made between different PYTHIA versions to examine the stability versus them. Between the PYTHIA versions 6.125, 6.131 and 6.156 no significant differences were found, therefore the obtained results for the values of the model parameters could be considered as general PYTHIA results.

3.6.6 Comparison with the standard DELPHI tuned parameters

The values for $\lambda_{\rm BE}$ and $r_{\rm BE}$ are compared with those commonly used by the DELPHI Collaboration in Figure 3.10. The results obtained by the global JETSET and LUBOEI tuning

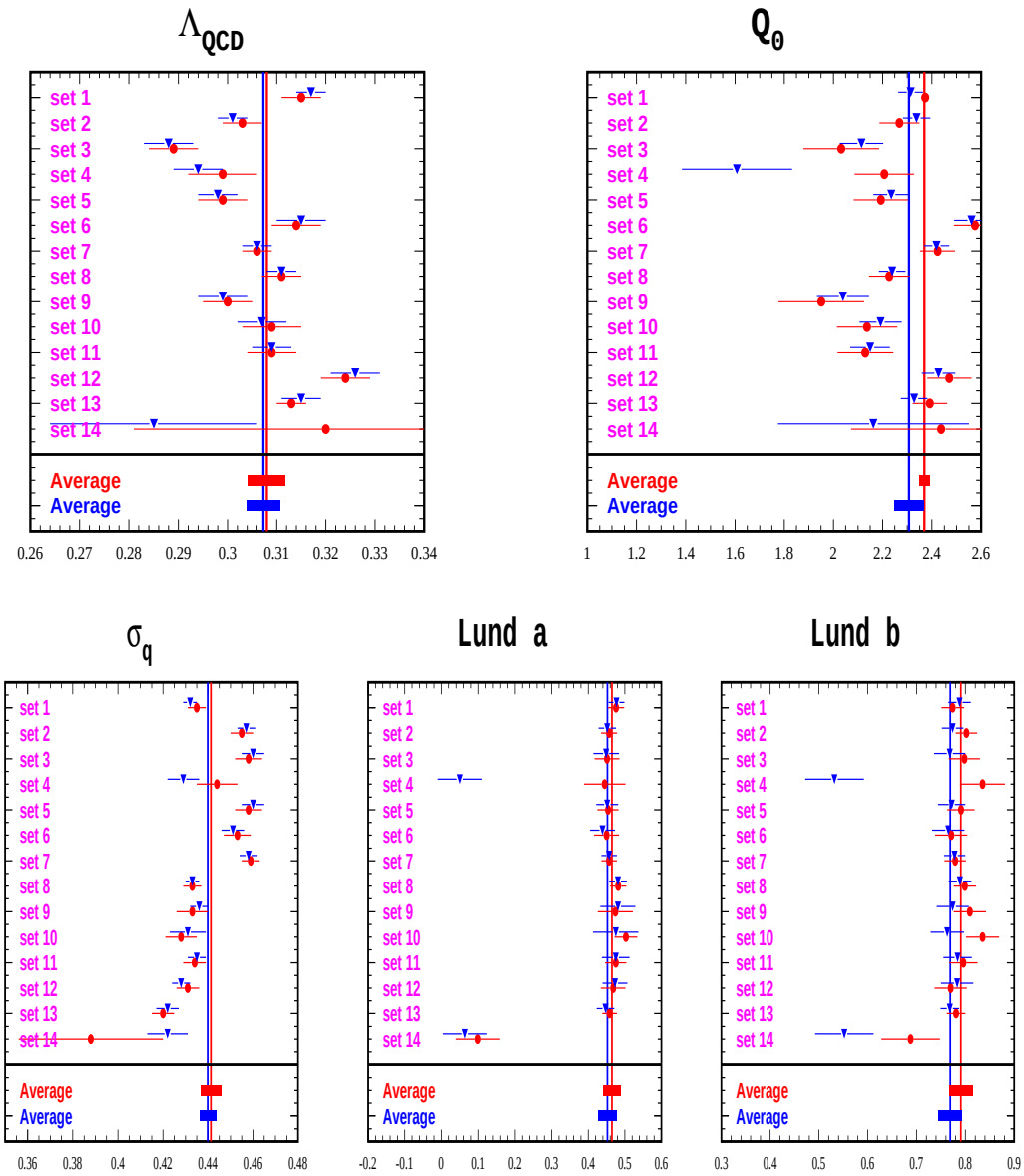

Figure 3.15: *Values of tuned JETSET model parameters obtained with different sets of observable distributions. Imposing the functional constraint between Lund a and b in the fit results in values shown by the blue markers, while the red markers indicate the values when this constraint was not used. The Gaussian enhancement function in LUBOEI was used. The weighted average of the parameter values over the 14 sets is shown at the bottom.*

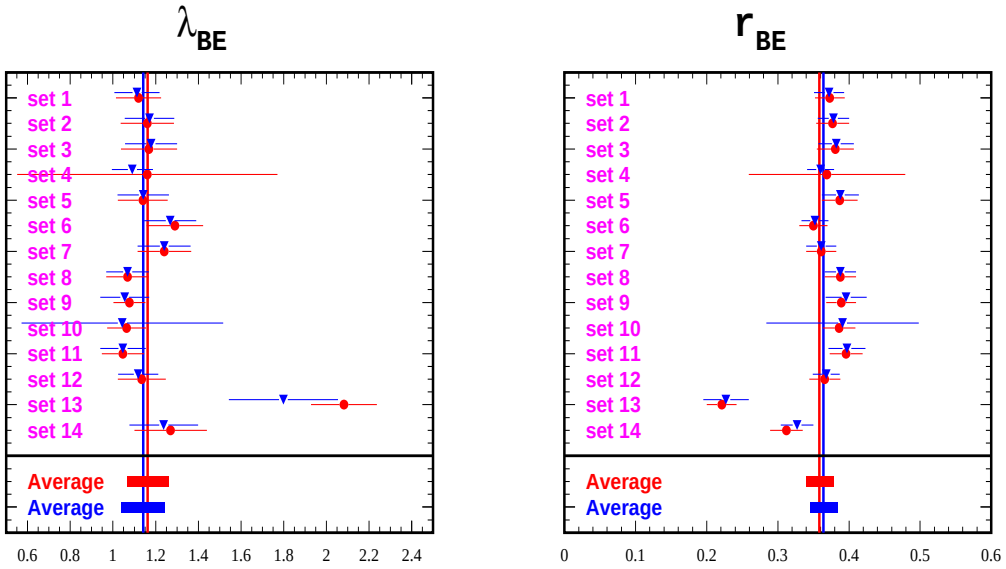

Figure 3.16: *Values of tuned LUBOEI model parameters obtained with different sets of observable distributions. Imposing the functional constraint between Lund a and b in the fit results in values shown by the blue markers, while the red markers indicate the values when this constraint was not used. The Gaussian enhancement function in LUBOEI was used. The weighted average of the parameter values over the 14 sets is shown at the bottom.*

are in agreement with those described in section 3.5.1.

Figure 3.18 illustrates the agreement of some distributions simulated with the tuned JETSET and LUBOEI model to those obtained from the LEP1 data taken by the DELPHI detector. Reference distributions simulated with the standard DELPHI tuned version of JETSET which neglects Bose-Einstein Correlations are shown as benchmarks. The transverse momentum distributions p_t^{in} and p_t^{out} are not well reproduced by the simulation, this is a well known feature in QCD physics. However the simulated p_t distributions with Bose-Einstein Correlations implemented with LUBOEI are in better agreement with the data. In general the single particle spectra measured from the data are better described if Bose-Einstein Correlations are included in the simulation. Including Bose-Einstein Correlations does not improve the description of the global event shape distributions.

The tuned model does not reproduce the $Q_{++,--}$ perfectly, as illustrated in Figure 3.19. In the interesting region $Q < 0.5$ GeV/c^2 the residual discrepancies are around 2-3 %, which is the same magnitude as those remaining with the standard DELPHI tuning of the LUBOEI parameters described in section 3.5.1.

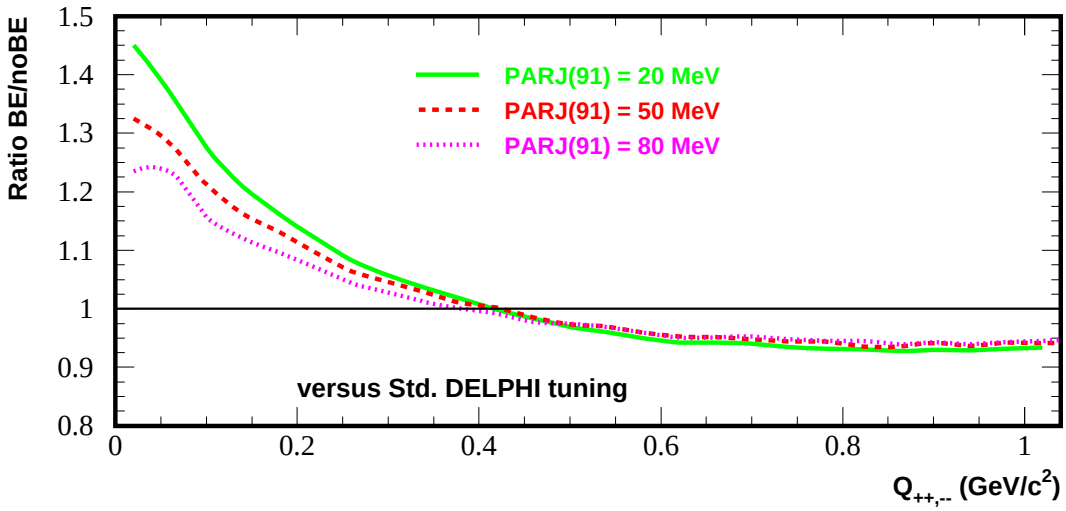

Figure 3.17: *The ratio of $Q_{++,--}(\mathrm{BE})$ with Bose-Einstein Correlations implemented with LUBOEI and $Q_{++,--}(\mathrm{noBE})$ with the standard DELPHI implementation of PYTHIA neglecting the Bose-Einstein effect is shown to illustrate the influence of the PYTHIA parameter parj(91) on the $Q_{++,--}$ distribution. The tuned parameters as denoted by QCD/BE(E) in Table 3.2 are used.*

3.6.7 Comments and conclusions

In the simulation of multi-hadron events one could use PYTHIA version 6 in combination with the LUBOEI algorithm version BE_{32} to emulate the effect of Bose-Einstein Correlations. After tuning the relevant model parameters the agreement between simulation and measured data distributions is in general better when including a modelization of the Bose-Einstein Correlations between the final state particles.

For the measurement of the Bose-Einstein phenomena (cfr. section 3.5.1) in hadronic decaying W^+W^- events, it is important to have a good description of the $Z^0 \to q\bar{q}$ background which is known to be influenced by Bose-Einstein Correlations and is expected to amount to 20-25% of the data sample after full event selection. Generally one subtracts the background from the data $Q_{++,--}$ distributions with Monte Carlo simulated events generated with PYTHIA including a Z^0 tuned version of the LUBOEI algorithm. Therefore a comparison on generator level was made [67] of the model predictions from individual tunings performed by the LEP Collaborations after a 4-jet like selection [68] at the Z^0 peak and at $\sqrt{s}$= 189 GeV. In general a good agreement between the experiments was observed for event shapes and single particle spectra at both energies, but differences add up to about 10% on the selection rate of those background events when using the same event selection criteria. The simulated charged particle multiplicity differs by about 4% and contributes significantly to a 10% difference in the normalization of two-particle distributions between the different

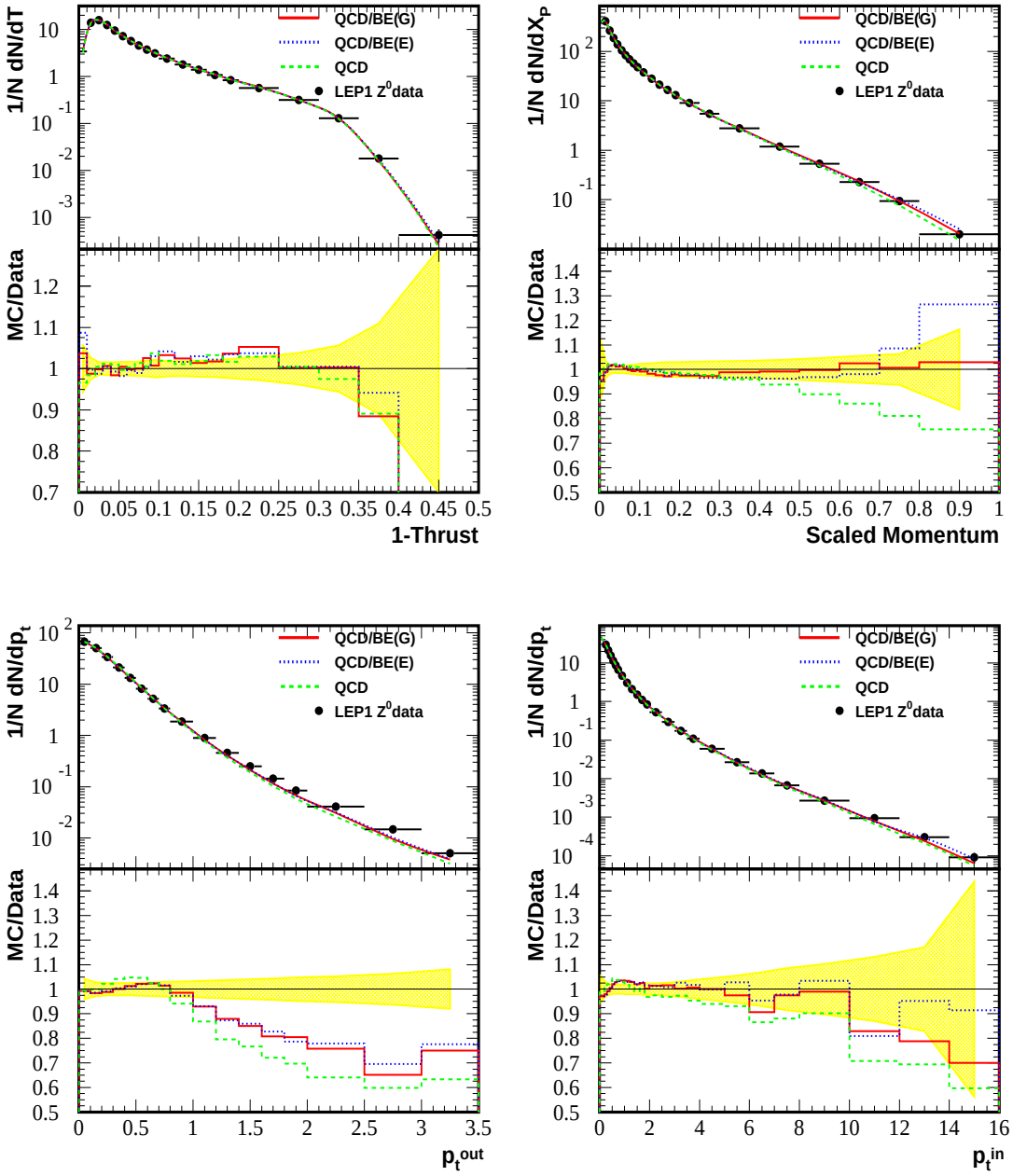

Figure 3.18: *Comparison between the data and simulated distributions using the standard DELPHI tuning neglecting Bose-Einstein Correlations and the obtained distributions with the tuning as described in the text. The legend refers to Table 3.2, while the yellow band reflects the one standard deviation of the total uncertainty on the data.*

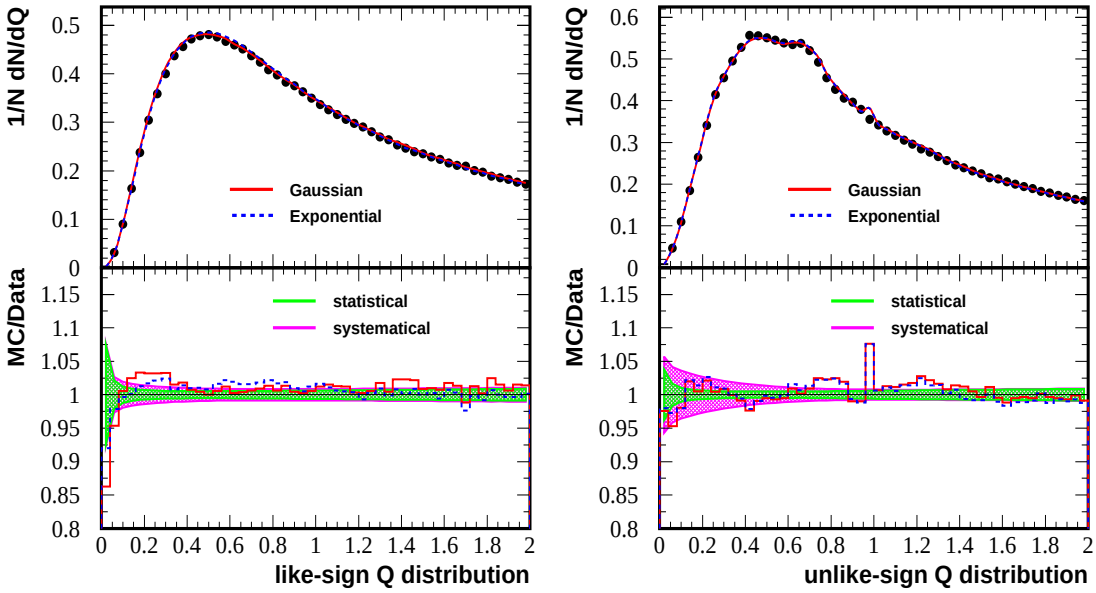

Figure 3.19: *Comparison between data and Monte Carlo distributions obtained with the tuned model as described in the text using the Gaussian or the exponential parametrization of the two-particle enhancement functions R(Q) in the LUBOEI model.*

tunings. Taking into account the normalization, the shape of the $Q_{++,--}$ distributions differs by about 10-20% in the low Q region, which is a value comparable with the inherent uncertainty of the LUBOEI model in this background simulation. This raises the question if the model tuning or equally the background subtraction in these Bose-Einstein Correlation measurements has to be treated as a correlated source of systematic uncertainties between the LEP experiments. For the estimation of systematic uncertainties arising from possible Bose-Einstein effects on measurements using the $W^+W^- \to q\bar{q}'Q'\bar{Q}$ events, like the measurements of the W boson resonance to be presented in this thesis, it is important that the rather good agreement between data and tuned simulated distributions observed at the m_Z scale, is equally valid at higher scales around 200 GeV. These rather good agreements were found to be invariant between those two $\sqrt{s}$ scales.

3.7 Overview of W^+W^- phenomenology

This chapter contains a thorough discussion of the different phenomena present in $e^+e^- \to W^+W^- \to q\bar{q}'Q'\bar{Q}$ events produced in the LEP2 energy range. The approximate factorization between the physics of those phenomena made possible to use separate Monte Carlo

algorithms for their implementation in dedicated simulation programs. All steps in the evolution of the event from the simple e^+e^- initial state to the rather complicated multi-hadron final state, are simulated in great detail. The successive application of the algorithms results in one complete simulation package, covering all physics effects in the production of the detected final state. The Monte Carlo simulation can be used to study the properties of parameter estimators which are designed to infer information from the detected W^+W^- final state of real data events. In chapters 4 and 5 this strategy will be used to construct estimators for the mass and the width of the W boson.

All neglected phenomena in the nominal simulation, like Bose-Einstein Correlations and Colour Reconnection, should be treated as systematic uncertainties on the measurements, together with the effect of possible intrinsic uncertainties in the factorized modelization of each step. This will be the main topic of chapters 6 and 7.

The nominal Monte Carlo simulation was generated with WPHACT and the partons were fragmented with the PYTHIA or JETSET model. To avoid statistical fluctuations on the estimators due to the limited number of Monte Carlo simulated events, about thousand times more Monte Carlo events were produced than the number of events expected in the data.

Chapter 4

Experimental event reconstruction techniques

From the data recorded as described in chapter 2 the momenta of individual charged particles were obtained. The calorimetry within DELPHI associates with these tracks an energy deposit and reconstructs the energy and flight direction of the neutral particles from the remaining detected energy clusters. In this chapter the selection of the particles to be used in the analysis is discussed together with the energy flow associated to those particles (section 4.1). An algorithm to tag beauty flavored jets is described in section 4.2. Rather than using the kinematics of the individual particles in a complicated m_W analysis, the particles are clustered into so-called jets initiated by the primary partons in the decay of $W^+W^- \rightarrow q\bar{q}'Q'\bar{Q}$ events. An overview is given of the relevant clustering algorithms to reconstruct the kinematics of those jets (section 4.3). In order to use the knowledge of the kinematics of the leptons before collision as a constraint on the kinematics of the reconstructed jets in the final state of the event, a kinematical fit procedure is described based on four-momentum conservation (section 4.4). An undetected photon radiated by one of the initial leptons can however dilute the kinematical knowledge of the initial state. The fit allows to incorporate this possibility as a reduction of the number of the kinematic constraints.

4.1 Energy flow reconstruction and particle selection

The energy flow in the event is determined by using all the information available from the tracking detectors and the calorimeters. The precision with which we measure the kinematic structure of the event is a function of the intrinsic resolution of the detectors, their efficiency and the efficiency of the reconstruction algorithms used to combine the data. The relative precision of the tracking detectors is such that the energy of charged particles is best estimated using the tracking detectors rather than the calorimeters. The masses of these particles are estimated using the standard DELPHI particle identification [26]. The hadron calorimeters are used mainly for measuring the energy of long lived neutral hadrons such as neutrons or K_L^0's. Clearly the main smearing of the energy resolution per particle comes from the non-perfect differentiation between hadronic and purely electromagnetic showers nearby directions with a large particle density, for example within jets.

The clustering of energy in the calorimeters is performed in two steps. In a first step we associate with all charged particle tracks their corresponding energy clusters in both the electromagnetic and hadron calorimeter, this by adding all energy deposits within a specified angle around the extrapolated direction of the track. In the next step the remaining energy deposits are used to reconstruct the showers initiated by neutral particles. The residual energy within a radial cone with a fixed angle around the hits is associated to neutral particles. This procedure starts with the highest energy deposit hit and is stopped when all energy hits are associated to a particle.

Run Quality selection

During data taking the many subdetectors in DELPHI were not always fully operational. The quality of their data, can be different from run to run. An appropriate criterion was applied to select only those runs when the main detectors relevant for the m_W analysis were efficient. An azimuthal symmetry of the detector quality was assumed.

In a first selection level only those runs were kept during which the TPC, HPC and EMF were, averaged over the full run, more than 80% efficient. After these cuts one can easily calculate the integrated luminosity of the data sample as the integrated luminosity per run is available. The second level was based on event-by-event information about the subdetectors status, again by requiring an efficiency of more than 80% for TPC, HPC and EMF. Of course there is nothing such as event-by-event luminosity, therefore one has to renormalize the integrated luminosity of the run after these event-by-event cuts. For this purpose the integrated luminosity of the data sample was multiplied by the efficiency of selecting hadronic events in this second stage.

Hadronic events were defined as those which pass the 'TEAM4' hadronic selection [26]. This selection criterion was meant to guarantee a high and well understood efficiency and is the basis of the selections used for measurements of the $e^+e^- \rightarrow Z^0 \rightarrow hadrons$ cross-

Year	Nominal $\sqrt{s}$ [GeV]	Integrated Luminosity (pb^{-1}) before	after
1997	182.65	54.070	51.765
1998	188.63	157.637	152.530
1999	191.58	25.850	24.361
1999	195.51	76.414	74.635
1999	199.51	83.368	81.640
1999	201.64	40.637	40.188
2000	205.8	163.829	158.505
TPC-S6	206.3	60.062	57.432
total		661.867	641.056

Table 4.1: *DELPHI estimate of the luminosity weighted centre-of-mass energies and integrated luminosities per data sample, before and after the selection based on the quality of the relevant subdetectors. The period when one sector of the TPC was 0% effi cient is marked as 'TPC-S6'.*

section. Hadronic Z^0 decays are selected as events with a multiplicity above 4 of charged particles which have a momentum $p > 400$ MeV/c, a polar angle in the range $20^o < \theta < 160^o$ and a track length of at least 30 cm in the TPC. The total energy deposit of these charged particles must be above 12% of the centre-of-mass energy. A clear separation of the events thrust axis from the beam pipe was required by cutting on $|\cos\theta_{Thrust}| < 0.95$. The efficiency for selecting hadronic Z^0 decays is over 95%, while the background, mainly from $\tau^+\tau^-$pairs and $\gamma\gamma$ collisions, is below 0.7%.

On the 1st of September 2000 one of the twelve TPC sectors ceased its operation [29]. As a result it was not possible to detect the tracks left by charged particles inside the broken sector. The data affected corresponds to about 1/4 of the data collected in 2000. As described in section 2.4 a modified track reconstruction was performed in this sector. As a result, the track reconstruction efficiency was only slightly reduced in the region covered by the broken sector, but on average the resolution on the track parameters was worse than prior to the failure of the sector. This period will be denoted by 'TPC-S6' in the continuation of this thesis.

In Table 4.1 the integrated luminosity is quoted before and after this run quality selection. Around 3% of the full luminosity was rejected by those cuts. The total integrated luminosity for the relevant LEP2 period corresponds to approximately 641 pb^{-1} after run quality selection.

Particle selection

To reduce the influence of ambiguous tracks on the final analysis a track selection [32] was applied. Tracks used in the m_W analysis fulfill the following criteria:

- track momentum $|\vec{p}| > 100$ MeV/c ;
- relative momentum uncertainty $|\Delta\vec{p}/\vec{p}| < 1$;
- impact parameter [1] in $r\phi < 4$ cm ;
- impact parameter in $z \cdot \sin\theta < 4$ cm ;
- the track is not associated with a reconstructed secondary vertex.

The first two cuts reject bad reconstructed tracks, while the next two reject tracks not originating from the interaction point, for example tracks induced by cosmic muons and beam interactions other than the one of interest. The last criterion insures that a track originating from the decay of a reconstructed long lived resonance is not counted twice.

Showers in the calorimeters are treated as deposits from neutral particles if their energy exceeds the following minimum:

- in the STIC > 0.3 GeV ;
- in the HPC > 1.5 GeV ;

[1] The distance of closest approach to the interaction point.

- in the FEMC > 0.5 GeV ;
- in the HCAL > 1.3 GeV.

In addition to these standard quality criteria an extra cut was applied to eliminate possible energy deposits from off-momentum beam electrons,

- rejecting all particles with a polar angle outside the range $3^o < \theta < 177^o$

and a special treatment was included to protect the analysis against particles reconstructed with an unphysical high momentum ($p > E_{\rm beam}$). Charged particles with a momentum larger than 60 GeV/c were rescaled to 10 GeV/c with a high relative momentum uncertainty, if the momentum was between 10 and 60 GeV/c and the relative momentum uncertainty larger than 0.3, then they were rescaled to 10 GeV/c. For neutral particles any excess of associated energy above 100 GeV was discarded.

Systematic study of the energy flow reconstruction

The reconstruction of the energy flow in the DELPHI detector can be studied with the data from the calibration runs accumulated each year at centre-of-mass energies around the Z^0 peak. The kinematic structure of hadronic $Z^0 \rightarrow q\bar{q}$ events is well understood, therefore event shapes and single particle distributions can be simulated with a tuned JETSET Monte Carlo model (cfr. section 3.3 and [53]) fragmenting the partons initiated by the KK2f event generator. The relatively large cross-section of those events at the Z^0 peak and the negligible background contamination permits a detailed comparison between the recorded data and the simulation. Any observed deviation between both must be taken into account when performing a measurement using the jets in $W^+W^- \rightarrow q\bar{q}'Q'\bar{Q}$ events recorded by the same detector in the same qualitative status. In the simulation of those complicated W^+W^- events the same tuned version of the JETSET fragmentation model was used as for the Z^0 simulation and the same particle selection was applied.

For the following study the hadronic decaying Z^0 events were selected by applying the following sequential cuts :

- Charged multiplicity ≥ 5 ;
- $\sum_{i\in\{p_z\geq 0\}} |\vec{p}_i|^{ch.} \geq 3$ GeV/c ;
- $\sum_{i\in\{p_z\leq 0\}} |\vec{p}_i|^{ch.} \geq 3$ GeV/c ;
- $\sum_{i\in\{p_z\geq 0\}} |\vec{p}_i|^{ch.} + \sum_{i\in\{p_z\leq 0\}} |\vec{p}_i|^{ch.} \geq 15$ GeV/c ;
- Missing momentum (from charged particles) ≤ 30 GeV/c ;
- Thrust $T = \max_{\vec{n}_{Thrust}} \frac{\sum_{i=1}^{N_{particle}} |\vec{p}_i \cdot \vec{n}_{Thrust}|}{\sum_{i=1}^{N_{particle}} |\vec{p}_i|} \geq 0.95$.

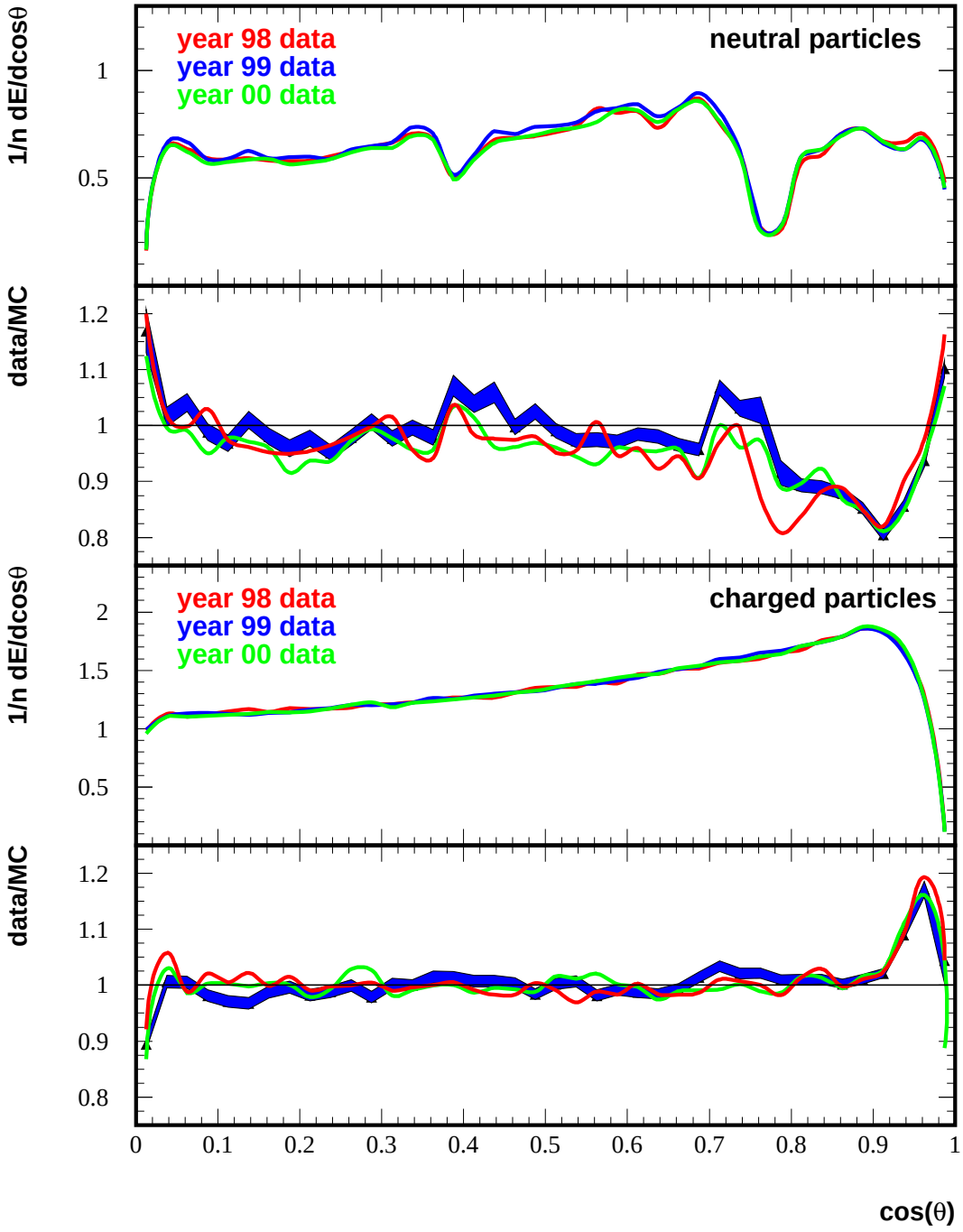

Figure 4.1: *Mean charged or neutral energy flow per selected $Z^0 \to q\bar{q}$ event as a function of the cosine of the polar angle θ. The data of different years are compared with the corresponding KK2f simulation. To illustrate the significance of the fluctuations, the variance on the ratio is shown as a 1σ band for the year 1999. In a good approximation one can assume that this variance is equal over the different years.*

Applying the sequential cut on the thrust value of the event was done to have clear back-to-back $Z^0 \rightarrow q\bar{q}$ events. The reconstructed energy flow of the selected events from the Z^0 calibration runs recorded during the years 1998, 1999 and 2000 was studied. The average charged and neutral energy per event as a function of the cosine of the polar angle θ is shown in Figure 4.1, assuming that the forward and backward directions are symmetrical. In the forward (backward) region there is an excess of reconstructed charged energy in the data compared to the Monte Carlo simulation, while a deficit is observed for the neutral energy. The shape of the discrepancies is invariant over the years. This is not necessarily true for their global scale as can be observed for the neutral energy in the year 1999. Possible systematic uncertainties on the measured W mass induced by these discrepancies will be examined in section 6.3.1.

More important for the jet reconstruction and therefore for the measurement of the W mass is the energy flow reconstruction within a jet, where the particle density is large. An original study of energy flow systematics related to jet kinematics is presented in section 6.3.1.

4.2 Identification of b quark-jets or 'b-tagging'

The Z^0 bosons have an intrinsic probability of about 15% to decay into a $b\bar{b}$ final state, which is a useful property to distinguish them from $W^{\pm}$ bosons. In the hadronization of a b-quark the formation of B mesons becomes possible, which have a mean life time of about 1.6 ps. Beauty flavored mesons cannot originate from the direct decay of light-quarks (u,d,s,c) and are therefore only rarely present in hadronic decays of $W^{\pm}$ bosons. The subsequent, electroweak dominated, decay of the B mesons produces a secondary decay vertex separated by the B mesons flight distance from the primary vertex where the collision took place. The separation was of the order of 3-4 mm for typical high energy events at LEP2, which was large enough to be resolved by DELPHI's Vertex Detector with a resolution of about 65μm. Together with other kinematic information this secondary vertex measurement provided a combined b-tag variable for each event. A full description of this observable can be found in [69]. Anti-b tagging was used in the selection of $W^+W^- \rightarrow q\bar{q}'Q'\bar{Q}$ events in section 5.1.

4.3 Particle clustering algorithms or jet finders

The design of an analysis at particle level would be extremely complicated due to the large dimensionality of the information concerning the observed final state. By taking the large number of particles produced and clustering them into a small number of jets, a simplified characterization of the event is achieved which helps us in the study of the main properties of its underlying dynamics. In section 3.3 it was shown that most of the particles are produced in the flight direction of the original primary parton, or around the radiated hard gluons. Most clustering algorithms are based on a binary joining procedure to combine particles which are nearby according to some predefined distance scale. Throughout this thesis three clustering algorithms have been studied and were used in the different analyses:

- **DURHAM** [64] : This algorithm is based on the original JADE k_T-algorithm [63] where a distance measure d_{ij} between two clusters [2] i and j is defined as a function of their respective four-momenta $p_{i,j} = (E_{i,j}, \vec{p}_{i,j})$. Starting from the initial list of all selected particles the two clusters with the smallest relative distance are merged into one. The four-momentum of the new cluster k is simply $p_k = p_i + p_j$. For the DURHAM algorithm the distance d_{ij} measure is defined as:

$$d_{ij}^2 = 2\ \min(E_i^2, E_j^2)\ (1 - \cos\theta_{ij}) \tag{4.1}$$

where θ_{ij} is the opening angle between the momentum vectors of the two clusters with energies E_i and E_j. To obtain an expression without dimensions, an event-by-event scaling is performed as:

$$y_{ij} = \frac{d_{ij}^2}{E_{vis}^2} \tag{4.2}$$

where E_{vis} denotes the visible energy in the event and would agree with the centre-of-mass energy $\sqrt{s}$ for a perfect detector. This distance measure reflects the transverse energy of the combined cluster k. The joining procedure can be repeated until only one cluster remains or until all pairs have a separation distance y_{ij} larger than the jet resolution parameter y_{cut}. By changing the value of y_{cut}, the final state is resolved into a varying number of jets. The transition value at which the event classification changes from a n-jet to a m-jet topology, when going to larger values for y_{cut}, will subsequently be referred to as the $y_{m \leftarrow n}$ value.

- **CAMBRIDGE** [70] : This is a modified version of the DURHAM algorithm. The same distance measure y_{ij} is applied to define the cut-off scale y_{cut}, while for the ordening of which pairing to perform first the angle between the two candidate clusters was taken:

$$d_{ij}^2 = 2\ (1 - \cos\theta_{ij})\ . \tag{4.3}$$

With this procedure the risk of 'junk-jet' formation is reduced compared to DURHAM, which starts in general by clustering the soft particles and therefore tends in some configurations to create a stand-alone cluster of daughter soft gluons separated from its mother leading parton. Such a junk-jet in fully hadronic W^+W^- final states could consist out of soft particles from both W decays and therefore dilute the kinematic information about the primary partons. A second improvement was the implementation of the sterilization of the softest particle in a resolved pair, a procedure called 'soft-freezing'. When the value y_{ij} of a pair of clusters is larger than y_{cut}, then the cluster i or j with the smaller energy is defined as a separated jet and remove from the list of possible clusters. The remaining cluster with the highest energy still continues to

[2] A cluster is defined as an intermediate jet during the clustering procedure and could therefore also be a single particle.

participate in the clustering procedure. This prevents the softer jet from attracting any extra particles.

- **DICLUS** or **ARCLUS** [71] : This algorithm is not based on the binary joining of two clusters to one but rather the joining of three clusters to two. This is well matched to the dipole fragmentation picture of a cascade evolution, used in the ARIADNE program, where the hadron is produced in the colour field between two partons. As DICLUS tries to reconstruct a dipole cascade, the same ordening variable is chosen as in the ARIADNE model which is the Lorentz invariant transverse momentum defined for an emitted parton i with respect to the two emitting partons j and k as:

$$p^2_{\perp i(jk)} = \frac{(s_{ij} - (m_i + m_j)^2)(s_{ik} - (m_i + m_k)^2)}{s_{ijk}} \tag{4.4}$$

where s_{ij} and s_{ik} (s_{ijk}) are the squared invariant masses of two (three) partons. For each cluster i, the two other clusters j and k for which $p^2_{\perp i(jk)}$ is minimized are found. When this measure $p^2_{\perp i(jk)}$ is below the cut-off, the cluster i is removed and its energy and momentum are distributed among j and k.

The resemblance of the perturbative fragmentation models and the jet clustering algorithms is not only limited to the DICLUS case. Each clustering algorithm is an attempt to reconstruct the QCD cascade backwards in time, however the notion of time in those cascades is not unambiguous. Within the three fragmentation models described in section 3.3 a different ordening of parton emissions is present, therefore the use of different clustering algorithms could dilute the systematic differences between observables from those fragmentation models. None of the clustering algorithms is the ultimate one for all purposes, therefore an optimal combination of them will be used in the analyses described in the next chapter [72].

The hadronic data from the Z^0 calibration runs, as mentioned in section 4.1, show in average a small deviation in reconstructed jet properties, like energy, polar and azimuthal angle, compared to the simulated KK2f events. At reconstruction level a Gaussian smearing and shifting function was applied on the jet kinematics of the simulated events to reduce these discrepancies. For the jet energy the smearing parameters are function of the polar angle of the jet as well as of the energy. It was found that the jet energies need to be smeared by about 1.5 GeV or 2.4 GeV respectively for jets in the forward and barrel region (1.2 and 3.3 GeV for the TPC-S6 period) and decreased in value by about 0.5 GeV in both regions. The angles were not shifted, but smeared both in azimuthal and polar direction by about 0.5 to 1 degrees. These smearing parameters were extrapolated to jet kinematics in high energy ($\sqrt{s} > 2m_W$) events, by comparing in a similar way jets in high energy $Z^0 \to q\bar{q}g$ data events with the corresponding ones in the KK2f Monte Carlo.

An example of a data event recorded with DELPHI is shown in Figure 4.2. The particles and the energy flow were reconstructed by the methods described above. Subsequently the particles were clustered into 4 jets, which are clearly visible in the figure.

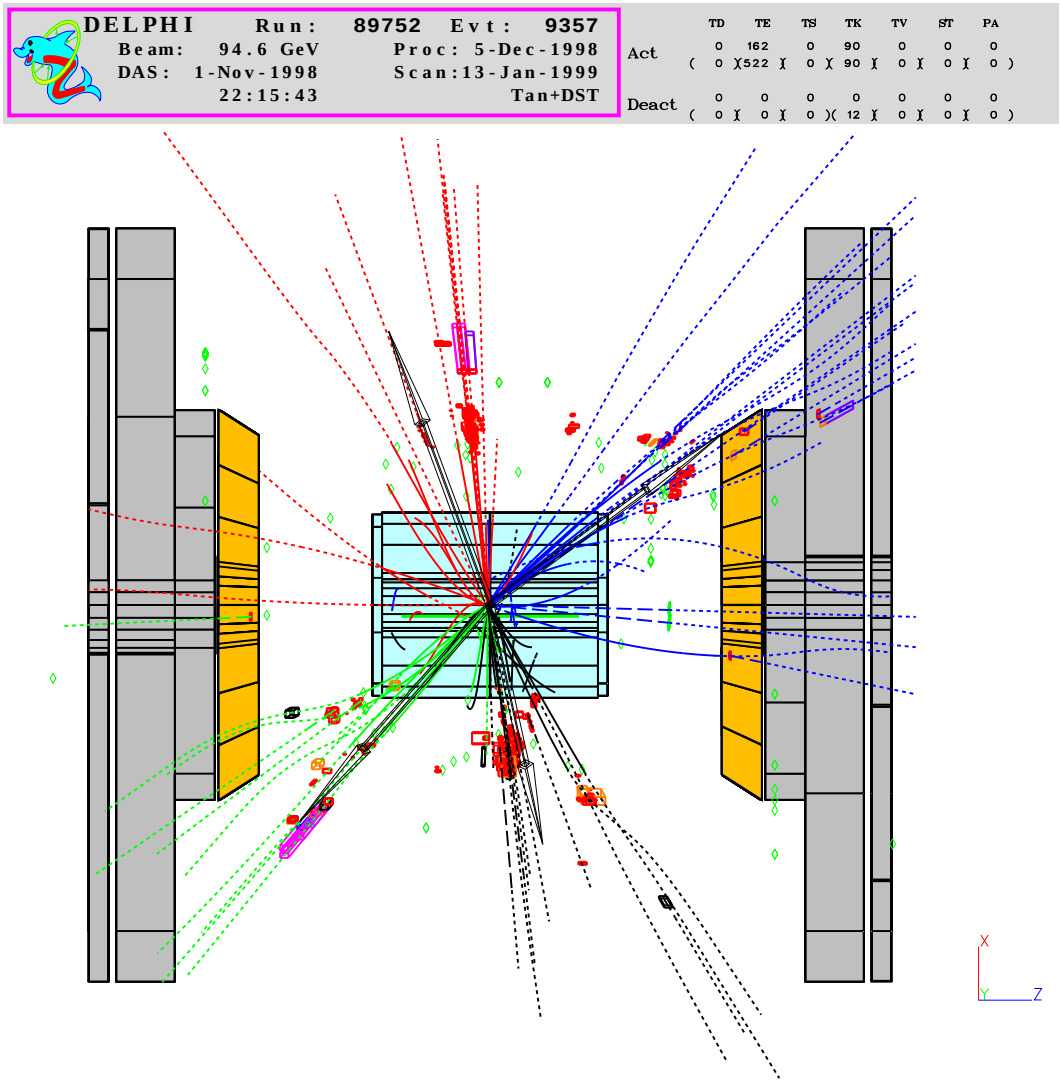

Figure 4.2: *Example of a 4 jet event from the data taken by DELPHI during the year 1998 (Run : 89752 and Event : 9357). The reconstructed particles were clustered into jets from which the momentum vector is shown. Both endcaps illustrate the dimensions of the detector, where the TPC is coloured in the middle around the impact position.*

4.4 Kinematic constraints between initial and final state

The event-by-event uncertainty on the beam energy at LEP is typically 0.1% (cfr. section 2.2), while the overall momentum and energy resolution of the observed final state is about 10%. The precise knowledge of the kinematics in the initial state can be used to constrain the kinematic information on the clustered jets in the final state. This is accomplished by means of a χ^2 fit based on the conservation law of energy and momentum.

Due to the fully symmetric collision, the initial state as no boost in the lab frame, while its intrinsic invariant mass is $\sqrt{s} = 2E_{\mathrm{beam}}$. These observations define four kinematic constraints (4C) which can be propagated to the final state :

$$\left(\sum_{j=1}^{jets} E_j, \sum_{j=1}^{jets} \vec{p}^{\,j} \right) \; = \; (\sqrt{s}, \vec{0}) \; . \tag{4.5}$$

In order to further constrain the event kinematics, the reconstructed jets of the event can be classified as coming from one of the two hypothetical heavy objects which reflect the W bosons. A fifth constraint on top of the energy-momentum conservation could be considered by asking that the masses of these heavy objects are equal (5C), because they reflect respectively the W^+ and the W^- bosons which have the same mass properties in the Standard Model. From the knowledge that the decay width of the $W^{\pm}$ bosons is finite, this constraint is of course non-physical. It is however a useful constraint when constructing a single event observable connected directly to the reconstructed W mass of the event.

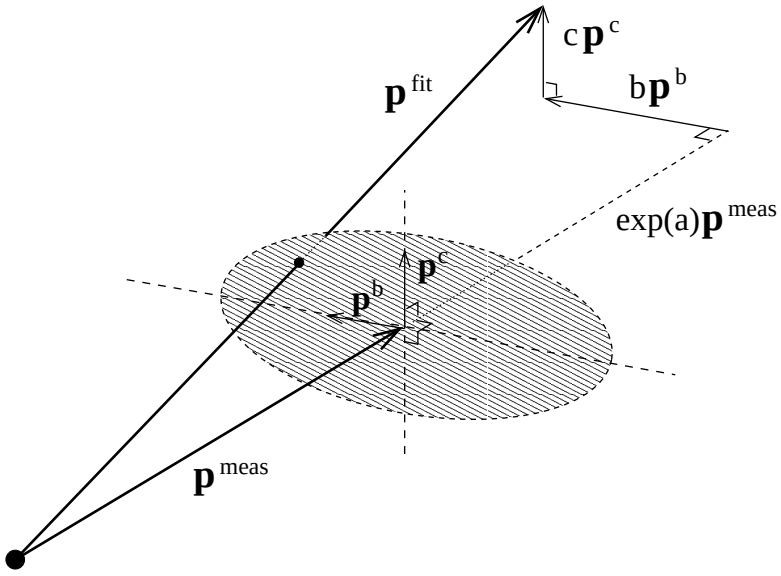

Figure 4.3: *Parametrization used for jets in the constrained fit, as explained in the text and Equation 4.6.*

Each fitted jet momentum $\vec{p}_j^{\,f}$ was projected onto a set of axes with one component parallel to the measured jet momentum $\vec{p}_j^{\,m}$ and two transverse components, $\vec{p}_j^{\,b}$ and $\vec{p}_j^{\,c}$, both normalized in magnitude to 1 GeV/c. In this coordinate system $\vec{p}_j^{\,f}$ can be described by three parameters a_j, b_j and c_j:

$$\vec{p}_j^{\,f} = e^{a_j}\vec{p}_j^{\,m} + b_j\vec{p}_j^{\,b} + c_j\vec{p}_j^{\,c} \tag{4.6}$$

where each component is shown in Figure 4.3. The measured jet energy $E_j^{\,m}$ was rescaled with the same factor e^{a_j} as the jet momentum. The exponential parametrization e^{a_j} of the factor in front of $\vec{p}_j^{\,m}$ makes the fit more stable and results in more Gaussian uncertainties. The values of the parameters and the transverse directions are determined by the constrained fitting package PUFITC+ [73].

The algorithm minimizes a χ^2, defined as:

$$\chi^2 = \sum_{j=1}^{jets} \frac{(a_j - a_0)^2}{\sigma_{a_j}^2} + \frac{b_j^{\,2}}{\sigma_{b_j}^2} + \frac{c_j^{\,2}}{\sigma_{c_j}^2} \tag{4.7}$$

while forcing the fitted event to obey the constraints. The expected energy loss parameter a_0 and the energy spread parameter σ_{a_j}, together with the parameters σ_{b_j} and σ_{c_j}, were parametrized as functions of the jet polar angles.

In a first stage of the fit the uncertainties on the jet parameters are defined as:

$$\begin{aligned} a_0 &= 0.15 + 0.40 \cdot \cos^4\theta_j \\ \sigma_{a_j} &= 0.15 + 0.40 \cdot \cos^4\theta_j \\ \sigma_{b_j} &= \sigma_{c_j} = (1.0 + 0.6 \cdot \cos^4\theta_j) \cdot 1.62 \end{aligned} \tag{4.8}$$

where θ_j is the polar angle of the jet and an azimuthal invariance of the energy reconstruction efficiency was used.

This functional dependency was motivated by Z^0 studies, illustrated in Figure 4.4. The energy scale of reconstructed jets in hadronic events selected by the TEAM4 criteria in the data from the Z^0 calibration runs, or from the corresponding Monte Carlo simulation, was compared with the kinematically available energy per jet, which was the beam energy. The DURHAM jet clustering algorithm with a y_{cut} value of 0.006 was used, and events were required to have a 2 jet topology. In general an energy loss of around 10% was observed for jets in the barrel region of the detector, while this increased to 15% in the forward regions. A good agreement between the jet energy scale in data and simulation was found. The energy loss increases if the event jet topology becomes more ambiguous, resulting in energy losses around 15% for the barrel region and up to 35% in the forwards regions. It was found that the inclusive parametrization of the jet parameters and their uncertainties in Equation 4.8 is well motivated. In reality they depend however slightly on the jet properties.

This dependency on the jet properties was included in a second stage of the fit, where the parametrization of the transverse momentum uncertainties will depend on the broadness of the jet. This broadness was calculated by projecting the momenta of all particles in the jet on the plane transverse to the jet axis. From those projections a two dimensional momentum tensor $\mathcal{T}_{\beta\gamma}$ was created:

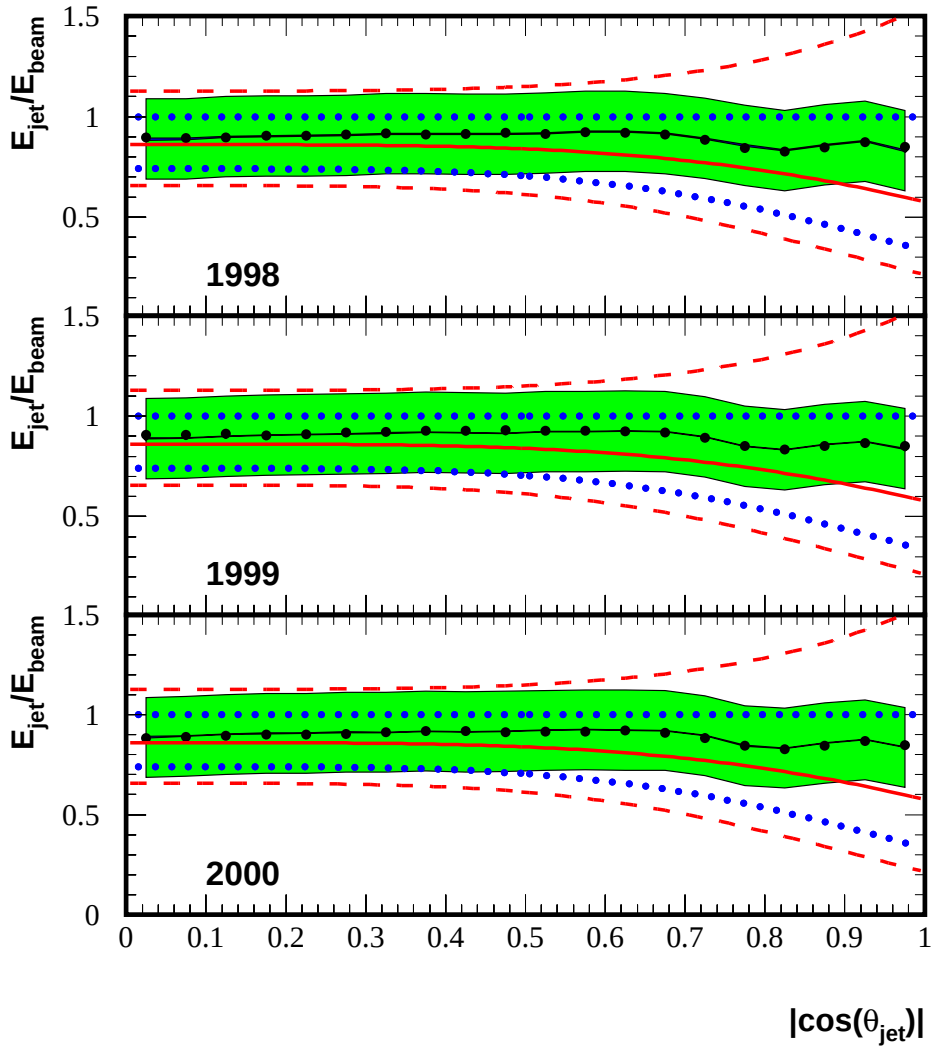

Figure 4.4: *The ratio of the reconstructed jet energy scale and the beam energy, or jet energy reconstruction efficiency, as a function of the polar angle of the jet. The narrow blue band indicates the average jet efficiency, while the green band reflects its resolution as determined from the Monte Carlo simulation for the Z^0 calibration runs in 1998, 1999 and 2000. The dots give the corresponding data values. The solid red line is the parametrized energy loss (a_0) as described in Equations 4.8 and 4.10, the dotted lines reflect the one standard deviation 'freedom' (σ_{a_0}) of a_0 in Equation 4.8, while the dashed line is its 'freedom' in Equation 4.10.*

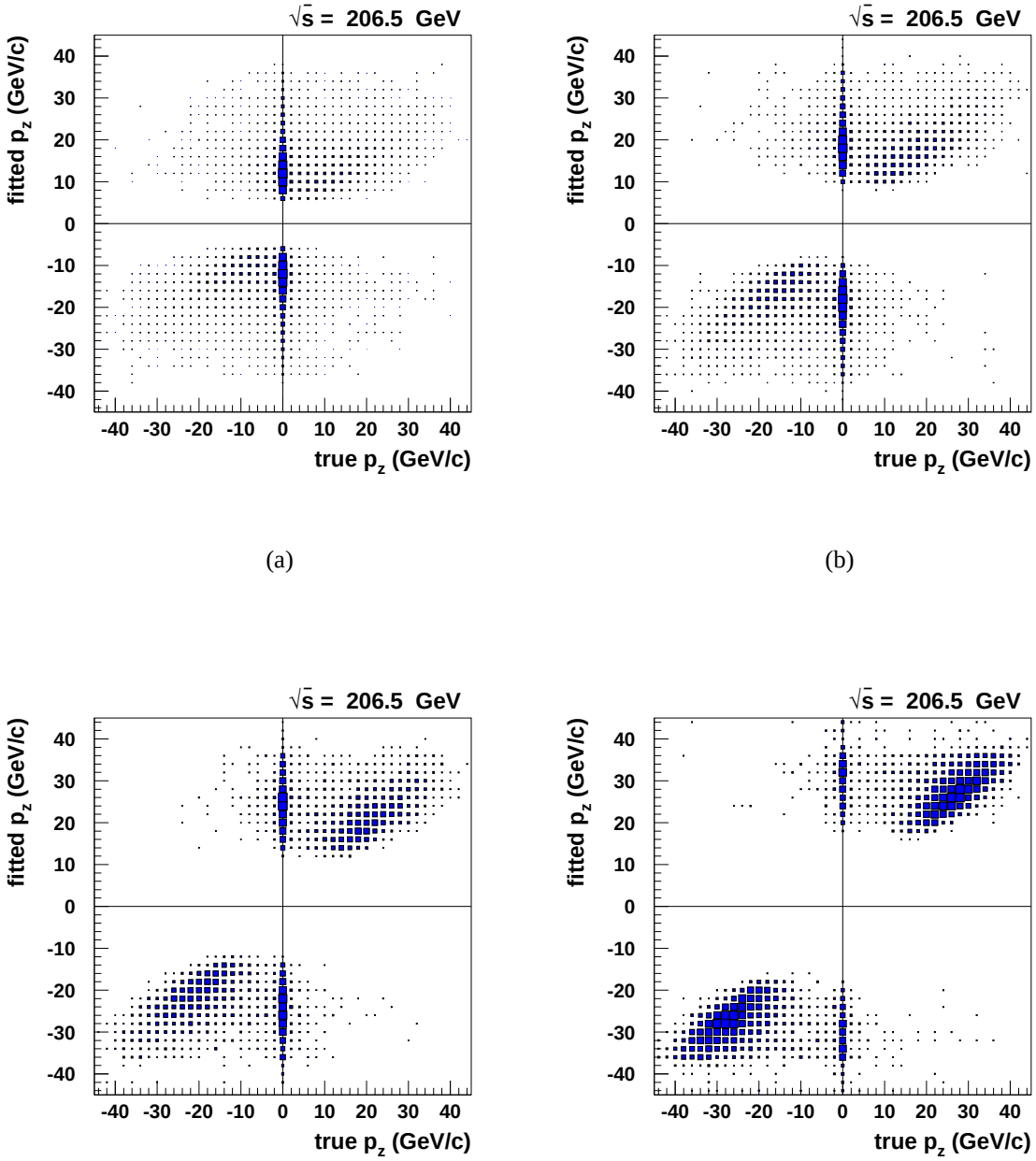

Figure 4.5: *The total p_z of the event obtained from the kinematic fit versus the generated true p_z for a sample of $e^+e^- \to W^+W^-(\gamma) \to q\bar{q}'Q'\bar{Q}$ events after the full event selection described in section 5.1 and in bins of $x = |p_z/\Delta p_z|$. For plot (a) the range is $1.5 < x < 2.0$, for plot (b) $2.5 < x < 3.0$, for plot (c) $3.5 < x < 4.0$ and for plot (d) $5.0 < x < 7.0$.*

$$\mathcal{T}_{\beta\gamma} = \sum_k p_\beta^k p_\gamma^k \tag{4.9}$$

where p_β^k and p_γ^k are the two components of the projection of the momentum of particle k in the transverse plane. The normalized eigenvectors of the tensor, $\vec{p}_j^{\,b}$ and $\vec{p}_j^{\,c}$, reflect the directions where the jet is broadest and slimmest. The corresponding eigenvalues are B_b and B_c. By comparing the resulting jet energies from the first stage of the fit with the measured ones, an estimate was made of how much energy remained undetected in the jet, referred to as $E_{j,miss}$. The resulting functional dependencies of the parameter uncertainties were:

$$\begin{aligned}
a_0 &= 0.15 + 0.40 \cdot \cos^4\theta_j \\
\sigma_{a_j} &= 0.27 + 0.72 \cdot \cos^4\theta_j \\
\sigma_{b_j}^2 &= 0.36 + 1.8\ (\mathrm{GeV}/c)^{-2} \cdot B_b \frac{\sqrt{1\mathrm{GeV} \cdot E_j^{\mathrm{m}} + E_{j\mathrm{miss}}^2}}{E_j^{\mathrm{m}}} \\
&\quad +0.036\ (\mathrm{GeV}/c)^{-4} \cdot B_b^2 \\
\sigma_{c_j}^2 &= 0.36 + 1.8\ (\mathrm{GeV}/c)^{-2} \cdot B_c \frac{\sqrt{1\mathrm{GeV} \cdot E_j^{\mathrm{m}} + E_{j\mathrm{miss}}^2}}{E_j^{\mathrm{m}}} \\
&\quad +0.036\ (\mathrm{GeV}/c)^{-4} \cdot B_c^2\ .
\end{aligned} \tag{4.10}$$

In Figure 4.4 those parametrizations are illustrated and a good agreement was found between the reality and these simple functional dependencies. The χ^2 of the resulting fit is a function of the collection of jet parameters $\{(a_j, b_j, c_j) | \forall j \in jets\}$ and therefore contains statistical information about the kinematics of the jets. When choosing a jet pairing into two hypothetical heavy objects which reflect both W bosons, this χ^2 can be mapped into the two dimensional parameter space $\vec{m}$ = (m_W^1,m_W^2). This event-by-event observable will be the basic ingredient for the analysis presented in chapter 5.

The constraints of the fit become less tight by allowing for a hypothetical undetected photon radiated in the initial state. Assuming that the photon is emitted collinear with the beam pipe only one constraint is lost, hence 4C becomes 3C :

$$\left(\sum_{j=1}^{jets} E_j, \sum_{j=1}^{jets} p_x^j, \sum_{j=1}^{jets} p_y^j, \sum_{j=1}^{jets} p_z^j \right) = (\sqrt{s} - |p_z^\gamma|, 0, 0, -p_z^\gamma) \tag{4.11}$$

where p_z^γ is the unknown momentum of this photon whose flight direction is assumed to be along the beam pipe. From the 4C kinematic fit, estimates for p_z^γ and its uncertainty Δp_z^γ are obtained. It is shown in Figures 4.5(a) till 4.5(d) that the more standard deviations, $|p_z^\gamma / \Delta p_z^\gamma|$, separate the fitted value of p_z^γ from zero, the more confidence one has in the hypothesis of a true ISR photon radiated in the beam pipe.

Instead of using only the $\chi^2(\vec{m})$ observable or the related probability

$$P(\vec{m}) d\vec{m} \sim \exp(-\frac{1}{2}\chi^2(\vec{m})) \tag{4.12}$$

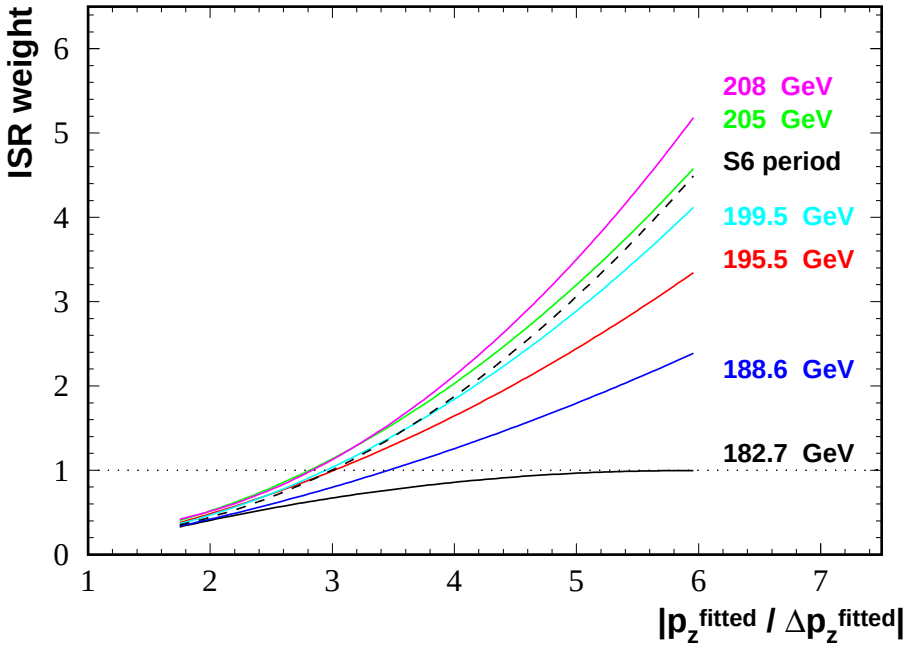

Figure 4.6: *Parametrized weight given to the ISR solution of the kinematic fit as function of the $|p_z/\Delta p_z|$ value of the event and this for different centre-of-mass energies. The TPC-S6 period is shown separately.*

from the 4C fit, a mixed observable was determined from the results of both the 3C and 4C fits:

$$\chi^2(\vec{m}) = w_{isr} \cdot \chi^2_{3C}(\vec{m}) + \chi^2_{4C}(\vec{m}) \tag{4.13}$$

where w_{isr} denotes the relative weight between both fit hypotheses. This weight was defined as the ratio between the number of events which indeed have intrinsic ISR in the beam pipe (with generated $p_z^\gamma \neq 0$ GeV/c) and the number of events in which fake ISR was observed (with generated $p_z^\gamma = 0$ GeV/c). Figures 4.5(a) till 4.5(d) indicate that this ratio increases with the fitted value of $|p_z^\gamma/\Delta p_z^\gamma|$ of the event, because the density of events around the diagonal increases. The weight was Monte Carlo parametrized as a function of $|p_z^\gamma/\Delta p_z^\gamma|$ and the centre-of-mass energy $\sqrt{s}$ of the event, as illustrated in Figure 4.6. The effect is much more pronounced at higher centre-of-mass energies, as the energy of the ISR photon becomes kinematically less constraint by $\sqrt{s}$, via the inequality $\sqrt{s} - 2m_W \geq E_\gamma$. To first order the parametrization of the weight $w_{isr}(|p_z^\gamma/\Delta p_z^\gamma|, \sqrt{s})$ does not depend on the clustering algorithm used, neither does it depend on the jet pairing. Furthermore it was only applied for events which had a fitted value of p_z^γ separated by more than 1.5 standard deviations from zero. At a centre-of-mass energy $\sqrt{s}$ of 183 GeV these events amount up to 11% of the selected $W^+W^- \rightarrow q\bar{q}'Q'\bar{Q}$ events; at $\sqrt{s}$ = 206.5 GeV this number was about 15%.

The definition of the effective centre-of-mass energy $\sqrt{s'}$ is closely related to the ISR photons, as it is the centre-of-mass energy calculated after the ISR photons have been produced, therefore $\sqrt{s'} \leq \sqrt{s}$. Within DELPHI this observable is estimated with the SPRIME(+) algorithm [74], which also identifies the photons observed in the detector and subtract their energy from $\sqrt{s}$ to obtain $\sqrt{s'}$.

Chapter 5

The 2D ideogram analysis

This chapter presents the method used to extract likelihood information from the data about the W boson resonance characteristics, like its mass m_W and its width Γ_W. The relevant W^+W^- events containing this information were separated from the background events by sequential cuts. The influence of the many ambiguities in the event reconstruction, which dilute the statistical information, was minimized by an optimal weighting of the different hypotheses possible in the direct reconstruction of m_W or Γ_W from the detected final state particles. All relevant information about these quantities was summarized in a likelihood estimator, of which the statistical properties were studied with Monte Carlo simulation.

5.1 Event selection

Three different stages can be considered in the event selection. The first two are based on sequential cuts, giving each event a multiplicative weight of zero or unity (cfr. sections 5.1.1 and 5.1.2). In the third stage an observable was designed which reflects the kinematic jet structure of the event (cfr. section 5.1.3). This observable was used both to obtain a Monte Carlo parametrized weight for each event and as a differentiator for a sequential cut.

5.1.1 Sequential cut selection of fully hadronic $\mathbf{W^-W^+}$ events

After the particle selection, described in section 4.1, the expected topologies of reconstructed events were studied with Monte Carlo simulation. An event selection was designed to separate the events which contain statistical information about the intrinsic kinematics of the W boson from others which do not have this direct information. The influence of background events on the W mass estimator presented in this thesis was found to be small. Therefore the selected data sample should have a reasonable purity, while still preserving a large selection efficiency for $W^+W^- \to q\bar{q}'Q'\bar{Q}$ signal events.

In a first stage of the event selection, sequential cuts were applied on the values of general event observables, in order to remove as much as possible $Z^0 \to q\bar{q}$ and $Z^0Z^0 \to q\bar{q}Q\bar{Q}$ background events. Observables were chosen which are, within some approximation, centre-of-mass energy independent. Therefore on all events the same selection criteria were applied, defined by:

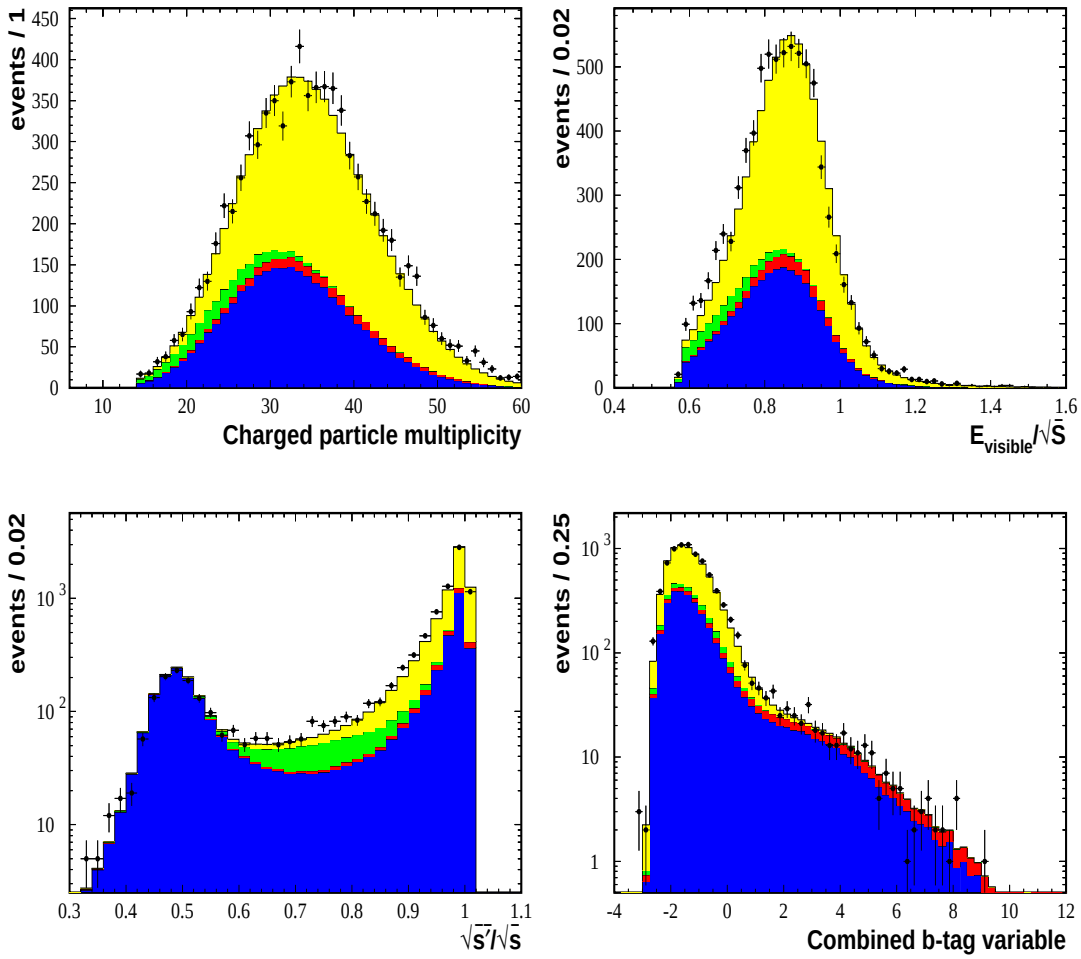

Figure 5.1: *Comparison between combined data (except those from the TPC-S6 period) and corresponding simulated distributions of general selection observables. The color scheme is shown in Figure 5.2. The top plots were made after applying all selection cuts as described in the text, without the cut on the event purity. The bottom plots were made after applying all cuts except for the cut on the observable shown and without the cut on the event purity.*

- The charged particle multiplicity should be larger than 13.
- The total visible energy of the event must exceed $1.15\frac{\sqrt{s}}{2}$.
- The scaled effective centre-of-mass energy $\frac{\sqrt{s'}}{\sqrt{s}}$ was required to be larger than or equal to 0.8.
- Anti-b tagging was done by rejecting all events which had a combined b-tag variable larger than 2 (cfr. section 4.2).

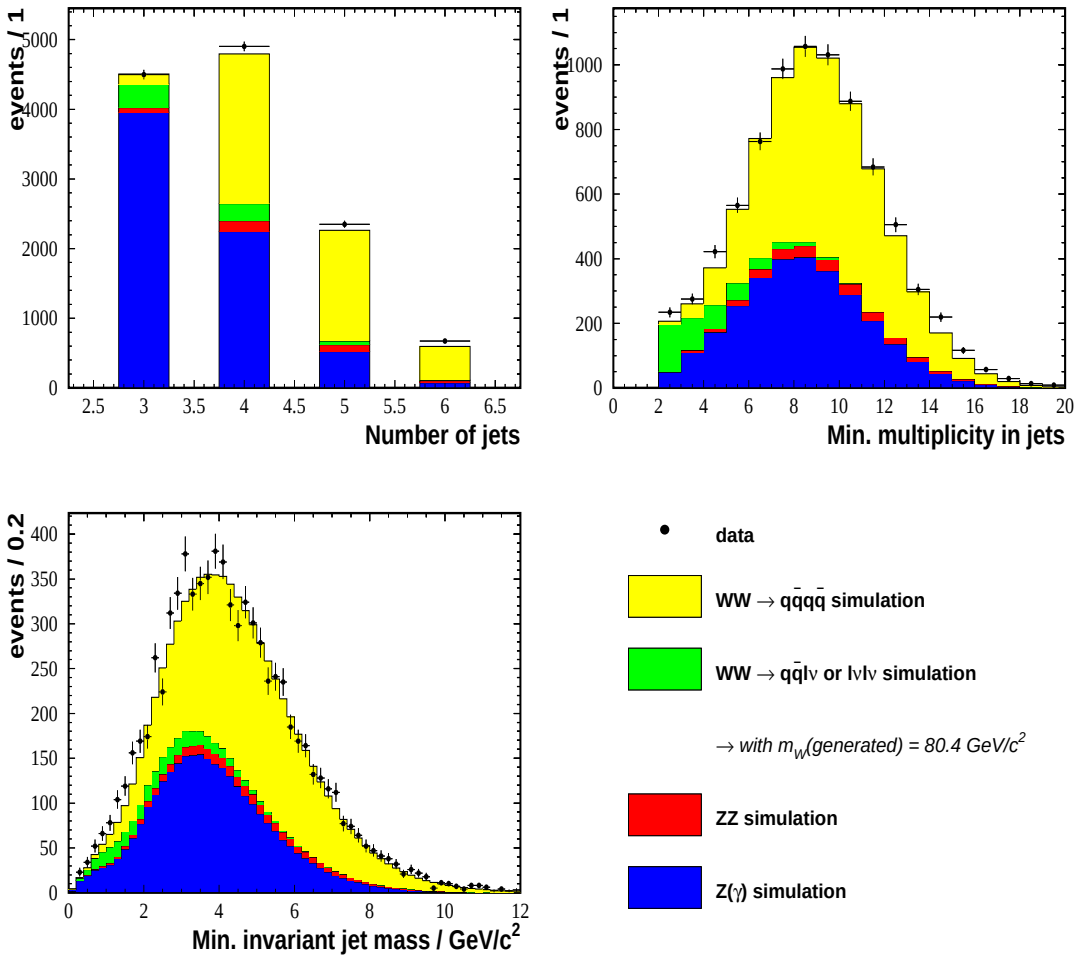

Figure 5.2: *Comparison between combined data (except those from the TPC-S6 period) and corresponding simulated distributions of jet related selection observables. The plots were made after all cuts except for the cut on the observable shown and without the cut on the event purity.*

All these sequential cuts are motivated by studying the Monte Carlo simulated samples. The differential distributions of the selection observables are in reasonable agreement with those measured from data, see Figure 5.1. For the WPHACT distributions the simulated events were weighted as described in section 3.2.3 to account for radiative corrections on the matrix elements. This reweighting procedure is applied for all remaining results presented in this thesis. Due to the $\sqrt{s}$ invariance of the observables, all data were combined and compared with the corresponding Monte Carlo simulation.

A particle clustering was performed in the second stage of the selection. The DURHAM clustering algorithm of section 4.3 was used with a fixed y_{cut} of 0.002. The obtained jets must obey the following criteria:

- The invariant mass of each jets must be larger than 1 GeV/c^2.
- Each jet should contain at least 3 particles.

When this criterion was not fulfilled, the particle clustering was continued to higher values of y_{cut} until the resulting jets did satisfy these minimal requests. At this point the event was required to have at least 4 jets. For all events clustered into a topology of more than 5 jets the clustering was again continued to higher values of y_{cut} until a 5 jet topology was obtained. The differential distributions of these jet properties are shown for data and Monte Carlo simulation in Figure 5.2 and a good agreement between both was found.

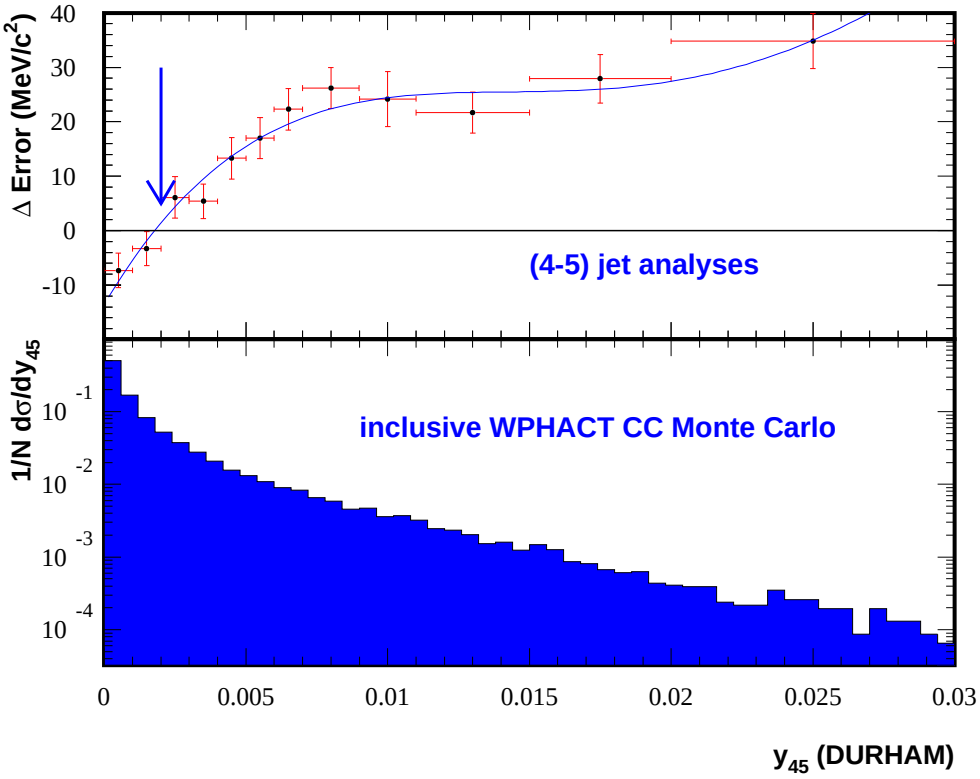

Figure 5.3: *The difference in expected uncertainty on the final m_W estimator when forcing all selected events into a 4 or 5 jet topology, with the separation at $y_{4\leftarrow5}$ = 0.002 indicated by the arrow. The bottom plot gives the inclusive normalized differential cross-section of WPHACT generated Charged-Current events (CC03).*

The selected events were classified according to their jet topology. This was motivated by comparing the expected resolution or variance of the final m_W estimator for two different analyses. In the first analysis all jets were clustered into a 4 jet topology, while in the second analysis clustering was stopped at 5 jets. Still all jets needed to pass the minimal quality

criteria on their mass and multiplicity. In Figure 5.3 the difference in expected uncertainty between these two correlated m_W estimators is shown as a function of the $y_{4\leftarrow 5}$ of the event, together with the inclusive distribution of $y_{4\leftarrow 5}$ for WPHACT generated events. The expected uncertainty was calculated for 100 selected events, including background and signal events. Below a $y_{4\leftarrow 5}$ value of 0.002 the 4 jet analysis performs better, while it performs worse above this value. The optimal use of this behavior was to cluster all selected events having a value of $y_{4\leftarrow 5}$ below 0.002 into 4 jets (this reflects about 50% of the events in the selected sample), while the others were clustered into a 5 jet topology.

5.1.2 Monte Carlo parametrized purity of the event

The particles of the events which passed the first two stages of the selection were, as mentioned above, clustered with the DURHAM algorithm into jets. The kinematics of those jets were constrained to obey energy and momentum conservation via the χ^2 minimization as presented in section 4.4. From the fitted jets a topological observable was created:

$$D_{pur} = \theta_{ij}^{fit} \cdot E_j^{fit} \cdot \sqrt{\frac{\tilde{\theta}_{ij}^{fit} \cdot \tilde{E}_j^{fit}}{100\,\mathrm{rad}\cdot\mathrm{GeV}}} \tag{5.1}$$

where E_j^{fit} and $\tilde{E}_j^{fit}$ are the smallest and the second smallest fitted jet energies and θ_{ij}^{fit} and $\tilde{\theta}_{ij}^{fit}$ are the smallest and the second smallest fitted inter-jet angles. This observable was used to differentiate the 4-fermion events (generated by WPHACT) from the 2-fermion events (generated with KK2f). Because the Z^0Z^0 events produce also a 4-fermion final state, they were treated as being signal events. The purity of the selected sample towards this definition of signal events was Monte Carlo parametrized as a function of the D_{pur} observable. The following parametrization was used:

$$P^{4f}(D_{pur}) = \frac{(A\cdot D_{pur}) + (B\cdot D_{pur})^2 + (C\cdot D_{pur})^3}{1 + (A\cdot D_{pur}) + (B\cdot D_{pur})^2 + (C\cdot D_{pur})^3} \tag{5.2}$$

where the value of P^{4f} is constrained between 0 and 1, allowing it to be used as an effective probability for the event with a certain value for D_{pur} to be a 4-fermion signal event. The parameters A, B and C were separately determined for 4 jet events and for 5 jet events. It was found that the parametrization for 5 jet events is more stable when fixing A to zero.

In Figure 5.4 the combined data distribution of D_{pur} is compared with the corresponding Monte Carlo simulation. The fitted curve represents the parametrized relation between the events purity P^{4f} and its value of D_{pur} as shown in Equation 5.2. Because data events, and certainly those recorded during the last year of data taking, have no fixed centre-of-mass energy, while the Monte Carlo samples were generated at fixed values of $\sqrt{s}$, the parameters A, B and C were fitted as a function of the centre-of-mass energy in Figure 5.5:

$$P^{4f} \;\longrightarrow\; P^{4f}(D_{pur}, \sqrt{s}) \;\; . \tag{5.3}$$

The χ^2 divided by the number of degrees of freedom (ndf) of these fits is significantly larger than unity. Due to the imperfect parametrization defined in Equation 5.2 (also observed in Figure 5.4), the χ^2/ndf of the fit to determine A, B and C at a fixed centre-of-mass energy was

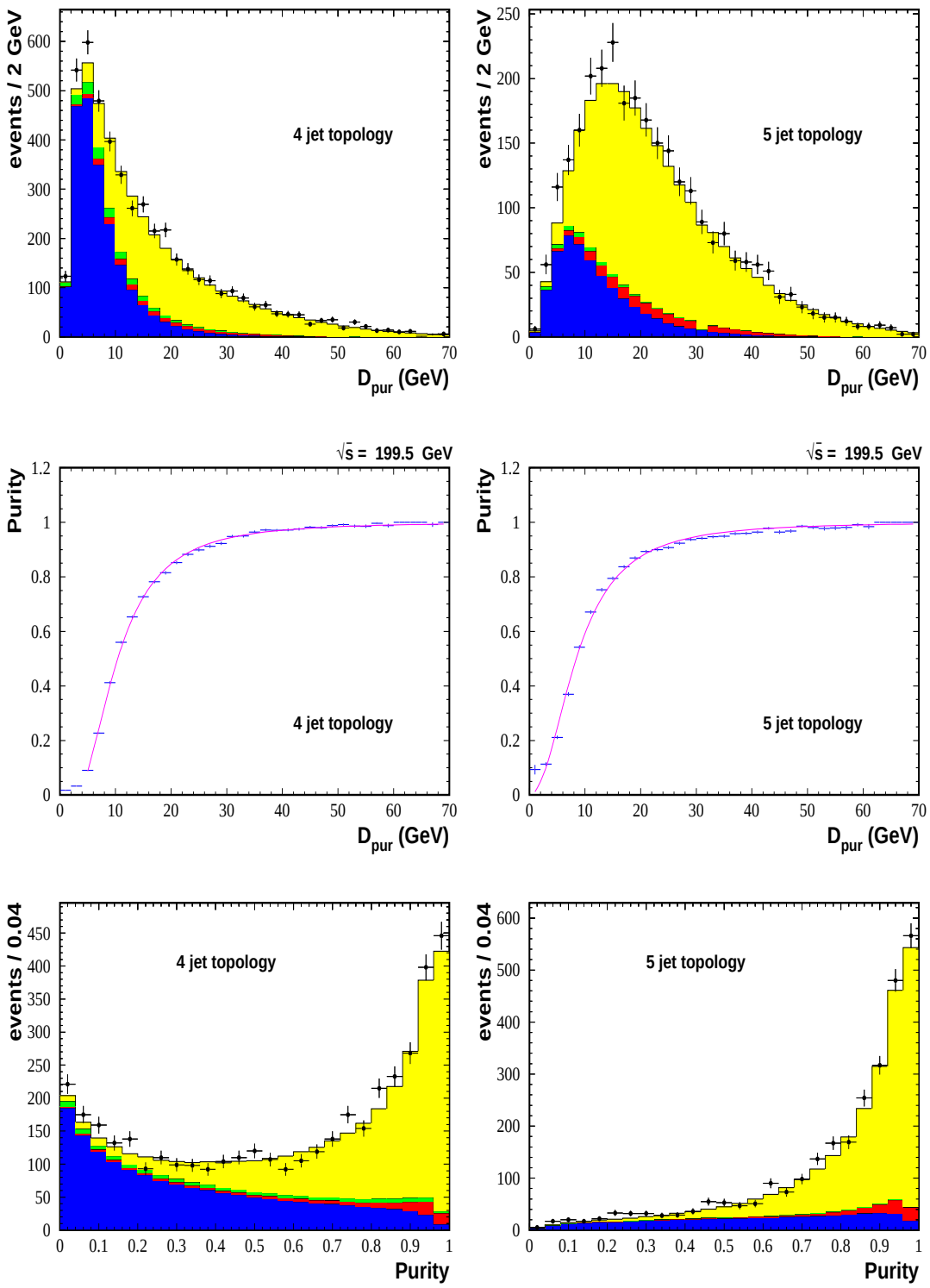

Figure 5.4: *Differential distributions of D_{pur} (top) and P^{4f} (bottom) for the combined selected data events, compared with the corresponding Monte Carlo simulation. The color scheme is shown in Figure 5.2. The data from the TPC-S6 period are neglected.*

about 2 to 3. Therefore the uncertainties on the fitted values of A, B and C are underestimated in Figure 5.5.

The parameters A, B and C resulting from Monte Carlo simulation reflecting the data taken during the TPC-S6 period do not deviate much from these parameters obtained with the nominal samples. Therefore the events from that period were not treated separately.

In the event selection a parametrized purity P^{4f} larger than 0.25 was required. The events which were rejected have little information content about the W boson properties, therefore the effect of this cut was marginal. Except that it reduced the computing time by a similar factor of about 20%.

5.1.3 Properties of the event selection

All events remaining after the selection described above were used for the measurements presented in this thesis. The efficiency for selecting $W^+W^- \to q\bar{q}'Q'\bar{Q}$ events was about 89%, while the purity of the selected sample was about 71%. The evolution of these numbers as a function of the centre-of-mass energy is shown in Table 5.1, together with the breakdown of the background contributions. The analysis of the TPC-S6 period did not deviate significantly from the nominal periods.

Nominal $\sqrt{s}$ GeV	ϵ %	Purity %	$q\bar{q}'Q'\bar{Q}$	$q\bar{q}'l\nu$	4f	2f	Expected	Data
182.65	89.6	71.9	330.2	12.1	10.6	106.5	459.3	511
188.63	89.5	70.7	1029.9	34.0	50.8	341.6	1456.3	1506
191.58	89.4	70.6	167.9	5.2	9.7	55.0	237.9	257
195.51	89.1	70.8	521.9	15.5	33.0	167.2	737.6	795
199.51	88.8	70.9	574.7	16.5	38.6	180.6	810.5	827
201.64	88.5	71.1	281.9	7.8	19.3	87.7	396.7	416
203.7	88.3	71.0	-	-	-	-	-	-
205	88.0	71.1	-	-	-	-	-	-
205.8	87.9	71.4	1112.1	30.0	78.8	335.7	1556.6	1593
208	87.8	71.1	-	-	-	-	-	-
206.3 (TPC-S6)	87.6	70.9	402.4	10.6	29.0	125.2	567.1	541
total			4421.0	131.6	269.8	1399.5	6222.0	6446

Table 5.1: *Monte Carlo determined properties of the event selection, like the selection efficiency for $W^+W^- \to q\bar{q}'Q'\bar{Q}$ events and the purity of the selected sample. The total number of expected events at each centre-of-mass energy is compared with the number of selected events from the data. Some lines reflect only simulation, as the data from the year 2000 was combined in the line at $\sqrt{s}$ = 205.8 GeV. The column 4f denotes the other 4-fermion final state processes and 2f denotes the KK2f generated events. The statistical uncertainties on the Monte Carlo estimates are negligible.*

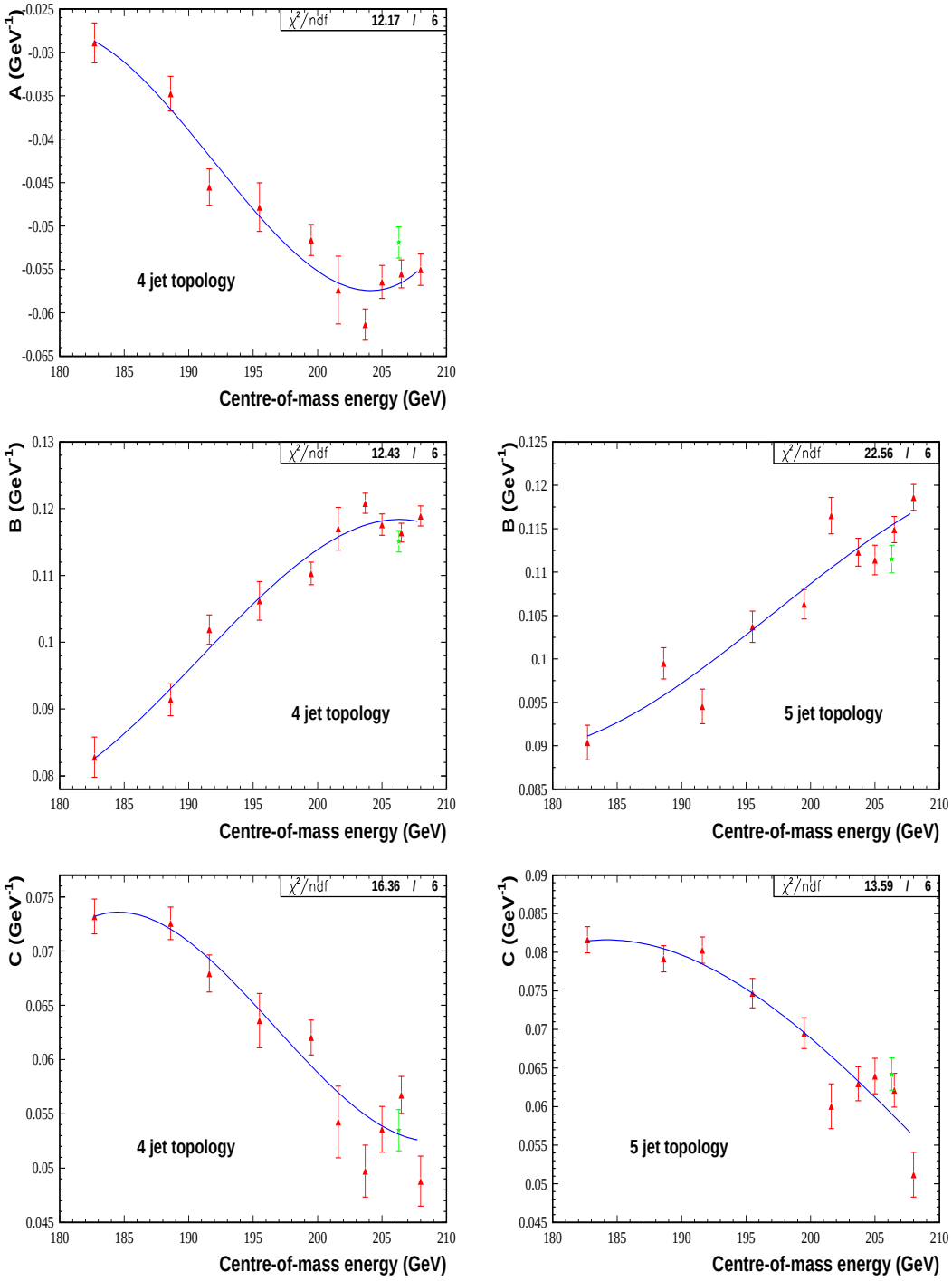

Figure 5.5: *Fits of the Monte Carlo determined parameters A, B and C as a function of the centre-of-mass energy. The left plots are those for the 4 jet events, while on the right similar plots are shown for the 5 jet events. The green stars reflect the parameters for the TPC-S6 period.*

An excess of selected events in the data was found compared to the number expected from the Monte Carlo simulation, see Table 5.1. When the number of expected events was estimated, some of the Neutral Current processes leading to a 4-fermion final state were omitted. As a verification those processes were also generated with WPHACT and 43 events were expected in the combined selected data sample. It must be noticed that when using the ARIADNE fragmentation model rather than the PYTHIA one for the simulation of the 2-fermion background, an increase of about 6% of this background contribution is expected after applying the event selection. Comparative studies, using the runquality selection and the calculation of the integrated luminosity as in [68], have indicated that the luminosity calculation used for this thesis could be wrong by around 1% (or vica-versa). With this alternative setup in total 6304.5 events were expected from the nominal Monte Carlo simulation (to be compared to the 6222.0 of Table 5.1) while 6468 events were effectively selected in the data sample (compared to 6446) which has an integrated luminosity after this runquality selection of 649.6 pb^{-1} (compared to 641.1 pb^{-1}).

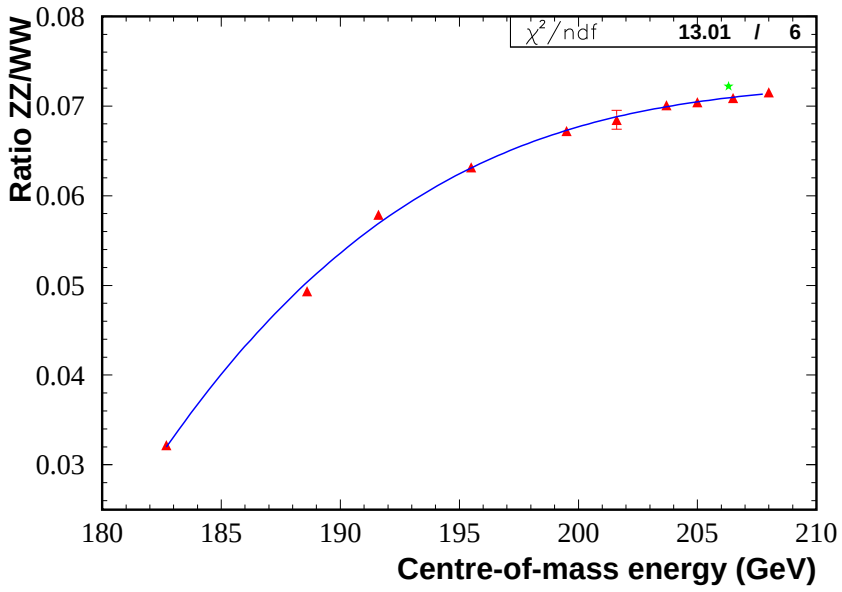

Figure 5.6: *Monte Carlo estimate of the ratio of the accepted Z^0Z^0 and $W^+W^- \to q\bar{q}'Q'\bar{Q}$ cross-sections after the full event selection including the cut on the parametrized purity observable. The green star reflects the Monte Carlo expectation during the TPC-S6 period.*

The events effective purity, P^{4f}, was calculated in the hypothesis that the Z^0Z^0 contribution in the selected sample is signal. To renormalize this purity to $W^+W^- \to q\bar{q}'Q'\bar{Q}$ signal events only, the ratio of the accepted cross-section of Z^0Z^0 events to $W^+W^- \to q\bar{q}'Q'\bar{Q}$ events was determined after the full selection including the sequential cut on the purity. In Figure 5.6 this ratio was fitted as a function of the centre-of-mass energy of the event. From $\sqrt{s}$ = 183 GeV to $\sqrt{s}$ = 208 GeV the ratio increased in a similar way as the Z^0Z^0 cross-section evolves with energy. It was found that the Monte Carlo expectation of the ratio

during the TPC-S6 period was significantly different from that calculated during the nominal periods. Therefore for the analysis of this TPC-S6 period its individual determined ratio was used rather than the fitted function through the nominal points.

5.2 Event-by-event reconstruction of the kinematic properties

The particles in the events remaining after the event selection were clustered according to the DURHAM clustering algorithm into a 4 or 5 jet topology. This reduced the dimensionality of the final state information to a level which can be handled in a statistical event analysis. To obtain one single value summarizing the W mass information, a jet pairing into W bosons had to be chosen. For events clustered into 4 (5) jets there are 3 (10) combinatorial possibilities for the jet pairing. After having defined the jet pairing, it becomes possible to impose 5 kinematic constraints on the event : energy and momentum conservation from the initial to the final state together with the non-physical assumption that the masses of the two reconstructed W bosons are equal. Via the kinematic fit described in section 4.4 this results in an event observable, χ^2_{5C}. Subsequently a simple criterion to treat the jet pairing ambiguity was defined. The jet pairing with the lowest χ^2_{5C} was chosen to reflect the correct kinematic information on the W bosons, hence in approximation the one with the smallest difference between the two reconstructed boson masses.

The kinematic 5C fit prefers one unique value, m, reflecting the value of the reconstructed W mass, namely the one where the one-dimensional $\chi^2_{5C}(m)$ is minimized. The invariant mass spectrum of m for the combined data sample (excluding the TPC-S6 period) is shown in Figure 5.7(a) and compared with the corresponding distribution expected from Monte Carlo simulation [1]. Separately the invariant mass spectrum obtained from data taken during the TPC-S6 period is compared with its expectation in Figure 5.7(b). For both data taking periods a good agreement was observed between data and Monte Carlo, except for the integrated excess in the data as discussed in section 5.1.3.

Clearly the W boson resonance becomes visible when using these techniques, nevertheless for a relatively large number of signal $W^+W^- \rightarrow q\bar{q}'Q'\bar{Q}$ events a mass was obtained which does not reflect the theoretical expected pole mass of the W boson of about 80 GeV/c^2. The tails of the Breit-Wigner resonance are populated with events which have been wrongly reconstructed. The information on the W boson was completely lost when the wrong choices were made during the reconstruction process, for example as a consequence of the inefficiency of the jet pairing algorithm. It was found that a simple global line-shape fit of the resonance is not the optimal estimator to extract the information about the measurants m_W or Γ_W. Therefore the Figures 5.7(a) and 5.7(b) should be regarded as illustrations of the reconstructed resonance rather than reflecting the full information. In section 5.3 an approach is presented which solves many of these limitations or ambiguities in the reconstruction by changing from a global inclusive analysis to an analysis using event-by-event kinematic information.

[1] In Figures 5.7(a) and 5.7(b) the best pairing is chosen from a slightly more complicated χ^2_{5C} as discussed in section 5.3 and summarized in Equation 5.14.

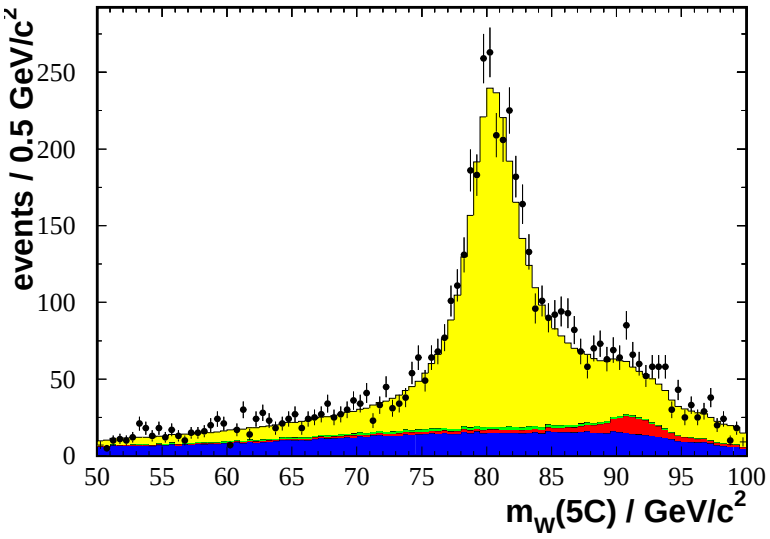

(a)

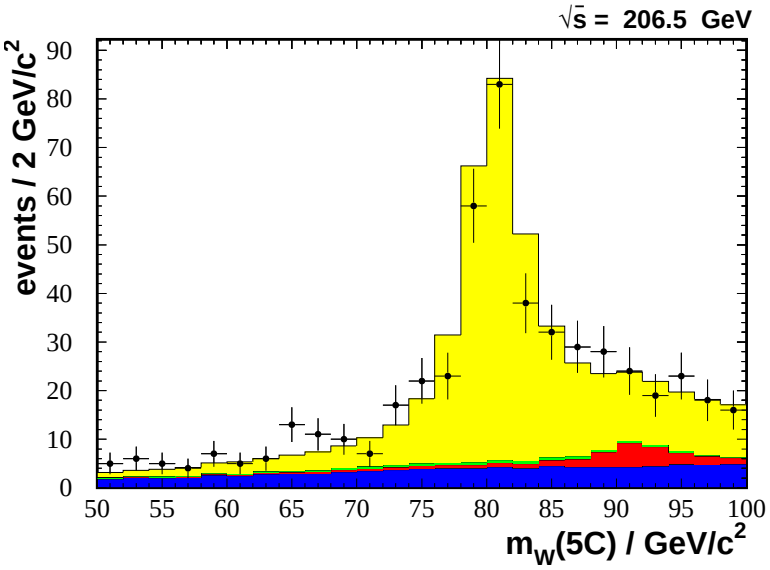

(b)

Figure 5.7: *Invariant mass spectra obtained from imposing a 5C kinematic fit on the events. In plot (a) the combined data (excluding the TPC-S6 data taking period) is compared with the expected differential distribution from Monte Carlo simulation. Plot (b) reflects the same comparison for the data taken during the TPC-S6 period. The color scheme is shown in Figure 5.2.*

5.3 Construction of the event-by-event 2D ideogram

The analysis of the W boson resonance was based on the Theorem of Bayes, which relates information of the observed event with information on the measurant by the following relation [2]:

$$P(m_W|\{\bar{p}_j\}) \;=\; \frac{P(\{\bar{p}_j\}|m_W)\cdot P(m_W)}{P(\{\bar{p}_j\})} \tag{5.4}$$

where m_W denotes the model parameter [3] to be inferred and $\{\bar{p}_j\}$ reflects the observed jet kinematics of the reconstructed final state. As a general working hypothesis the Standard Model was assumed with, apart from m_W, fixed model parameters. This obvious hypothesis is implicit throughout the equations in this section. The normalization factor $P(\{\bar{p}_j\})$ does not depend on the parameter m_W to be estimated and can therefore be omitted. All prior knowledge about the measurant m_W is summarized in $P(m_W)$. In the analysis of the W boson resonance no prior knowledge was assumed by choosing a uniform distribution for this Bayesian prior [4]. These simplifications reduce the Equation 5.4 for the posterior distribution to:

$$P(m_W|\{\bar{p}_j\}) \;\sim\; P(\{\bar{p}_j\}|m_W) \tag{5.5}$$

where $P(\{\bar{p}_j\}|m_W)$ is not normalized and reflects a likelihood ratio function which was called the ideogram of the event [73]. The kinematic fit described in section 4.4 provided statistical information about the $\{\bar{p}_j\}$ of the event for each pair of test masses $\vec{m} = (m^1_W, m^2_W)$ using the reconstruction hypothesis h_i. Among those reconstruction hypotheses h_i one need to specify for the reconstruction of $\{\bar{p}_j\}$ one finds: the definition of the particle-jet association (clustering algorithm), the jet pairing and the hypothesis concerning Initial State Radiation of photons which are lost in the beam pipe. This information was summarized by the $\chi^2_{4C}(\{\bar{p}_j\}|\vec{m}, h_i)$ of the fit, which can be related to $P(\{\bar{p}_j\}|\vec{m}, h_i)$ as:

$$P(\{\bar{p}_j\}|\vec{m}, h_i)\; d\vec{m} \;\sim\; \exp\left(-\frac{1}{2}\cdot\chi^2_{4C}(\{\bar{p}_j\}|\vec{m}, h_i)\right) \tag{5.6}$$

where $P(\{\bar{p}_j\}|\vec{m}, h_i)$ now represents the resolution function or the likelihood ratio of the event reconstructed under hypothesis h_i. This ideogram reflects the relative compatibility of the reconstructed kinematics of the event with the hypothesis that two heavy objects with the corresponding masses m^1_W and m^2_W were produced. To obtain information about the true value of m_W, the two-dimensional $\vec{m}$-space needs to be related with the one-dimensional physical m_W-space. Therefore the reconstructed ideogram in the $\vec{m}$-space was convoluted with the theoretical expected probability density in this space which depends on the value of m_W:

[2] The conditional probability, denoted by P(X|Y), reflects the probability that X is true, given as a condition that Y is true.

[3] All inference methods described for m_W are equally valid for Γ_W.

[4] If the amount of experimental information increases, then the dependence of the final likelihood on the shape of the prior gets weaker. This is true as long as the width of the prior distribution is larger than that of the final likelihood.

$$P(\{\bar{p}_j\}|m_W, h_i) \;=\; \int\int P(\{\bar{p}_j\}|\vec{m}, h_i) \cdot P(\vec{m}|m_W)\; d\vec{m} \tag{5.7}$$

where it has been assumed that the construction of $\chi^2_{4C}(\{\bar{p}_j\}|\vec{m}, h_i)$ does not depend on the value of m_W. The theoretical probability density function $P(\vec{m}|m_W)$ will be further discussed in section 5.4.1. When applying the convolution procedure, the event did not had to obey the non-physical constraint that both reconstructed masses m^1_W and m^2_W are equal. The Bayesian inference method described above, allows the possibility to include the $\chi^2_{4C}(\{\bar{p}_j\}|\vec{m}, h_i)$ information of all possible hypotheses $\{h_i\}$ for the event reconstruction into one ideogram:

$$P(\{\bar{p}_j\}|\vec{m}, \{h_i\}) \;=\; \sum_i w_i \cdot P(\{\bar{p}_j\}|\vec{m}, h_i) \tag{5.8}$$

where w_i reflects the probability $P(h_i|\vec{m})$ for the hypothesis h_i to be the correct one. From the point of goodness-of-fit all different jet pairings have an equal absolute value of χ^2_{4C}, this is however not true for different hypotheses about the particle-jet association or the ISR hypothesis. The probabilities $\{w_i\}$ were determined from Monte Carlo studies and are described in the following sections. In Figure 5.8 two examples of reconstructed ideograms are shown. For all possible jet pairings a value $\chi^2(\vec{m})$ was determined, and this at each point in the $\vec{m}$-space. The first ideogram reflects the kinematic information of a 4 jet clustered Monte Carlo event, where the three possible jet pairings into hypothetical W bosons were weighted with $\{w_i\}$ and prefer three different well separated regions in the $\vec{m}$-space. For the

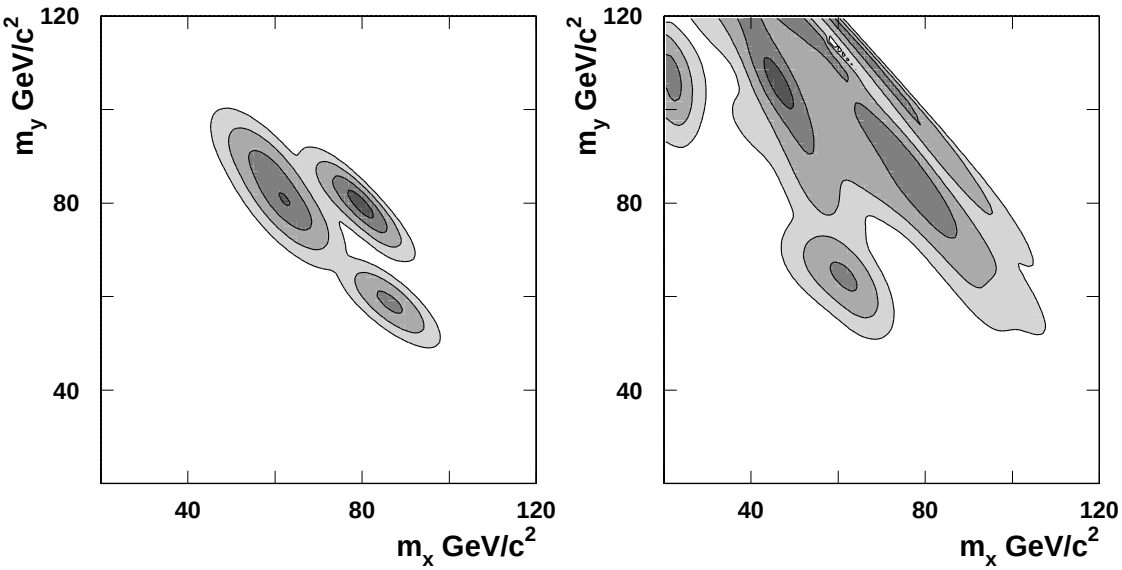

Figure 5.8: *Examples of two-dimensional probability ideograms for a simulated 4 jet (left) and 5 jet (right) hadronic event. The 1-2-3-4 sigma contours are shown.*

second example, results from a 5 jet clustered event are shown, which had 10 possible jet pairing combinations. The $\vec{m}$-space was kinematically limited by Equation 3.10, therefore the integrated probability that the event was compatible with two masses m^1_W and m^2_W where the sum of both exceeds $\sqrt{s}$ was zero.

In the final analysis the χ^2 was only calculated once per hypothesis h_i at the minimum of the $\chi^2_{4C}(\vec{m})$ in the full $\vec{m}$-space. The probability in all other points $\vec{m} = (m^1_W, m^2_W) = (m_x, m_y)$ was calculated using a Gaussian approximation for the $\chi^2(\vec{m})$:

$$\chi^2_i(m_x, m_y) \simeq \chi^2_{4C} + (\mathbf{m} - \mathbf{m}^{\text{fit}})^T \mathbf{V}^{-1} (\mathbf{m} - \mathbf{m}^{\text{fit}}) \tag{5.9}$$

with

$$\begin{aligned} \mathbf{V} &= \begin{pmatrix} \sigma^2_{m_x} & \sigma_{m_x}\sigma_{m_y}\rho_{xy} \\ \sigma_{m_x}\sigma_{m_y}\rho_{xy} & \sigma^2_{m_y} \end{pmatrix} \\ \mathbf{m} &= \begin{pmatrix} m_x \\ m_y \end{pmatrix} \\ \mathbf{m}^{\text{fit}} &= \begin{pmatrix} m^{\text{fit}}_x \\ m^{\text{fit}}_y \end{pmatrix}. \end{aligned} \tag{5.10}$$

The masses m^{fit}_x, m^{fit}_y, their uncertainties σ_{m_x}, σ_{m_y} and the correlation between them, ρ_{xy}, were taken from the 4C kinematic fit. When the χ^2_{4C} was larger than the number of degrees of freedom (ndf=4), the $\chi^2_i(m_x, m_y)$ was rescaled with a factor ndf/χ^2_{4C} in order to compensate for non-Gaussian resolution effects. This procedure decreased the computing time by an order of magnitude compared with the calculation of the $\chi^2(\vec{m})$ in the full $\vec{m}$-space, while resulting in only a minimal reduction in the W mass precision obtained of about 1%.

5.3.1 Monte Carlo parametrized weight for possible jet pairings

For each jet pairing k a kinematic 4C fit was performed, resulting in the ideogram $P(\{\bar{p}_j\}|\vec{m}, h_i, k)$. The relative weight w_k which accompanies the ideogram of each jet pairing in Equation 5.8, was Monte Carlo parametrized according to the value of the reconstructed polar angle of the W^+ boson $\theta_{W^+,k}$, the estimated charge difference ΔQ_k between the reconstructed W bosons and in case of a 5 jet event also the transverse momentum of the gluon jet.

The W production angle

In the process $e^+e^- \to W^+W^-$ at LEP the production angle of the W^+ (W^-) boson tends to be aligned in the flight direction of the e^+ (e^-) initial lepton. Figure 5.9 illustrates this alignment in the signal events at different centre-of-mass energies. For these figures the jet pairing was chosen which reflected the smallest χ^2 according to Equation 5.14. When the jet pairing was correct, the polar angle θ_{W^+} variable should take values according to the theoretical probability density function $P_\theta(\theta_{W^+})$. This expected population was parametrized as a function of the centre-of-mass energy by studying its expectation from Monte Carlo simulation and for each jet pairing k a value $P_\theta(\theta^k_{W^+})$ was calculated.

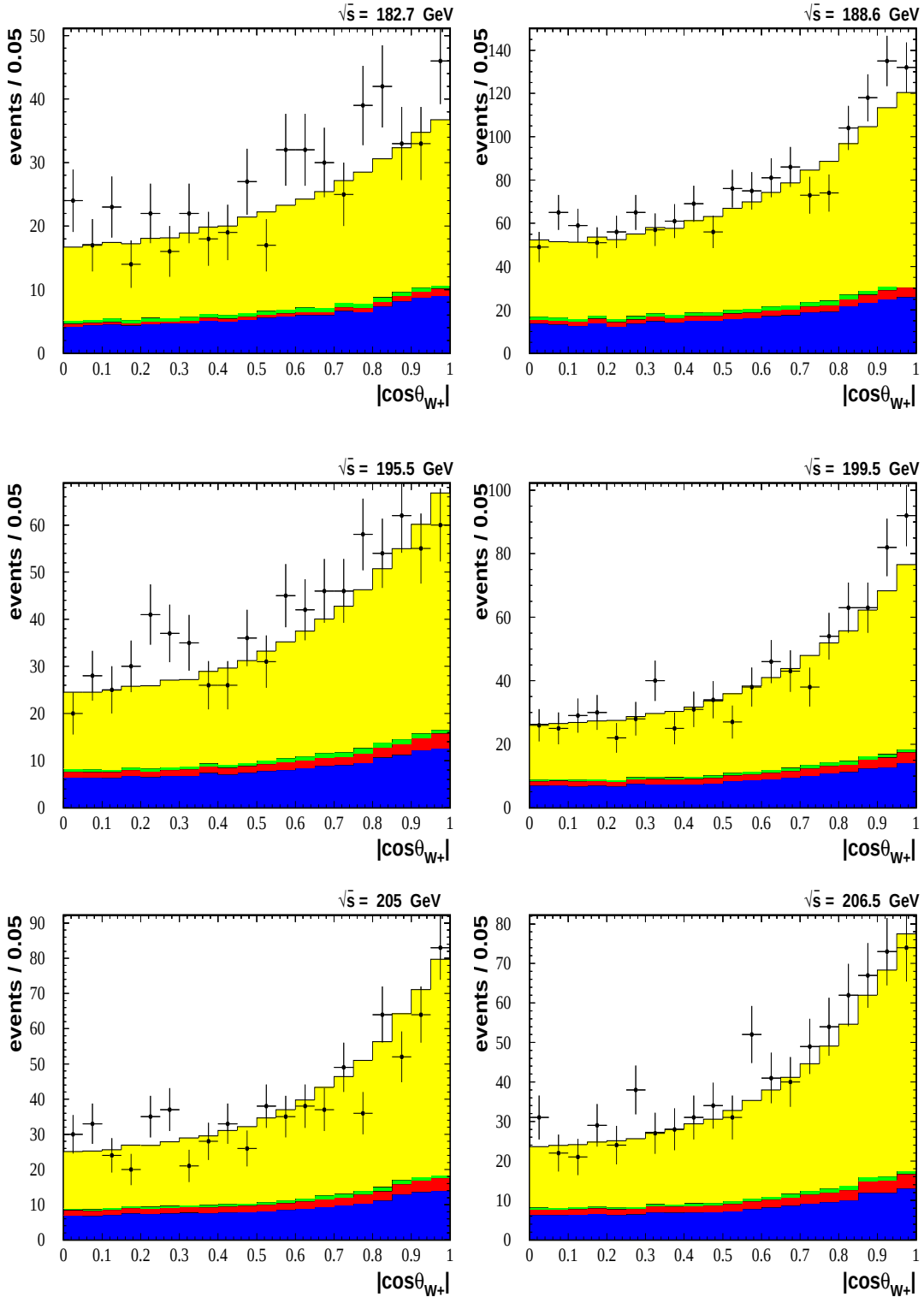

Figure 5.9: *Absolute value of the cosine of the polar angle of the reconstructed W bosons, for several values of $\sqrt{s}$, using the DURHAM algorithm and the jet pairing with the smallest χ^2_{tot} as defined in Equation 5.14. The color scheme is shown in Figure 5.2.*

Reconstructed charge difference

The jet charge Q^i_{jet} for jet i in the clustered event can be measured as:

$$Q^i_{jet} = \frac{\sum_{n=1}^{n_{jet}} \sqrt{|\vec{p}_n|} \cdot q_n}{\sum_{n=1}^{n_{jet}} \sqrt{|\vec{p}_n|}} \tag{5.11}$$

where n_{jet} are all charged particles in jet i, while q_n and $\vec{p}_n$ are their charge and momentum. For each jet pairing k the charge difference $\Delta Q_k = Q^{W_1}_k - Q^{W_2}_k$ was obtained. A Monte Carlo parametrized probability P_{W^+} that W_1 corresponds to the W^+ boson was determined from the value ΔQ_k. Figure 5.10 illustrates the differential distributions for ΔQ_k for three different clustering algorithms. The small shift between the data and Monte Carlo distributions did not influence the estimated m_W or Γ_W. The expected density of P_{W^+} as a function of ΔQ_k for the correct jet pairing was parametrized as the weighted sum of two Gaussians with the same central value but different widths. The parameters describing this parametrization were found to be independent of the centre-of-mass energy. However for the TPC-S6 period significant different parameter values were obtained, hence the data analysis in this period used these individual parameter values.

The value of $P_\theta(\theta^k_{W^+})$ was combined with the measured charge difference ΔQ_k between the two reconstructed bosons W_1 and W_2, to determine a relative weight for each jet pairing:

$$w^W_k = P_{W^+}(\Delta Q_k) \cdot P_\theta(\theta^k_{W_1}) + (1 - P_{W^+}(\Delta Q_k)) \cdot P_\theta(\pi - \theta^k_{W_1}) \ . \tag{5.12}$$

In this procedure the combinatorial background was assumed to reproduce a uniform distribution for the polar angle $\theta^k_{W_1}$. At this point the symmetry of the $\vec{m}$-space induced by the 4C kinematic fit was broken according to the charge of the reconstructed boson, $\vec{m}$=(m_{W_1},m_{W_2}) becomes $\vec{m}$=(m_{W^+},m_{W^-}).

Transverse momentum of gluon jet

Equation 3.21 defines the probability for the $q\bar{q}$ pair to radiate a single gluon. A useful approximation of this differential cross-section was:

$$\frac{d\sigma}{dk_T} \sim \frac{\alpha_s(k_T)}{k_T} \tag{5.13}$$

where k_T represents the transverse momentum of the gluon with respect to the original $q\bar{q}$ pair. This inverse k_T dependency was exploited to estimate the relative probability for each jet pairing k that the fifth jet was indeed originating from the fragmentation of a gluon. The most probable gluon jet candidate in every jet pairing was chosen from the three jets supposed to belong to one W boson by taking the jet with the lowest k_T with respect to the two other jets in the rest frame of the reconstructed W boson. The relative weight for that jet pairing k was multiplied by the probability $p_k \sim w^{\text{gluon}}_k = 1/k_T$ to emit a gluon with the observed transverse momentum.

The combined relative weight for each jet pairing was therefore $w_k = w_k^W \cdot w_k^{\text{gluon}}$. In Figures 5.7(a) and 5.7(b) a single mass was plotted for each selected event, reflecting the mass obtained from a 5C kinematic fit where the jet pairing was chosen as the one with the lowest χ^2_{tot}:

$$\chi^2_{tot,k} = \chi^2_{5C,k} - 2 \cdot ln(w_k^W) - 2 \cdot ln(w_k^{\text{gluon}}). \tag{5.14}$$

This $\chi^2_{tot,k}$ was also used to define the jet pairing in Figures 5.9 and 5.10.

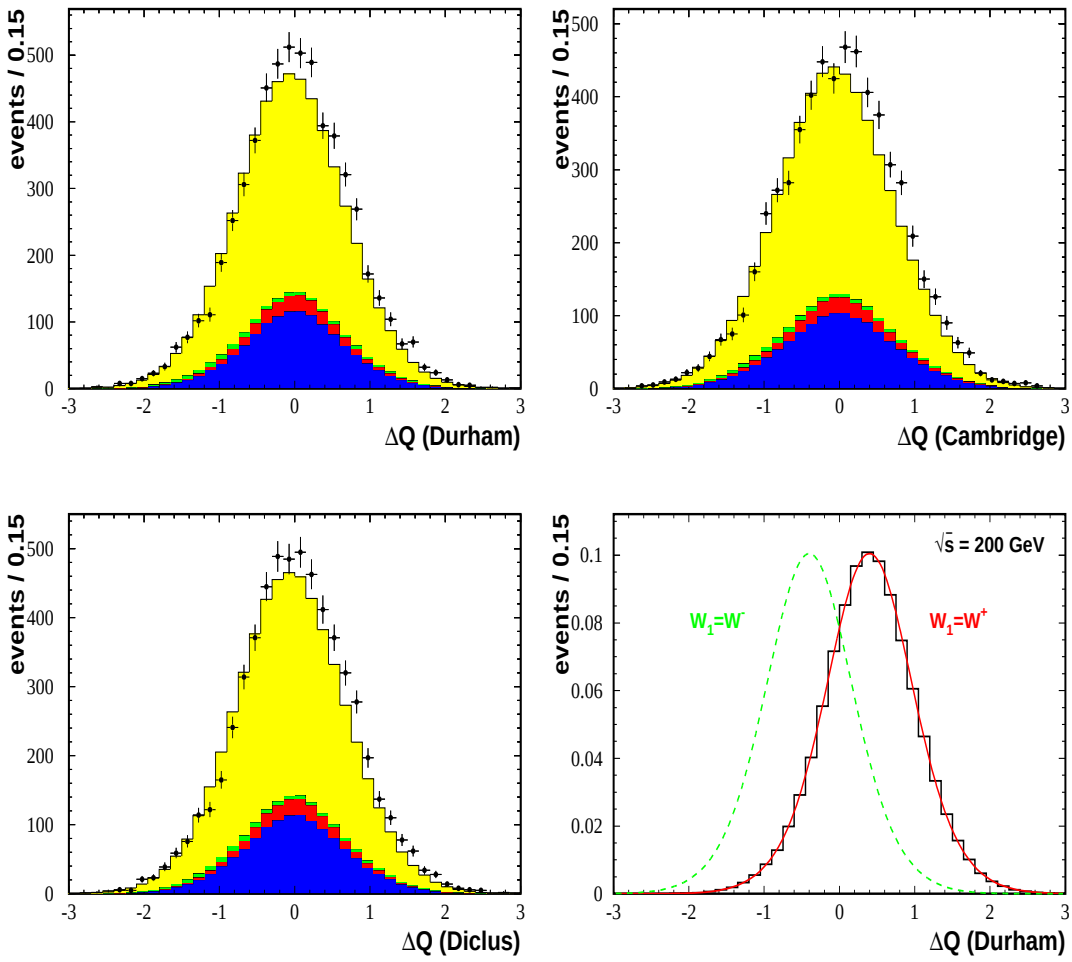

Figure 5.10: *Comparison between combined data (except those from the TPC-S6 period) and corresponding simulated distributions of the reconstructed charge difference ΔQ, using three different clustering algorithms. The color scheme is shown in Figure 5.2. The bottom right plot illustrates the parametrization for P_{W_1} in both cases where $W_1 = W^-$ and $W_1 = W^+$. The histogram is the Monte Carlo expectation for the observable when the correct pairing is chosen, the functions reflect the parametrization which has been used.*

5.3.2 Use of different clustering algorithms

As was observed in Figure 5.10, different clustering algorithms give overall similar performances, but on an event-by-event basis their results can be wildly different. This is illustrated in Figure 5.11, where the effect of using a different clustering algorithm on the reconstructed value of ΔQ is shown. The ambiguity of the particle to jet association was reduced by including the information on $\{\bar{p}_j\}_c$ from three clustering algorithms, DURHAM (c=1), CAMBRIDGE (c=2) and DICLUS (c=3). The ideograms resulting from each clustering algorithm were summed with optimized relative weight w_c:

$$\vec{w}_c = (\ 0.45 \pm 0.02\ ,\ 0.36 \pm 0.02\ ,\ 0.19 \pm 0.02\ )\ . \tag{5.15}$$

The optimization was performed in [72] and will not be repeated in this thesis. It was found that the DURHAM algorithm had the best performance in this m_W analysis towards the final resolution, while the DICLUS algorithm obtained a significant lower weight. The improvement of the m_W resolution when using these optimized weights instead of using uniform weights for all clustering algorithms was only about 1%.

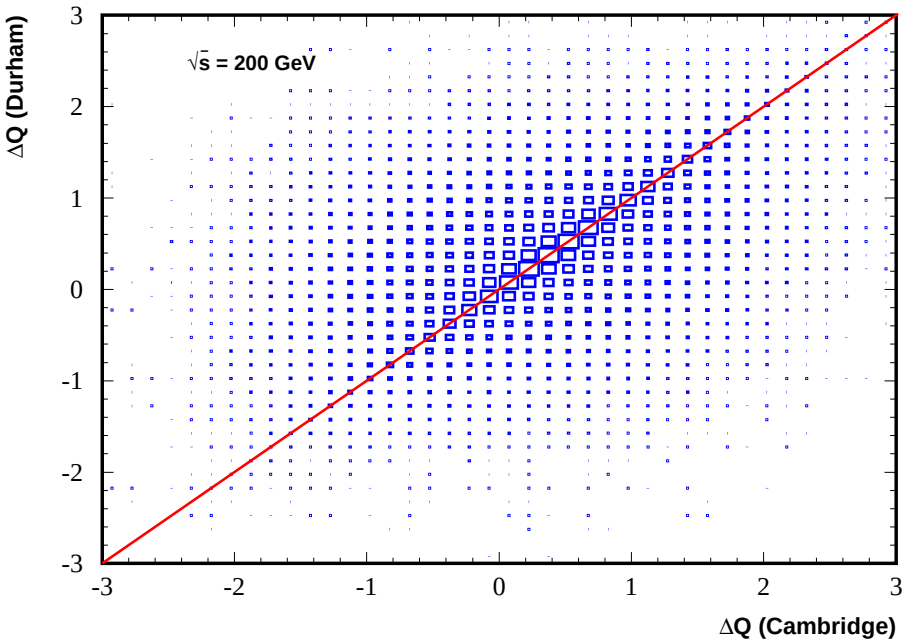

Figure 5.11: *For the $W^+W^- \to q\bar{q}'Q'\bar{Q}$ signal events generated at $\sqrt{s}$ = 200 GeV, the reconstructed ΔQ is shown for two different clustering algorithms. The correct jet pairing was used.*

5.3.3 Hypothesis about Initial State Radiation

When reconstructing the $\{\bar{p}_j\}$ information of the event via a kinematic 4C fit, the hypothesis was assumed that the initial leptons e^- and e^+ have an energy equal to the beam energy. However, when one of those leptons radiated a collinear photon with energy E_γ before colliding with its anti-lepton, the centre-of-mass energy of the collision was reduced from $\sqrt{s}$ to $\sqrt{s'} = \sqrt{s} - E_\gamma$. Due to this energy loss the number of constraints in the kinematic fit had to be changed from 4 to 3. This was discussed in section 4.4 where a relative weight w_{isr} was obtained for both hypotheses. The weight was parametrized by use of Monte Carlo simulation as a function of the $|p_z/\Delta p_z|$ value of the event and its centre-of-mass energy $\sqrt{s}$.

In Figure 5.12 the ideograms are shown of one simulated event in both hypotheses. For this particular event the reconstructed information using the hypothesis that one photon is lost in the beam pipe reflects much better the true generated information compared to the nominal 4C fit information.

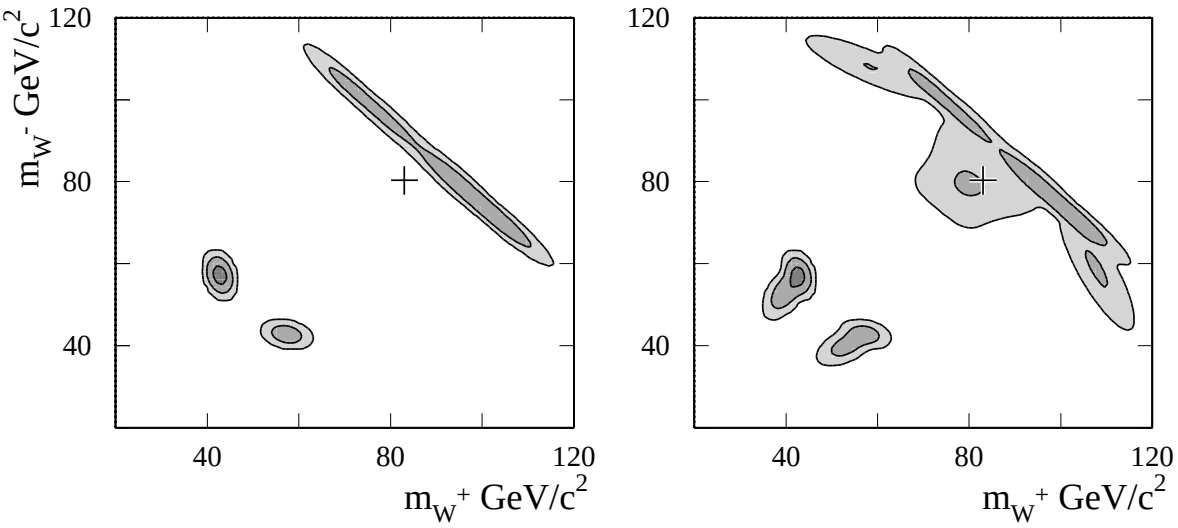

Figure 5.12: *An example of the reconstructed probability density function as a function of the invariant masses in a simulated 4-jet event without (left) and with (right) the hypothesis of collinear ISR. The 1-2-3 sigma contours are shown. The normalization of the different solutions prevents the high mass contours from reaching the 1 sigma probability level, while the small difference in the low mass solutions originates from the jet charge information. The generated masses of the two W bosons in the event are marked with a cross.*

5.3.4 Weighted sum of all possible ideograms

Taking into account all possible hypotheses $\{h_i\}$ for the reconstruction of $\{\bar{p}_j\}$ there were up to 18 different ideograms for a 4 jet clustered event and up to 60 for an event with a 5 jet topology. To determine the total ideogram which takes into account the information from all hypotheses, the Equation 5.8 can be rewritten as:

$$P(\{\bar{p}_j\}|\vec{m},\{h_i\}) \;=\; \sum_{k=1}^{3 \text{ or } 10} \sum_{isr=1}^{2} \sum_{c=1}^{3} w_k \cdot w_{isr} \cdot w_c \cdot P(\{\bar{p}_j\}|\vec{m}, h_{k,isr,W}) \tag{5.16}$$

where the sum over k takes into account the 3 or the 10 possible jet pairings in the event, the sum over 'isr' the two different hypotheses used in the kinematic fit (4C and in case that $|p_z/\Delta p_z|$ is more than 1.5 standard deviations from zero also 3C) and finally the sum over c the three different clustering algorithms. The more ambiguous the event reconstruction was, the broader the resolution in the combined ideogram, and therefore the less information could be inferred from it. The next step was to translate the information obtained in the $\vec{m}$-space to the real physical (m_W,Γ_W)-space of interest.

5.4 Maximum likelihood inference of the W boson resonance parameters

The ideogram in the $\vec{m}$-space was transformed into a likelihood in the (m_W,Γ_W)-space by convoluting it with the theoretical predicted population density of events $P(\vec{m}|m_W,\Gamma_W)$. From Equation 5.7 one obtains for each event:

$$\mathcal{L}_e(m_W,\Gamma_W) = \int_{m_{\min}}^{m_{\max}} \int_{m_{\min}}^{m_{\max}} P(\{\bar{p}_j\}|\vec{m},\{h_i\}) \cdot P(\vec{m}|m_W,\Gamma_W)\, d\vec{m} \tag{5.17}$$

where the two-dimensional integral is over the relevant kinematic region in the $\vec{m}$-space. This region was taken to be $m_{\min}$ = 60 GeV/c^2 and $m_{\max}$ = 110 GeV/c^2, and the combined ideogram was normalized to unity in the same region:

$$\int_{m_{\min}}^{m_{\max}} \int_{m_{\min}}^{m_{\max}} P(\{\bar{p}_j\}|\vec{m},\{h_i\})\, d\vec{m} \;=\; 1 \tag{5.18}$$

to allow a proper definition of the likelihood $\mathcal{L}_e(m_W,\Gamma_W)$. The measurements of the m_W and Γ_W parameters of the W boson resonance were based on the well known maximum likelihood technique [5].

5.4.1 Bayesian construction of the event-by-event likelihood via 2D convolution

A correct definition of the physical probability density function $P(\vec{m}|m_W,\Gamma_W)$ must take into account the $W^+W^- \to q\bar{q}'Q'\bar{Q}$ signal events as well as the main background contribu-

[5] An introduction to the statistical techniques used for parameter inference can be found in for example [75], while a more complete work is found in [76].

tions from $Z^0Z^0 \to q\bar{q}Q\bar{Q}$ and $Z^0 \to q\bar{q}(\gamma)$ processes. The background process $Z^0 \to q\bar{q}(\gamma)$ does not contain intrinsic information about the W boson properties and its final state does not show a double resonant structure. A uniform population of these events is expected in the $\vec{m}$-space independent of the values of the parameters (m_W,Γ_W). Therefore the probability density function of the background, denoted $B(\vec{m}|m_W,\Gamma_W)$, is assumed to be equal to B. For both the W^+W^- and the Z^0Z^0 events however a double Breit-Wigner structure was expected in the $\vec{m}$-space, modulated by a phase-space correction factor due to the nearby kinematic limit $m_{W^+} + m_{W^-} \leq \sqrt{s}$. Hence obtaining the following expression for the probability density function for the signal:

$$S(\vec{m}|m_W,\Gamma_W) = PS(\vec{m}|\sqrt{s})\cdot \\ \cdot \left[\frac{\sigma_s^{\mathrm{WW}}}{\sigma_s^{\mathrm{WW}}+\sigma_s^{\mathrm{ZZ}}} \cdot BW_{\mathrm{WW}}(\vec{m}|m_W,\Gamma_W) + \frac{\sigma_s^{\mathrm{ZZ}}}{\sigma_s^{\mathrm{WW}}+\sigma_s^{\mathrm{ZZ}}} \cdot BW_{\mathrm{ZZ}}(\vec{m}|m_Z,\Gamma_Z)\right] \tag{5.19}$$

with

$$PS(\vec{m}|\sqrt{s}) = \frac{1}{s}\sqrt{(s - m_{W^+}^2 - m_{W^-}^2)^2 - 4m_{W^+}^2 m_{W^-}^2} \tag{5.20}$$

where σ_s^{WW} and σ_s^{ZZ} reflect the accepted cross-sections of respectively the W^+W^- and the Z^0Z^0 final states. This function $S(\vec{m}|m_W,\Gamma_W)$ is intrinsically $\sqrt{s}$ dependent via the phase-space factor $PS(\vec{m}|\sqrt{s})$ and the parametrization of σ_s^{WW} and σ_s^{ZZ} as described in section 5.1.3. The background from ideograms in which jets were not correctly paired, and therefore not containing correct information about the parameters m_W or Γ_W, was assumed to have a uniform distribution in the $\vec{m}$-space. This hypothesis was checked and confirmed by studies using Monte Carlo simulations.

In the assumption of factorized W boson decays, the expression for the two-dimensional Breit-Wigner distribution was the product of both one-dimensional Breit-Wigners:

$$BW_{\mathrm{WW}}(\vec{m}|m_W,\Gamma_W) = BW_{\mathrm{W}}(m_{W^+}|m_W,\Gamma_W)\cdot BW_{\mathrm{W}}(m_{W^-}|m_W,\Gamma_W) \tag{5.21}$$

and a similar expression was defined for the Z^0Z^0 double Breit-Wigner, with

$$BW_{\mathrm{W}}(m|m_W,\Gamma_W) = \frac{1}{\pi}\frac{\Gamma_W}{m_W}\frac{m^2}{(m^2-m_W^2)^2 + \left(m^2\frac{\Gamma_W}{m_W}\right)^2} \tag{5.22}$$

following Equation 3.7. In the construction of the combined expected density $P(\vec{m}|m_W,\Gamma_W)$ the background and the double Breit-Wigner signal terms have a relative weight, which was the parametrized purity of the event P^{4f} as defined in section 5.1.2 [6]. When the event reflects a clear double Breit-Wigner structured final state, it is more likely to contain relevant information about the parameters m_W and Γ_W compared to events with a low purity variable. The total theoretical density in the $\vec{m}$-space can now be written as:

$$P(\vec{m}|m_W,\Gamma_W,\sqrt{s}) = P^{4f}\cdot S(\vec{m}|m_W,\Gamma_W,\sqrt{s}) + (1-P^{4f})\cdot B \tag{5.23}$$

[6] This was the reason to define both W^+W^- and Z^0Z^0 final states as being signal events in section 5.1.2.

where the dependency on the centre-of-mass energy $\sqrt{s}$ was explicitly included. Also in the reconstruction of the experimental resolution function or ideogram, all weights $\{w_i\}$ were parametrized as a function of the centre-of-mass energy. The convolution in Equation 5.17 can therefore be performed for all events at all values of $\sqrt{s}$. With this procedure for each selected event a likelihood $\mathcal{L}_e(m_W, \Gamma_W)$ was obtained. The combined likelihood for the full data sample of uncorrelated events, was determined by multiplication of their likelihoods or by summing their related $\Delta\chi^2$ curves:

$$\Delta\chi^2_{tot}(m_W, \Gamma_W) \equiv L_{tot}(m_W, \Gamma_W) = \sum_i L_i(m_W, \Gamma_W) \equiv \sum_i -2 \cdot ln(\mathcal{L}_i(m_W, \Gamma_W)) \quad (5.24)$$

where the sum is over all events i. The minimum of the $\Delta\chi^2_{tot}$ curve in the (m_W,Γ_W)-parameter space was an estimator for both values of m_W and Γ_W. The variance on both estimators was calculated from the second derivative at the minimum $\Delta\chi^2_{tot}$ via the Minimum Variance Bound or Cramér-Rao equation:

$$\frac{1}{\sigma^2_{x^{fit}}} = \frac{1}{2}\left(\left.\frac{\partial^2 \Delta\chi^2_{tot}(x)}{\partial x^2}\right|_{x=x^{fit}}\right)^2 \quad (5.25)$$

with $x = m_W$ or $x = \Gamma_W$. This equation extracts the optimal amount of information out of the likelihoods. Its event-by-event properties are studied in [72].

The m_W inference

To infer information only about m_W, the W width was fixed to its value defined in the WPHACT Monte Carlo generator, Γ_W = 2.09 GeV/c^2. The resolution function $P(\{\bar{p}_j\}|\vec{m}, \{h_i\})$ reconstructed for each event has a Gaussian behavior, therefore event likelihoods $\Delta\chi^2(m_W)$ will locally exhibit a parabolic dependency on m_W. It was assumed that the combined likelihood $\Delta\chi^2_{tot}(m_W)$ was indeed parabolic around its minimum. All higher orders were completely negligible when calculating the uncertainty on the parameter m_W via Equation 5.25.

The Γ_W inference

This time the parameter m_W was fixed to 80.40 GeV/c^2 to infer information about the parameter Γ_W. The effect of including higher order terms in the analytic expression of the combined likelihood was more important for the Γ_W estimator than for the m_W case. It was found that for data samples containing few events the third order term has important contributions. When performing the analysis on the large Monte Carlo samples these contributions were negligible. But for the inference of Γ_W from the individual or combined data set asymmetric uncertainties will be quoted.

5.4.2 The 2D inference of m_W and Γ_W

When estimating the individual values for the parameters m_W and Γ_W as mentioned above, the correlation between both was neglected. The W width, used as a fixed parameter when estimating m_W, is not known with infinite precision; Γ_W = 2.118 $\pm$ 0.042 GeV/c^2 [12]. The

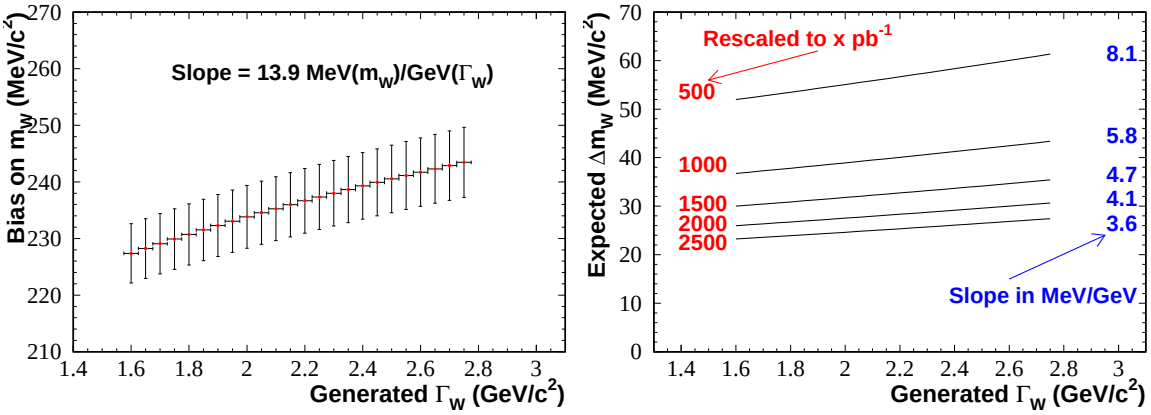

(a) (b)

Figure 5.13: *Plot (a) illustrates the correlation between the measured bias on the m_W estimator and the hypothetical value for Γ_W used in the generator. Plot (b) reflects the influence of Γ_W on the expected uncertainty on the m_W estimator for data samples of different integrated luminosity.*

effect of this uncertainty on the m_W estimator was calculated by changing the W width in the hypothesis during the convolution. Figures 5.13(a) and 5.13(b) demonstrate the influence of this fixed but hypothetical value for Γ_W on the measured bias and uncertainty of the m_W estimator. The effect of $\Delta\Gamma_W$ = 42 MeV/c^2 on the estimated m_W was about 0.6 MeV/c^2, hence completely negligible. In a similar way, the effect of $\Delta\Gamma_W$ on the measured uncertainty Δm_W was smaller than 0.5 MeV/c^2, when the integrated luminosity of the LEP combined data sample is taken as reference scale. The two-dimensional simultaneous measurement of m_W and Γ_W, was abandoned as it did not give extra information.

5.5 Monte Carlo calibration of the inference method

In the Bayesian framework presented, the inference was performed by calculating the distribution of the random variable associated with the true value of the physical quantities from all available information. The random variables were m_W or Γ_W, while the true values are the mass and the width of the W boson. The distribution of interest was called the likelihood of the combined event sample, $\Delta\chi^2_{tot}(m_W)$ or $\Delta\chi^2_{tot}(\Gamma_W)$, and can be interpreted in two different ways:

- Bayesians normalize the likelihood and give it via Bayes' Theorem (Equation 5.4) a probabilistic meaning. They state that the true parameter value for the mass or the width of the W boson is with a fixed probability in a certain interval. When Gaussian

uncertainties are assumed the constant true parameter value μ has 68% probability to be in the interval defined by $[\mu-\sigma_\mu, \mu+\sigma_\mu]$. Therefore they do not say anything about the value of μ.

- Frequentists do not give a probabilistic meaning to the likelihood $\Delta\chi^2_{tot}$. They claim that the value which minimizes the likelihood is the best estimate of the true parameter value μ and quote uncertainties $\pm\sigma_\mu$ on the true value.

Both philosophies have their virtues and their drawbacks.

Bias of the estimators

The convolution method described does not take into account all possible detector and physics effects in its constructed likelihood. The bias on the estimator induced by these effects was determined in a frequentist way using Monte Carlo simulated event samples. The shift between the fixed input value $m_W = m_W^{gen}$ in the Monte Carlo and the value which minimizes the reconstructed likelihood was defined as the bias of the estimator.

The input value for the W mass was m_W^{gen} = 80.40 GeV/c^2, while for the W width Γ_W^{gen} = 2.09 GeV/c^2 was used. From Monte Carlo samples which have an integrated luminosity about 1000 times larger than the real data samples, this bias was determined. Figure 5.14

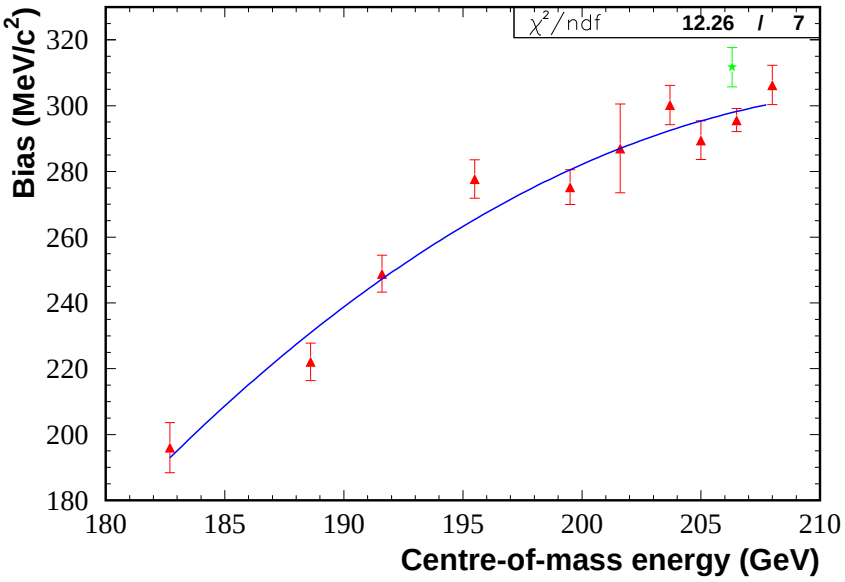

Figure 5.14: *The bias of the m_W estimator as discussed in the text as a function of the centre-of-mass energy $\sqrt{s}$. The green star reflects the bias for the analysis performed on the TPC-S6 data. A second order polynomial is fitted through the points. The uncertainty on the bias determined by each individual Monte Carlo at a fixed $\sqrt{s}$ indicates the amount of events in that simulated sample.*

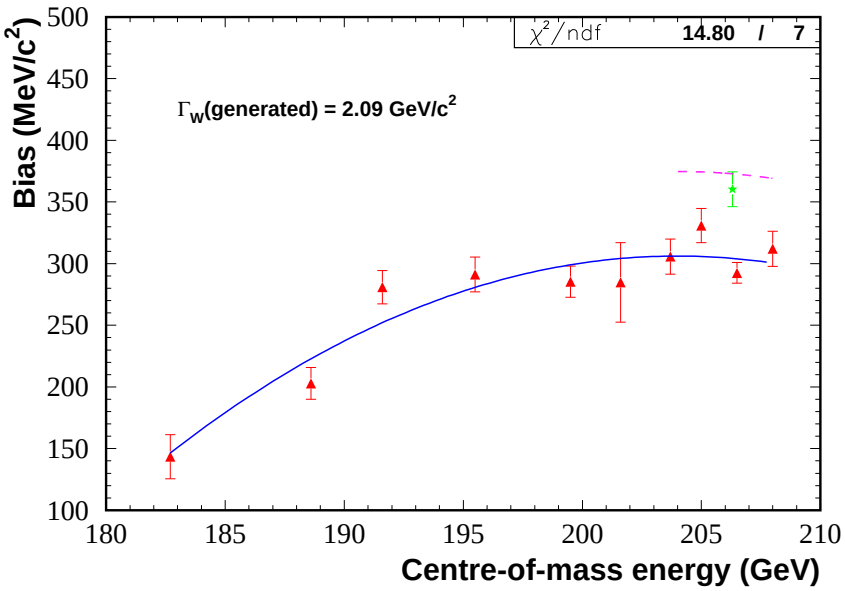

Figure 5.15: *The bias of the Γ_W estimator as discussed in the text as a function of the centre-of-mass energy $\sqrt{s}$. The green star reflects the bias for the analysis performed on the TPC-S6 data. A second order polynomial is fitted through the points. The functional dependency used in the analysis for the TPC-S6 data is shifted as described in the text.*

shows the bias on the m_W estimator as a function of the centre-of-mass energy $\sqrt{s}$, while Figure 5.15 illustrates the bias for the Γ_W estimator. It was found that these biases are not invariant over the relevant $\sqrt{s}$ range. Mainly because during the last year of data taking events were collected at different centre-of-mass energies, the bias was parametrized as a function of $\sqrt{s}$ for the whole energy range studied in this thesis. The increase of the bias on m_W with centre-of-mass energy was expected from the increasing effect of Initial State Radiation. The bias of the m_W estimator for the TPC-S6 analysis did not deviate significantly from the nominal analyses, therefore these data were treated with the same bias function. For the Γ_W estimator however the TPC-S6 analysis did deviate from the nominal ones. The functional dependency of the bias with $\sqrt{s}$ was kept from the nominal Monte Carlo studies, but the bias was shifted according to the expected shift at $\sqrt{s}$ = 206.5 GeV between the TPC-S6 and the nominal analyses.

Non-invariant biases : Monte Carlo reweighting

The Monte Carlo parametrized bias does not only depend on the centre-of-mass energy at which the analysis was performed, but also on the input value m_W^{gen} (Γ_W^{gen}). If the bias b is invariant for all relevant values of m_W^{gen} then the so-called slope a of the estimator is unity. Assuming a linear dependency between the input mass, m_W^{gen}, and the reconstructed mass, the bias b and the slope a are defined as:

$$m_W^{rec} - m_W^{ref} = a \cdot (m_W^{gen} - m_W^{ref}) + b \tag{5.26}$$

where m_W^{rec} is the mass as reconstructed with the maximum likelihood technique and m_W^{ref} is some reference value taken to be equal to the nominal value m_W^{ref} = 80.40 GeV/c^2. The calibration curve in Equation 5.26 was determined by a Monte Carlo reweighting technique. The weights given to each event were determined from their individual matrix elements provided by the WPHACT generator, including corrections for electroweak radiative effects. Therefore they depend intrinsically on the W mass at which they were calculated, m_W^{gen}. When changing the value of m_W^{gen} for the full Monte Carlo sample, the magnitude of the squared matrix elements or equivalently the probabilities for the events to occur were recalculated. Different weights were obtained for the individual events. With this reweighting procedure it was not necessary to produce Monte Carlo samples at different m_W^{gen}. Instead, the Equation 5.26 was verified at many values of m_W^{gen} using the matrix element reweighting and the slope a was calculated. The slope for the m_W estimator was compatible with unity at all centre-of-mass energies. Maximal deviations of 2% were found, hence to analyse the data events a unity slope was assumed.

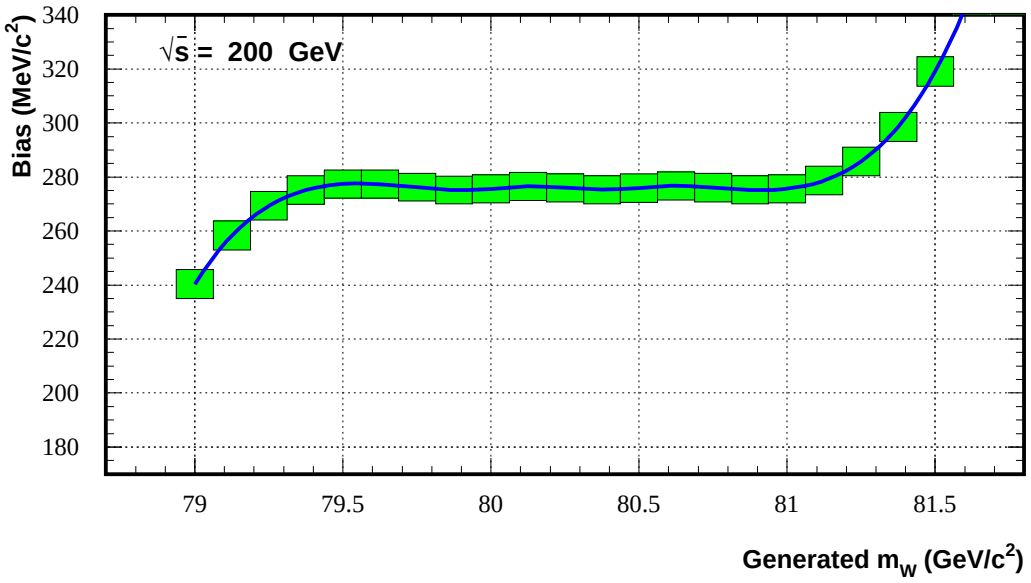

Figure 5.16: *Calibration curve of the m_W estimator at $\sqrt{s}$ = 200 GeV, indicating the invariant behavior of the bias in the relevant range of the Monte Carlo input value m_W^{gen}. An intrinsic effect of the Monte Carlo reweighting technique is that the different points are highly correlated.*

An illustration of the invariance of the bias of the m_W estimator determined via Monte Carlo reweighting is found in Figure 5.16. In the relevant range of m_W^{gen} between 79.5 GeV/c^2

and 81.0 GeV/c^2 the bias does not depend on the Monte Carlo input value m_W^{gen}. The analytic functions used to facilitate the reweighting can only be used in this relevant range, therefore the behavior of the calibration curve outside this region should not be taken seriously. When analyzing the real data events an event-by-event bias was applied on their reconstructed likelihoods as a function of the centre-of-mass energy of the event.

A similar procedure was applied for the Γ_W estimator. However it was found that the relation between Γ_W^{gen} and the reconstructed Γ_W from the likelihood is not perfectly linear, neither was the bias of the Γ_W estimator invariant for a change of Γ_W^{gen}. Figure 5.17 shows the dependency of the bias as a function of Γ_W^{gen}. Assuming the linear behavior as defined in Equation 5.26, the slope a increases with the centre-of-mass energy. The plot was inverted in Figure 5.19 where the bias is this time shown as a function of $\sqrt{s}$ for different input values Γ_W^{gen}. From these observations it was possible to parametrize the Monte Carlo expected bias on the Γ_W estimator as a function of both $\sqrt{s}$ and Γ_W^{gen}. When analyzing the real data those calibration curves were applied event-by-event on the reconstructed likelihoods before combining them.

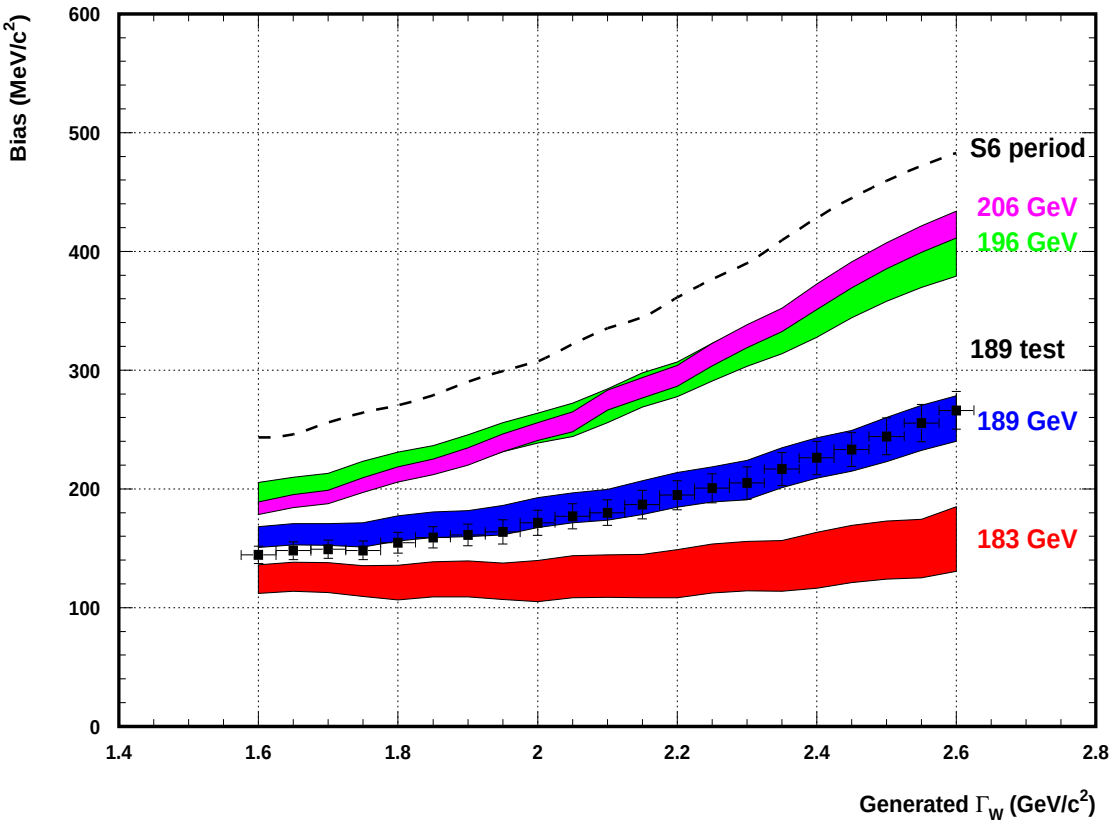

Figure 5.17: *Calibration curves determined by Monte Carlo reweighting for the Γ_W estimator at different centre-of-mass energies $\sqrt{s}$. The TPC-S6 period clearly deviates from the nominal analyses, while the test curve at $\sqrt{s}$ = 189 GeV is described in the text.*

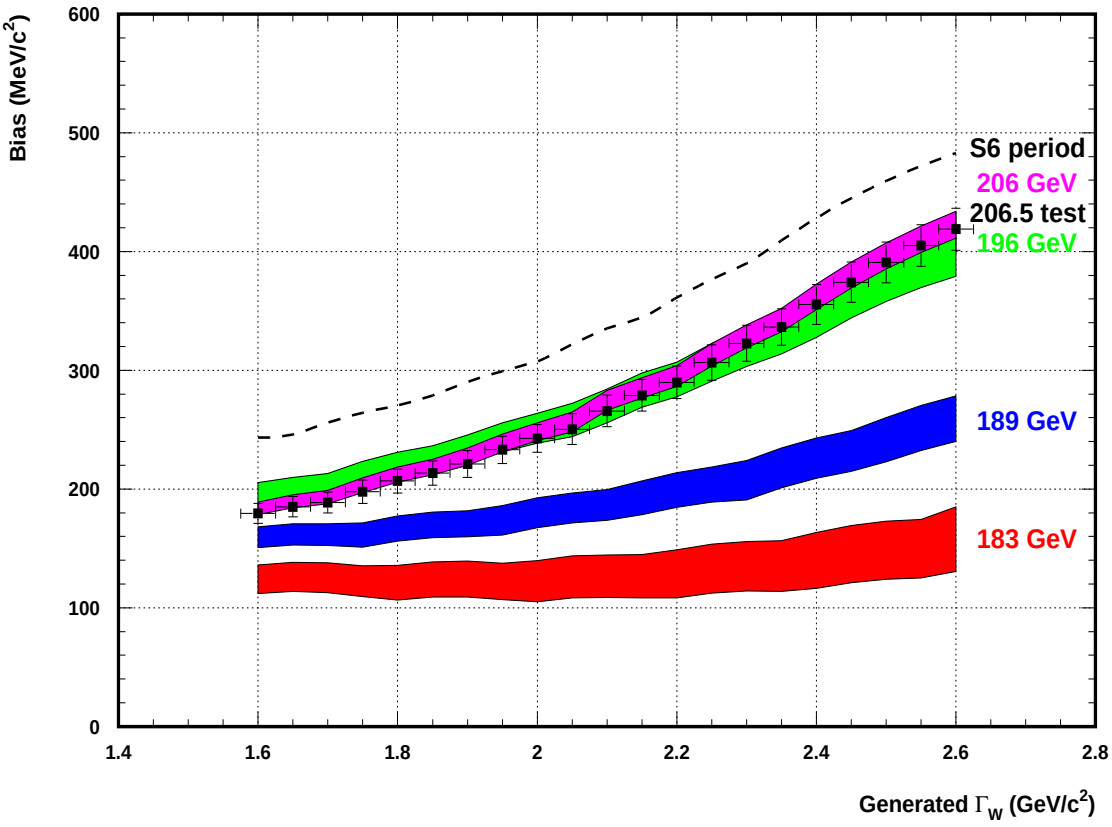

Figure 5.18: *Calibration curves determined by Monte Carlo reweighting for the* Γ_W *estimator at different centre-of-mass energies* $\sqrt{s}$*. The TPC-S6 period clearly deviates from the nominal analyses, while the test curve at* $\sqrt{s}$ *= 206.5 GeV is described in the text.*

To check the reliability of the Monte Carlo reweighting procedure event samples at $\sqrt{s}$ = 189 GeV and 206.5 GeV were produced with the input value Γ_W^{gen} = 2.6 GeV/c^2 and the analysis was performed on those events. The calibration curve obtained via the same reweighting techniques was determined and shown in Figures 5.17 and 5.18 as dots. The Γ_W estimator was however very sensitive to the amount of 2-fermion background in the selected sample. Due to an expected change in the 4-fermion production cross-section induced by going from Γ_W^{gen} = 2.09 GeV/c^2 to Γ_W^{gen} = 2.6 GeV/c^2 this background level in the Monte Carlo sample should also change. Because the WPHACT generator could not predict the 4-fermion cross-section at Γ_W^{gen} = 2.6 GeV/c^2, its value was kept from the calculation using Γ_W^{gen} = 2.09 GeV/c^2. It was observed that both the level and the shape of the calibration curves at both centre-of-mass energies, when the reweighted starting from Γ_W^{gen} = 2.09 GeV/c^2 or Γ_W^{gen} = 2.6 GeV/c^2 respectively, are in good agreement. This observation was a positive cross-check for the reliability of the applied Monte Carlo reweighting algorithm.

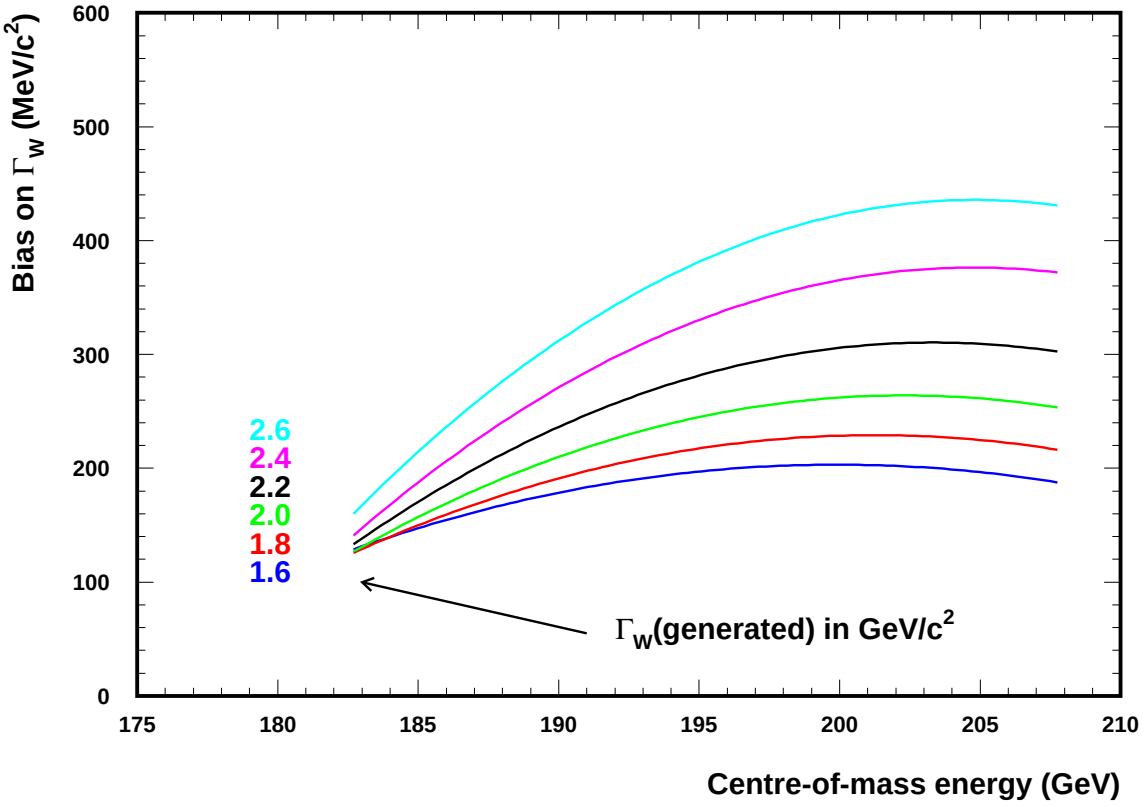

Figure 5.19: *Parametrization of calibration curves of the Γ_W estimator as a function of the centre-of-mass energy $\sqrt{s}$ with a second order polynomial.*

5.6 Consistency checks of the estimator with the bootstrap method

Another important statistical property of an estimator for a precise measurement is its random uncertainty or variance. Standard resampling or bootstrap techniques were applied to determine the expected value of this uncertainty. With the large amount of Monte Carlo simulated events available, subsamples were created with the same integrated luminosity as the real data sample. The number of events in each subsample was randomly chosen according to Poissonian statistics where the mean value was obtained from the accepted cross-section of both 4-fermion and 2-fermion processes and the integrated luminosity of the data sample of interest. From each subsample i the likelihoods $\Delta\chi^2_{tot,i}(m_W)$ and $\Delta\chi^2_{tot,i}(\Gamma_W)$ were reconstructed and a value for m^i_W and Γ^i_W was inferred. The Root Mean Squared (RMS) of the distribution of all m^i_W (Γ^i_W) reflects the expected value of the uncertainty on m_W (Γ_W) when applying the same measurement on the real data. Those values are summarized in Table 5.2 for each centre-of-mass energy.

Fixed $\sqrt{s}$ GeV	exp. σ_{m_W} MeV/c^2	RMS of m_W pull	exp. σ_{Γ_W} MeV/c^2	RMS of Γ_W pull (-)	(+)
182.7	129.5	1.024	209.6	1.024	0.963
188.6	128.5	1.023	211.4	1.029	0.973
191.6	130.2	1.031	218.1	1.042	0.979
195.5	130.3	1.028	219.6	1.045	0.984
199.5	130.1	1.020	220.8	1.049	0.994
201.6	131.2	1.024	221.9	1.048	0.987
203.7	131.8	1.021	224.1	1.055	0.997
205.0	132.5	1.022	226.9	1.056	0.996
206.5	132.2	1.019	223.4	1.049	0.993
208.0	132.8	1.022	225.5	1.056	1.000
206.5 (TPC-S6)	135.3	1.021	232.1	1.051	0.989

Table 5.2: *With Monte Carlo resampling determined properties of the parameter estimators. The expected uncertainty on both the m_W and Γ_W estimator are scaled to an integrated luminosity of 100 pb^{-1} for the samples analyzed by the m_W estimator and 200 pb^{-1} for those analyzed by the Γ_W estimator, together with the width of the pull distribution. For the Γ_W estimator asymmetric uncertainties were used.*

The distribution of the uncertainty on m_W^i (Γ_W^i) for all subsamples i shows the expected variation of the random uncertainty on the estimator m_W (Γ_W). Figure 5.20(a) illustrates this distribution for the m_W estimator and for an integrated luminosity equal to that of the combined data samples, excluding the data taken during the TPC-S6 period. The obtained uncertainty from performing the measurement on the data is indicated and agrees with the expected values. The same distribution for the Γ_W estimator can approximately be interpreted similarly taking into account that the bias was depending on the Γ_W^{gen}. The approximation arises from the observation that the calibration curves were not perfectly linear. The presents of a strong positive correlation between the estimated value of Γ_W and its random uncertainty also complicates the interpretation. Due to the non-unity slope of the $\sqrt{s}$ dependent calibration curves the data likelihoods were not only shifted but also their curvature at the minimum was slightly changed. Therefore the measured uncertainty on the inferred value of the Γ_W estimator was different before and after applying the event-by-event calibration. The correct uncertainty is the one before applying the calibration. In Figure 5.20(b) its expected value is compared with the measured one and a good agreement was found.

To verify if the calculated uncertainty $\sigma_{m_W}^{calc}$ is in agreement with the spread of the distribution of all m_W^i values, the so-called pull was defined:

$$\text{pull} = \frac{m_W^{\text{measured}} - < m_W^{\text{measured}} >}{\sigma_{m_W}^{\text{calc}}} \tag{5.27}$$

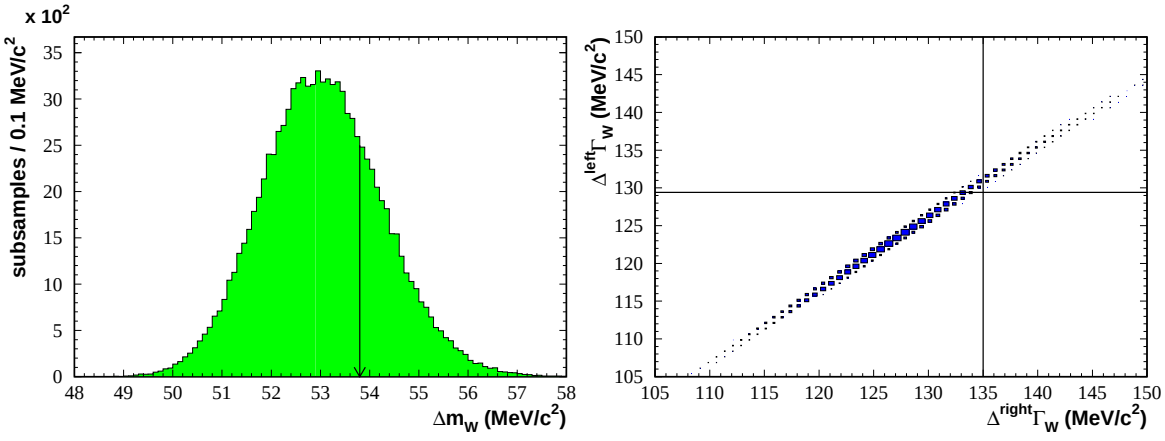

(a) (b)

Figure 5.20: *The expected distribution of the random uncertainty on the m_W estimator is shown in plot (a). The arrow indicates the value obtained from performing the analysis on the combined data sample (excluding the TPC-S6 period). For the Γ_W analysis the distribution of both the left (-) and right (+) uncertainty are shown in plot (b). Again the lines indicate the values obtained from the combined data sample (excluding the TPC-S6 period).*

where the measured W mass m_W^i for each sample i was corrected for the expected bias on the estimator. A similar definition was applied for the Γ_W analysis. The pull value was calculated for each sample i and its distribution should reflect a normal Gaussian, centered around zero and with a unity width. To obtain these constraints on the pull two parameters were introduced in the reconstruction of the likelihood. The first parameter f was a scaling factor for the input uncertainties of the kinematic fit in Equation 4.10, while the second parameter ϵ_c was a multiplicative factor on the events purity, $P^{4f} \rightarrow \epsilon_c \cdot P^{4f}$, used in the construction of the theoretical probability density function in the $\vec{m}$-space, Equation 5.23. The value of f was taken to be 1.1 and the value of ϵ_c was tuned to obtain approximately a unity width of the m_W pull distribution, resulting in an optimal value of 0.77. A variation in the value of both parameters did not change the bias of the estimators by a significant amount. Using this procedure almost perfect pull distributions were found for the m_W estimator, while for the W width estimator deviations of 4% were seen. In Table 5.2 the RMS of the pull distributions are shown as a function of the centre-of-mass energy of the Monte Carlo event sample with which they were determined. The final uncertainties obtained when analyzing the real data samples were corrected for these non-unity RMS value of the pull distribution.

5.7 Alternative m_W estimators

In the following chapters it will become clear that the m_W estimator is highly sensitive to many systematic effects. The largest contribution to the systematic uncertainty will arise from the hypothesis, used throughout the likelihood reconstruction, that the fragmentation of the partons from both W bosons happens independently. Effects such as Bose-Einstein Correlations (section 3.5.1) and Colour Reconnection (section 3.5.2) could destroy this hypothesis. Alternative estimators have been designed which were less sensitive to the Colour Reconnection effects. In chapter 7 it will be shown that the difference between the W mass value obtained with the nominal m_W estimator and the alternative ones is a sensitive measure of the systematic effects in question.

The effect of Colour Reconnection on the structure of the $W^+W^- \rightarrow q\bar{q}'Q'\bar{Q}$ event is expected to be visible in the region between the reconstructed jets in the final state or on particles with a relative low momentum. This was the motivation to construct two different m_W estimators which are still highly correlated with the standard one as presented previously.

- **The momentum cut alternative m_W estimator**

  For this alternative m_W estimator the event selection was done in exactly the same way as for the standard m_W estimator. The particle-jet association was also taken from this analysis. However, when reconstructing the event for the m_W extraction a more severe track selection was applied. The momentum and energy of the jets were calculated only from those tracks having a total momentum higher than a certain p_{cut} value. An event-by-event likelihood $L_i^{p_{cut}}(m_W)$ was calculated with the same convolution technique as described in this chapter. Because the Colour Reconnection effect is supposed to perturb the low momentum particles, the value of p_{cut} was optimized to obtain the largest sensitivity to measure Colour Reconnection model parameters from the expected difference in reconstructed W mass from the nominal and the $m_W^{p_{cut}}$ estimator. In chapter 7 a value of p_{cut} = 2 GeV/c was found.

- **The hybrid cone alternative m_W estimator**

  In this second alternative m_W estimator the reconstruction of the event was the same as for the standard analysis, except when calculating the jet momenta used for the m_W extraction. An iterative procedure was used within each jet (defined by the clustering algorithms used in the standard analysis) to find a stable direction of a cone excluding some particles in the calculation of the jet momentum, illustrated in Figure 5.21. Starting with the direction of the original jet $\vec{p}_{std}^{jet}$, the jet direction was recalculated (direction (1) on the figure) only from those particles which have an opening angle smaller then R_{cone} with this original jet. This process was iterated by constructing a second cone (of the same opening angle R_{cone}) around this new jet direction and the jet direction was recalculated again. The iteration was continued until a stable jet direction $\vec{p}_{cone}^{jet}$ was found. The obtained jet momenta $\vec{p}_{cone}^{jet}$ were rescaled to compensate for the lost energy of particles outside the stable cone,

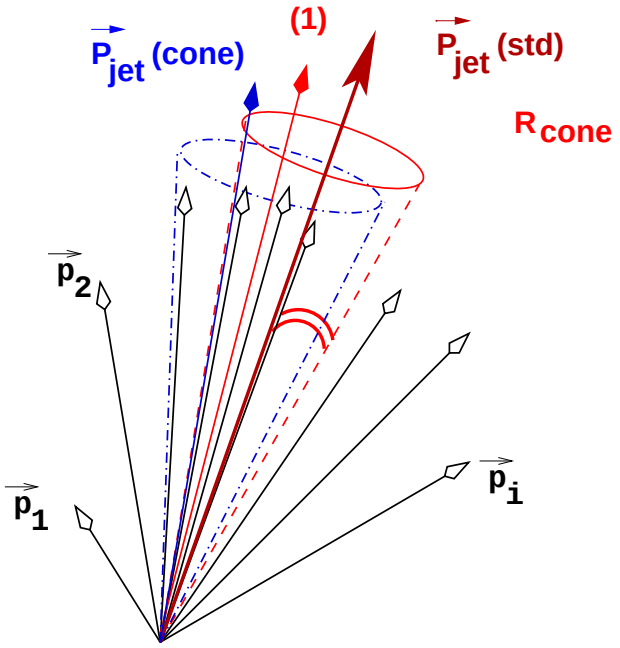

Figure 5.21: *Illustration of the iterative cone algorithm within a predefined jet as explained in the text.*

$$\vec{p}_{cone}^{\,jet} \rightarrow \vec{p}_{cone}^{\,jet} \cdot \frac{E^{jet}}{E_{cone}^{jet}} \quad . \tag{5.28}$$

The energies of the jets were taken to be the same as those obtained with the standard clustering algorithm ($E_{cone}^{jet} \rightarrow E^{jet}$). Again the result was an event-by-event likelihood $L_i^{R_{cone}}(m_W)$ and the value of R_{cone} was optimized with the same criterion as the $m_W^{p_{cut}}$ estimator. A value of R_{cone} of 0.5 rad was found.

The expected statistical bias on both estimators was estimated in the frequentist way by using large numbers of Monte Carlo samples. As for the nominal m_W estimator a dependency on the centre-of-mass energy was observed, Figures 5.22(a) and 5.22(b), and an event-by-event bias correction was applied on the reconstructed likelihoods from the selected data events. The global scale of the bias on these estimators was however different from the nominal one shown in Figure 5.14. This demonstrates for example how sensitive the m_W estimator is to the goodness of the simulation of low momentum particles, as their information shifts the bias by about 1% of the expected value for m_W. In Table 5.3 the statistical properties of the uncertainty on these alternative estimators are shown. The expected uncertainty increased when neglecting the information of the low momentum particles ($m_W^{p_{cut}}$ estimator) or when neglecting the information of the particles in the regions between the reconstructed jets (m_W^{cone} estimator). Also the width of the pull distribution changed by about 5 to 6%

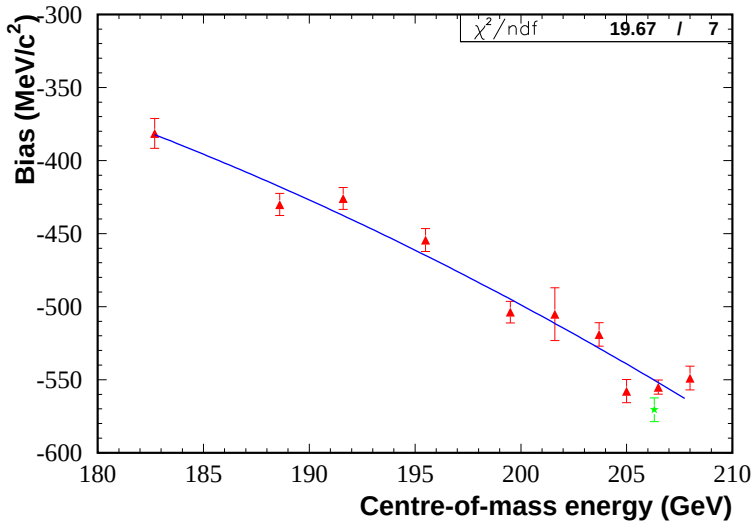

(a)

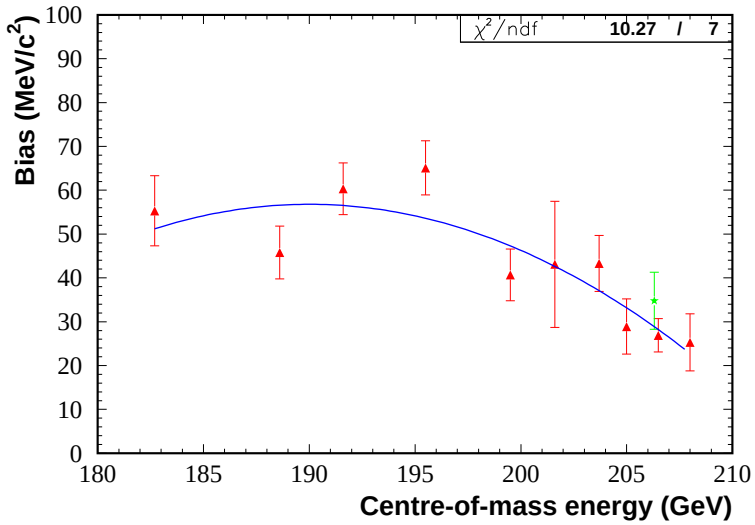

(b)

Figure 5.22: *Estimated bias of the alternative m_W estimators. Plot (a) shows the bias dependency on the centre-of-mass energy $\sqrt{s}$ for the p_{cut} estimator, while plot (b) is the Monte Carlo result for the cone-like estimator. Both use the optimal values of respectively the momentum cut and the opening angle of the cone. The green stars reflect the expected bias on the estimators when the TPC-S6 data is analyzed. A similar fit was performed as in Figure 5.14.*

compared to the nominal analysis. The calculated uncertainty on the data inferred values of both estimators, discussed in the next section, were corrected for this non-unity RMS of the pull distribution. Their expected values for the full real data sample, excluding the TPC-S6 period, were 70.2 MeV/c^2 for the $m_W^{p_{cut}}$ estimator and 55.5 MeV/c^2 for the m_W^{cone} estimator. After pull correction they can be compared with the measured values of respectively 76.0 MeV/c^2 and 61.8 MeV/c^2.

Fixed $\sqrt{s}$ GeV	exp. $\sigma_{m_W^{p_{cut}}}$ MeV/c^2	RMS of $m_W^{p_{cut}}$ pull	exp. $\sigma_{m_W^{cone}}$ MeV/c^2	RMS of m_W^{cone} pull
182.7	182.4	1.075	143.6	1.063
188.6	182.6	1.080	144.7	1.074
191.6	184.6	1.086	146.7	1.081
195.5	186.2	1.087	147.7	1.080
199.5	188.7	1.091	148.9	1.082
201.6	190.0	1.092	149.4	1.078
203.7	194.3	1.105	152.3	1.090
205.0	193.5	1.097	152.5	1.087
206.5	194.2	1.099	152.7	1.086
208.0	193.0	1.095	153.9	1.091
206.5 (TPC-S6)	199.2	1.100	156.3	1.089

Table 5.3: *With Monte Carlo resampling determined properties of the alternative estimators. The expected uncertainty on both the $m_W^{p_{cut}}$ and m_W^{cone} estimator are scaled to an integrated luminosity of 100 pb^{-1}.*

5.8 Inferred results from the data

The resulting values from the inference of the W mass using the standard m_W^{std} estimator, and both alternative ones, $m_W^{p_{cut}}$ and m_W^{cone}, on the data samples are summarized in Table 5.4. All values for the measured uncertainties on those estimators were corrected to obtain a unity width of the pull distribution in the corresponding Monte Carlo studies. The values for the combined data sample (including the TPC-S6 period) were determined by summing the calibrated log-likelihoods from all events, as in Equation 5.24. Possible systematic uncertainties on the standard m_W estimator will be discussed in chapter 6.

In Figure 5.23 the inferred m_W values are shown as a function of the centre-of-mass energy. The dependence on $\sqrt{s}$ was fitted assuming that the W mass is an invariant quantity within the energy range accessible by LEP2. The results obtained with the standard m_W estimator clearly confirm this Standard Model prediction, while for the alternative estimators some discrepancies were found. The disagreement for the $m_W^{p_{cut}}$ estimator was mostly due

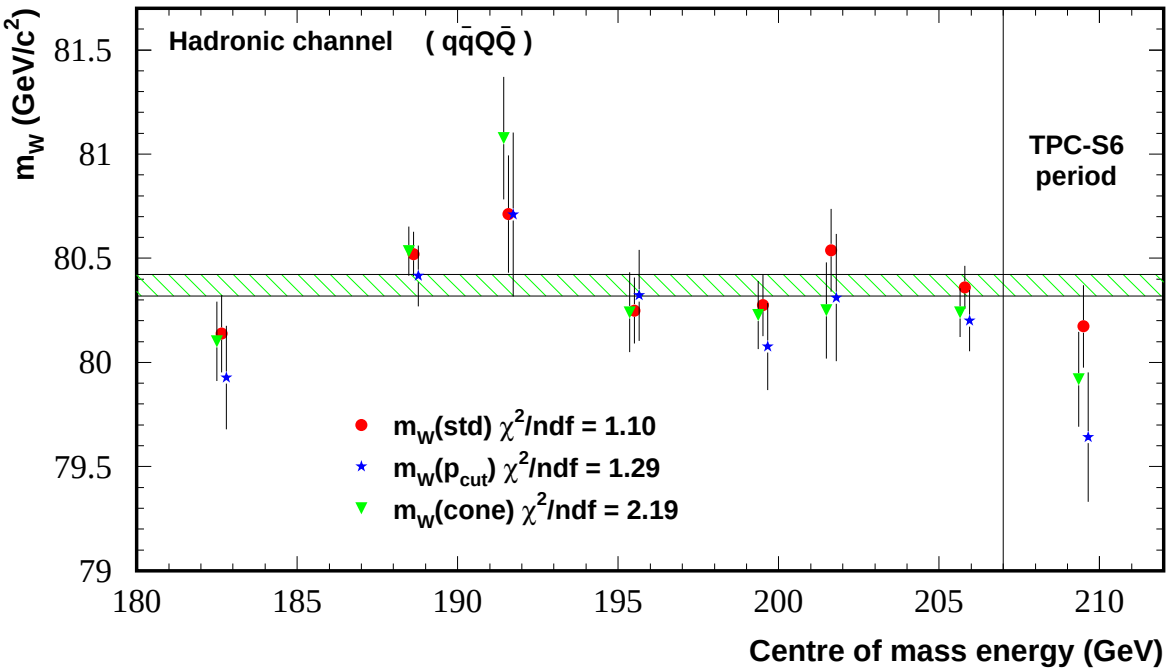

Figure 5.23: *Inferred data values on the W mass obtained with different m_W estimators as a function of the nominal centre-of-mass energy $\sqrt{s}$ of each subsample. The band indicates the 1σ statistical contour belt of m_W determined with the m_W^{std} estimator using all data (including the TPC-S6 period). The χ^2/ndf of a fit assuming an invariant W mass in this energy range, is quoted for each estimator (including the TPC-S6 values). The results from the TPC-S6 period are shown separately from the other subsamples, those events have a nominal centre-of-mass energy of about 206.3 GeV.*

to the results inferred from the data taken during the TPC-S6 period, while for the m_W^{cone} estimator the W mass value at $\sqrt{s} \sim 192$ GeV had the largest contribution to the χ^2.

As indicated in Table 5.4 the resulting central value for the three different m_W estimators tend to show some discrepancy between each other. This difference was enhanced due to the strong correlation between the m_W estimators. Taking into account this correlation the following values were obtained for the combined data set (including the TPC-S6 period):

$$\begin{array}{lcrcrl} m_W^{std} & - & m_W^{p_{cut}} & = & 142.6 \pm 61.4 & \mathrm{MeV/c^2} \\ m_W^{std} & - & m_W^{cone} & = & 58.5 \pm 35.1 & \mathrm{MeV/c^2} \\ m_W^{p_{cut}} & - & m_W^{cone} & = & -84.1 \pm 59.3 & \mathrm{MeV/c^2} \end{array} \quad (5.29)$$

where the uncertainties were calculated with the Jackknife method [7]. These observed differences could indicate the presence of systematic effects which were not correctly taken into account by the Monte Carlo simulation and will be studied in chapter 7.

Nominal $\sqrt{s}$ GeV	m_W^{std} GeV/c^2	$m_W^{p_{cut}}$ GeV/c^2	m_W^{cone} GeV/c^2
182.65	80.138 ± 0.185	79.927 ± 0.249	80.101 ± 0.191
188.63	80.520 ± 0.107	80.415 ± 0.145	80.534 ± 0.119
191.58	80.712 ± 0.281	80.710 ± 0.393	81.077 ± 0.294
195.51	80.249 ± 0.159	80.322 ± 0.218	80.241 ± 0.192
199.51	80.275 ± 0.149	80.076 ± 0.209	80.228 ± 0.164
201.64	80.539 ± 0.199	80.311 ± 0.305	80.250 ± 0.231
205.8	80.360 ± 0.104	80.200 ± 0.147	80.240 ± 0.117
206.3 (TPC-S6)	80.173 ± 0.198	79.641 ± 0.311	79.919 ± 0.228
total	80.371 ± 0.053	80.222 ± 0.075	80.310 ± 0.060

Table 5.4: *Results inferred from the data with the different m_W estimators ('std' denotes the standard analysis).*

The results inferred about Γ_W are shown in Table 5.5. Again the uncertainties were corrected to obtain a width of the pull distribution of unity. The fit assuming an invariant W width in the energy range of LEP2, showed a perfect agreement between Standard Model expectation and observation.

Nominal $\sqrt{s}$ GeV	Γ_W GeV/c^2		
182.65	2.552	+ 0.524	- 0.396
188.63	2.317	+ 0.280	- 0.240
191.58	2.370	+ 0.897	- 0.615
195.51	2.525	+ 0.593	- 0.424
199.51	2.190	+ 0.408	- 0.344
201.64	1.777	+ 0.541	- 0.436
205.8	1.905	+ 0.262	- 0.234
206.3 (TPC-S6)	2.216	+ 0.598	- 0.478
total	2.189	+ 0.137	- 0.124

Table 5.5: *Results inferred from the data with the Γ_W estimator. A third order polynomial was used as parametrization of the likelihoods.*

[7] The Jackknife method is used throughout this thesis and is therefore described in Appendix A.

Chapter 6

Systematic uncertainties

In the previous chapter two main estimators were discussed. The first for inferring information about the W mass, m_W, the other was meant to extract information about the W width, Γ_W. Applying Bayesian techniques a likelihood was constructed, which was calibrated in a frequentist way using Monte Carlo simulation. Because the same analysis method was used on both Monte Carlo and real data samples, the main systematic uncertainties arise from effects which were not perfectly or not at all included in the simulation of the data. This chapter aims for a thorough description of these effects as well as their influence on the central value of both estimators.

6.1 Hypothesis of factorisable systematic uncertainties

The inference methods used to extract information about the W mass and width were based on Monte Carlo simulation. Similar measurements which are intrinsically Monte Carlo independent do no exist. It was discussed in section 3.1 that the response functions of several physical phenomena were factorized in these Monte Carlo algorithms. As a consequence also systematic effects on the bias of the m_W or Γ_W estimator due to changes in those response functions can be factorized. This hypothesis is only an approximation as it was sometimes not possible to classify the source of the disagreement between observable distributions from the real data and the corresponding Monte Carlo. For example the modelization of the fragmentation (sections 3.3 and 3.4) as well as the energy flow reconstruction (section 4.1) could lead to disagreements between reality and simulation within the core of the jets where the particle density is high. Although these limitations, it was possible to factorize four major sources of uncertain effects in the production of a Monte Carlo event, as shown in Figure 3.1: the knowledge of the kinematics in the initial state, the calculation of the electroweak hard process, the modelization of the fragmentation and the simulation of detector effects. Together with the effects arising from the finite statistics of the simulated event sample and the description of background events, all those possible sources of systematic uncertainties are discussed in the remainder of this chapter.

The possibility of Colour Reconnection effects between the decay products of both W bosons will be the topic of chapter 7.

6.2 Monte Carlo calibration

Monte Carlo event samples were simulated at fixed centre-of-mass energies ranging from $\sqrt{s} \sim$ 183 to 208 GeV. The uncertainty on the calculated bias on the m_W and Γ_W estimators, σ_{bias}, depended on the amount of events, n, in these samples as $\sigma_{bias} \sim \frac{1}{\sqrt{n}}$. When assuming a continuous evolution of the bias with centre-of-mass energy, as shown in Figures 5.14 and 5.15, this uncertainty for each individual sample was reduced by taking into account the information available at other centre-of-mass energies. Because a second order polynomial fitted this evolution rather well, the final uncertainty on the scale of the bias was small. The uncertainties on the bias of the m_W estimator were on average about 6 MeV/c^2, while for the Γ_W estimator values around 14 MeV/c^2 were found. The use of 10 uncorrelated Monte Carlo samples should reduce these numbers by about a factor 3. Taking into account the χ^2/ndf of the fit, systematic uncertainties were quoted of 4 MeV/c^2 on m_W and 9 MeV/c^2 on Γ_W due to the finite statistics of the Monte Carlo samples.

For the W mass and width values inferred from the data taken during the TPC-S6 period, extra uncertainties arose due to the difference in estimated bias from the nominal sample and the special sample using different particle reconstruction techniques (cfr. section 2.4) but both generated at the same centre-of-mass energy $\sqrt{s}$= 206.5 GeV. The following values were obtained:

$$\begin{array}{lrcrcrl} \Delta m_W & (\mathrm{nominal-TPC/S6}) & = & -16.1 & \pm & 6.9 & \mathrm{MeV/c^2} \\ \Delta \Gamma_W & (\mathrm{nominal-TPC/S6}) & = & -67.9 & \pm & 16.4 & \mathrm{MeV/c^2} \quad . \end{array} \tag{6.1}$$

For the Γ_W estimator the shift was applied and the uncertainty on the shift was quoted as a systematic source of uncertainty, while for the m_W estimator the shift was quoted as systematic uncertainty.

In the calibration procedure the slope of the calibration curve was another source of systematic uncertainty. For the m_W estimator the spread in slope over all Monte Carlo samples was estimated to be about 1%. Taking 1% of the expected uncertainty for m_W inferred from the combined data set results in about 0.5 MeV/c^2. The calibration curves for the Γ_W estimator were also function of the value Γ_W^{gen} itself, therefore they had non-unity slope. The χ^2/ndf of the fit of the bias as a function of $\sqrt{s}$ and Γ_W^{gen} was about 2. Hence the 9 MeV/c^2 quoted above was multiplied by this factor 2 to take into account the imperfect descriptions of the bias function versus Γ_W^{gen}, leading to a total systematic uncertainty of 18 MeV/c^2.

6.3 Detector effects

The simulation of the DELPHI detector relies on calibration studies performed for each subdetector. The $Z^0 \to q\bar{q}$ events selected from the data recorded during the Z^0 calibration runs (cfr. section 4.1) were used to confront this detector simulation with the reality. It was however not straightforward to make conclusions on the goodness of the $W^+W^- \to q\bar{q}'Q'\bar{Q}$ detector simulation from the Z^0 studies, as the energy scale of the produced jets is different in both processes.

6.3.1 Energy flow and jet reconstruction

In a first study the Z^0 events from the calibration runs accumulated during the years 1998, 1999 and 2000 were exploited to verify the energy flow reconstruction in the jets. The hadronic TEAM4 criterion was used to select $Z^0 \rightarrow q\bar{q}$ events (cfr. section 4.1), together with an anti-btag cut similar to that used for the m_W and Γ_W analyses. The remaining events were clustered with the DURHAM algorithm into jets using a y_{cut} value of 0.006. In the event selection a minimum of 2 jets was requested. Events which had a $y_{2\leftarrow 3}$ value smaller than 0.006 were clustered into 2 jets, those with a higher value into 3 jets. As for the reconstruction of the $W^+W^- \rightarrow q\bar{q}'Q'\bar{Q}$ events, a minimal jet multiplicity of 3 particles and a minimal jet mass of 1 GeV/c^2 were requested. By applying this procedure the jets should have the same characteristics as those reconstructed within hadronic decaying W^+W^- events, apart from their energy scale. About 50% of the selected Z^0 events were reconstructed into a 2 jet topology, while the other 50% reflected a 3 jet topology.

From the reconstructed jets the average energy flow was calculated as a function of the angle away from the jet axis, $\theta_{jet-particle}$. When comparing those distributions obtained from the real Z^0 data with the corresponding ones from the KK2f Monte Carlo simulation, some discrepancies were found. In Figure 6.1 these disagreements are shown for jets in the barrel, between and forward regions of the detector. The region between the barrel and the forward parts of the detector was defined as the 'between' region and covered a polar angle range from 30 to 50 degrees. The data of all three years were combined as no significant difference was found between them. Comparisons were separately made for the neutral and charged energy flow. The green band reflects the RMS on the ratio between the data and Monte Carlo distribution, when using the PYTHIA fragmentation model in the simulation. In a good approximation the same uncertainties can be quoted for the two other models which were tested, ARIADNE and HERWIG. Therefore also the simulated energy flow distribution as a function of the angle away from the jet axis obtained from these fragmentation models was also in disagreement with the data.

The figures indicate that the Monte Carlo jets contain in average too much energy in the core of the jet carried by neutral particles, while too little further away from the jet axis. Around the jet axis the excess was compensated by a deficit in energy carried by charged particles. The shape of the disagreements as a function of $\sin(\theta_{jet-particle})$ was found to be invariant over all jet directions, while in the forward region the Monte Carlo excess in the core of the jets was about twice as large as in the barrel region.

The discrepancies were found to be insensitive to the applied clustering algorithm, because the same tendencies were observed for the CAMBRIDGE and DICLUS algorithms. Also the $y_{2\leftarrow 3}$ separation between 2 jet and 3 jet topologies did not influence the observations, neither did the applied anti-btag sequential cut. To study the influence of fragmentation model parameters special samples were produced with a value of σ_q (cfr. section 3.4) which was two standard deviations shifted up or down from its tuned value. The 2σ shifts in the value of σ_q did not change the disagreements between data and Monte Carlo. Implementing Bose-Einstein Correlations between identical bosons with the LUBOEI model version BE_{32} as described in section 3.5.1 with the tuned values of $\lambda_{\rm BE}$ and $r_{\rm BE}$ as mentioned in the same section, also did not change the disagreements.

From all these observations together, it was concluded that certainly a non-negligible

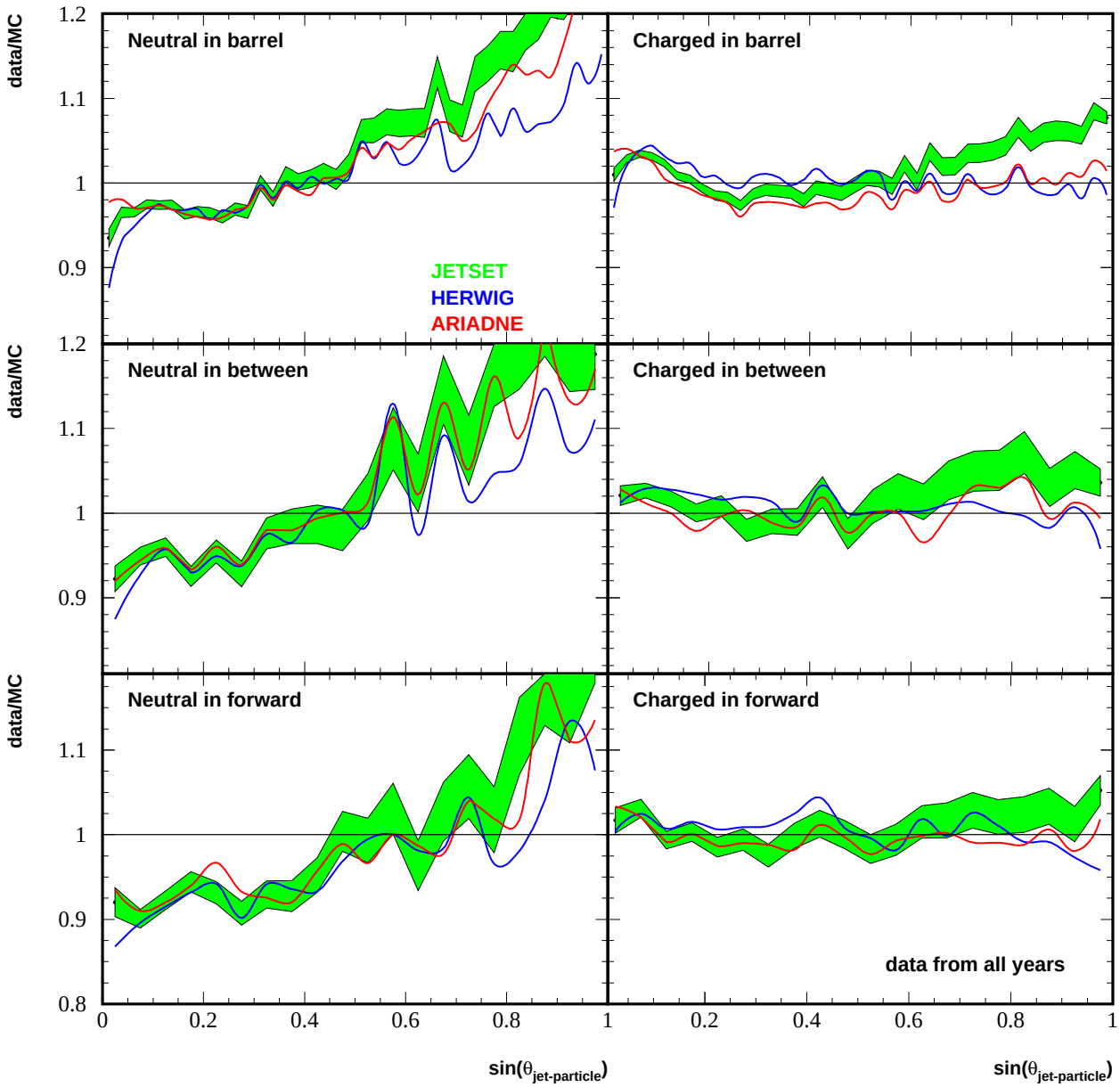

Figure 6.1: *Comparison between data and simulation of the average energy flow from jets reconstructed in selected Z^0 events as a function of the sinus of the angle away from the jet axis. The distributions are separated according to the jets polar angle and the electric charge of the particle carrying the energy. In the simulation three different fragmentation models have been tested. Only for the comparison of the data with the PYTHIA fragmented simulation, the RMS on the disagreements is shown. To a good approximation the same RMS can be quoted for the two other models, ARIADNE and HERWIG.*

fraction of the energy flow discrepancies was arising from possible errors in the energy flow reconstruction. Therefore part of the systematic uncertainty induced by these differences should be classified as a detector systematic. The other part should be classified as a fragmentation uncertainty. As discussed in section 3.6 the tuning of the fragmentation model parameters did not take into account the correlation between the observables, such as the energy of the particle and its momentum transverse to the jet axis. Hence it was possible to have a well described inclusive spectrum of the energy of the particles together with a well described spectrum of the transverse momentum (which was not the case for all fragmentation models [53]), while discrepancies appear in the two dimensional distribution. It was however difficult to estimate which fraction of the data versus simulation discrepancies was due to detector effects and due to the modelization of the fragmentation process. This could be important when combining the results on m_W or Γ_W with other LEP experiments.

Due to the rather small amount of real data statistics compared to samples of selected $Z^0 \to q\bar{q}$ events, it was impossible to estimate if these disagreements also occurred between the real and simulated $W^+W^- \to q\bar{q}'Q'\bar{Q}$ events. Therefore the disagreements observed in the $Z^0 \to q\bar{q}$ simulation should be translated to the $W^+W^- \to q\bar{q}'Q'\bar{Q}$ simulation of interest. In this non-trivial operation one has to realize that the reconstructed jets in both

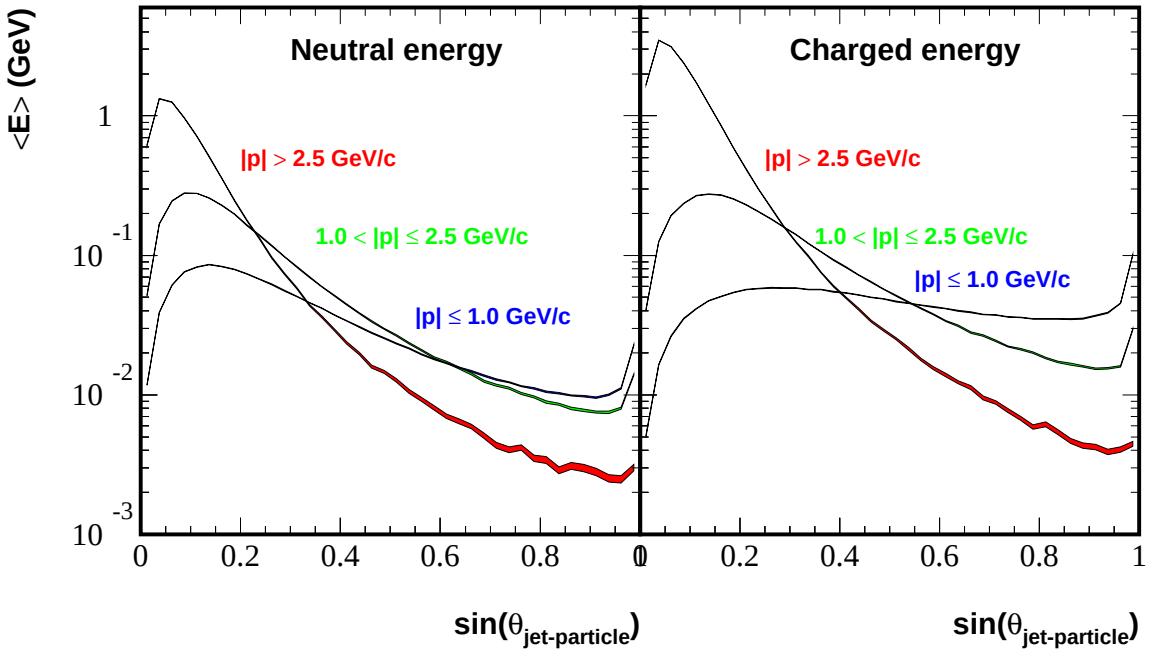

Figure 6.2: *Average charged or neutral reconstructed energy from data events as a function of the sinus of the angle away from the jet axis. The energy flow is splitted into three bins according to the momentum of the particle carrying the energy. The last bin shows the pile-up effect of all particles in the jet from the other hemisphere defined by the jet direction.*

types of processes are not the same. Mainly the average energy scale and broadness are different. The discrepancies observed in Figure 6.1 were found to be invariant for different values of the energy scaled broadness of the jet, B_{jet}/E_{jet}, defined in section 4.4. To a good approximation the parametrized inclusive energy flow ratios between data and simulation as a function of the sinus of the angle away from the jet axis, could be applied on all jets reconstructed in the $W^+W^- \to q\bar{q}'Q'\bar{Q}$ events.

In Figure 6.2 the average energy flow spectrum obtained from the data as a function of the sinus of the angle away from the jet axis, is shown in three different ranges of the momentum of the particles included in the spectrum. As expected from the phenomenology of the fragmentation, for both charged and neutral particles the distribution was broader for low momentum particles. The ratio of those spectra obtained from data and simulation was determined in 9 bins of the momentum of the particle. Neither the shape nor the level of the disagreement were invariant over these 9 bins. Therefore the inclusive ratio shown in Figure 6.1 was parametrized as a function of the angle between the jet axis and a test particle, and the momentum of this particle, resulting in

$$R_{i,j} = R_{i,j}(sin(\theta_{jet-particle}), |\vec{p}\,|). \tag{6.2}$$

This was separately done for both charged and neutral particles $i \in \{1, 2\}$, and for the three regions in the detector $j \in \{1, 2, 3\}$ = {barrel, between, forward}.

A simple particle reweighting procedure was designed to illustrate the effect of $R_{i,j}$ on the bias of the m_W and Γ_W estimators of interest. In section 6.3.2 a more complete method will be discussed to take into account most of the residual discrepancies. The simulated $W^+W^- \to q\bar{q}'Q'\bar{Q}$ events were reconstructed in the same way as described in chapter 5. The selected particles were clustered into jets with the DURHAM algorithm and for each particle the values for $\theta_{jet-particle}$ and $|\vec{p}\,|$ were calculated. A random dice $\mathcal{R} \in [0, 1]$ decided if the particle was duplicated or removed from the list. This discrete reweighting procedure gave the particles a weight w of 0, 1 or 2 according to the following criteria:

$$\begin{array}{lllllll}
R_{i,j} > 1 \to & \mathcal{R} \leq |R_{i,j} - 1| & \to & w = 2 \\
 & \mathcal{R} > |R_{i,j} - 1| & \to & w = 1 \\
R_{i,j} < 1 \to & \mathcal{R} \leq |R_{i,j} - 1| & \to & w = 0 \\
 & \mathcal{R} > |R_{i,j} - 1| & \to & w = 1 \\
R_{i,j} = 1 \to & & \to & w = 1 \quad .
\end{array} \tag{6.3}$$

The m_W or Γ_W analysis, including the event selection, was only started after this particle reweighting. It was found that about 1.5% of the selected events changed from a 4 jet to a 5 jet topology, while also about 1.5% changed from a 5 jet to a 4 jet configuration. The functions $R_{i,j}(sin(\theta_{jet-particle}), |\vec{p}\,|)$ were recalculated from the selected Z^0 events after applying the particle reweighting obtaining $\tilde{R}_{i,j}(sin(\theta_{jet-particle}), |\vec{p}\,|)$. The integrated agreement between data and simulation was improved:

$$\int_0^1 \int_0^\infty |R_{i,j}(x, y)| \cdot dxdy \;>\; \int_0^1 \int_0^\infty |\tilde{R}_{i,j}(x, y)| \cdot dxdy \tag{6.4}$$

where x reflects the angular and y the momentum dependency. However some regions in this multi-dimensional space still suffer from residual disagreements. Therefore the results

on the m_W and Γ_W should be regarded as illustrations of the possible effect of energy flow discrepancies between data and simulation on their respective bias. The following results were obtained at a centre-of-mass energy of about 189 GeV:

$$\begin{array}{lrcrcl} \Delta m_W & (\mathrm{Not.Rew.} - \mathrm{Rew.}) & = & 38.4 & \pm & 3.9 \quad \mathrm{MeV/c^2} \\ \Delta \Gamma_W & (\mathrm{Not.Rew.} - \mathrm{Rew.}) & = & -4.4 & \pm & 7.3 \quad \mathrm{MeV/c^2} \end{array} \tag{6.5}$$

and at $\sqrt{s}$ = 208 GeV:

$$\begin{array}{lrcrcl} \Delta m_W & (\mathrm{Not.Rew.} - \mathrm{Rew.}) & = & 41.0 & \pm & 3.4 \quad \mathrm{MeV/c^2} \\ \Delta \Gamma_W & (\mathrm{Not.Rew.} - \mathrm{Rew.}) & = & -33.7 & \pm & 7.3 \quad \mathrm{MeV/c^2} \end{array} \tag{6.6}$$

where the uncertainties were calculated with the Jackknife method to take into account the large correlation between the reconstructed likelihoods before and after the particle reweighting. It is well known that the charged particles are better described in fragmentation models compared to the neutral ones and that they are easier to reconstruct in the detector. Together with the observation in Figure 6.1 that the neutrals give the worst disagreements, it was expected that the large effect on the m_W and Γ_W estimators was mainly due to these neutral particles. Therefore the particle reweighting was separately applied on the Monte Carlo events at $\sqrt{s}$ = 208 GeV for neutral:

$$\begin{array}{lrcrcl} \Delta m_W & (\mathrm{Not.Rew.} - \mathrm{Rew.}) & = & 57.6 & \pm & 3.6 \quad \mathrm{MeV/c^2} \\ \Delta \Gamma_W & (\mathrm{Not.Rew.} - \mathrm{Rew.}) & = & -14.2 & \pm & 6.7 \quad \mathrm{MeV/c^2} \end{array} \tag{6.7}$$

and charged particles:

$$\begin{array}{lrcrcl} \Delta m_W & (\mathrm{Not.Rew.} - \mathrm{Rew.}) & = & -4.6 & \pm & 3.4 \quad \mathrm{MeV/c^2} \\ \Delta \Gamma_W & (\mathrm{Not.Rew.} - \mathrm{Rew.}) & = & -18.0 & \pm & 6.8 \quad \mathrm{MeV/c^2} \quad . \end{array} \tag{6.8}$$

These numbers confirm the hypothesis for the m_W estimator, while for the Γ_W estimator the inclusive effect had equal contributions from neutral and charged particles.

The same reweighting procedure as in Equations 6.3 was applied to illustrate the effect of the discrepancies observed in Figure 4.1 rather than in Figure 6.1 on the m_W estimator at $\sqrt{s} \sim$ 189 GeV, resulting in a shift of:

$$\Delta m_W \quad (\mathrm{Not.Rew.} - \mathrm{Rew.}) \quad = \quad 1.8 \quad \pm \quad 1.9 \quad \mathrm{MeV/c^2} \tag{6.9}$$

hence basically a negligible effect.

6.3.2 Mixed Lorentz Boosted Z^0's

A novel technique was proposed in [77] to study systematic uncertainties on jet reconstruction and fragmentation in W physics measurements with high statistical precision. The main advantage of this method was that Monte Carlo simulated jet properties in W^+W^- events could be directly compared with the corresponding ones from real data and this using the large amount of Z^0 statistics. In this thesis an improved version was used to verify systematic uncertainties on the W mass and width estimators.

The MLBZ method

As already mentioned it is very difficult to classify the source of several systematic effects related to the jet reconstruction which could manifest themselves in the comparison between real data hadronic Z^0 events and their simulation. Also it was not trivial to translate these Z^0 discrepancies into systematic uncertainties on the m_W and Γ_W estimators. The Monte Carlo smearing or reweighting methods applied to cover the disagreements could still introduce residual features which should also be taken into account in the systematic uncertainty. The only known technique up to now which takes into account the almost complete set of systematic effects at once is the so-called Mixed Lorentz Boosted Z^0's or MLBZ method. Its main strategy is illustrated in Figure 6.3.

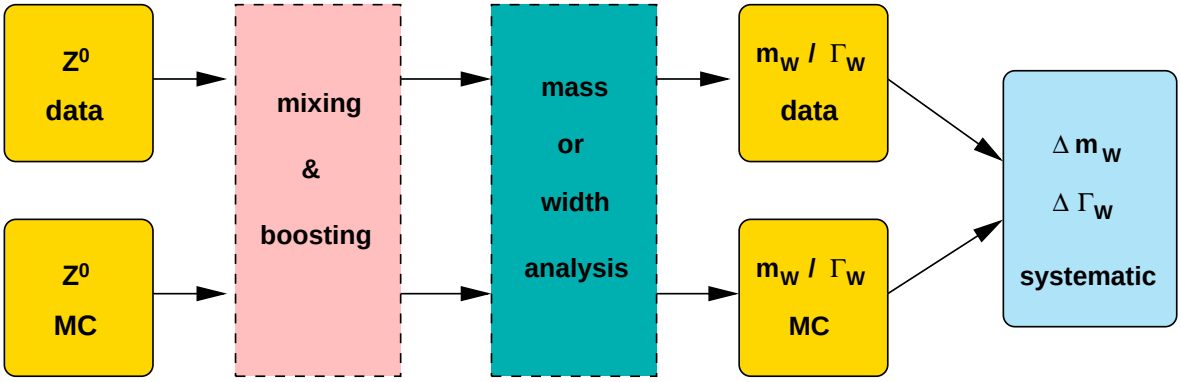

Figure 6.3: *Illustration of the MLBZ strategy.*

To emulate a realistic $W^+W^- \to q\bar{q}'Q'\bar{Q}$ event, two hadronically decaying Z^0 events were rotated and boosted in order that their superposition reflects a true W^+W^- event. Applying the TEAM4 hadronic selection described in section 4.1, the Z^0 events were selected in the data or within the corresponding KK2f simulated samples. The m_W or Γ_W analysis was performed on those MLBZ events and systematic uncertainties were obtained from the difference between the data MLBZ's and the Monte Carlo MLBZ's. Due to the large amount of available Z^0 statistics accumulated during the calibration runs and the advantage that the same Z^0 event could be used many times in the construction of different MLBZ events, the statistical uncertainties of these systematic shifts were small.

The main extension of the method beyond that described in [77] consisted in an improved mixing and boosting procedure of the Z^0 events into MLBZ's, demonstrated in Figure 6.4. The four momenta of the primary quarks in a WPHACT generated $W^+W^- \to q\bar{q}'Q'\bar{Q}$ event in the lab frame were re-boosted to the W^+W^- rest frame. The particles in the final state of two selected Z^0 events were rotated to match these primary quark directions in the rest frame. The direction of the first Z^0 thrust axis was aligned to the quark momenta in a first

W decay. For the second Z^0 event one of the quarks of the remaining W decay was chosen as reference. The kinematic properties of the reconstructed fermions in the Z^0 decays were rescaled to match the mass of the W bosons in the generated WPHACT event rather than the Z^0 mass. After the rotation, the mixed Z^0 event was boosted back to the initial W^+W^- lab frame. All particles having an absolute polar angle with the beam direction smaller than 11^o were removed from the event. The same generated WPHACT events were used for the construction of both the data MLBZ's and Monte Carlo MLBZ's in order to increase the correlation between both emulated samples to about 31%. This correlation was taken into account when quoting the statistical uncertainty on the systematic shift in m_W or Γ_W between data and Monte Carlo MLBZ's.

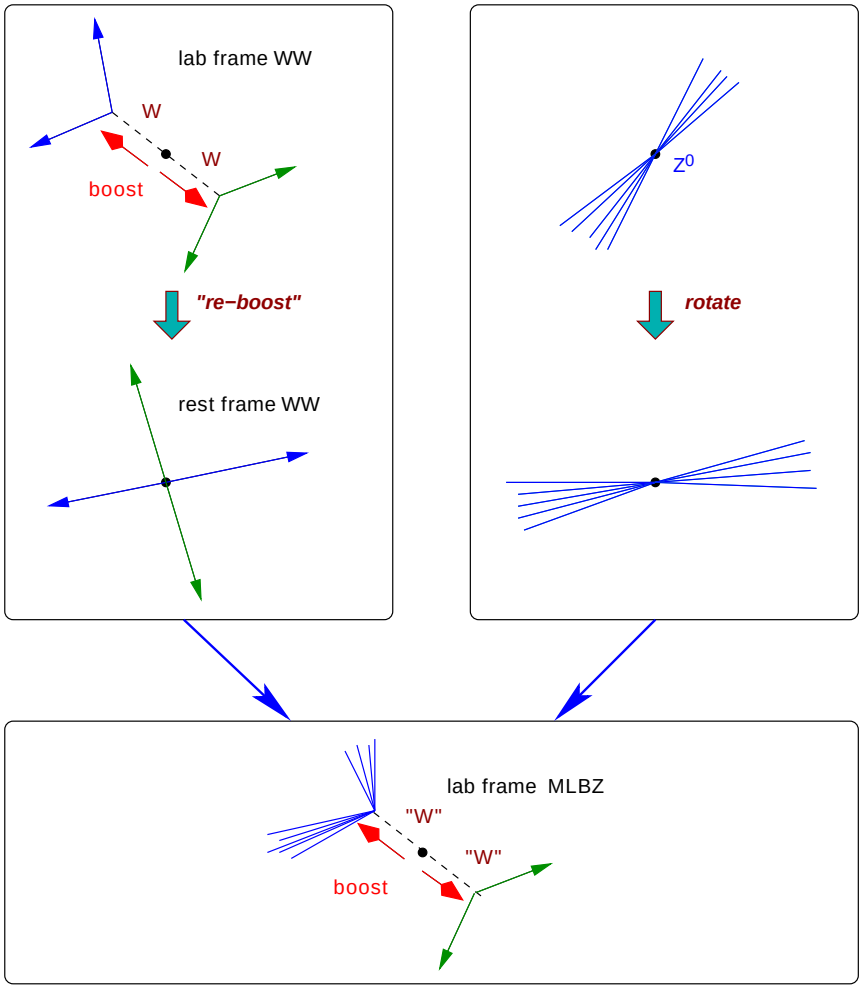

Figure 6.4: *Illustration of the mixing and boosting procedure within the MLBZ method.*

Compared to [77] this procedure includes besides all fragmentation effects, also the W width, Initial State Radiation and angular features of a real W^+W^- event. The influence of systematic effects in the reconstruction or simulation of W^+W^- events that are fully covered with the difference between the inferred values of m_W or Γ_W from data and Monte Carlo MLBZ's, are the following:

- Bose-Einstein Correlations between identical bosons arising from the decay of the same W boson;
- Colour Reconnection effects inside each hadronic W boson decay;
- the hard and soft gluon radiation;
- fragmentation;
- the jet energy scale at 45 GeV.

Those which are only partly covered are:

- non-linearity in the jet energy response;
- track density effects in track or energy flow reconstruction.

Obviously effects from Bose-Einstein Correlations between particles from the decay of different W bosons and effects from Colour Reconnection cannot be studied with the MLBZ method. Further comments on the coverage of the method are formulated in [77].

Results concerning $\mathbf{m_W}$ and $\mathbf{\Gamma_W}$

The MLBZ method was used to create emulated W^+W^- event samples at two different centre-of-mass energies, $\sqrt{s} \sim 189$ GeV and 206.5 GeV. The Z^0 events were selected from data recorded during the calibration runs of the year 1998 or from the corresponding Monte Carlo samples generated with KK2f and fragmented with the PYTHIA, HERWIG or ARIADNE model. Values for the m_W and Γ_W estimators were determined for each sample, and a comparison between them was made in Table 6.1. The inferred values of m_W obtained with different models agree well with each other and there is a good agreement between simulation and real data. For the Γ_W determination two standard deviations separated the PYTHIA result and the data. The absolute value of this shift was about equal in size for the ARIADNE model, but for the HERWIG model the shift with data was twice as large.

Verifications of the reliability of the method

The MLBZ method aims to produce a large Monte Carlo or real data sample of 'fake' W^+W^- events. It is known however that the MLBZ events will never reflect the true W^+W^- events with infinite precision. For example the particle multiplicity in a jet arising from a Z^0 or $W^{\pm}$ decay is on average different. In Figure 6.5 the value of m_W inferred from Monte Carlo MLBZ's and Monte Carlo W^+W^- events, is shown as a function of several event observables. Overall, the shape of the observed tendency as a function of $y_{4\leftarrow 5}$ is in rather

good agreement between emulated MLBZ events and generated W^+W^- events. This indicates that the difference in gluon radiation between a Z^0 jet and a $W^\pm$ jet was well treated in the mixing and boosting procedure. Deviations are observed where they were expected, for example as a function of the charged particle multiplicity. At $\sqrt{s}$ = 200 GeV the inclusive shift was $m_W^{MLBZ} - m_W^{WW}$ = -28.9 $\pm$ 7.1 MeV/c^2. For the W width this was estimated at a centre-of-mass energy of 206.5 GeV, resulting in $\Gamma_W^{MLBZ} - \Gamma_W^{WW}$ = -5.7 $\pm$ 11.7 MeV/c^2.

In order to evaluate the reliability of the method for the estimation of systematic uncertainties in the determination of the mass and width of the W boson, it was important to verify that the expected shifts in m_W or Γ_W between different fragmentation models determined from the true W^+W^- Monte Carlo were in agreement with the ones from the MLBZ samples. The results mentioned in Table 6.1 confirm this hypothesis to some extend, although the expected shift was very small or even compatible with zero. The expected shifts on m_W estimated from the true W^+W^- Monte Carlo samples were on average larger than the ones observed from the MLBZ samples. For the Γ_W the tendency was different, large shifts were observed with the MLBZ samples, while the corresponding shifts with the true W^+W^- samples were compatible with zero. The statistical significance of this test was however small. To show that also large shifts can be reproduced, the difference between the expected bias on the m_W^{std} estimator and the one on the m_W^{cone} estimator was calculated. Table 6.2 indicates that when using the true W^+W^- Monte Carlo samples a value around 270 MeV/c^2 is predicted. At the same centre-of-mass energy MLBZ's were constructed from Z^0 Monte Carlo simulation applying the same fragmentation model. A value around 320 MeV/c^2 was found

model	$\sqrt{s}$ GeV	Δm_W MeV/c^2	$\Delta\Gamma_W$ MeV/c^2
MLBZ			
PYTHIA-HERWIG	188.6	8.2 $\pm$ 6.3	28.2 $\pm$ 13.5
PYTHIA-ARIADNE	188.6	-1.8 $\pm$ 6.3	-0.7 $\pm$ 14.0
PYTHIA-HERWIG	206.5	3.6 $\pm$ 5.0	27.3 $\pm$ 10.7
PYTHIA-ARIADNE	206.5	4.3 $\pm$ 4.9	3.7 $\pm$ 10.5
data-PYTHIA	206.5	-7.9 $\pm$ 4.9	20.1 $\pm$ 10.5
data-HERWIG	206.5	-4.3 $\pm$ 4.9	47.4 $\pm$ 10.6
data-ARIADNE	206.5	-3.6 $\pm$ 4.9	23.8 $\pm$ 10.5
WPHACT			
PYTHIA-HERWIG	188.6	15.3 $\pm$ 6.8	1.7 $\pm$ 13.7
PYTHIA-ARIADNE	188.6	10.0 $\pm$ 6.8	-4.3 $\pm$ 13.6
PYTHIA-HERWIG	206.5	-0.6 $\pm$ 8.6	3.1 $\pm$ 16.5
PYTHIA-ARIADNE	206.5	23.4 $\pm$ 8.6	3.4 $\pm$ 16.8

Table 6.1: *Overview of the results obtained with the MLBZ method. In the top part a comparison is made between the estimators using MLBZ events created with Z^0's from different Monte Carlo simulation or from the real data. In the bottom part the same comparisons are made with true WPHACT generated simulation.*

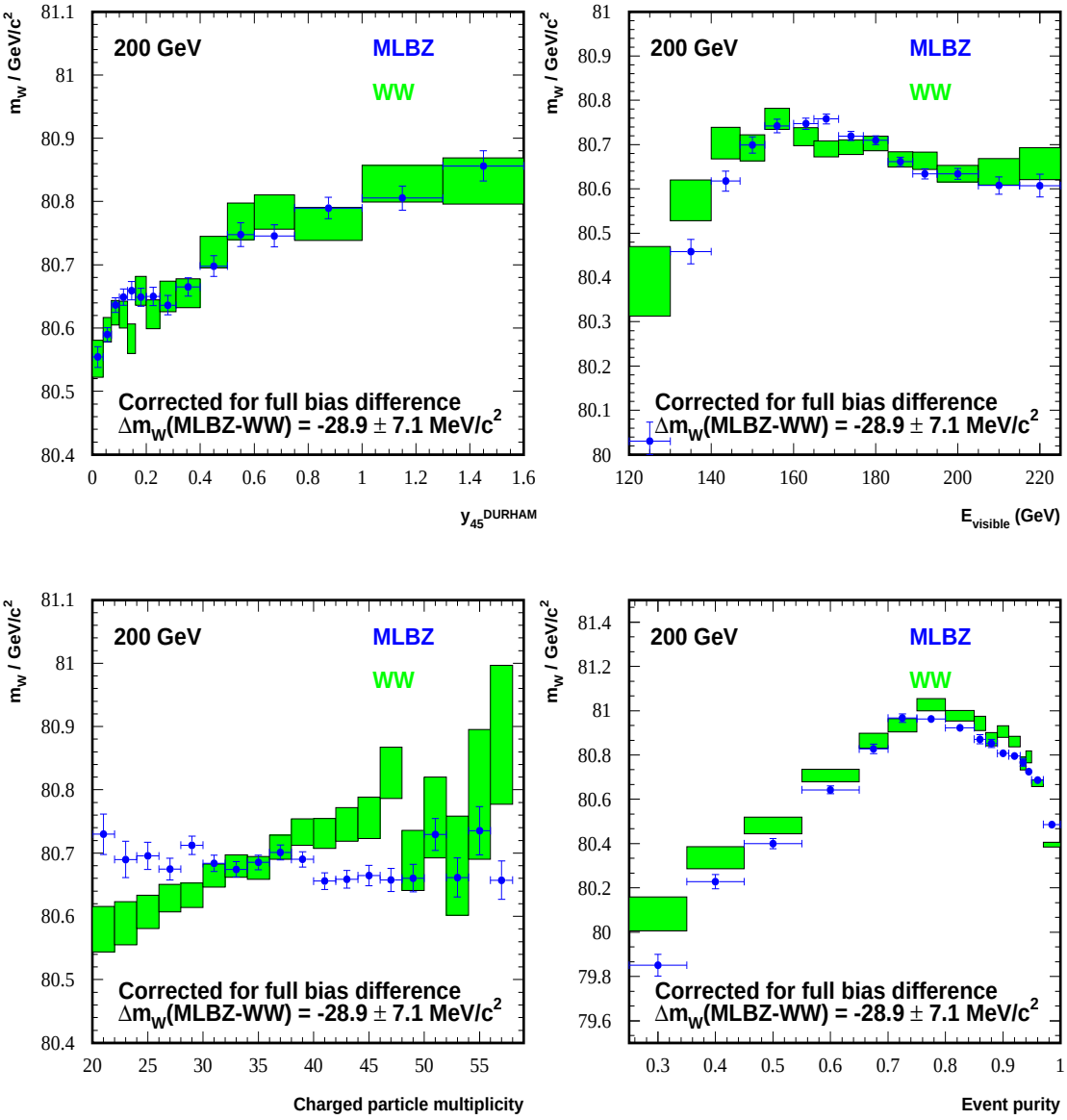

Figure 6.5: *Inferred value of m_W as a function of several event observables. A comparison is made between results obtained with true W^+W^- Monte Carlo (boxes) and MLBZ Monte Carlo (dots) at a centre-of-mass energy of 200 GeV. The MLBZ results were scaled to correct for the inclusive shift between both results as indicated in the plots.*

model	$\sqrt{s}$	$\Delta[m_W^{std} - m_W^{cone}]$ MeV/c^2
MLBZ PYTHIA	206.5	323.4 $\pm$ 5.1
MLBZ HERWIG	206.5	318.5 $\pm$ 5.3
MLBZ ARIADNE	206.5	327.2 $\pm$ 5.3
MLBZ data	206.5	329.1 $\pm$ 5.1
WW PYTHIA	206.5	268.7 $\pm$ 4.3

Table 6.2: *Overview of the results obtained with the MLBZ method. The $m_W^{std} - m_W^{cone}$ observable is estimated with MLBZ events created with Z^0's from different Monte Carlo simulation or from the real data. The bottom line reflects the value obtained with true WPHACT generated simulation fragmented with PYTHIA.*

for the MLBZ difference. Therefore it can be concluded that the MLBZ method reproduces shifts of the order of 300 MeV/c^2 with a 15% uncertainty. Because the expected systematic uncertainties on the m_W and Γ_W estimators are one order of magnitude smaller than 300 MeV/c^2, the method can easily be used.

A similar cross check was performed by changing the value of Λ_{QCD} in the PYTHIA fragmentation model with about 10 standard deviations up to 0.5 and downwards to 0.1. Within the statistical accuracy of the test, the behavior of the estimated m_W versus Λ_{QCD} was equal when using MLBZ or true W^+W^- events.

Conclusions

The MLBZ method initiated in [77] was extended in a way that reliable systematic uncertainties can be studied on both the m_W and the Γ_W estimators. The obtained results indicate that the m_W estimator is not sensitive to residual discrepancies in jet reconstruction between real data and the PYTHIA fragmentation model used in the Monte Carlo algorithms. A systematic uncertainty of 8 MeV/c^2 was quoted. For the determination of the W width however, some difference was found resulting in a systematic uncertainty of 20 MeV/c^2. These numbers are quoted in Table 6.1 when estimating the difference between the real data and the PYTHIA simulation with the MLBZ emulated events. The intrinsic uncertainties within the MLBZ method studied in [77] were small compared to those values.

6.3.3 Aspect ratio

A possible source of angular distortion in DELPHI was the uncertainty on the aspect ratio of the detector defined as its length to width ratio. The detector was aligned relative to the vertex detector, the largest uncertainty being the radius of this detector which was known to a precision of $\pm 0.1\%$. When this ratio is changed the momenta $\vec{p}_i$ of all particles i will systematically change accordingly:

$$p_{z,i}^{new} = p_{z,i} \cdot [1 + \delta] \tag{6.10}$$

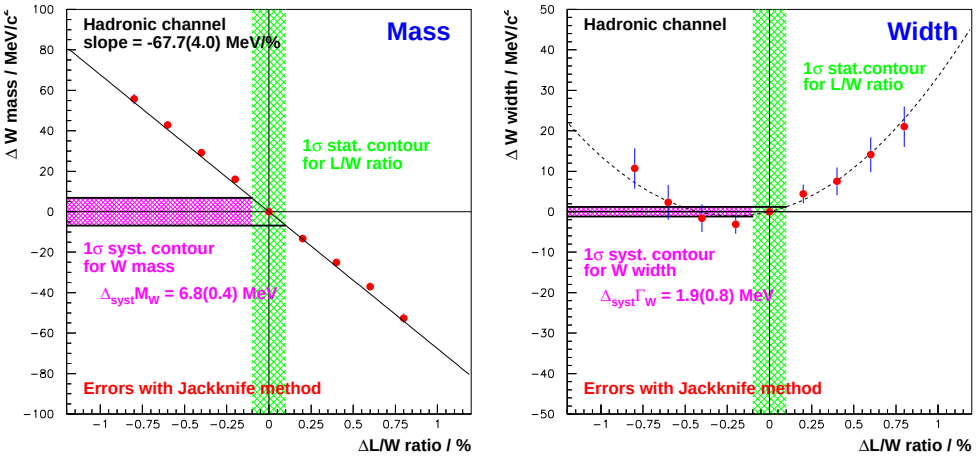

(a) (b)

Figure 6.6: *Monte Carlo determined relation between a deviation in the length to width ratio of the detector (δ) and a deviation from the nominal bias of both m_W and Γ_W estimators.*

where δ is a relative change of the length of the detector along the beam pipe or similarly a relative change in the aspect ratio of the detector. Similarly the width of the detector could have been changed. After applying these shifts on the momenta, for each particle the energy was recalculated assuming that the mass of the particle is invariant under this scaling procedure. Throughout this study the background was neglected, which is a good approximation. In Figures 6.6(a) and 6.6(b) the relation between a systematic deviation of the length to width ratio of the detector, δ, and a deviation from the nominal bias of the m_W and Γ_W estimators are shown. The correlation between the measured points was taken into account with the Jackknife method. When fitting the behavior with a suitable polynomial the following systematic uncertainties were found:

$$\begin{aligned} \Delta m_W &= 6.8 \pm 0.4 \quad \mathrm{MeV/c^2} \\ \Delta \Gamma_W &= 1.9 \pm 0.8 \quad \mathrm{MeV/c^2}. \end{aligned} \tag{6.11}$$

In the Figures 6.6(a) and 6.6(b) the possible statistical shift in the length to width ratio was made artificially much larger than expected in order to be able to interpolated to the value of $\pm 0.1\%$. It was found however that the statistical uncertainty on the difference

$$m_W(\delta = 0) - m_W(\delta = \epsilon) \tag{6.12}$$

increases linearly with ϵ, with a slope of the same order of magnitude as the difference itself increased with ϵ. Therefore it was concluded that no extra information could be extracted about this systematic effect on m_W or Γ_W when making ϵ even larger.

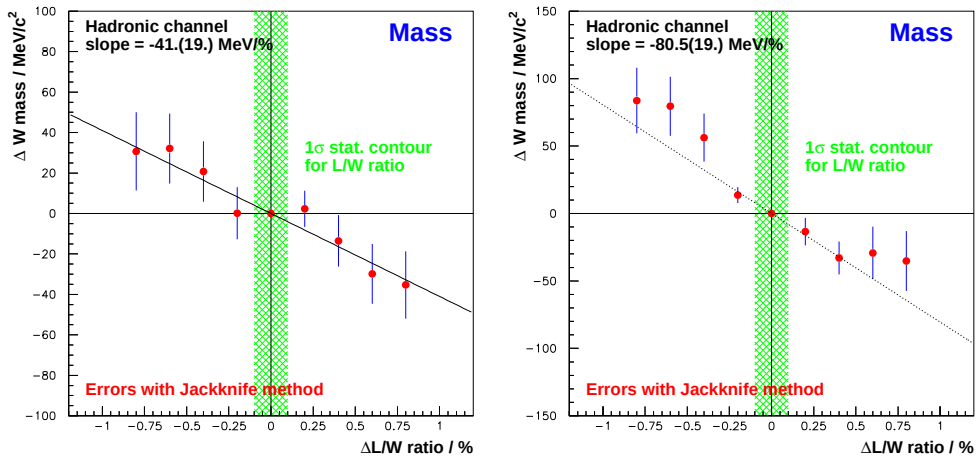

(a) (b)

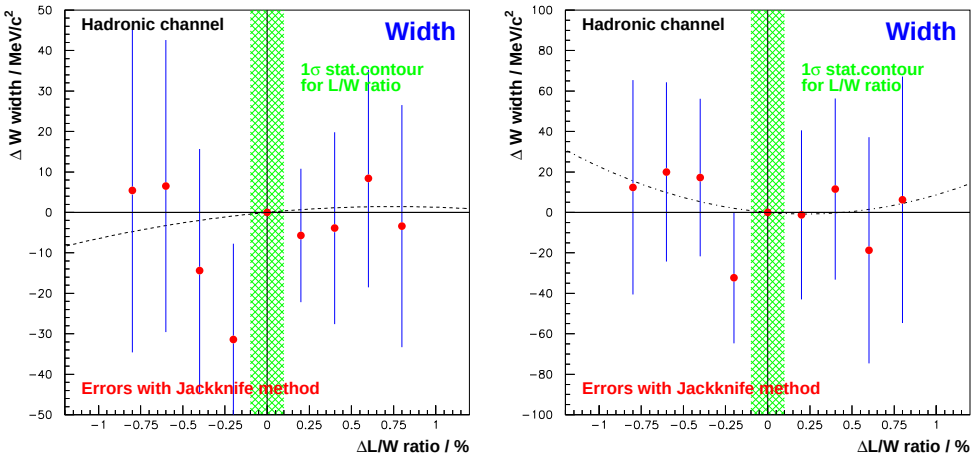

(c) (d)

Figure 6.7: *Relation between a deviation in the length to width ratio of the detector (δ) and a deviation from the nominal inferred value of both m_W and Γ_W estimators, determined with the real data samples at $\sqrt{s} \sim 189$ and 200 GeV. Plots (a) and (c) reflect the behavior at $\sqrt{s} \sim 189$ GeV, while plots (b) and (d) are constructed with data recorded at $\sqrt{s} \sim 200$ GeV.*

As a cross check it was verified that the inferred values of the m_W or Γ_W estimators from the real data behaved in a similar way versus a change in δ. In Figures 6.7(a), 6.7(b), 6.7(c) and 6.7(d) this is confirmed for the data collected at centre-of-mass energies of $\sqrt{s} \sim 189$ and 200 GeV. From the data samples themselves it was found that the systematic effect calculated with a value for δ of 0.1%, increases with the centre-of-mass energy. As this systematic uncertainty was small compared to others, no further studies were performed towards this non-invariant behavior and the values denoted in 6.11 were quoted for all centre-of-mass energies.

6.3.4 Non-linearity of energy scale

The studies at the Z^0 peak performed in section 4.4 and shown in Figure 4.4, were done with $Z^0 \rightarrow q\bar{q}$ events which have a 2 jet topology. Therefore the energy of those jets was always around 45 GeV. It can however be that the efficiency of the detector description or the energy flow reconstruction is not invariant when the jet energy is different from 45 GeV. The dependence of the energy calibration as a function of the jet energy was checked using low energy jets from $Z^0 \rightarrow q\bar{q} + gluon$ events at the Z^0 peak and high energy jets from radiative Z^0's at higher centre-of-mass energies. The relevant energy range for jets produced in W^+W^- events is between 25 and 75 GeV. It was found that the non-linearity of the energy response observed in the data is well described by the Monte Carlo. A 1% change per 50 GeV in the slope of the ratio of the energy flow reconstruction efficiency between the data and Monte Carlo, was used to calculate a systematic uncertainty. For jet energies of 70 GeV a scaling of -0.5% applied, while the scaling was +0.5% for those at 20 GeV. The scaling for intermediate values was obtained by a linear interpolation. Table 6.3 summarizes the shifts induced on the bias of the m_W and Γ_W estimators when applying this scaling. This systematic uncertainty appears to be dependent on the centre-of-mass energy.

$\sqrt{s}$ GeV	Δm_W MeV/c^2	$\Delta \Gamma_W$ MeV/c^2
182.7	-6.0 $\pm$ 4.0	-4.7 $\pm$ 9.3
188.6	-6.8 $\pm$ 3.0	-5.8 $\pm$ 6.0
199.5	-8.4 $\pm$ 2.8	-8.1 $\pm$ 6.7
208.0	-9.1 $\pm$ 3.2	-11.2 $\pm$ 9.0

Table 6.3: *Centre-of-mass energy dependence of the shift 'Δ=nominal-test' induced by a discrepancy in the non-linear detector response between data and Monte Carlo, as described in the text.*

6.4 Background description

In was discussed in section 3.2.4 that the predicted cross-section of the $Z^0 \rightarrow q\bar{q}(\gamma)$ process is in rather good agreement with its measurement. The background level was changed by

$\pm 10\%$ in the simulation, which easily covers the expected uncertainty in the accepted cross-section after the applied event selection. The influence on the bias of the m_W estimator was relatively small. Ranging from a value of 29 MeV/c^2 at $\sqrt{s} \sim 183$ GeV and 13 MeV/c^2 at 189 GeV to values below 4 MeV/c^2 around 206.5 GeV. An effect of about 40 MeV/c^2 on the bias of the Γ_W estimator was observed and found to be invariant with the centre-of-mass energy.

6.5 The LEP beam

In the construction of the events ideogram the information on the initial state was used in the kinematic fit. The energy of the initial leptons was assumed to be known with infinite precision and for the real data its value was provided by dedicated measurements (cfr. section 2.2). In the analyses all relevant weights were determined by Monte Carlo simulation and parametrized as a continuous function of the centre-of-mass energy. Therefore the most relevant systematic uncertainty on the measurement of the W mass is induced by the statistical limited precision on the beam energy determined by LEP. Due to the direct constraint between the fitted W boson mass of the event and the beam energy in the kinematic fit, the relative uncertainty on both quantities is equal:

$$\frac{\Delta m_{\text{fit}}}{m_{\text{fit}}} = \frac{\Delta E_{\text{beam}}}{E_{\text{beam}}} \, . \tag{6.13}$$

For the Γ_W measurement the differential evolution of Γ_W as a function of m_W had to be used, resulting in the relation:

$$\Delta\Gamma_{\text{fit}} = \frac{\partial\Gamma_W}{\partial m_W} \cdot \frac{\Delta E_{\text{beam}}}{E_{\text{beam}}} \cdot m_W \, . \tag{6.14}$$

The statistical uncertainty on E_{beam} had a small impact on the central value of the inferred Γ_W. A value of 5 MeV/c^2 was taken for $\Delta\Gamma_{\text{fit}}$ at all centre-of-mass energies and assumed to be correlated between different years.

Table 6.4 summarizes the systematic uncertainties due to the beam energy. The natural spread $\sigma_{\sqrt{s}}$ in the beam energy mentioned in Table 2.2 introduces an extra smearing of $m_W \cdot \sigma_{\sqrt{s}}/\sqrt{s}$ in the fitted m_W and introduces a systematic bias for the Γ_W measurement. Fortunately for the W mass this effect scales with the number of selected events and was therefore negligibly small. The bias on the W width was negligible and therefore not applied.

6.6 Uncertainties on the hard process

Theoretical uncertainties on the measurement of the W boson mass related to electroweak corrections in the evaluation of the matrix elements, are discussed in [78] for idealized event selections and simple m_W-fitting procedures. For the real m_W and Γ_W estimators of interest similar studies were performed and discussed in this section.

$\sqrt{s}$ GeV	Δm_W MeV/c^2	$\Delta\Gamma_W$ MeV/c^2
182.65	22.0	5.0
188.63	17.0	5.0
191.58	17.6	5.0
195.51	17.2	5.0
199.51	16.9	5.0
201.64	16.7	5.0
205.8	19.5	5.0
206.3 (TPC-S6)	19.5	5.0

Table 6.4: *Centre-of-mass energy dependence of the systematic uncertainty due to the imprecise knowledge of the LEP beam energy.*

Three special exclusive event samples were produced of the $(s\bar{c})(u\bar{d})$ flavoured final state at a centre-of-mass energy of about 189 GeV. Each of them included the higher order radiative effects differently. The first so-called WandY setup used WPHACT as an event generator with the electroweak corrections implemented in the matrix elements via YFSWW reweighting. Hence this reflects the nominal four-fermion Monte Carlo simulator in the DELPHI experiment where the Leading Pole Approximation scheme a (LPA$_a$) was used for the calculation of the $\mathcal{O}(\alpha)$ corrections. RacoonWW was used to create the second sample. The third sample was generated directly with YFSWW using the LPA$_b$ scheme for the matrix element evaluation. The analyses were performed on all three samples.

In Table 6.5 the shifts induced on the biases of the m_W and Γ_W estimators are indicated for different setups. Also shifts in these values from changes within the WandY framework were determined. The largest difference on both estimators was found in the direct comparison between the result obtained with the nominal WandY setup and the RacoonWW one. The WandY result cannot be directly compared with the YFSWW one which was mainly used to discuss the ambiguity in definition of the LPA implementation.

The comparison of WandY and RacoonWW is interesting because the two calculations differ in almost every aspect of the implementation of the Initial State Radiation, the Final State Radiation, the non-leading and non-factorisable corrections. The large shift between WandY and RacoonWW was splitted into two subclasses of events, those which were clustered into a 4 jet and into a 5 jet topology. The following results were obtained for the 4 jet events:

$$\begin{array}{lrcrcrl} \Delta m_W & (\mathrm{WandY} - \mathrm{RacoonWW}) & = & 27.7 & \pm & 6.3 & \mathrm{MeV/c^2} \\ \Delta\Gamma_W & (\mathrm{WandY} - \mathrm{RacoonWW}) & = & 53.4 & \pm & 12.7 & \mathrm{MeV/c^2} \end{array} \tag{6.15}$$

and for the 5 jet events:

$$\begin{array}{lrcrcrl} \Delta m_W & (\mathrm{WandY} - \mathrm{RacoonWW}) & = & 37.7 & \pm & 8.1 & \mathrm{MeV/c^2} \\ \Delta\Gamma_W & (\mathrm{WandY} - \mathrm{RacoonWW}) & = & 74.8 & \pm & 16.9 & \mathrm{MeV/c^2} \end{array} \tag{6.16}$$

where no significant difference was observed between both classes. The treatment of Initial State Radiation as discussed in section 5.3.3 reduced the inclusive effect on the W mass between WandY and RacoonWW from 40.5 $\pm$ 4.9 MeV/c^2 to the 31.4 $\pm$ 4.9 MeV/c^2 mentioned in Table 6.5. But no significant dependency of the effect as a function of the weight w_{isr} in Equation 5.16 was found. A clear understanding of this difference between both implementations of the radiative corrections has yet to emerge as these results are the first in their kind. In the semi-leptonic decay channel a similar study was performed [79], resulting in a difference between WandY and RacoonWW of -4.3 $\pm$ 5.1 MeV/c^2. Hence this channel is not influenced by large systematic uncertainties due to the implementation of the electroweak radiative corrections.

The effect of changing from LPA$_a$ to LPA$_b$ scheme can be estimated from the double difference:

$$\delta\mathrm{LPA_a} - \delta\mathrm{LPA_b} = (\mathrm{LPA_a}[\mathcal{O}(\alpha)] - \mathrm{LPA_a}[ISR]) - (\mathrm{LPA_b}[\mathcal{O}(\alpha)] - \mathrm{LPA_b}[ISR]) \quad (6.17)$$

where $[\mathcal{O}(\alpha)]$ uses the full LPA correction, while $[ISR]$ does not. The effect for both the mass and the width are:

$$\begin{array}{lrcrcl} \Delta m_W & (\delta\mathrm{LPA_a} - \delta\mathrm{LPA_b}) & = & 1.3 & \pm & 1. \quad \mathrm{MeV/c^2} \\ \Delta\Gamma_W & (\delta\mathrm{LPA_a} - \delta\mathrm{LPA_b}) & = & -1.6 & \pm & 1. \quad \mathrm{MeV/c^2} \end{array} \quad (6.18)$$

which is a negligible effect.

model	Δm_W MeV/c^2	$\Delta\Gamma_W$ MeV/c^2
WandY		
no weight	-10.1 $\pm$ 1.	-17.0 $\pm$ 1.
normal DPA weight	0.1 $\pm$ 1.	-0.1 $\pm$ 1.
DPA $\mathcal{O}(\alpha)$+interference	0. $\pm$ 0.	0. $\pm$ 0.
put $\lvert CC03_{K-C}\rvert$=1	-1.9 $\pm$ 1.	-0.4 $\pm$ 1.
$\mathcal{O}(\alpha^2) \rightarrow \mathcal{O}(\alpha^3)$ ISR	0. $\pm$ 1.	0. $\pm$ 1.
$\mathcal{O}(\alpha^2) \rightarrow \mathcal{O}(\alpha)$ ISR	-0.3 $\pm$ 1.	-0.7 $\pm$ 1.
RacoonWW		
no weight	31.4 $\pm$ 4.9	62.3 $\pm$ 10.0

Table 6.5: *Overview of the results obtained with the special $s\bar{c}u\bar{d}$ Monte Carlo samples for the study of electroweak radiative corrections generated at a centre-of-mass energy of about 189 GeV. All results are relative to those obtained in the third row, as Δ=(WandY DPA+interference)-(X). The uncertainties on the differences between correlated event samples are conservatively quoted as 1 MeV/c^2.*

The nominal evaluation of the event weight within the WandY setup as explained in section 3.2.3 included the DPA calculation up to $\mathcal{O}(\alpha)$ and the interference term between

the $CC03$ part and the rest. In Table 6.5 the shifts are indicated when these weights were completely omitted or when not taking into account the interference part. Also results were determined when not using the Khoze-Chapovsky ansatz for the Coulomb screening [41] or when turning off the LPA_a correction. The effect of going to $\mathcal{O}(\alpha^3)$ or $\mathcal{O}(\alpha)$ calculations for the Initial State Radiation instead of $\mathcal{O}(\alpha^2)$ was negligible.

Because all relevant changes within the WandY setup resulted in changes on m_W and Γ_W below 2 MeV/c^2, the systematic uncertainty from radiative corrections on both the m_W and the Γ_W estimator were quoted as the difference between the WandY and RacoonWW implementation.

6.7 Fragmentation of primary quarks into colour singlet particles

In the direct measurements of the W boson properties presented, the kinematics of the detected particles in the final state were used on an event-by-event basis to infer information about the primary fermions from the W boson decays. The fragmentation of the primary partons into colour singlet hadrons is part of the transition between both information spaces, the multi-dimensional kinematic space of the detected particles and the kinematic space of the fermions from the W boson decays. The fragmentation process is however not calculable from first principles (see sections 3.3 and 3.4) and therefore modelizations of the effect have to be used in the Monte Carlo algorithms.

All these systematic effects should be covered with the MLBZ study (cfr. section 6.3.2). However in this section a traditional approach will be applied and the maximum effect of the two methods will be quoted as systematic uncertainty. Systematic shifts in the estimators bias were evaluated when replacing the PYTHIA model by others, like the ARIADNE or HERWIG model. Also effects on the m_W and Γ_W estimators were investigated for variations of model parameters within the nominal fragmentation model, namely the PYTHIA model. The effect of introducing Bose-Einstein Correlations in the PYTHIA framework with the LUBOEI algorithm was determined.

6.7.1 Fragmentation models

Three different fragmentation models were used to hadronize the quarks simulated with the WPHACT generator, the PYTHIA, ARIADNE and HERWIG model. The first one was the nominal model used throughout this thesis, because its performance in describing the event shape and single particle spectra of the LEP1 Z^0 data was better. The systematic shifts between the three models are mentioned in the bottom part of Table 6.1 for two centre-of-mass energies, $\sqrt{s} \sim 189$ and 206.5 GeV.

For the W width all deviations from the nominal bias estimated with PYTHIA were found to be compatible with zero. Assuming that the shifts between the models are invariant with $\sqrt{s}$, the m_W estimator is influenced by about 15 MeV/c^2 when changing PYTHIA for the ARIADNE fragmentation model. Studies with the MLBZ method indicate however that the m_W estimator is not sensitive to the fragmentation model applied in the Monte Carlo, while the inverse conclusion is true for the Γ_W estimator.

Therefore the systematic uncertainty quoted on the measurement of m_W was 15 MeV/c^2, while 20 MeV/c^2 for the W width estimation. These values can be extracted from Table 6.1.

In the framework of LEP WW Workshops common event samples were created by the ALEPH Collaboration using the PYTHIA, ARIADNE and HERWIG fragmentation schemes at a centre-of-mass energy of about 189 GeV. The results obtained for m_W from those Monte Carlo samples are:

$$\begin{array}{lrcrcll} \Delta m_W & (\mathrm{PYTHIA} - \mathrm{HERWIG}) & = & -16.4 & \pm & 8.6 & \mathrm{MeV/c^2} \\ \Delta m_W & (\mathrm{PYTHIA} - \mathrm{ARIADNE}) & = & -0.4 & \pm & 9.5 & \mathrm{MeV/c^2} \quad . \end{array} \tag{6.19}$$

The shift in m_W between the PYTHIA and HERWIG model determined from those ALEPH samples was different from the one indicated in Table 6.1 for DELPHI's own samples. The absolute difference between the ALEPH and the DELPHI estimate was 31.7 $\pm$ 11.0 MeV/c^2. Because each experiment used its own tuned values for the model parameters in PYTHIA and HERWIG, it seems that the m_W estimator is sensitive to variations in those model parameters.

6.7.2 Uncertainty on Monte Carlo tuned model parameters

Within the PYTHIA fragmentation model the most important model parameters were tuned [53] to obtain a good comparison of event shape and single particle spectra between the tuned Monte Carlo model and the LEP1 Z^0 data. When estimating the sensitivity of the model parameters to the m_W and Γ_W estimators, the statistical uncertainty of the tuned model parameters must be translated into systematic shifts on the m_W and Γ_W estimators. The values of four essential parameters in PYTHIA were individually changed by a significant amount of about 10 standard deviations. A linear dependency between the model parameters and the relevant estimators was assumed. Via an interpolation of the effect between the extreme values, more realistic statistical deviations of the parameters value were obtained. These studies were performed before the generators including electroweak radiative corrections with the DPA formalism became available. The EXCALIBUR event generator [81] was used instead, neglecting all background contributions. Therefore the overall bias on the both m_W and Γ_W estimators should not be compared with those determined in chapter 5.

In Figure 6.8 the linear behavior is confirmed. Roughly an equal sensitivity of m_W on each of these four model parameters was found. This was however not the case for the Γ_W determination, shown in Figure 6.9, where the parameter Λ_{qcd} has one order of magnitude more effect on Γ_W compared the other three. After interpolating the observations to a one standard deviation in the value of the model parameter, the systematic shifts quoted in Table 6.6 were obtained.

The results in Table 6.6 agree with the observations in the MLBZ study, where the difference in m_W between data and Monte Carlo MLBZ's was negligible. Because the Monte Carlo simulation of W^+W^- events used fragmentation model parameters tuned on the Z^0 data, the sizable difference in Γ_W between data and Monte Carlo MLBZ's in Table 6.1 could be understood by the observation that the inferred value of Γ_W is very sensitive to Λ_{qcd}.

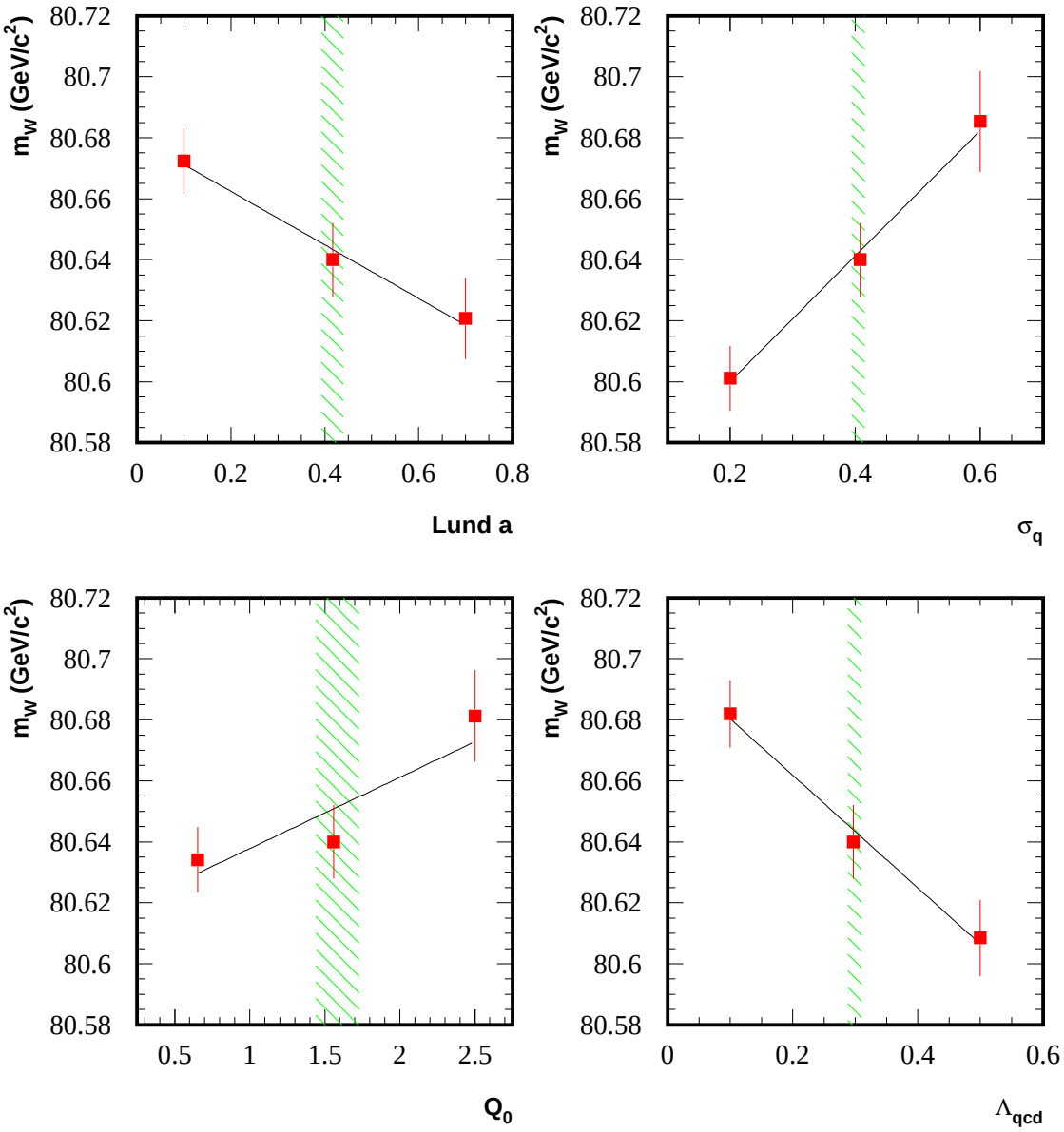

Figure 6.8: *Influence of the PYTHIA model parameters on the inferred value of m_W. Four relevant model parameters were individually changed without taking into account the correlation between them. The green band reflects the estimated statistical uncertainty on the tuned model parameter values. As in [80] the EXCALIBUR generator [81] was used for this study.*

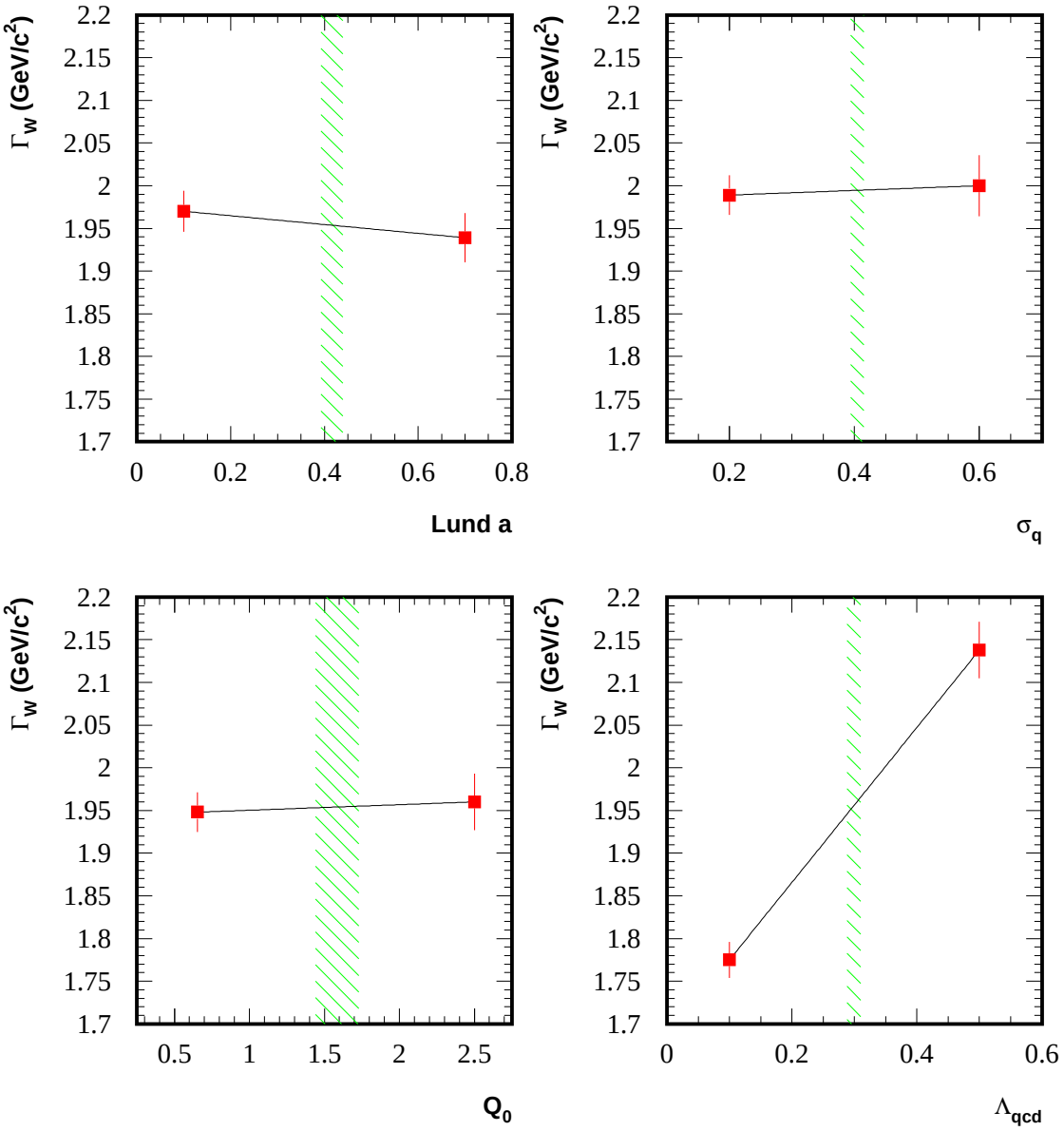

Figure 6.9: *Influence of the PYTHIA model parameters on the inferred value of* Γ_W*. Four relevant model parameters were individually changed without taking into account the correlation between them. The green band reflects the estimated statistical uncertainty on the tuned model parameters value. As in [80] the EXCALIBUR generator [81] was used for this study.*

model parameter	Stat.Unc. 1σ	Δm_W MeV/c^2	$\Delta\Gamma_W$ MeV/c^2
Lund a	0.023	2.0 ± 0.6	1.2 ± 1.5
σ_q	0.011	2.3 ± 0.4	0.3 ± 1.1
Q_0	0.150	3.8 ± 1.0	1.0 ± 3.4
Λ_{qcd}	0.011	2.0 ± 0.3	10.0 ± 1.1

Table 6.6: *Effect on the W mass and width determination of a change in the value of some relevant model parameters by one standard deviation. The statistical uncertainties were evaluated from the uncertainty on the slope in the linear fit.*

6.7.3 Bose-Einstein Correlations

The hypothesis used throughout the analyses that both W bosons decay and hadronize independently was only an approximation. The effect of Bose-Einstein Correlations discussed in section 3.5.1 is known to exist between the decay products of one W boson. Up to now, there is no theoretical motivation why Bose-Einstein Correlations could not exist between the decay products of different W bosons. In the nominal Monte Carlo event samples produced to design the m_W and Γ_W analyses in chapter 5, the effect of Bose-Einstein Correlations on the kinematic structure of the event was neglected, denoted by 'BEO' (Bose-Einstein Off). To estimate the value of the residual biases the effect could induce, the LUBOEI model (version BE_{32}) was used within the PYTHIA fragmentation program.

Assuming no correlation between QCD and BEC model parameters

In a first study the standard DELPHI tuned values of the LUBOEI model parameters $\lambda_{\rm BE}$ and $r_{\rm BE}$, mentioned in section 3.5.1, were used. This local reweighting algorithm was applied on the nominal WPHACT events between identical bosons from the decay of the same W boson, denoted by 'BEI' (Bose-Einstein Inside), or between all identical bosons in the final state of the events, denoted by 'BEA' (Bose-Einstein All). The analyses were performed again on those new samples and the effect on the m_W and Γ_W estimators are shown in Figure 6.10 for several centre-of-mass energies. A fit assuming an invariant effect versus $\sqrt{s}$ combined the information. These combined results are quoted on the figures. The χ^2/ndf of this fit confirmed the invariance of the effect. For the Γ_W estimator the correlation between the events in the BEA and BEO scenario was larger compared to those shown in Figure 6.10, and the χ^2/ndf of the $\sqrt{s}$ invariant fit was about 1.2.

For the standard estimators the naive hypothesis that the BEI effect should not induce residual biases was confirmed. When including the BEA effect in the W^+W^- events however large systematic shifts were obtained of about 40 MeV/c^2 for the m_W estimator when comparing with the BEI hypothesis. The bias of the Γ_W estimator was stable when including Bose-Einstein Correlations, at least within the obtained statistical uncertainties on the shifts. In previous analyses [82] it was demonstrated that these shifts are very sensitive to the input values of $\lambda_{\rm BE}$ and $r_{\rm BE}$, but rather insensitive to the version of the LUBOEI model used.

In the framework of common LEP Workshops on the topic of WW physics, event samples were generated by the ALEPH Collaboration using the KORALW generator and were reconstructed in the DELPHI detector. A shift of Δm_W(BEI-BEA) = 27 $\pm$ 7 MeV/c^2 was obtained, compatible with the DELPHI internal results. It was found that the m_W analyses of all LEP experiments are equally sensitive to the effect of Bose-Einstein Correlations.

It was discussed in section 3.5.1 that at least part of the LEP2 data prefers the hypothesis of no Bose-Einstein Correlations between the decay products of both W bosons. Therefore the 40 MeV/c^2 effect on m_W can be reduced to a more realistic 10 MeV/c^2 systematic uncertainty, as the data preferred fraction of the strength predicted by LUBOEI is only 3$\pm$18%. The DELPHI Collaboration however presented recently new results [56] which indicate that the data disfavors the BEI model by about 3σ, while only 1.5σ deviate the data from the LUBOEI BEA model. A new LEP combination would prefer a fraction of $\sim$25% of the full strength predicted by the LUBOEI BEA model. Hence the value of 10 MeV/c^2 for the systematic uncertainty on m_W is still realistic.

All global reweighting models gave systematic shifts compatible with zero.

Taking into account the correlation between QCD and BEC model parameters

As the effect of including Bose-Einstein Correlations between all identical bosons in the final state was largely suppressed by the data measure of the correlation strength, the tuning of the model parameters describing the BEI effect becomes important. The results quoted above were determined by the implementation of the LUBOEI algorithm on top of the PYTHIA fragmentation model. Therefore the correlations between the parameters in both models were neglected. In was however shown in section 3.6 that those correlations are non-negligible. Event samples were produced with the WPHACT generator at a centre-of-mass energy of about 189 GeV and different fragmentations were performed:

- the standard DELPHI fragmentation using PYTHIA with the tuned values according to [53] (denoted by 'PY'), denoted by BEO in previous paragraph;
- the PYTHIA fragmentation using the tuned model parameters as indicated in the first and third column in Table 3.2 without the implementation of Bose-Einstein Correlations or $r_{\rm BE} = \lambda_{\rm BE} = 0$ (denoted by 'PY BEO');
- the combined PYTHIA and LUBOEI fragmentation using the tuned values from the same table (denoted by 'PY BEI').

The last two samples were created both with the model parameters from the global tuning using the Gaussian (denoted by 'G' - first column in Table 3.2) and exponential (denoted by 'E' - third column in Table 3.2) correlator $R_{32}(Q)$.

The residual biases on both the m_W and Γ_W estimator were evaluated and are summarized in Table 6.7. The bias of the m_W estimator was invariant for the change in PYTHIA model parameters from the standard values in [53] to the global tuned ones and also the implementation of LUBOEI on top of the DELPHI standard PYTHIA model parameters did not change its value (Figure 6.10). It was only when combining the effect of the LUBOEI implementation with the change in the PYTHIA model parameters according to the global

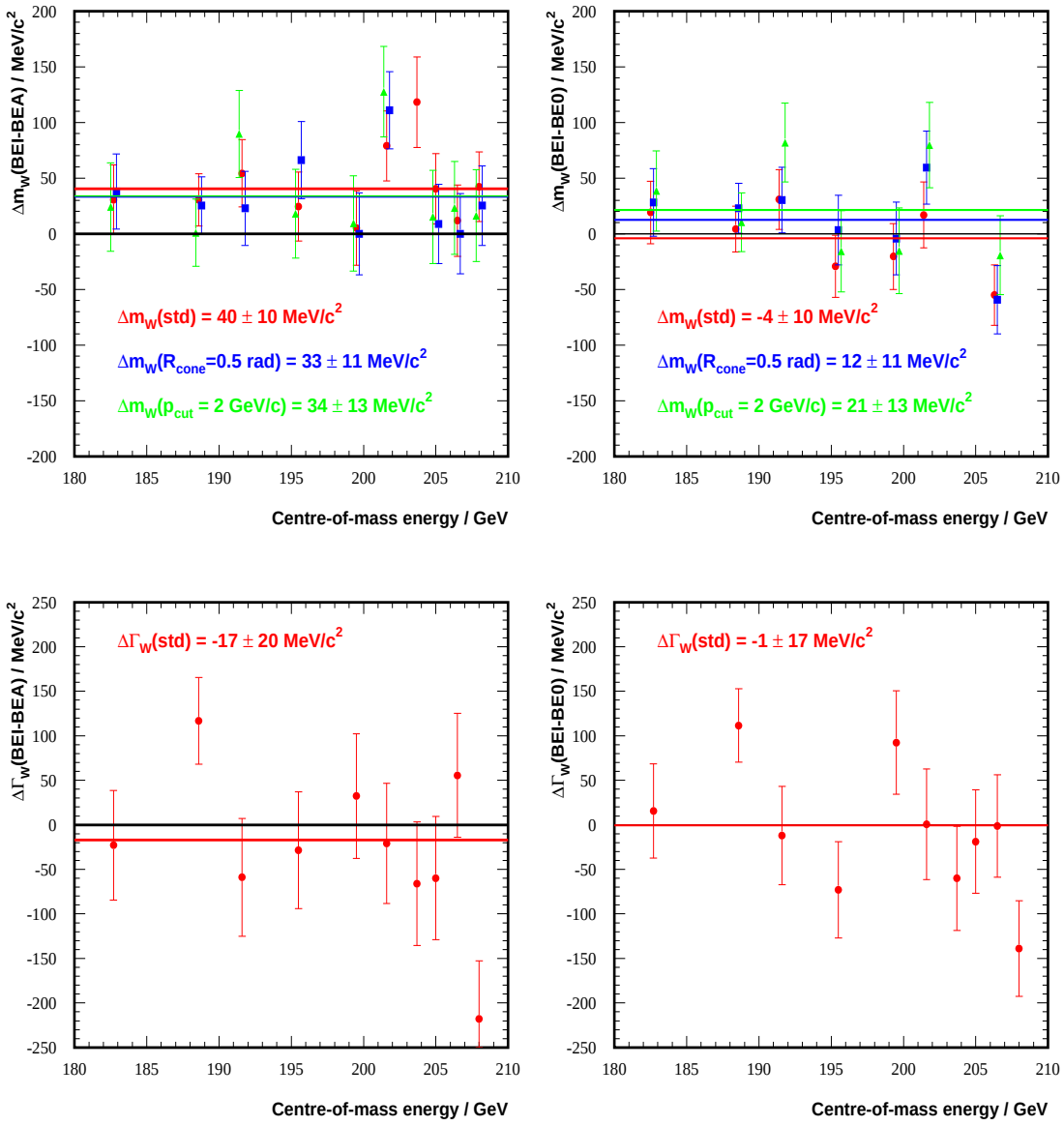

Figure 6.10: *Monte Carlo evaluation of the shift induced by Bose-Einstein Correlations on the biases of the m_W and Γ_W estimators as a function of the centre-of-mass energy $\sqrt{s}$. Results from a linear fit are shown, combining all information assuming that the effect is invariant with $\sqrt{s}$ in the relevant LEP2 energy range. The statistical uncertainty on the differences was estimated with the Jackknife method.*

tuning that some shift for m_W was observed. The change of the values of the PYTHIA model parameters from the [53] to the global tuned ones, did cause a significant shift on the bias on the Γ_W estimator.

model	Δm_W MeV/c^2	$\Delta\Gamma_W$ MeV/c^2
PY - PY BEO (G)	-0.3 $\pm$ 6.9	-19.7 $\pm$ 14.1
PY - PY BEO (E)	6.2 $\pm$ 6.9	-41.4 $\pm$ 14.2
PY BEO (G) - PY BEI (G)	28.3 $\pm$ 7.0	-27.4 $\pm$ 14.3
PY BEO (E) - PY BEI (E)	14.5 $\pm$ 7.3	-13.6 $\pm$ 14.4

Table 6.7: *Overview of the results obtained with the global tuning of the PYTHIA and LUBOEI model parameters. The Monte Carlo samples were created at a centre-of-mass energy of about 189 GeV. The statistical uncertainties were determined with the Jackknife method. The symbols are explained in the text.*

In section 3.6 it was demonstrated that the global tuned PYTHIA and LUBOEI model parameters perform at least equally well in describing event shape quantities compared to the separately tuned ones (section 3.5.1 and [53]). For the single particle spectra even better descriptions were obtained. It was also discussed that this data to Monte Carlo comparison of event shape, single and double particle distributions was at least equally good for both tunings for $Z^0 \rightarrow q\bar{q}$ events after a WW-like event selection. It must be mentioned that residual disagreements between inclusive or exclusive data and global tuned Monte Carlo distributions could be present, which are not observed when comparing data and Monte Carlo with the tuned parameters of [53]. However none of those were found.

This study illustrates that even when the effect of BEA becomes negligible due to its direct measurement, the effect of BEI could be large due to the correlations between the different model parameters. Therefore a systematic uncertainty on the m_W estimator should be quoted of 28 MeV/c^2, while 55 MeV/c^2 should be quoted for the Γ_W measurement. These values can be extracted from Table 6.7 as a linear sum of both the effect of changing the fragmentation model parameters and using the BEI LUBOEI model. The largest shift, observed with the Gaussian or exponential enhancement function in LUBOEI, is quoted.

Although these large effects, the MLBZ results indicate that the influence of BEI must be small, below 10 MeV/c^2 for m_W and below 20 MeV/c^2 for Γ_W. This could indicate that the LUBOEI model is inadequate to simulate the effect of Bose-Einstein Correlations between identical bosons in hadronic decaying W^+W^- events, therefore the MLBZ observations were taken as final systematic uncertainty on the estimators. Only the shift on the m_W and Γ_W estimators between the BEI and BEA LUBOEI models are quoted.

6.8 Summary

All relevant systematic uncertainties related to the detector and fragmentation simulation were studied, together with uncertainties in the calculation of the hard process. The only residual effect is the possibility of Colour Reconnection between the fragmentation products of both W bosons, which will be discussed in the next chapter. It was considered that all other possible effects which were not perfectly described in the Monte Carlo simulation, induce a negligible systematic uncertainty on the estimated W mass and width. Table 6.8 summarizes the absolute value of all studied systematic uncertainties, except for the one induced by the Colour Reconnection effect.

Systematic effect	m_W MeV/c^2	Γ_W MeV/c^2
Statistical uncertainty on the calibration	4	18
Jet reconstruction (MLBZ)	8	20
Aspect ratio of the detector	7	2
Non-linear energy scale	6-9	5-11
Radiative Corrections	31	62
Background	29-4	40
Fragmentation *	15	20
Bose-Einstein Correlation (BEA)	10	20
LEP beam energy scale	$\sim$20	5

Table 6.8: *Overview of all relevant systematic uncertainties on both the m_W and Γ_W estimators. The uncertainties marked with '*' are covered by the MLBZ method, but were conservatively quoted. For some systematic uncertainties the range is quoted from the lowest centre-of-mass energy to the highest ones.*

6.9 Correlation between systematic uncertainties

It was already mentioned in section 6.1 that the separation of the systematic uncertainty into several identified sources is non-trivial. The uncertainty arising from the jet reconstruction and the one from the modelization of the fragmentation process are highly correlated. In fact they could be determined by the same MLBZ method. In order to be conservative, both were treated separate and added quadratically. This will also be the case for the systematic uncertainties induced by the Bose-Einstein Correlations and the Colour Reconnection effect, which are both non perturbative fragmentation phenomena. The exact combination procedure of the data collected over all years will be discussed in chapter 8.

Chapter 7

Colour Reconnection

The effect of Colour Reconnection on the different m_W estimators and on the Γ_W estimator is discussed in this chapter. It was found that this effect could induce the largest systematic uncertainty on the m_W^{std} estimator, diluting completely the high statistical precision of the measurement. Therefore a complete chapter is devoted to its discussion. Several possibilities are proposed to reduce the total uncertainty on the inferred value of m_W. Results are presented for a measurement of the κ parameter used in the PYTHIA SK1 model of Colour Reconnection in $W^+W^- \to q\bar{q}'Q'\bar{Q}$ events at LEP2. The method is based on the observation that different m_W estimators have different sensitivity to the parametrized Colour Reconnection effect. Hence the difference between them contains information about κ, which could be optimally convoluted in the Bayesian m_W and Γ_W estimators.

7.1 The parametrized Colour Reconnection effect on the m_W and Γ_W determination

As mentioned in section 3.5.2 the effect of Colour Reconnection on the kinematic structure of a $W^+W^- \to q\bar{q}'Q'\bar{Q}$ event must be modeled. In each of the three fragmentation schemes used in this thesis, different phenomenological implementations exist of the effect. The PYTHIA implementation has the advantage compared to the ARIADNE and HERWIG ones, that the global scale of the effect can be tuned with a model parameter. None of these models are excluded by the data, hence the effect of all three on the W mass and width estimators must be studied.

Within the framework of the Lund string fragmentation implemented in PYTHIA the colour fields of both W boson strings can overlap in space-time. The event probability $\mathcal{P}_i$ to reconnect is related to the volume, $\mathcal{O}_i$, of the string overlap as in Equation 3.30. For simplicity only one reconnection per event was allowed. The constant model parameter κ is unknown and can only be tuned or measured from experimental data. This is the so-called SK1 model of Colour Reconnection. In their paper [57] the authors propose a value of κ around 0.66.

Within the DELPHI Collaboration, $W^+W^- \to q\bar{q}'Q'\bar{Q}$ events were generated with EXCALIBUR [80, 81] at centre-of-mass energies of 200 GeV and 206.7 GeV and fragmented with the DELPHI tuned version of PYTHIA [53]. The double resonant $Z^0Z^0 \to q\bar{q}Q\bar{Q}$

events which have a similar kinematic topology were treated as signal and were also subjected to the SK1 Monte Carlo algorithm. The event generators using the DPA formalism, like WPHACT, were still unavailable when those studies were performed, therefore the choice of EXCALIBUR to estimate the effect of Colour Reconnection. There is no indication that this swap between generators will change the results discussed in this chapter.

Each of the m_W estimators defined in chapter 5, m_W^{std}, $m_W^{p_{cut}}$ and m_W^{cone}, had to be calibrated. The slope of the linear calibration curve for the m_W estimators was found to be unity, therefore only a bias correction induced by the reconstruction method had to be applied. This bias was estimated with the WPHACT Monte Carlo events in chapter 5 and the dependency on the value of κ was determined with the EXCALIBUR simulation. Neglect-

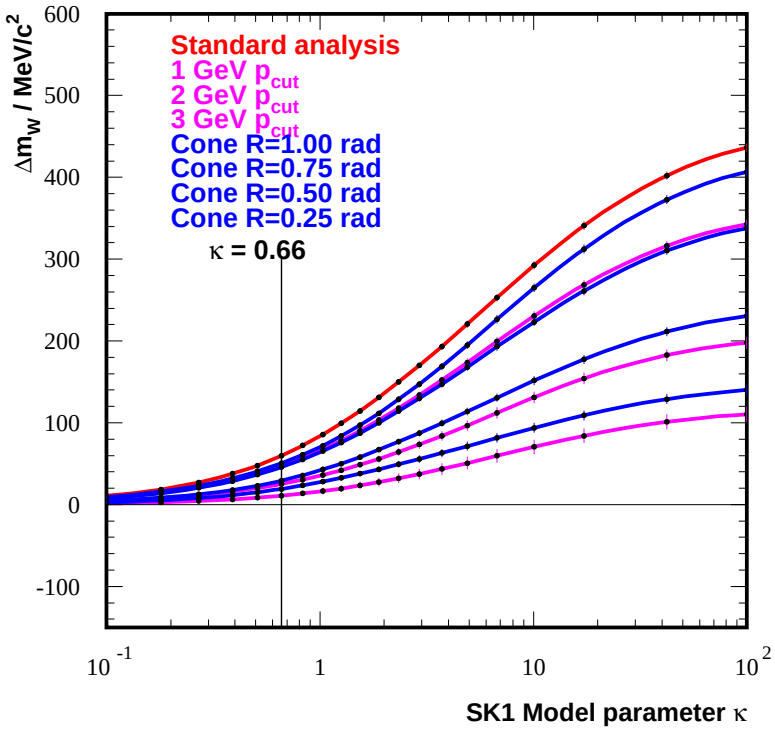

Figure 7.1: *The difference $m_W(\kappa) - m_W(\kappa = 0)$ is presented as a function of κ, this for different m_W estimators. The curve for the standard m_W estimator is shown in red. The curves obtained with the hybrid cone analysis for different values of the cone opening angle, starting from the top with 1.00 rad down to 0.75 rad, 0.50 rad and 0.25 rad are blue. The curves obtained with the momentum cut analysis for different values of p_{cut}, starting from the top with 1 GeV/c, down to 2 GeV/c and 3 GeV/c are purple. The vertical line indicates the value of κ preferred by the SK1 authors [57] and was used to estimate systematic uncertainties on measurements using $e^+e^- \to W^+W^- \to q\bar{q}'Q'\bar{Q}$ events.*

ing the possible existence of Colour Reconnection in the Monte Carlo simulation resulted in event likelihoods $\mathcal{L}_i(m_W|\kappa = 0)$, while $\mathcal{L}_i(m_W|\kappa = \infty)$ were the event likelihoods obtained when assuming the hypothesis that all events do reconnect.

In order to obtain those likelihood curves, the EXCALIBUR Monte Carlo samples were produced once without the implementation of SK1 in PYTHIA (κ = 0) and once with its implementation at full reconnection strength (κ = ∞), conserving the generated kinematics of the primary partons between both samples. To compare data observables with expected observables in the hypothesis of intermediate values of κ, a weighting routine was applied between both extreme hypotheses. This was possible because the event-by-event kinematics of the generated primary quarks were the same in both extreme samples. To construct the event likelihoods for intermediate values of κ the following formula was used:

$$\mathcal{L}_i(m_W|\kappa) = [1 - \mathcal{P}_i(\kappa)] \cdot \mathcal{L}_i(m_W|\kappa = 0) + \mathcal{P}_i(\kappa) \cdot \mathcal{L}_i(m_W|\kappa = \infty) \qquad (7.1)$$

where $\mathcal{P}_i(\kappa)$ is defined in Equation 3.30. This procedure was adopted for all generated events to optimize the sensitivity of the Monte Carlo tests. The combined likelihood was produced for the event sample and from the maximum likelihood principle the calibrated values for $m_W(\kappa)$ were obtained in different hypotheses for κ. In Figure 7.1 the difference $\Delta m_W(\kappa) = m_W(\kappa) - m_W(\kappa = 0)$ or the influence of κ on the bias of the m_W^{std} estimator is presented as a function of κ. The uncertainty on this difference was estimated with the Jackknife method to take the correlation between $\mathcal{L}_i(m_W|\kappa = 0)$ and $\mathcal{L}_i(m_W|\kappa)$ into account. Within the energy range between 200 and 206.7 GeV no significant indication was found for a possible energy dependence of these curves, hence the one at 200 GeV was taken to estimate systematic uncertainties on the W mass and width determinations and to infer κ in section 7.2.2.

At this centre-of-mass energy the shift in m_W between the $\kappa = 0$ and $\kappa = 0.66$ hypothesis was $\Delta m_W([\kappa = 0.66] - [\kappa = 0])$ = 60.6 $\pm$ 2.0 MeV/c^2. For the W width estimator a value of $\Delta\Gamma_W([P_{CR} = 30\%] - [P_{CR} = 0\%])$ = 54 $\pm$ 3 MeV/c^2 was obtained at a centre-of-mass

Syst. effect CR-noCR	$\sqrt{s}$ GeV	Δm_W^{std} MeV/c^2	$\Delta m_W^{p_{cut}}$ MeV/c^2	Δm_W^{cone} MeV/c^2	$\Delta\Gamma_W$ MeV/c^2
SK1 (P=30%)	189	46 $\pm$ 2	-	-	54 $\pm$ 3
SK1 (κ=0.66)	200	60.6 $\pm$ 2.0	25.6 $\pm$ 2.8	32.0 $\pm$ 2.0	-
SK1 (κ=∞)	200	409 $\pm$ 7	183 $\pm$ 10	224 $\pm$ 8	-
SK1 (κ=0.66)	206.7	58.1 $\pm$ 2.9	24.6 $\pm$ 4.2	26.3 $\pm$ 3.3	-
SK2	189	-2 $\pm$ 5	-	-	37 $\pm$ 10
ARIADNE	189	68.7 $\pm$ 6.8	59.3 $\pm$ 9.3	61.9 $\pm$ 7.2	106 $\pm$ 12
HERWIG	189	28.7 $\pm$ 6.6	5.9 $\pm$ 9.1	9.0 $\pm$ 7.0	18 $\pm$ 12

Table 7.1: *Overview of shifts induced on the different W boson estimators due to several phenomenological models of the Colour Reconnection effect with reference to the model without this Colour Reconnection implementation. The results on the first and fifth line are published in [80].*

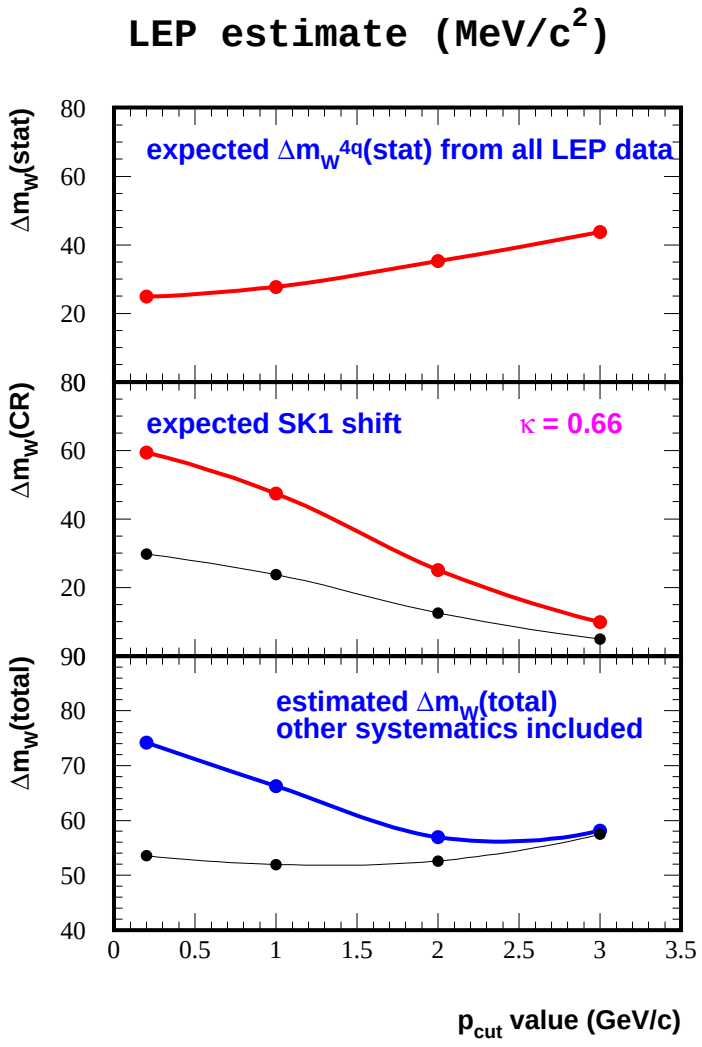

Figure 7.2: *Expected statistical uncertainty for a LEP combined m_W measurement in the hadronic W^+W^- decay channel as a function of the applied value of p_{cut} (top plot). The middle plot illustrates the estimated shift due to Colour Reconnection as implemented with the SK1 algorithm in PYTHIA, using a value of κ equal to 0.66. The bottom plot reflects the total uncertainty, taking into account all other systematic uncertainties as mentioned in [83]. The black line indicates the evolution versus p_{cut} when applying half of the shift on the central value of m_W and quoting the other half as a source of systematic uncertainty.*

energy of 189 GeV. For the SK2 model within PYTHIA, shifts were obtained compatible with zero for the W mass evaluation, while the width was about equally sensitive to this model as to SK1.

With a similar procedure shifts were calculated for the ARIADNE and HERWIG implementations of Colour Reconnection. However in these algorithms no direct free parameter

exist to scale the global effect. All results are summarized in Table 7.1. It was found that for the measurement of the W mass the statistical uncertainty was smaller than the systematic uncertainty due to Colour Reconnection, the largest coming from the ARIADNE phenomenological model.

Alternative m_W estimators were designed to be less sensitive to the Colour Reconnection effect in section 5.7. When neglecting the information content of low momentum particles or when using the hybrid cone algorithm, the influence of Colour Reconnection on the m_W estimator is decreased. The dependency $\frac{\partial m_W}{\partial \kappa}$ of the estimator to κ is decreasing when increasing the value of p_{cut} or when working with smaller cone opening angles R_{cone}.

In Figure 7.1 the difference $\Delta m_W(\kappa)$ is also shown for the $m_W^{p_{cut}}$ and m_W^{cone} estimators for several values of the momentum cut p_{cut} and of the opening angle of the cone R_{cone}. The shift due to the SK1 model decreases for these alternative estimators, while in Table 7.1 it was observed that the shift induced by the ARIADNE model of Colour Reconnection remains invariant. This is very much against our naive expectations of the Colour Reconnection effect. Up to now, despite the large efforts in LEP combined Workshops, no explanation of this behavior has been found. It was found in section 3.5.2 that also the particle flow method had no sensitivity to the Colour Reconnection effects as implemented by the ARIADNE model. The measurement did however disfavor this Colour Reconnection model by 2.1 standard deviations.

In the hypothesis that the SK1 model within PYTHIA reflects the true physics nature of the Colour Reconnection effect, the total uncertainty on the inferred value of m_W can be reduced by applying momentum cuts or cone algorithms [61]. Figure 7.2 illustrates the evolution of the expected statistical uncertainty of a LEP combined measurement of m_W versus the applied value of p_{cut}, while Figure 7.3 shows the same as a function of the cone opening angle R_{cone}. The statistical uncertainty increases as expected, while the systematic shift on m_W due to SK1 Colour Reconnection decreases accordingly. The total uncertainty however decreases optimally with about 24% for the $m_W^{p_{cut}}$ estimator and 30% for the m_W^{cone} estimator. These values were obtained in the hypothesis that other systematic uncertainties remain invariant under a change of p_{cut} or R_{cone}.

Because the direction of the shift is known and equal in all Colour Reconnection models (cfr. Table 7.1), a residual calibration could be envisaged. When applying half of the shift $\Delta m_W([\kappa = 0.66] - [\kappa = 0])$ on the central value of the estimator, the other half must be quoted as a source of systematic uncertainty. This procedure is statistically exactly the same as quoting asymmetric uncertainties, with zero uncertainty on one side of the central value and the full shift as uncertainty on the other side. After applying the residual bias the black lines in Figures 7.2 and 7.3 were obtained. This calibration procedure also dilutes the problem of the irreducible shift observed with the ARIADNE model. Without changing the standard m_W^{std} analysis, this statistical well motivated calibration procedure has the possibility to reduce the total LEP uncertainty on m_W measured in the hadronic decaying W^+W^- channel by about 32%. This value could still be improved by using an alternative m_W estimator on top of the residual calibration procedure.

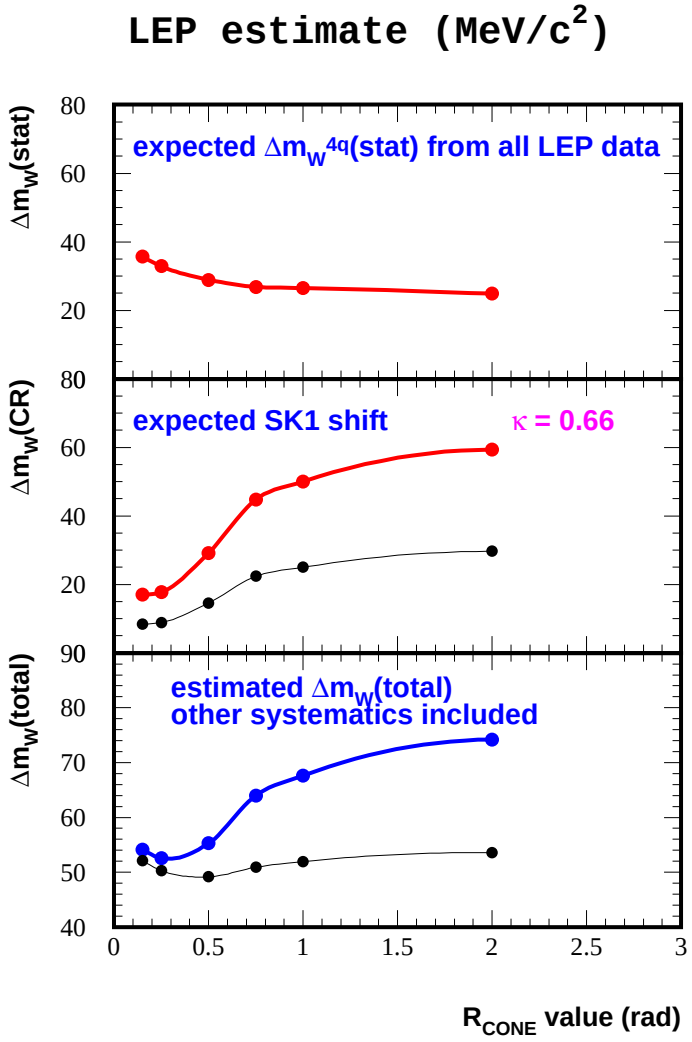

Figure 7.3: *Expected statistical uncertainty for a LEP combined m_W measurement in the hadronic W^+W^- decay channel as a function of the applied value of R_{cone} (top plot). The middle plot illustrates the estimated shift due to Colour Reconnection as implemented with the SK1 algorithm in PYTHIA, using a value of κ equal to 0.66. The bottom plot reflects the total uncertainty, taking into account all other systematic uncertainties as mentioned in [83]. The black line indicates the evolution versus R_{cone} when applying half of the shift on the central value of m_W and quoting the other half as a source of systematic uncertainty.*

7.2 Inferred likelihood information about the Colour Reconnection effect

Another calibration technique (Bayesian this time) consist in an optimal convolution of the statistical knowledge about Colour Reconnection models into the Bayesian m_W and Γ_W es-

timators of interest. The particle flow method provided information about the data preferred value of κ in the SK1 model and shows that the ARIADNE and HERWIG models of Colour Reconnection are disfavored by correspondingly 2.1 and 2.6 σ. In this section more information on the Colour Reconnection phenomena will be inferred. First the shift on m_W will be differentiated into the observable space and secondly, information will be obtained from the measured difference between the m_W^{std} estimator and the alternative ones, $m_W^{p_{cut}}$ and m_W^{cone}.

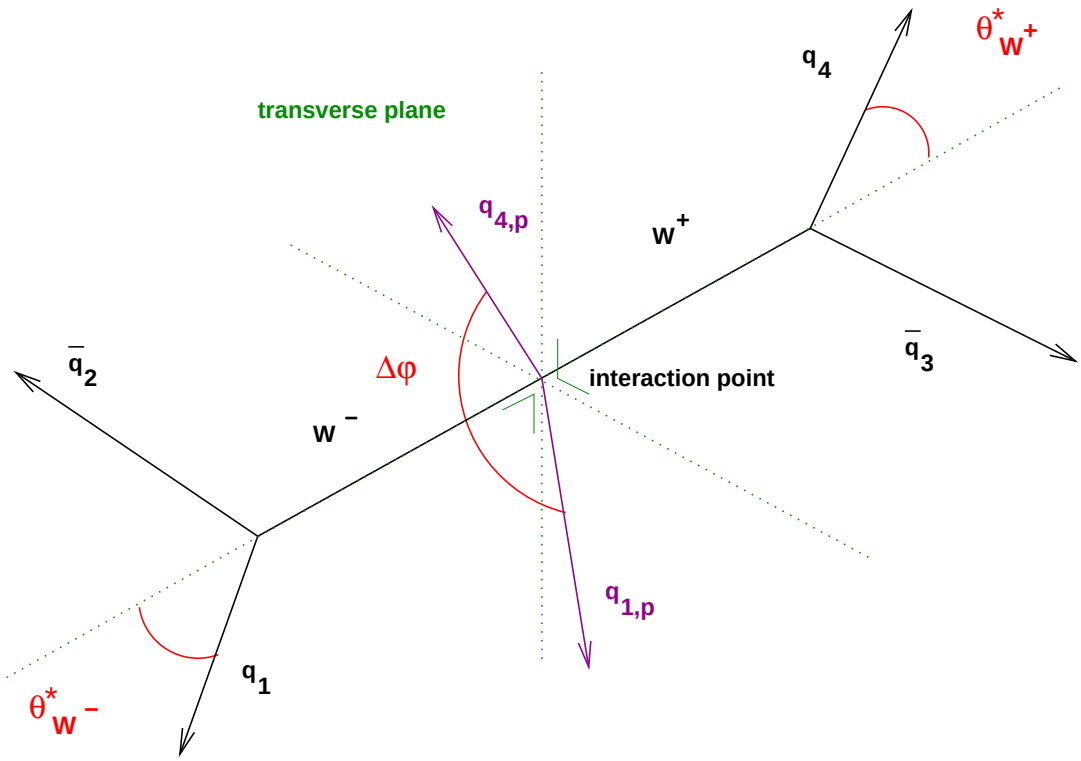

Figure 7.4: *Illustration of the three angles defining the topology of a hadronically decaying W^+W^- event.*

7.2.1 Direct information from geometrical energy flow observables

All the information in a 4 jet W^+W^- event about the kinematics of the primary quarks is given by 12 variables:

- the four energies of the quarks;
- two of them are the 2 masses of the W bosons;

- two form the polar and azimuthal angle of the W^- (or equivalent the W^+);
- and four angles describing the quark directions in the W bosons decays, the polar and azimuthal angle of one of the quarks in each W decay ($\cos\theta^*_{W^-}$, $\varphi^*_{W^-}$,$\cos\theta^*_{W^+}$, $\varphi^*_{W^+}$) .

Four of them are constrained due to the energy and momentum conservation between the initial to final state. This can be reduced to three main angles of interest:

- the minimum of both $\cos\theta^*_{W^-}$ and $\cos\theta^*_{W^+}$;
- the maximum of both $\cos\theta^*_{W^-}$ and $\cos\theta^*_{W^+}$;
- the absolute value of the difference $\Delta\varphi$ between the azimuthal decay angles $|\varphi^*_{W^-} - \varphi^*_{W^+}|$,

which are illustrated in Figure 7.4.

The shift induced by the SK1 model of Colour Reconnection has been determined as a function of these three topological angles in Figure 7.5 for κ=0.66. The topological angles for each event were determined from the EXCALIBUR generated information of the primary quarks in order not to dilute any effect. Except for a few bins where the decay angles θ^* of both W bosons are small and the difference $\Delta\varphi$ is small, the shift was invariant in these dimensions.

In Figure 7.6 the effect of Colour Reconnection was scaled to larger inclusive shifts by taking a fixed value of κ equal to 100. It was observed that the effect on m_W is decreasing when the decay angles θ^* are decreasing. Only when both θ^* angles were small the invariance of the shift versus $\Delta\varphi$ was broken. Due to the small sensitivity of the shift to the topological angles for κ=0.66, it was concluded that these variables only contain information about Colour Reconnection in the extreme SK1 scenario with an almost 100% inclusive probability to reconnect, a scenario which was proven by the particle flow method to be highly unrealistic.

When comparing Figure 7.5 and Figure 7.7 it was found that the shift on m_W due to SK1 Colour Reconnection is not necessary correlated with the average reconnection probability. In fact the opposite effect was observed in those figures. Therefore the calculated string overlap per event is not directly related to a shift in the inferred value of m_W.

The shift on m_W was evaluated in many other directions in the information space, but no golden observable was found which is highly correlated with this shift.

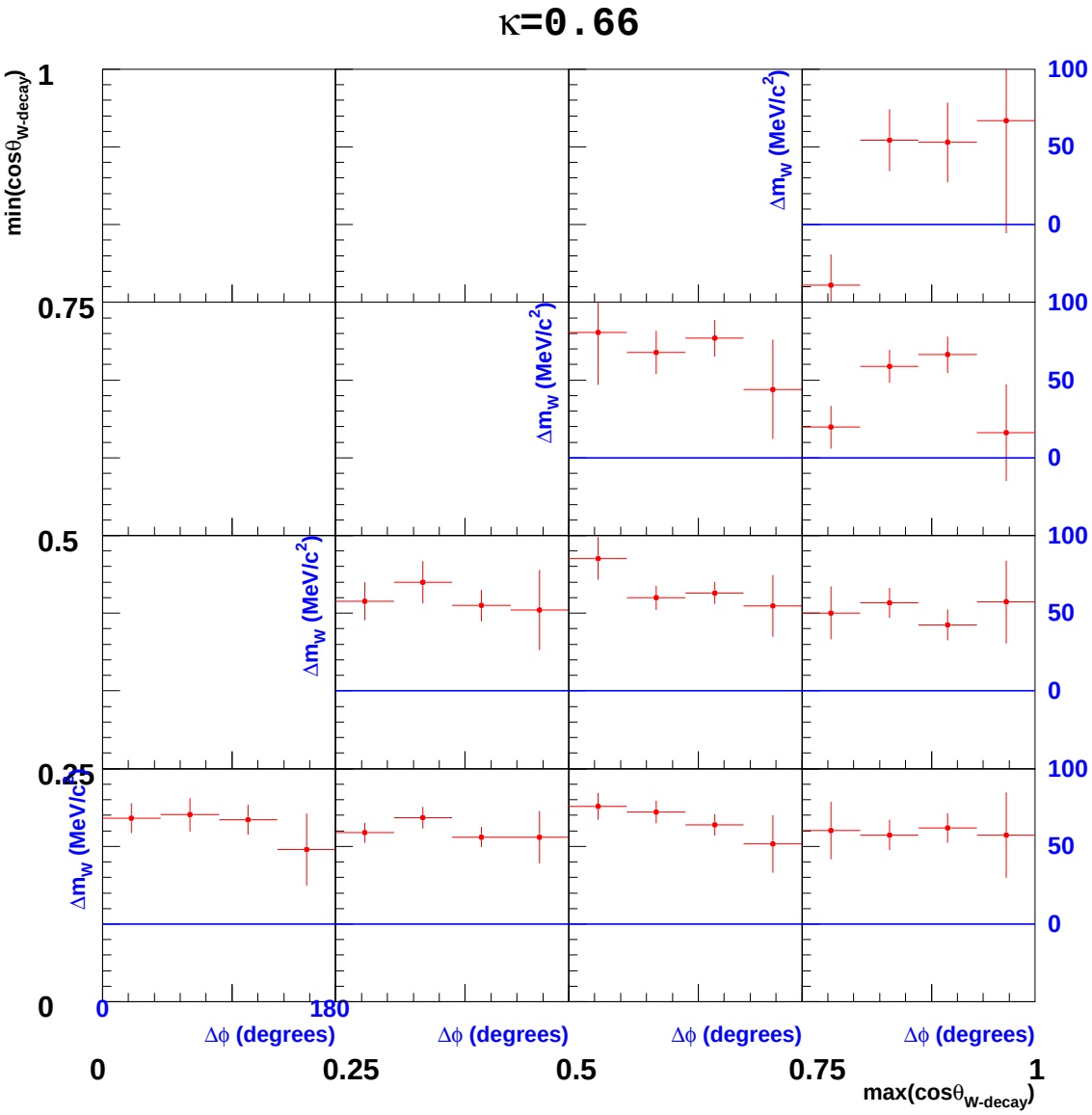

Figure 7.5: *Shift in m_W induced by the SK1 algorithm of Colour Reconnection (κ=0.66) in 4x4x4 bins of the relevant topological angles as defined in the text. The black axis labels define the angular variables min(cosθ^*) and max(cosθ^*) in the 16 boxes, while the blue labels define the Δm_W axis and the $\Delta\varphi$ axis in each of these boxes.*

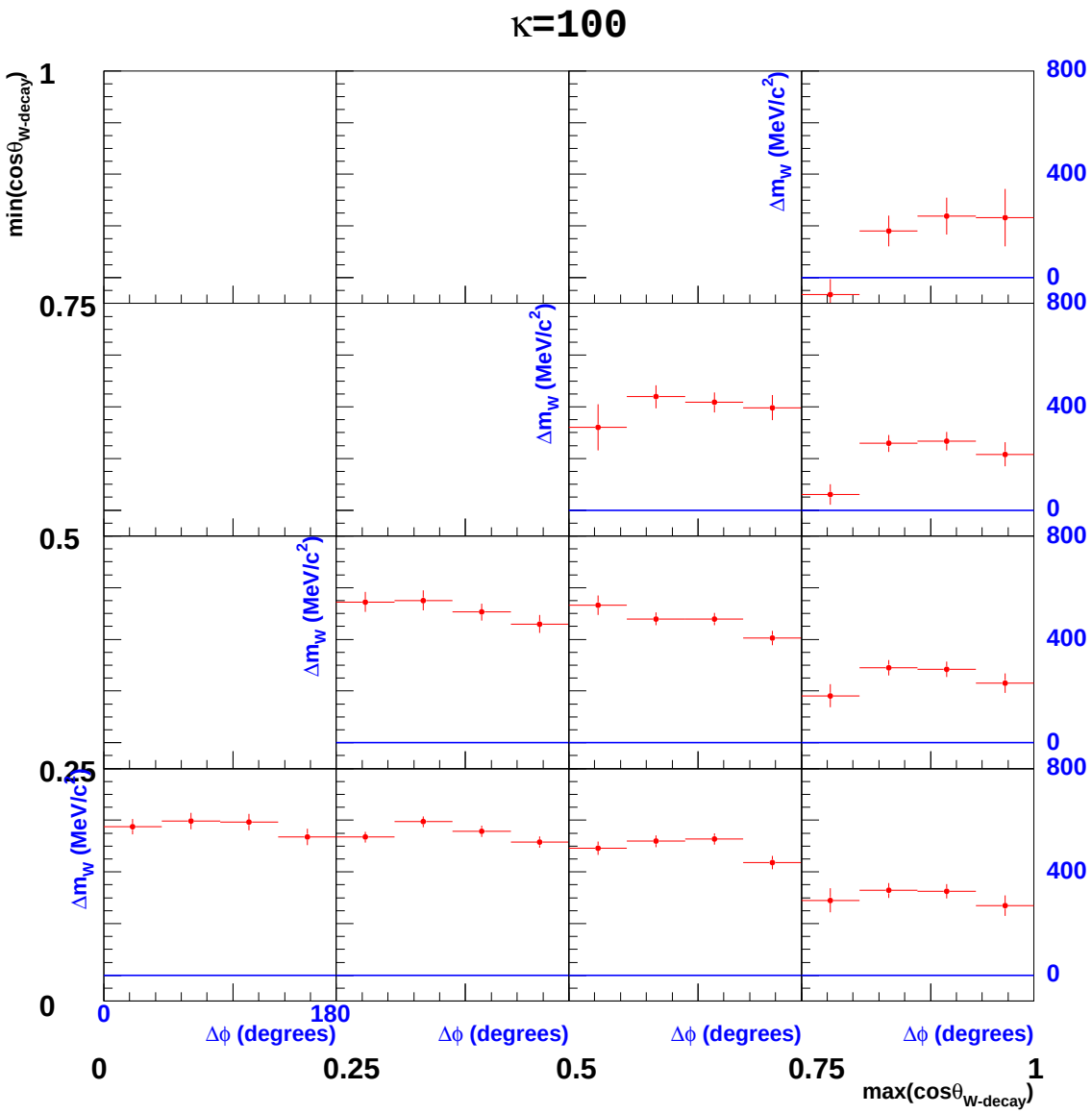

Figure 7.6: *Shift in m_W induced by the SK1 algorithm of Colour Reconnection (κ=100.) in 4x4x4 bins of the relevant topological angles as defined in the text. The black axis labels define the angular variables min(cosθ^*) and max(cosθ^*) in the 16 boxes, while the blue labels define the Δm_W axis and the $\Delta\varphi$ axis in each of these boxes.*

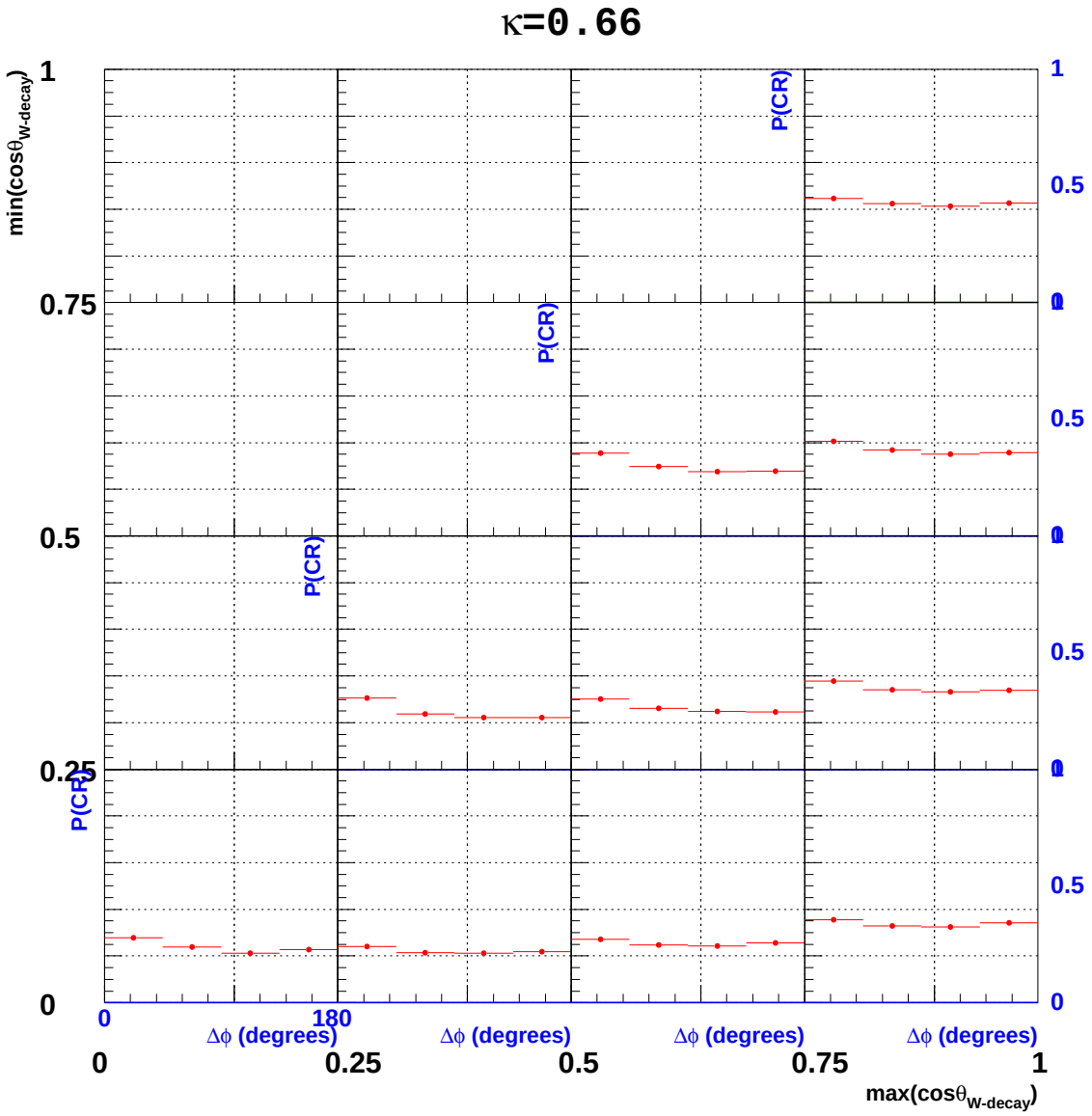

Figure 7.7: *Average SK1 reconnection probability as defined in the text for a fixed value of κ equal to 0.66, in 4x4x4 bins of the relevant topological angles as defined in the text. The black axis labels define the angular variables min(cosθ^*) and max(cosθ^*) in the 16 boxes, while the blue labels define the P_{CR} axis and the $\Delta\varphi$ axis in each of these boxes.*

7.2.2 Indirect information from the different m_W measurements

As mentioned in section 5.7 the difference of two correlated estimators measuring the same physical quantity can give information about systematic uncertainties in both analyses. On top of this, the statistical uncertainty on the difference is reducible with an increasing correlation between both estimators. In this section such a measurement will be performed to infer the data preferred value of κ in the SK1 Colour Reconnection model. This is an update of the preliminary results which were presented in [84].

The method

The observed difference $\Delta m_W(std, i) = m_W^{std} - m_W^i$ in the event sample, where *i* is a certain alternative analysis, provides a measurement of κ. When both estimators m_W^{std} and m_W^i are calibrated in the correct hypothesis of κ, their expectation values will be invariant under a change of p_{cut} or R_{cone}. This is illustrated in Figure 7.8 for different values of p_{cut}, using EXCALIBUR rather than WPHACT generated Monte Carlo samples. Some sensitivity to residual systematic effects in the m_W determination was observed.

Optimization of the inferred information

When neglecting part of the information content of the events in these alternative m_W analyses, also the statistical uncertainty on the value of the m_W estimator is increased when increasing p_{cut} or decreasing R_{cone}. Therefore a balance between the statistical precision on $\Delta m_W(std, i)$ and the dependency of this difference to κ was searched for in order to obtain the largest sensitivity for a κ measurement. This was done using the Monte Carlo simulated events. Assuming that the data follows the $\kappa = 0$ hypothesis, an estimate has been made to what precision one can infer κ from the difference between m_W analyses i and j or the $\Delta m_W(i, j)$ observables. This is done by constructing a log-likelihood function from the expected uncertainties on the $\Delta m_W(i, j)$ values. They reflect the expected information about κ inferred from different p_{cut} analyses or from the hybrid cone analyses. Figure 7.9 illustrates these log-likelihood functions for several possibilities.

For the analysis rejecting particles with momenta lower than p_{cut}, an optimal sensitivity was found when using the difference $\Delta m_W(std, p_{cut})$ with p_{cut} equal to 2 or 3 GeV/c. Even more information about κ could be extracted from the data, when using the difference $\Delta m_W(std, R_{cone})$, which was found to have an optimal sensitivity around $R_{cone} \simeq 0.5$ rad. No significant improvement in the sensitivity was found when combining the information from these two observables. Therefore the most optimal measure of κ using this method is extracted from the $\Delta m_W(std, R_{cone} = 0.5\,rad)$ observable. Nevertheless, the $\Delta m_W(std, p_{cut} = 2\,\mathrm{GeV}/c)$ observable was studied as a cross-check.

Systematic uncertainties

The estimation of systematic uncertainties on the observables $\Delta m_W(std, i)$ follows the same methods as those used within the m_W analysis. Now the double difference is a measure of the systematic uncertainty between Monte Carlo simulation ('MC') and real data ('DA'):

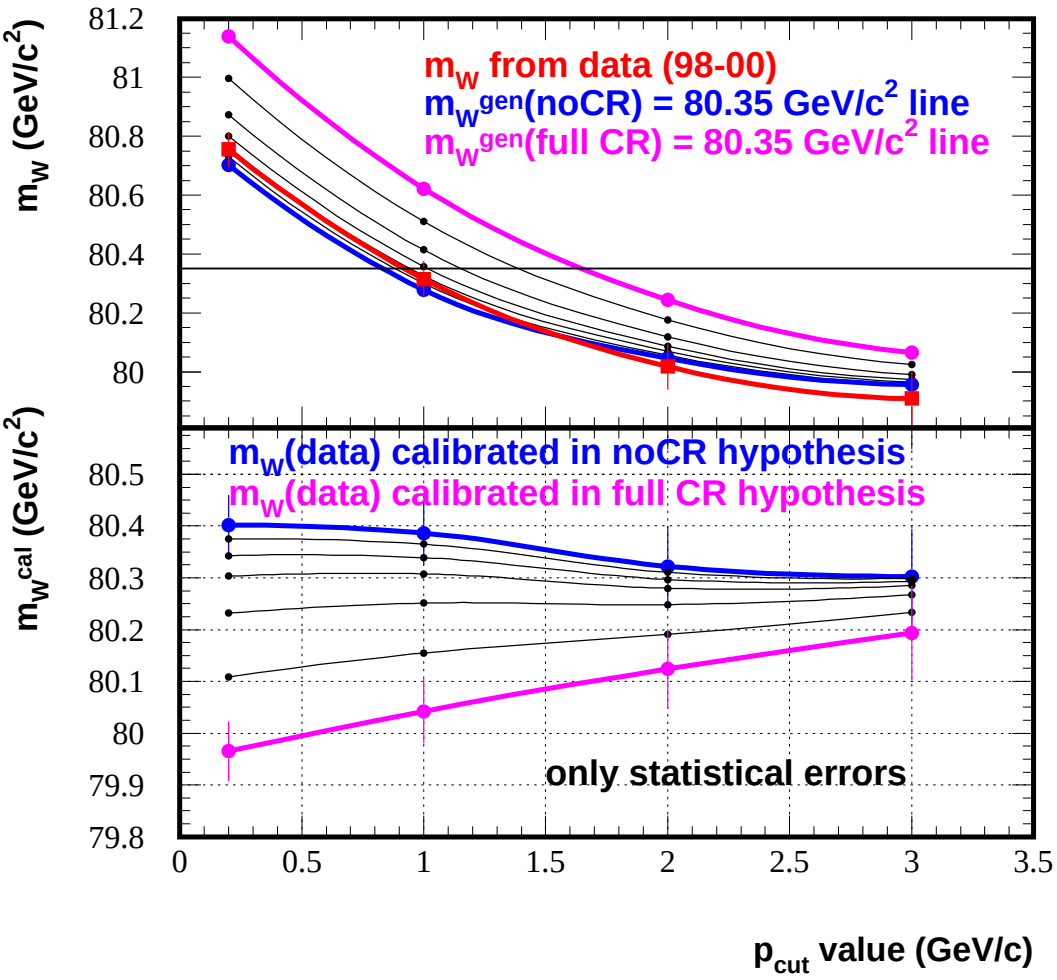

Figure 7.8: *The upper plot shows the Monte Carlo estimated value of m_W for different analyses (including the bias). The m_W value used by the event generator is 80.35 GeV/c^2. The standard m_W^{std} estimator uses a p_{cut} value of 0.2 GeV/c, while three other points from the alternative estimator are also shown : 1 GeV/c, 2 GeV/c and 3 GeV/c. The blue line reflects the Monte Carlo estimated m_W (including the bias) in the $\kappa = 0$ hypothesis, while the purple line reflects the Monte Carlo estimated m_W in the $\kappa = \infty$ hypothesis. The black curves indicate the tendency for some intermediate values of κ. The m_W values inferred from the data using different estimators are shown in red. In the bottom plot these data values are calibrated in different hypothesis of κ.*

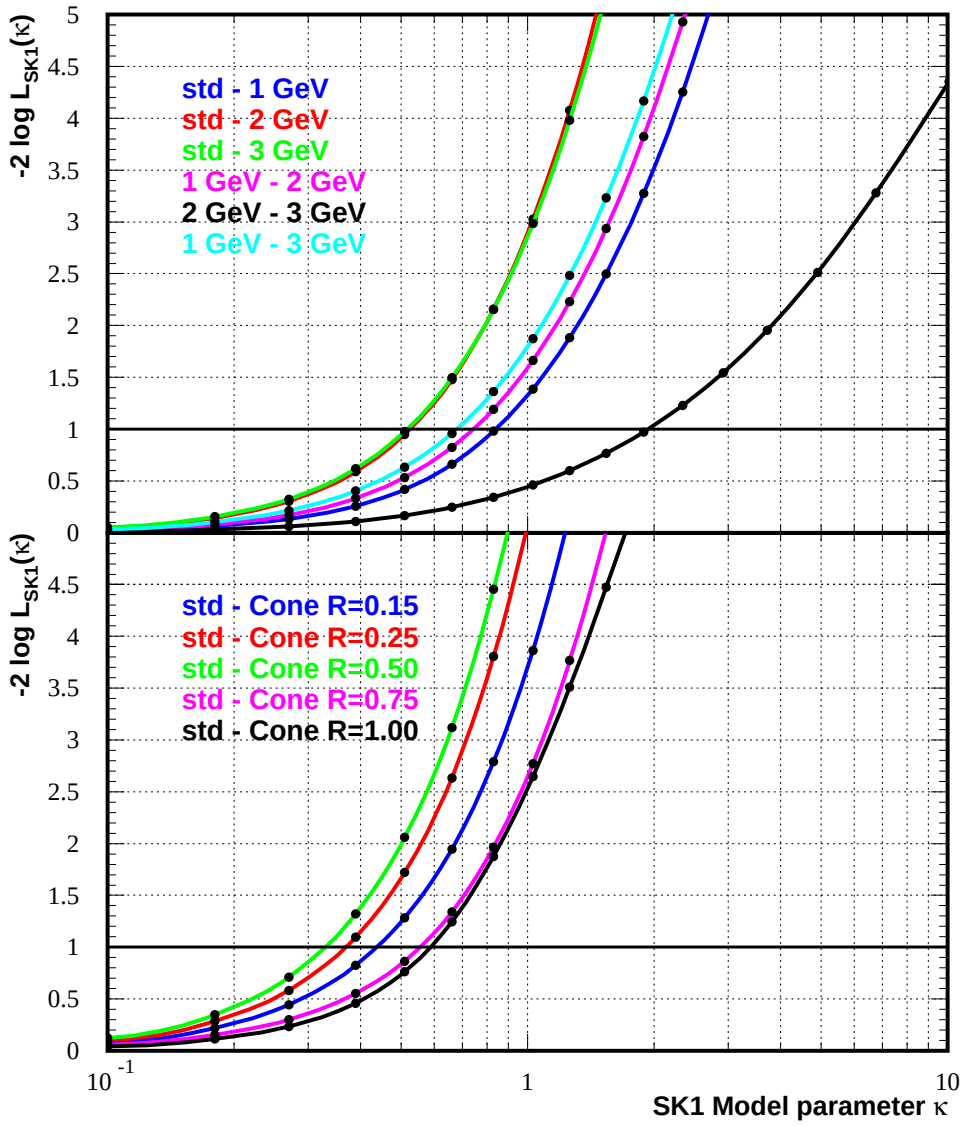

Figure 7.9: *Expected log-likelihood curve of a measurement of κ from observed differences in m_W estimators when assuming that four times the total luminosity of DELPHI was available, hence the LEP luminosity. The 1σ statistical uncertainty on κ is found where the line $-2logL_{SK1}(\kappa) = 1$ crosses the log-likelihood curve. In the top plot the $m_W^{p_{cut}}$ estimator was used, while for the bottom plot the m_W^{cone} estimator.*

$$\Delta_{\rm syst}(MC, DA) = \left|[m_W^{std}(MC) - m_W^{std}(DA)] - [m_W^i(MC) - m_W^i(DA)]\right| \qquad (7.2)$$

where i is one of the alternative m_W estimators. The details are described below and summarized in table 7.2.

- **Mixed Lorentz Boosted Z^0's** : The double difference of Equation 7.2 was determined with the MLBZ method using Z^0 events selected in the data sets collected during the 1998 calibration runs and Z^0 events from the corresponding Monte Carlo samples. The following results were obtained for the $\Delta m_W(std, R_{cone} = 0.5\,rad)$ observable:

$$\begin{array}{lcrcll} \Delta_{\rm syst}(\mathrm{ARIADNE, DA}) & = & -1.9 & \pm & 3.9 & \mathrm{MeV/c^2} \\ \Delta_{\rm syst}(\mathrm{PYTHIA, DA}) & = & -5.7 & \pm & 3.9 & \mathrm{MeV/c^2} \\ \Delta_{\rm syst}(\mathrm{HERWIG, DA}) & = & -10.6 & \pm & 3.9 & \mathrm{MeV/c^2} \end{array} \qquad (7.3)$$

  where the statistical uncertainty takes into account the correlation between the Monte Carlo and the data MLBZ events (as explained in section 6.3.2), together with the correlation between the two m_W estimators. This indicates that most of the fragmentation, detector and inter-W Bose-Einstein Correlation systematics are small. The study was not performed for the cross-check observable, $\Delta m_W(std, p_{cut})$.

- **Fragmentation** : The fragmentation of the primary partons was modeled in the Monte Carlo simulation used for the calibration of the m_W^i observables. The bias on the m_W estimators (in the $\kappa = 0$ hypothesis) is changed when using different fragmentation models, resulting in systematic uncertainties on the measured m_W^i observables and hence possibly also on the measurement of κ. In Figure 7.10 the systematic shift in the different m_W^i estimators is estimated when using HERWIG or ARIADNE rather than PYTHIA as the fragmentation model in the no Colour Reconnection hypothesis. When inferring κ from the data difference $\Delta m_W(std, p_{cut} = 2\,\mathrm{GeV}/c)$ the PYTHIA model was used to calibrate each m_W^i estimator. The double differences as mentioned in Equation 7.2 give an estimate for the systematic uncertainties on the $\Delta m_W(std, j)$ observables. The bias on $\Delta m_W(std, p_{cut} = 2\,\mathrm{GeV}/c)$ will however change by 27 ± 12 MeV/c^2 or 8 ± 12 MeV/c^2 when replacing PYTHIA by respectively HERWIG or ARIADNE. The observable $\Delta m_W(std, R_{cone} = 0.5\,rad)$ will change by -4 $\pm$ 10 MeV/c^2 or -6 $\pm$ 10 MeV/c^2 when replacing PYTHIA by respectively HERWIG or ARIADNE. The largest shift of the observable when interchanging fragmentation models is taken as systematic uncertainty on its value or the uncertainty on this shift whenever this exceeds the shift. Hence 27 MeV/c^2 for the $\Delta m_W(std, p_{cut} = 2\,\mathrm{GeV}/c)$ observable and 10 MeV/c^2 for the $\Delta m_W(std, R_{cone} = 0.5\,rad)$ observable. The MLBZ studies agree with those results, hence no extra systematic due to fragmentation was quoted for the $\Delta m_W(std, R_{cone} = 0.5\,rad)$ observable.

- **Calibration** : Because the large correlation between the standard and alternative m_W estimators, the statistical uncertainty on the bias calibration was negligible. A value of 3 MeV/c^2 is quoted for both $\Delta m_W(std, i)$ observables.

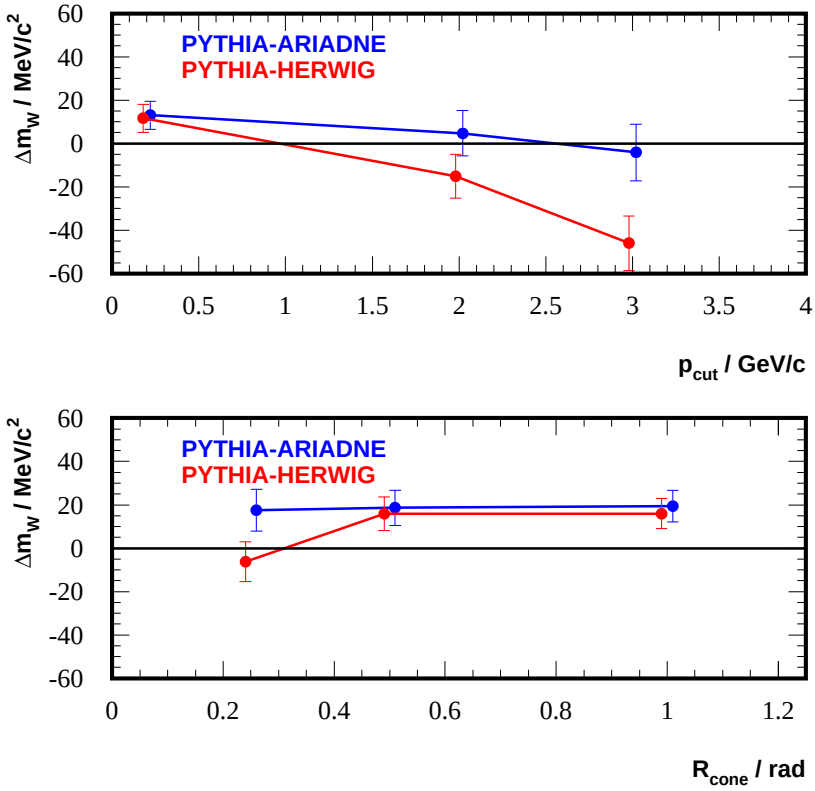

Figure 7.10: *Systematic shift in the different calibrated m_W estimators when using HERWIG or ARIADNE as fragmentation model instead of PYTHIA. These Monte Carlo estimates were obtained at a centre-of-mass energy of about 189 GeV. The uncertainties are determined with the Jackknife method.*

- **Background** : In both the standard and alternative estimators the same event selection was applied, therefore the same background contamination is present in all m_W estimators. It was also assumed that the background contribution is invariant when changing the value of p_{cut} or R_{cone}. In section 6.4 it was shown that the influence of the background on one m_W estimator is negligible, hence the quoted systematic uncertainties on both $\Delta m_W(std, i)$ observables is 3 MeV/c^2.

- **Bose-Einstein Correlations** : The relevant value for the systematic uncertainty on the observables is the difference between the observable obtained from the Monte Carlo events with Bose-Einstein Correlations inside individual W's (BEI) and those with Bose-Einstein Correlations between W's (BEA). This value was estimated to be 6.4 $\pm$ 9.3 MeV/c^2 for the $\Delta m_W(std, p_{cut} = 2\,\mathrm{GeV}/c)$ observable, while a value of 7.2 $\pm$ 8.2 MeV/c^2 was obtained for the $\Delta m_W(std, R_{cone} = 0.5\,rad)$ observable. Figure 6.10

shows that these values are energy independent. As a cross-check also the difference between the no Bose-Einstein scenario (BEO) and the only inside Bose-Einstein scenario was studied. Taking into account the correlations between the three absolute m_W estimators, a significant non-zero shift on the relevant Δm_W observables was found, a value of 25.4 $\pm$ 9.3 MeV/c^2 for the $\Delta m_W(std, p_{cut} = 2\,\mathrm{GeV}/c)$ observable and 16.4 $\pm$ 8.2 MeV/c^2 for the $\Delta m_W(std, R_{cone} = 0.5\,rad)$ observable. Hence an extra systematic uncertainty was quoted of respectively 25 and 16 MeV/c^2 on top of the 9 and 8 MeV/c^2 quoted above from the difference between the inside and between W correlation scenario. Those systematic effects between the BEO and BEI scenarios are covered by the MLBZ study, and show that the LUBOEI model is not perfect in describing the effects of Bose-Einstein Correlations in W^+W^- events. To be conservative the shifts evaluated with the LUBOEI algorithm are quoted as extra systematic uncertainties.

- **Cross-check in the semi-leptonic channel** : Colour Reconnection between the decay products originating from different W boson decays can only occur in the $W^+W^- \rightarrow q\bar{q}'Q'\bar{Q}$ channel. The semi-leptonic decay channel is by definition free of those effects. Therefore the determination of the Colour Reconnection sensitive observables, like $\Delta m_W(std, R_{cone} = 0.5\,rad)$, in this decay channel could hint for the presence of residual systematic effects. Within DELPHI preliminary measurements exist for the $\Delta m_W(std, R_{cone} = 0.5\,rad)$ observable in the semi-leptonic decay channel [85]. The semi-leptonic m_W analysis in [80] was used and the cone algorithm was implemented in a similar way as for the fully hadronic decay channel explained in section 5.7. The same data sets have been used as presented throughout this thesis and the following result was obtained:

$$\Delta m_W(std, R_{cone} = 0.5\,rad) = \ \ 8 \pm 56\ \mathrm{MeV/c^2} \tag{7.4}$$

where the statistical uncertainty was scaled to have a perfect χ^2/ndf of a combined fit over all individual data sets assuming an $\sqrt{s}$ invariant observable. Although the statistical significance of this cross-check is small, a good agreement was found for both m_W estimators.

All systematic uncertainties determined were found to be smaller than the statistical uncertainty, and therefore they do not dilute the large sensitivity to the SK1 model parameter κ.

Results

In this section different m_W estimators sensitive to the κ parameter in the SK1 Colour Reconnection model were studied. The observable $\Delta m_W(std, R_{cone})$ where $\mathrm{R_{cone}}$ is around 0.5 rad, was found to be most sensitive to measure κ. Its value measured from the combined DELPHI data at centre-of-mass energies ranging between 183 and 209 GeV is after PYTHIA $\kappa = 0$ calibration :

$$\begin{array}{lcllllll} m_W^{std} & - & m_W^{p_{cut}} & = & 143 & \pm & 61 & \pm & 38 & \mathrm{MeV/c^2} \\ m_W^{std} & - & m_W^{cone} & = & 59 & \pm & 35 & \pm & 21 & \mathrm{MeV/c^2} \end{array} \quad (7.5)$$

where the first uncertainty represents the statistical one and the second the combined systematic one. From these values an estimate was made for the κ parameter by comparing them with the Monte Carlo expected values in different hypothesis of κ, shown in Figure 7.11. The Gaussian uncertainty on the measured observables was used to construct a log-likelihood function $\mathcal{L}(\kappa) = -2logL$ for κ. The inferred log-likelihood functions $\mathcal{L}(\kappa)$ are shown in Figure 7.12 for both observables. The inferred log-likelihood from the $\Delta m_W(std, R_{cone} = 0.5\,rad)$ observable should be taken as the result on κ because of its larger sensitivity to the value of κ. The data preferred value of κ is 1.75. The result on κ inferred from the cross-check $\Delta m_W(std, p_{cut} = 2\,\mathrm{GeV}/c)$ observable is found to be not significantly different from the quoted result obtained with the more optimal $\Delta m_W(std, R_{cone} = 0.5\,rad)$ observable. The full breakdown of the statistical contributions on both observables can be found in Table 7.3.

Source	Uncertainty contribution (MeV/c^2)	
	$\Delta m_W(std, p_{cut} = 2\,\mathrm{GeV}/c)$	$\Delta m_W(std, R_{cone} = 0.5\,rad)$
MLBZ	-	11
Fragmentation	27	-
Calibration	3	3
Background	3	3
BEI-BEA	9	8
BEO-BEI	25	16
Total systematical	38	21
Statistical	61	35
Total	72	41

Table 7.2: Breakdown of the total uncertainty on both relevant observables.

The SK1 model for Colour Reconnection implemented in PYTHIA was studied because it parametrizes the effect as a function of the model parameter κ. Other phenomenological models implemented in the ARIADNE and HERWIG Monte Carlo fragmentation schemes exists and are equally plausible. Unfortunately their effect in $W^+W^- \rightarrow q\bar{q}'Q'\bar{Q}$ events cannot be scaled with some model parameter, like κ in SK1, without touching the fragmentation model parameters. Although this non-factorization property, the consistency of these models with the data can still be examined. The Monte Carlo predictions of the observables in the hypothesis with Colour Reconnection (calibrated in the hypothesis of no Colour Reconnection) give the following values:

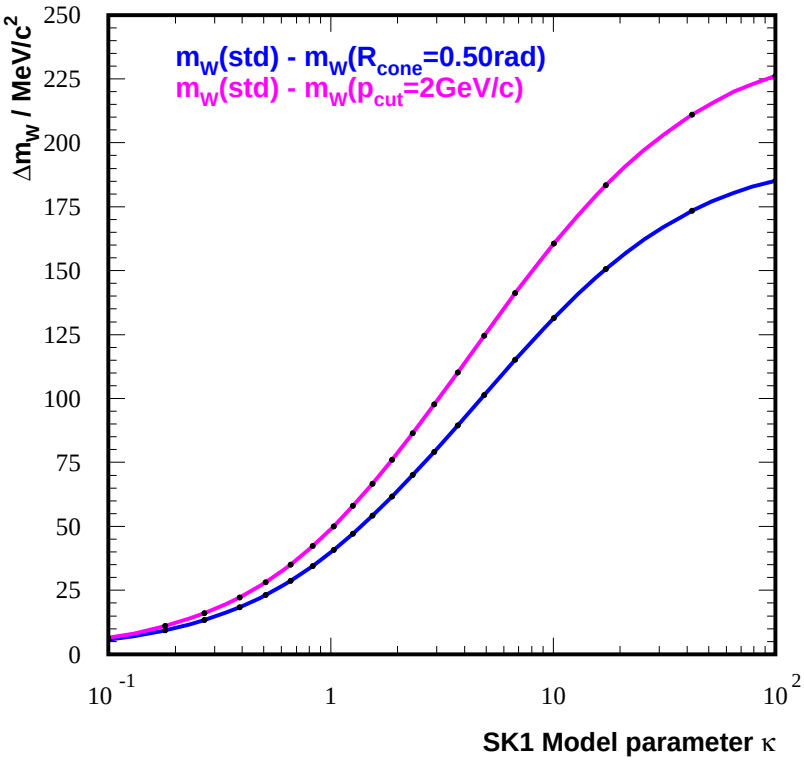

Figure 7.11: *Monte Carlo estimate of the dependency of observables* $\Delta m_W(std, R_{cone} = 0.5\,rad)$ *and* $\Delta m_W(std, p_{cut} = 2\,\mathrm{GeV}/c)$ *to the model parameter* κ*. This at a centre-of-mass energy of 200 GeV and background is not included.*

$$\begin{array}{llllllll}
\text{ARIADNE} & \rightarrow & m_W^{std} & - & m_W^{p_{cut}} & = & 9.4 \pm 7.0 & \mathrm{MeV/c^2} \\
\text{ARIADNE} & \rightarrow & m_W^{std} & - & m_W^{cone} & = & 7.2 \pm 4.1 & \mathrm{MeV/c^2} \\
\text{HERWIG} & \rightarrow & m_W^{std} & - & m_W^{p_{cut}} & = & 22.8 \pm 6.9 & \mathrm{MeV/c^2} \\
\text{HERWIG} & \rightarrow & m_W^{std} & - & m_W^{cone} & = & 19.7 \pm 4.0 & \mathrm{MeV/c^2}\ .
\end{array} \tag{7.6}$$

The ARIADNE implementation of Colour Reconnection does not follow our naive expectation as observed with the SK1 and HERWIG Monte Carlo. This could imply that it is impossible to rule out the ARIADNE Colour Reconnection model with these Δm_W methods without observing a positive effect in the SK1 ($\kappa \gg 0$) and HERWIG models. The small effects on m_W observed with the HERWIG implementation of Colour Reconnection compared to those predicted by SK1 are due to the fact that the fraction of events that reconnect is smaller in HERWIG ($\simeq 1/N_c^2 \simeq 11\%$) compared to SK1 ($\simeq 35\%$). After applying this scale factor between both models, their predicted effect on the W mass and on the $\Delta m_W(i,j)$ observables is comparable.

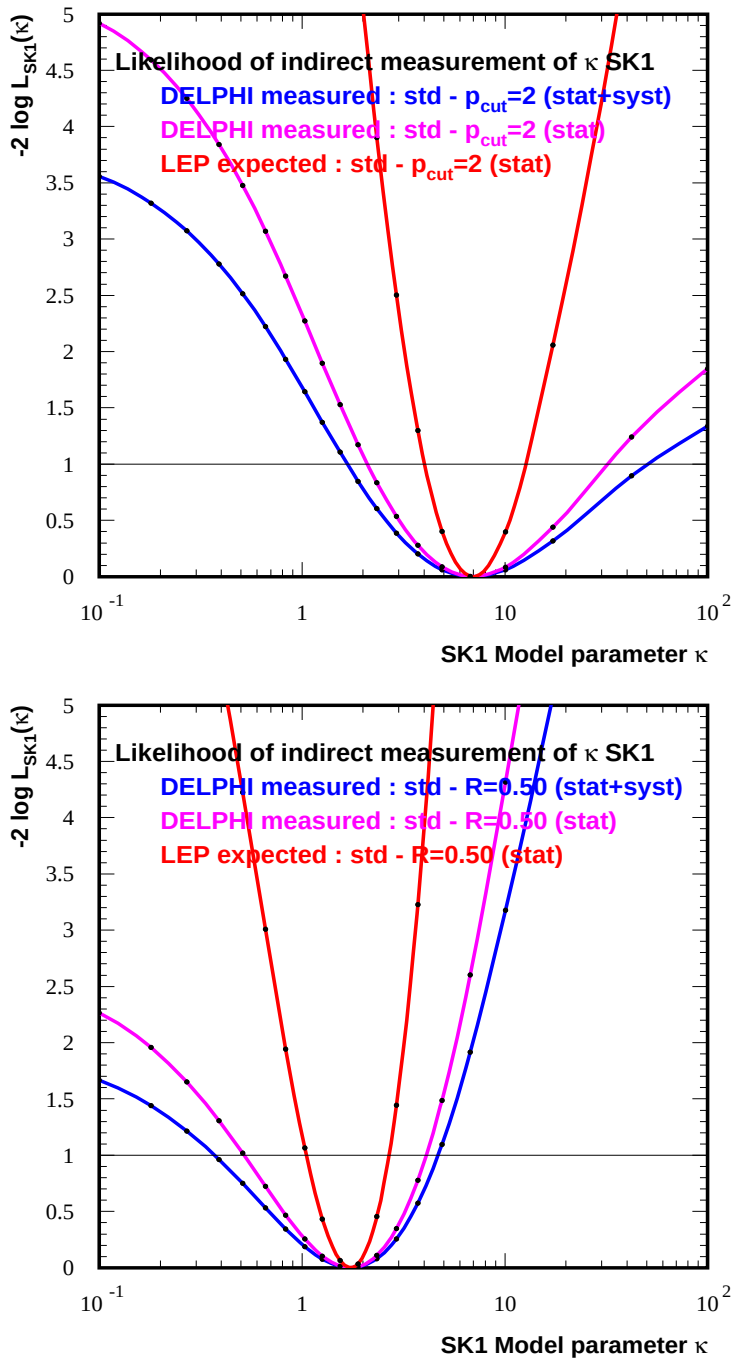

Figure 7.12: *The inferred log-likelihood function $\mathcal{L}(\kappa)$ from the combined DELPHI data measurement of $\Delta m_W(std, R_{cone} = 0.5\,rad)$ (bottom) and $\Delta m_W(std, p_{cut} = 2\,\mathrm{GeV}/c)$ (top). The blue curve reflects the final result including the statistical uncertainty on $\Delta m_W(std, i)$ and the investigated systematic uncertainty contributions. The purple and the red curve are centered on the same minimum and reflect the log-likelihood functions obtained when only taking statistical uncertainties into account. The red one is the Monte Carlo prediction when using 4 times the integrated luminosity of DELPHI.*

Nominal $\sqrt{s}$ GeV	$\Delta(m_W^{std} - m_W^{cone})$ MeV/c^2	$\Delta(m_W^{std} - m_W^{p_{cut}})$ MeV/c^2
182.65	38.5 $\pm$ 101.4	212.4 $\pm$ 207.6
189.63	-14.6 $\pm$ 69.7	103.6 $\pm$ 117.2
191.58	-370.1 $\pm$ 214.6	-2.9 $\pm$ 326.5
195.51	7.8 $\pm$ 129.4	-74.8 $\pm$ 188.9
199.51	44.7 $\pm$ 92.3	188.8 $\pm$ 167.9
201.64	285.5 $\pm$ 135.9	220.7 $\pm$ 284.0
205.85	115.5 $\pm$ 66.9	152.9 $\pm$ 113.1
206.3 (TPC-S6)	258.1 $\pm$ 140.7	530.3 $\pm$ 284.1
total	58.5 $\pm$ 35.1	142.6 $\pm$ 60.9
total (no TPC-S6)	44.4 $\pm$ 36.3	121.8 $\pm$ 62.3

Table 7.3: *Data results obtained for the differences between the standard and alternative m_W estimators. The statistical uncertainty was calculated with the Jackknife method.*

Correlation with the direct measurement of $\mathbf{m_W}$

When using a data observable to estimate systematic uncertainties on some parameter inferred from the same data sample, one should take into account the correlation between the estimator used to measure the systematic bias and the estimator of the absolute value of the parameter. Therefore the correlation between the Colour Reconnection sensitive observables $\Delta m_W(std, R_{cone} = 0.5\,rad)$ and $\Delta m_W(std, p_{cut} = 2\,\mathrm{GeV}/c)$ and the absolute m_W^{std} estimator was calculated. The correlation was determined from the Monte Carlo events and in the hypothesis of $\kappa = 0$ or no Colour Reconnection. The obtained values were found to be stable as function of κ within the statistical precision of a few percent. The correlation between $\Delta m_W(std, R_{cone} = 0.5\,rad)$ and m_W^{std} was found to be 11%, while for the one between $\Delta m_W(std, p_{cut} = 2\,\mathrm{GeV}/c)$ and m_W^{std} a value of 8% was obtained. Also the correlation between the different m_W estimators was estimated and found to be stable with the value of κ. A value of 83% was obtained for the correlation between m_W^{std} and $m_W^{cone}(R = 0.5\,rad)$, while 66% was obtained between m_W^{std} and $m_W^{p_{cut}}(p_{cut} = 2\,\mathrm{GeV}/c)$.

Combination with the particle flow method

The obtained log-likelihood for κ is in agreement with the measurements in [86]. However, due to a large difference in event selection efficiency ($\sim$89% for the m_W analyses versus $\sim$12% for the particle flow method), both analyses use largely different samples of data events, and hence are highly uncorrelated. Also the event information used in both analyses is largely different. Therefore one can assume that there is no statistical correlation between the measurement of κ via the observable $\Delta m_W(std, R_{cone} = 0.5\,rad)$ as presented in this thesis and its measurement via the particle flow of the hadronic decaying W^+W^- events [86]. In this approximative hypothesis a combination of the inferred information about κ of both measurements was performed. The resulting log-likelihood of this combination is shown

in Figure 7.13, where also the correlation between the systematical uncertainties in both analyses was neglected. The data preferred value of κ is 1.96 and the 68% confidence level interval is [0.66,4.56].

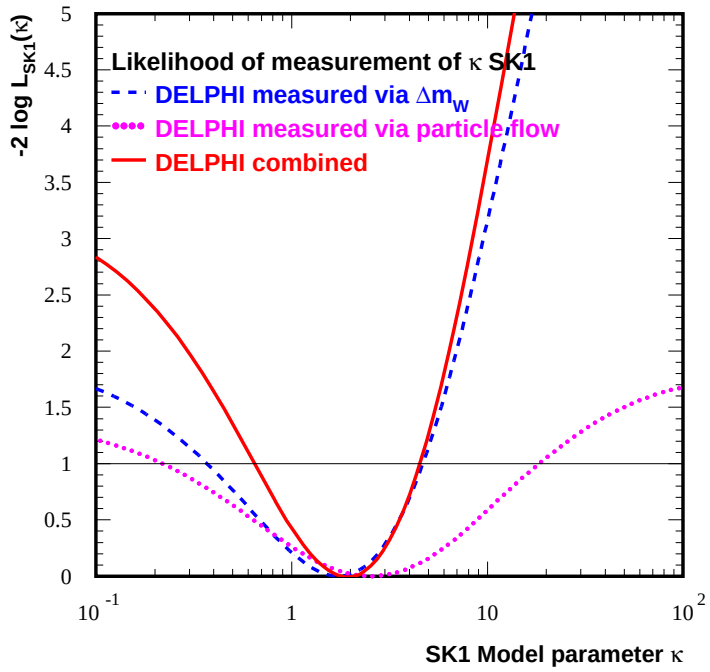

Figure 7.13: *The inferred log-likelihood function $\mathcal{L}(\kappa)$ from the combined DELPHI measurement via $\Delta m_W(std, R_{cone} = 0.5\,rad)$ and the particle flow. The red curve reflects the final result including the statistical and investigated systematic uncertainties. The log-likelihoods are combined in the hypothesis of no correlation between the statistical and systematical uncertainties of both measurements.*

From Figure 7.13 it can already be observed that the sensitivity of the method presented in this thesis is much higher compared to the one expected with the particle flow method. Monte Carlo studies within DELPHI have indicated that the sensitivity of the $\Delta m_W(std, R_{cone} = 0.5\,rad)$ observable to measure full SK1 Colour Reconnection effects is about 4.6σ, while only 2.7σ was found for the particle flow method. Also when combining all LEP data the systematic uncertainties on the $\Delta m_W(std, R_{cone} = 0.5\,rad)$ observable are smaller than the ones in the particle flow method.

Expectations when using full LEP luminosity

During LEP WW Workshops it was shown [82] that the m_W analyses within all four experiments are equally sensitive to the SK1 Colour Reconnection effects. Therefore it was expected that also the $\Delta m_W(std, R_{cone} = 0.5\,rad)$ observable had equal sensitivity to κ in each experiment. For this feasibility study it was assumed that the experiments can infer the different m_W estimator values with equal precision. Using these hypotheses and assuming that the four log-likelihoods $\mathcal{L}(\kappa)$ prefer the same central value for κ, the following virtual LEP combined result could be expected:

$$m_W^{std} \;-\; m_W^{cone} \;=\; 59 \;\pm\; 17 \;\pm\; 21 \quad \mathrm{MeV/c^2} \tag{7.7}$$

where only for the MLBZ determined and Bose-Einstein related systematic uncertainties full correlation between the LEP experiments was assumed.

The predicted log-likelihood for κ taking into account only statistical uncertainties is shown in Figure 7.9, where it is assumed that no Colour Reconnection is present in the LEP data or that the observable has a zero central value. Figure 7.12 shows the LEP expected log-likelihood at the DELPHI measured central value of κ not taking into account systematic uncertainties. The log-likelihood curve on κ including systematic uncertainties obtained from this virtual $\Delta m_W(std, R_{cone} = 0.5\,rad)$ observation is shown in the bottom plot of Figure 7.14, together with the log-likelihood representing the LEP combined information inferred with the particle flow information [1]. This indicates that relevant information about κ could be extracted from the LEP data. The top plot in Figure 7.14 shows a combination of the result obtained in this thesis with the preliminary particle flow information from all LEP experiments.

In both studies no correlation was assumed between the observables used in both types of analyses. Also the correlation between the systematic uncertainties on both observables was neglected. This is believed to be a rather good approximation of the true situation.

According to these studies it would be very interesting for the m_W measurement if all LEP experiments performed a similar $\Delta m_W(std, R_{cone} = 0.5\,rad)$ analysis and combined their resulting log-likelihoods. Unfortunately this has not been done yet. When combining the information from both the $\Delta m_W(std, R_{cone} = 0.5\,rad)$ analysis and the particle flow method, LEP data has the sensitivity to disfavor the ARIADNE and HERWIG models of Colour Reconnection by about 4 to 5 standard deviations.

For the $\Delta m_W(std, p_{cut} = 2\,\mathrm{GeV}/c)$ observable the expected LEP statistical uncertainty is 28.4 MeV/c^2, resulting in a predicted log-likelihood for κ shown in Figure 7.9, where it is again assumed that no Colour Reconnection is present in the LEP data. Figure 7.12 illustrates the LEP expected log-likelihood at the DELPHI measured central value of κ not taking into account systematic uncertainties.

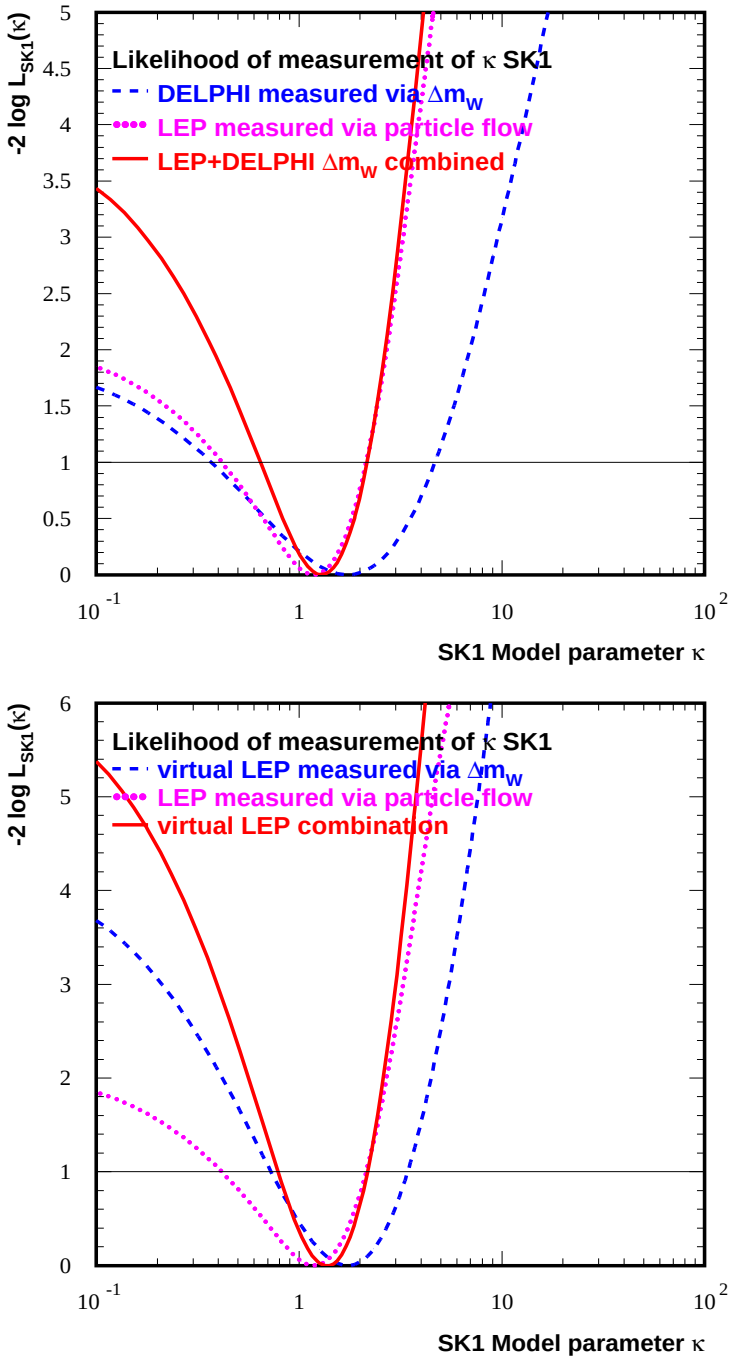

Figure 7.14: *The inferred log-likelihood function $\mathcal{L}(\kappa)$ from the DELPHI measurement of $\Delta m_W(std, R_{cone} = 0.5\,rad)$ and the LEP combined particle flow method [1] (top). In the bottom plot the virtual combination of all LEP virtual measurements of $\Delta m_W(std, R_{cone} = 0.5\,rad)$ is shown as described in the text. The dashed curves reflect the results inferred from the $\Delta m_W(std, R_{cone} = 0.5\,rad)$ observable, while the dotted ones represent the particle flow result. The full line indicates the combination of both.*

7.3 Optimal convolution

The feasibility studies performed above could result in two different scenarios depending on the LEP combined information: one scenario where the ARIADNE and HERWIG models of Colour Reconnection are strongly disfavored by 4 to 5 standard deviations, while in the other scenario they are not that strongly disfavored. For both scenarios a proposal is described to reduce the total uncertainty on the m_W measurement in the fully hadronic W^+W^- decay channel.

Scenario I: ARIADNE and HERWIG models are strongly disfavored

When those implementations of Colour Reconnection are disfavored, this always implies that a significant amount of events reconnect according to the SK1 model in PYTHIA. Hence the data inferred value of m_W could be calibrated with the residual shift predicted by the SK1 model. The estimated statistical uncertainty on κ reflects the remaining systematic uncertainty due to Colour Reconnection on m_W. Following the virtual LEP combined log-likelihood of both the $\Delta m_W(std, R_{cone} = 0.5\,rad)$ and the particle flow information, shown in the bottom plot of Figure 7.14, the LEP preferred value of κ is 1.37 with a 68% confidence level interval of [0.78,2.18]. At a centre-of-mass energy of 200 GeV a shift $\Delta m_W([\kappa = 0] - [\kappa = 1.37])$ of -106 MeV/c^2 was found, while the confidence interval in κ can be translated into a statistical lower limit of -70 MeV/c^2 and an upper limit of -144 MeV/c^2. The correlation between the absolute value of the m_W estimator and the $\Delta m_W(std, R_{cone} = 0.5\,rad)$ observable was measured to be small, therefore it can to a good approximation be neglected. When applying this residual bias procedure the systematic uncertainty due to Colour Reconnection on m_W is due to the finite statistical precision of the κ measurement, resulting in a value around 40 MeV/c^2. Systematic influences of several model parameters, like for example the uncertainty on Q_0 (cfr. section 3.3), should be studied and added quadratically to this 40 MeV/c^2 uncertainty. The resulting value for m_W inferred from the data would be 106 MeV/c^2 lower and will by consequence show some 2σ deviation with the same physics quantity measured preliminary in the semi-leptonic W^+W^- decay channel [1]. After this bias correction the analysis could still be optimized by using the alternative m_W estimators.

Scenario II: ARIADNE and HERWIG models are not strongly disfavored

In this scenario the optimization of the total uncertainty is less trivial, as all three models are valid. On top of that, the irreducible shift due to the ARIADNE Colour Reconnection model remains a valid systematic uncertainty on the m_W determination. Therefore the application of alternative m_W estimators do not necessary reduce the total uncertainty. The following numbers are available in this scenario:

- $m_W^{std}(\mathrm{PYTHIA}, \tilde{\kappa})$;
- $m_W^{std}(\mathrm{ARIADNE}, \mathrm{noCR})$ and $m_W^{std}(\mathrm{ARIADNE}, \mathrm{CR})$;
- $m_W^{std}(\mathrm{HERWIG}, \mathrm{noCR})$ and $m_W^{std}(\mathrm{HERWIG}, \mathrm{CR})$;

where $\tilde{\kappa}$ is the data preferred value of κ measured from both $\Delta m_W(i,j)$ like observables and the particle flow method. Because all those Monte Carlo determined analyses are plausible, the systematic uncertainty on m_W to be quoted is the largest difference between any of those 5 numbers. The only possible procedure to reduce this systematic uncertainty is by applying a residual calibration. One calibrates the central value of m_W measured from the data with a virtual Monte Carlo model of which the estimated central value of m_W is in the middle of both the minimum and maximum of the 5 mentioned numbers. Again following the virtual LEP combination shown in Figure 7.14 and the results quoted in Table 7.1, the maximal difference would be between the ARIADNE or HERWIG values for m_W in the no Colour Reconnection hypothesis and the PYTHIA value at the data preferred value of κ, denoted by $m_W^{std}(\mathrm{PYTHIA}, \tilde{\kappa})$, hence about 106 MeV/c^2. Applying the procedure reduces the data inferred value of m_W by about 53 MeV/c^2 and leaving a systematic uncertainty due to Colour Reconnection of 53 MeV/c^2. The statistical 1σ lower and upper limits on κ reflect the values of $m_W^{std}(\mathrm{PYTHIA}, \tilde{\kappa} \pm 1\sigma)$. The difference between $m_W^{std}(\mathrm{PYTHIA}, \tilde{\kappa})$ and $m_W^{std}(\mathrm{PYTHIA}, \tilde{\kappa} \pm 1\sigma)$ which is due to a possible statistical fluctuation of κ measurement, should be added quadratically with 53 MeV/c^2. According to the feasibility study this difference is about 40 MeV/c^2, and therefore the total uncertainty due to Colour Reconnection would be around 66 MeV/c^2. This scenario is therefore less optimal compared to the previous one, but could still be improved when applying alternative m_W estimators in case if the reducible value of $m_W^{std}(\mathrm{PYTHIA}, \tilde{\kappa})$ is larger than the irreducible value $m_W^{std}(\mathrm{ARIADNE}, \mathrm{CR})$. The statistical precision on these alternative m_W estimators is however much lower.

In this scenario it could also be possible that the largest shift between the 5 above numbers is arising from the difference between the ARIADNE model in the no Colour Reconnection hypothesis and the ARIADNE model in the hypothesis that Colour Reconnection is present. This happens when the data preferred value of κ is smaller than about 0.7. The total uncertainty can in this case also be reduced by applying half of the shift as a residual calibration and quote the other half as a systematic uncertainty on m_W.

In both scenarios the precision on the measurement of κ in the SK1 model was found to be of major importance. A LEP combined measurement of the $\Delta m_W(std, R_{cone} = 0.5\,rad)$ or similar observable must be envisaged in order not to dilute completely the intrinsic information content on m_W of the hadronic decaying W^+W^- channel.

7.4 Structure of final analysis

From the studies explained in this chapter it was concluded that the LEP combined measurement of the W mass is dominated by systematic rather than statistical uncertainties. The most important systematic uncertainty is induced by the possible Colour Reconnection effect. To obtain a more optimal LEP combined measurement of the W mass which aims for the smallest total uncertainty on the inferred parameter, a residual calibration must be performed. Similar procedures could have been applied for the W width measurement. It was

shown that the W mass estimators in the hadronic W^+W^- channel applied by the four LEP experiments are equally sensitive to the parametrized SK1 effect [1, 82]. Therefore the same residual calibration as proposed in the feasibility studies could be employed for all experiments. The structure of the final W mass estimators in the hadronic channel must be defined according to the outcome of the true measurement of the Colour Reconnection effect.

In the following chapter the DELPHI results on m_W and Γ_W will be combined with the preliminary results from the three other LEP experiments in all possible scenarios. For scenario I it will be assumed that the virtual measurement of κ demonstrated by the log-likelihood in the bottom plot of Figure 7.14 is true. Almost the same data preferred value of κ is found when this hypothesis is compared with to the true combination performed in the top plot in Figure 7.14. Hence the assumption that the virtual measurement is a true measurement, is a very good approximation. When applying scenario II, it will be assumed that the shift due to the ARIADNE model of Colour Reconnection is larger compared to that predicted by the SK1 model in PYTHIA.

Chapter 8

Results on W boson resonance properties

In this chapter the results obtained on the W mass and width are combined with the preliminary DELPHI results obtained in the semi-leptonic W^+W^- decay channel and with preliminary results of the other LEP experiments [1]. The correlation between the systematic uncertainties will be taken into account. The combination procedure is optimized in order to result in the smallest possible variance on the inferred parameter. For the W mass estimators also different scenarios are considered for the treatment of the systematic uncertainty arising from the possible Colour Reconnection effect.

8.1 Individual data samples

The results obtained for the W mass and width in this thesis in a range of centre-of-mass energies are presented in Table 5.4 and Table 5.5. Also the central value and its statistical uncertainty are determined with a maximum likelihood technique when combining the likelihoods of all events from all centre-of-mass energies. The systematic uncertainties studied and estimated in chapter 6 and the one arising from Colour Reconnection effects, studied in chapter 7, will be added in quadrature together with the quoted statistical uncertainty. It was found however that some systematic uncertainties depend on the centre-of-mass energy at which the data sample has been collected. Therefore some event samples have more statistical power than others when combining all event likelihoods. In order to obtain the smallest variance on the inferred parameters from the combined event sample, some events should get more relative weight according to the component in their total uncertainty which is uncorrelated with other events.

In Figure 8.1 the individual W mass measurements for each year of data taking are shown. The value inferred from the data collected during the TPC-S6 period is shown separately. This plot indicates that, at least within the uncertainties of the measurements, the W boson mass is invariant within the LEP2 energy range.

8.2 Combination

In order to combine experimental measurements of the same physical quantity but with varying and correlated systematic uncertainties, a special procedure must be applied. At LEP2

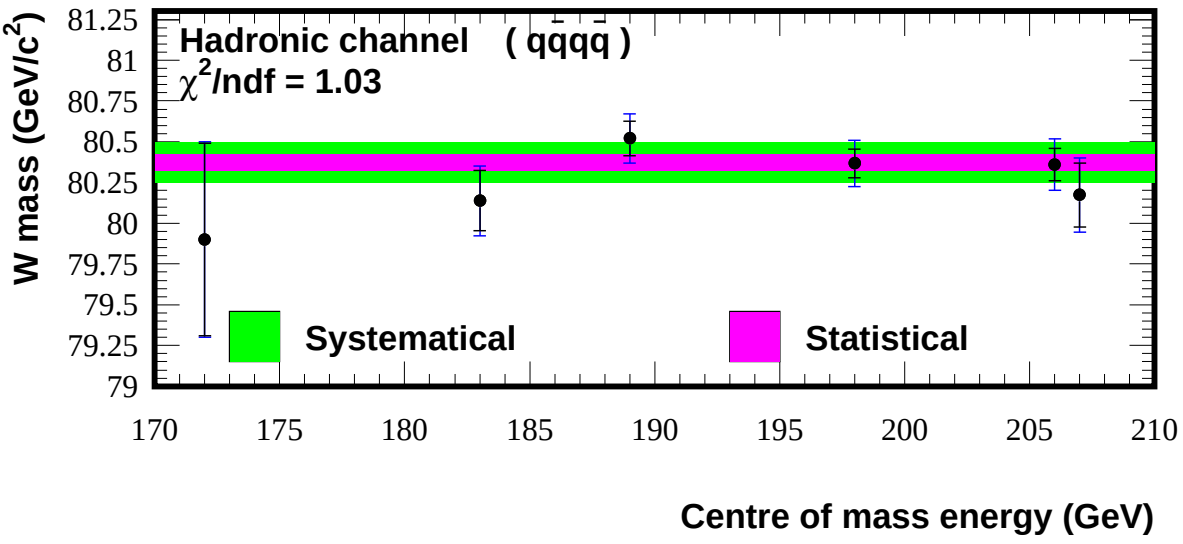

Figure 8.1: *Values of the W mass inferred from data samples collected during the different years of data taking by the DELPHI experiment. The inner bars reflects the statistical uncertainty, while the outer bars represent the total uncertainty. Also the combined value and the χ^2/ndf of the combined fit are shown as quoted in Table 8.1 with in purple the 1σ statistical uncertainty and in green the total uncertainty when taking into account the systematic uncertainties.*

the BLUE technique [87] (i.e. Best Linear Unbiased Estimate) is applied for combining these correlated measurements.

8.2.1 Combination procedure

Assume to have measured several unbiased estimates y_i with $i \in \{1, ..., n\}$ of a physical quantity, together with their covariance matrix E_{ij}. The different components of the uncertainty are supposed to be Gaussian. The diagonal elements E_{ii} reflect the variances of the individual estimates, while the off-diagonal elements of the matrix describe the correlations between pairs of estimates. The BLUE method provides an unbiased estimate $\hat{y}$ which is a linear combination of the individual estimates and aims for a minimum variance σ^2 on $\hat{y}$. Hence from the linearity condition it follows that:

$$\hat{y} = \sum_{i=1}^{n} \alpha_i y_i \tag{8.1}$$

where α_i is the weight of the measurement i in the combination, with the condition:

$$\sum_{i=1}^{n} \alpha_i = 1 \tag{8.2}$$

arising from the assumption that the measurements y_i and the combination $\hat{y}$ are unbiased. The variance on $\hat{y}$ can be written as:

$$\sigma^2 = \tilde{\alpha}\mathbf{E}\alpha = \sum_{i=1}^{n}\sum_{j=1}^{n} \alpha_i \alpha_j E_{ij} \ . \tag{8.3}$$

The BLUE technique consists of finding the n values of α_i which minimize σ^2, subject to the constraint of Equation 8.2. This can be achieved in several ways, resulting in

$$\alpha_i = \frac{\mathbf{E}^{-1}\mathbf{U}}{\tilde{\mathbf{U}}\mathbf{E}^{-1}\mathbf{U}} = \frac{\sum_{j=1}^{n}(E^{-1})_{ij}}{\sum_{i=1}^{n}\sum_{j=1}^{n}(E^{-1})_{ij}} \tag{8.4}$$

where $\mathbf{U}$ is a vector whose n components are all unity and $\mathbf{E}^{-1}$ is the inverse of the covariance matrix. From the obtained values of α_i it is possible to calculate $\hat{y}$ and σ^2 numerically. In a next step the procedure can estimate whether the individual measurements y_i are self consistent. A weighted sum of squares is constructed as:

$$S = \sum_{i=1}^{n}\sum_{j=1}^{n}(\hat{y} - y_i)(\hat{y} - y_j)(E^{-1})_{ij} \tag{8.5}$$

which measures the extent to which the individual values y_i are consistent with the combined value $\hat{y}$. From the minimum of S, which is expected to follow a χ^2 distribution with $n-1$ degrees of freedom, one can calculate the probability of observing the values y_i with their respective uncertainties when $\hat{y}$ is the true value of the physics quantity. The total uncertainty on $\hat{y}$ can be broken down into its component contributions from each independent source of type k:

$$(\sigma^k)^2 = \sum_{i=1}^{n}\sum_{j=1}^{n} \alpha_i \alpha_j \sigma^{k_i} \sigma^{k_j} \rho^{k_{ij}} \tag{8.6}$$

where $\rho^{k_{ij}}$ is the correlation coefficient for measurement i and j arising from the uncertainty of type k.

This method is applied for combining the results obtained in this thesis for each separate bin in centre-of-mass energy. Also via this BLUE technique those results will be combined with the preliminary DELPHI results obtained in the semi-leptonic W^+W^- channel and with other results obtained by the ALEPH, L3 and OPAL Collaborations.

8.2.2 Combination of all data points

For each year of data taking the W mass and width are determined with their corresponding statistical and systematical uncertainty components. The direct measurements performed by DELPHI at $\sqrt{s}$ = 172 GeV and indirectly from the threshold scan of the W^+W^- production cross-section are taken from publications [73] and [88]. Hence the full LEP2 period can be combined into one optimal measurement. The first and last columns denoted by 'general' in Table 8.1 summarize the results, with their uncertainty components separated according to the standard LEP defined classification [1]. The correlations between the years of for example the systematic uncertainty due to the LEP beam energy uncertainty, were taken into account.

Source of uncertainty	general m_W MeV/c^2	full calibration m_W MeV/c^2	half calibration m_W MeV/c^2	general Γ_W MeV/c^2
Statistical uncertainty	53	52	52	107
Detector	13	13	13	22
Fragmentation	15	15	15	20
Radiative Corrections	31	31	31	62
LEP beam energy	17	17	17	5
Others	11	10	11	41
Bose-Einstein Correlations	10	10	10	20
Colour Reconnection	94	-	43	106
Colour Reconnection measurement	40	40	-	-
Total systematic uncertainty	111	59	61	134
Total	123	78	80	172
Inferred value	80371	80261	80327	2192
χ^2 probability (in %)	40	39	39	53

Table 8.1: *Overview of the data results in the DELPHI combined hadronic W^+W^- channel for different scenarios for the treatment of the Colour Reconnection induced systematic uncertainty. The line denoted by 'Others' groups systematic uncertainties arising from for example the Monte Carlo calibration, the description of the background and the aspect ratio.*

The magnitude of the large systematic uncertainty due to Colour Reconnection is yet unclear to assess, because the measurements of the effect are still preliminary or yet unavailable. Therefore it was assumed that the final prior knowledge of the Colour Reconnection effect will be that arising from the feasibility study presented in section 7.2.2, hereafter called the virtual measurement of κ. The data preferred value of κ equal to 1.37 (bottom plot of Figure 7.14) was taken for assessing systematic uncertainties with the SK1 model of Colour Reconnection. For the W mass measurements, the ARIADNE and HERWIG models were not considered, as they give smaller systematic shifts compared to that expected with the SK1 model. The slope of the energy dependence of the SK1 systematic shift indicated in [1] and estimated at κ = 2.13 was taken for this study and the absolute scale of the curve was defined

by the DELPHI predicted value of the shift for κ = 1.37 at a centre-of-mass energy of 200 GeV. This procedure results in the following values for the shift : 83, 94, 100, 106 and 117 MeV/c^2 corresponding to the centre-of-mass energies 172, 183, 189, 200 and 207 GeV. As mentioned in section 7.2.2 there is a residual uncertainty of 40 MeV/c^2 on the predicted shift of the SK1 model using κ = 1.37. This is due to the statistical limitation on the measurement of the κ parameter. This residual systematic uncertainty, denoted by 'Colour Reconnection measurement' in the table, must be added in quadrature with the predicted systematic shift due to Colour Reconnection estimated with the tuned or measured SK1 model. It was assumed that the residual 40 MeV/c^2 is invariant in the whole LEP2 energy range, which is a reasonable approximation. Whenever the shift determined with ARIADNE or HERWIG was larger than the one estimated with the SK1 model (κ = 1.37) , as turn out to be the case for the W width measurement, this residual systematic uncertainty was for simplicity not added. For the W width estimator the largest shift was due to the difference between the ARIADNE model with and without the implementation of Colour Reconnection. The final values for the inferred W mass and width were:

$$\begin{array}{rcrcrl} m_W & = & 80.371 & \pm & 0.123 & \mathrm{GeV/c^2} \\ \Gamma_W & = & 2.192 & \pm & 0.172 & \mathrm{GeV/c^2} \end{array} \tag{8.7}$$

where both total uncertainties are dominated by the systematic uncertainty components. The statistical weights of the data measurement at $\sqrt{s}$ = 172 GeV and of the results obtained from the threshold scan are negligible. Therefore this thesis covers basically all data collected by the DELPHI experiment in the hadronic W^+W^- channel relevant for the measurement of the W mass and width.

A more optimal treatment of the systematic uncertainty due to Colour Reconnection was discussed in section 7.3. The solution proposed in scenario I applies a full calibration according to the virtual measured value of κ in the SK1 model, κ = 1.37. The resulting central value and uncertainties on the combined W mass measurement for the hadronic W^+W^- channel in DELPHI are quoted in the column denoted by 'full calibration' in Table 8.1. The results arising from the procedure described by scenario II are mentioned in the column named 'half calibration'. The largest systematic shift in m_W due to Colour Reconnection was assumed to be the one between the no Colour Reconnection hypothesis of ARIADNE and the ARIADNE model with its implementation of the Colour Reconnection effect. The evolution of this ARIADNE determined shift with the centre-of-mass energy was taken to be linear and interpolated (or extrapolated) between the values:

$$\begin{array}{rcrcrl} \Delta m_W \ (\mathrm{noCR-CR}, \sqrt{s}{=}\ 189\mathrm{GeV}) & = & -70 & \pm & 6 & \mathrm{MeV/c^2} \\ \Delta m_W \ (\mathrm{noCR-CR}, \sqrt{s}{=}\ 200\mathrm{GeV}) & = & -93 & \pm & 6 & \mathrm{MeV/c^2} \end{array} \tag{8.8}$$

which were determined by the OPAL Collaboration [89], but can be generally used for all LEP experiments.

After the residual calibrations, applied according to the procedures described, the total uncertainty on m_W is reduced by a significant amount. Because it is too preliminary to assess a final systematic uncertainty due to Colour Reconnection, the numbers quoted in 8.7 should be taken as the preliminary results of this thesis, but can be optimized whenever the full information about κ becomes available.

8.2.3 Combination with the semi-leptonic channel

The results obtained in the hadronic W^+W^- channel can be combined with the preliminary measurements in the semi-leptonic channel performed by the DELPHI experiment [90]:

$$\begin{array}{rcrcrcrcl} m_W & = & 80.414 & \pm & 0.074(\mathrm{stat}) & \pm & 0.048(\mathrm{syst}) & \mathrm{GeV/c^2} & \\ \Gamma_W & = & 2.158 & \pm & 0.189(\mathrm{stat}) & \pm & 0.082(\mathrm{syst}) & \mathrm{GeV/c^2} & . \end{array} \tag{8.9}$$

The components of the systematic uncertainty arising from the jet energy scale, aspect ratio, Initial State Radiation and LEP beam energy are taken as correlated between the analyses in the different decay channels. The LEP energy correlation matrix [22] is used to combine the results of different years of data taking. Except for the uncertainty arising from the finite calibration statistics, all other systematic uncertainties are conservatively assumed to be fully correlated between the different years. Combining these measurements yields:

$$\begin{array}{rcrcrcrcl} m_W & = & 80.404 & \pm & 0.053(\mathrm{stat}) & \pm & 0.053(\mathrm{syst}) & \mathrm{GeV/c^2} \\ \Gamma_W & = & 2.179 & \pm & 0.100(\mathrm{stat}) & \pm & 0.093(\mathrm{syst}) & \mathrm{GeV/c^2} \end{array} \tag{8.10}$$

with a χ^2/ndf = 0.64 (probability of 80.0%) for the W mass combination and a χ^2/ndf = 1.60 (probability of 12.0%) for the W width combination for being self consistent. The statistical weight of the information inferred in the fully hadronic channel in this combination is 31% for the W mass and 60% for the W width in the presence of the systematic uncertainties, while it would be respectively 67% and 76% in the absence of systematic uncertainties. This is due to the fact that the measurements of the W boson resonance characteristics in the semi-leptonic channel are not dominated by systematic uncertainties. Without the systematic uncertainties in both decay channels the statistical uncertainty would be 42 MeV/c^2 on the W mass and 93 MeV/c^2 on the W width measurement. The values of m_W estimated in the fully hadronic and semi-leptonic W^+W^- channels are in good agreement (cfr. section 9.1). Although the small significance of this test, of the order of 100 MeV/c^2, this observation constraints the effects on m_W in the hadronic channel due to Bose-Einstein Correlations and Colour Reconnection between the decay products of different W systems.

8.3 Combination with other LEP experiments

All LEP experiments provide measurements of the W mass and width from events collected in several but fixed bins of centre-of-mass energy, similar to those applied in this thesis. This they do for both the fully hadronic and semi-leptonic W^+W^- decay channels. It was shown in [1] that the m_W estimators of all LEP experiments are equally sensitive to the Colour Reconnection effect. When looking at the influence of the same Colour Reconnection model similar biases are observed by all experiments. Therefore this particular uncertainty was equalized between all experiments. The systematic uncertainties which are correlated between the different experiments arise from the following sources: Colour Reconnection, Bose-Einstein Correlations, fragmentation, the LEP beam energy, Initial and Final State Radiation. The LEP combination will be performed with different treatments for the Colour Reconnection uncertainty. Preliminary results from the ALEPH, L3 and OPAL Collabo-

rations will be used as mentioned in [1]. The comparison of all these results is shown in Figure 8.2.

8.3.1 Most general result

As for the combined DELPHI results, the most general case is to assess the full shift due to Colour Reconnection as a systematic uncertainty. Again the value of κ = 1.37, obtained from the virtual LEP combined likelihood $\mathcal{L}(\kappa)$ of the particle flow and $\Delta m_W(i,j)$ measurements was taken as a reference. The same energy dependence of the SK1 predicted shift, at κ = 1.37, as for the DELPHI only combination was taken. For the W width, the ARIADNE model of Colour Reconnection was taken as a reference because the shift induced by this model was the largest compared to other models. Combining only the information inferred from the hadronic decay channel yields values indicated in the columns denoted by 'general' in Table 8.2.

Source of uncertainty	general m_W MeV/c^2	full calibration m_W MeV/c^2	half calibration m_W MeV/c^2	general Γ_W MeV/c^2
Statistical uncertainty	36	30	31	86
Detector	7	7	7	23
Fragmentation	19	18	19	33
Radiative Corrections	12	12	12	31
LEP beam energy	17	17	17	10
Others	6	5	6	21
Bose-Einstein Correlations	14	14	14	32
Colour Reconnection	90	-	41	62
Colour Reconnection measurement	40	40	-	-
Total systematic uncertainty	104	51	50	83
Total	110	59	59	119
Inferred value	80448	80337	80414	2165
χ^2 probability (in %)	33	32	31	74

Table 8.2: *Overview of the data results in the LEP combined hadronic W^+W^- channel for different scenarios for the treatment of the Colour Reconnection induced systematic uncertainty.*

When combining the results determined in the fully hadronic and semi-leptonic decay channels, the results indicated in the columns denoted by 'general' in Table 8.3 are obtained. In this table also the relative weight of the information inferred from the fully hadronic channel is quoted. The difference with 100% is the relative weight of the information obtained from the semi-leptonic channel. A small fraction of this weight, of about 2-3%, is arising from the information of the indirect measurement of the W mass via the threshold scan of W^+W^- production. Due to the large uncertainties from possible cross talk effects

like Colour Reconnection the 4q weight is reduced to 8.5% for the m_W measurement, while is remains significant, 50.8%, for the W width measurement. Taking into account that the branching ratios for W^+W^- decay into both channels is about equal, this is not an ideal situation. Performing the LEP combination in the hypothesis that all systematic uncertainties are zero, the statistical uncertainty on the W mass would be 21.3 MeV/c^2 with still 62.1% probability for the combined fit. Similarly an uncertainty of 57.6 MeV/c^2 would be obtained for the W width with a probability of 50.9% for being self consistent.

Source of uncertainty	general m_W MeV/c^2	full calibration m_W MeV/c^2	half calibration m_W MeV/c^2	general Γ_W MeV/c^2
Statistical uncertainty	30	25	25	66
Detector	11	10	10	28
Fragmentation	18	17	18	28
Radiative Corrections	7	8	8	24
LEP beam energy	17	17	17	9
Others	4	3	3	15
Bose-Einstein Correlations	1	4	4	16
Colour Reconnection	8	-	11	27
Colour Reconnection measurement	3	11	-	-
Total systematic uncertainty	29	30	30	58
Total	42	39	39	88
Inferred value	80450	80420	80442	2172
χ^2 probability (in %)	72	59	70	61
weight 4q channel (in %)	8.5	28.4	28.2	50.8

Table 8.3: *Overview of the data results in both the LEP combined hadronic and semi-leptonic W^+W^- channels for different scenarios for the treatment of the Colour Reconnection induced systematic uncertainty.*

8.3.2 Colour Reconnection scenario I : 'full SK1 calibration'

The residual calibration procedure applied for the DELPHI results in the hadronic decay channel, can in a similar way be used in the LEP W mass combination. The central values of the estimated W mass from each individual data sample in this channel are shifted according to the predictions of the SK1 model using the data preferred value of κ = 1.37 from the feasibility study. The same energy dependent values are taken as mentioned in section 8.1.

The total uncertainty on the combined W mass measurement from the fully hadronic decay channel is reduced by almost a factor 2 after this residual calibration, cfr. column denoted by 'full calibration' in Table 8.2. Also the statistical component in the total uncertainty becomes more important, hence the result uses much better the available statistical information compared to the general case described above.

The column denoted by 'full calibration' in Table 8.3 shows the results from an optimal combined W mass measurements using the information from all W^+W^- decay channels. Also for this combination the total uncertainty is reduced after this residual calibration compared to the column denoted by 'general', but with a much smaller factor due to the small systematic uncertainties on the measurement in the semi-leptonic channel. The weight of the hadronic channel in the combination is however increased significantly to 28.4 % compared to 8.5 % in the 'general' case. As a result the statistical component in the total uncertainty becomes more important and therefore the determination of the central value will use the statistical available information in a more optimal way.

Applying this residual calibration procedure shifts the LEP combined W mass by about 30 MeV/c^2. This could alter the interpretation of the result when comparing the direct measurement obtained by the LEP Collaborations with the indirect measurements from the electroweak fits (see section 9.3).

In the absence of systematic uncertainties, but after applying the residual calibration procedure, the LEP combined statistical uncertainty on m_W is again 21.3 MeV/c^2 as expected, while the probability of the combined fit is reduced to 35.2% compared to 62.1% for the 'general' case without systematic uncertainties.

8.3.3 Colour Reconnection scenario II : 'half ARIADNE calibration'

In the case that the largest shift due to Colour Reconnection is observed with the ARIADNE implementation rather than the PYTHIA (SK1) implementation of the effect, only half of this shift can be applied as a residual calibration to obtain a more optimal measurement. The other half is then quoted as a systematic uncertainty on the W mass measurement. For all LEP experiments the shifts between the hypotheses with and without Colour Reconnection in ARIADNE were equalized to the ones interpolated (or extrapolated) from the values mentioned in Equations 8.8. After applying this calibration procedure all W mass information from the hadronic channel is combined and the result is quoted in the column denoted by 'half calibration' in Table 8.2. The improvement of the total uncertainty is about equal to the one observed in scenario I. Remember that the statistical uncertainty on the κ measurement was not translated into a systematic uncertainty on m_W for this scenario.

In the column denoted by 'half calibration' in Table 8.3 the LEP combination is shown of all W^+W^- decay channels. Again a similar improvement in total uncertainty is observed compared to that found by applying the calibration procedure in scenario I.

In the absence of systematic uncertainties, but after applying the residual calibration procedure, the probability of the LEP combined fit is 57.8%, which is only a small reduction compared to the 'general' case without systematic uncertainties, which gave 62.1% probability.

8.3.4 Systematic uncertainty due to radiative corrections

The absolute difference between WandY and RacoonWW determined in this thesis (cfr. section 6.6) was about 31 MeV/c^2 for the W mass estimator in the hadronic channel, while about 62 MeV/c^2 was found for the W width estimator. For the semi-leptonic channel a negligible shift was observed. Up to now the other LEP experiments do not have a similar estimate for

the systematic uncertainties due to the implementation of the electroweak radiative corrections in the matrix elements of the events. As for the influence of the Colour Reconnection effect on the W mass and width measurements, there is no indication that this shift would be different between the LEP experiments. It is therefore reasonable to assume that the same systematic uncertainty should be quoted by all experiments, rather than only by DELPHI. Also this systematic uncertainty is assumed to be correlated between the experiments.

The above performed combinations of the information inferred in all channels are repeated when equalizing the systematic uncertainty in the hadronic channel arising from the source labeled by 'Radiative Corrections' to the one estimated in this thesis. Table 8.4 summarizes the obtained results. The relative weight of the fully hadronic channel in the LEP combination is reduced in all scenarios compared to Table 8.3. Because also the central value is slightly shifted, it is recommended that LEP experiments other than DELPHI study this difference between WandY (or a similar generator) and RacoonWW.

Source of uncertainty	general m_W MeV/c^2	full calibration m_W MeV/c^2	half calibration m_W MeV/c^2	general Γ_W MeV/c^2
Statistical uncertainty	30	27	27	67
Detector	11	10	10	29
Fragmentation	18	17	17	28
Radiative Corrections	9	12	12	38
LEP beam energy	17	17	17	9
Others	4	3	3	15
Bose-Einstein Correlations	1	3	3	14
Colour Reconnection	7	-	9	26
Colour Reconnection measurement	3	9	-	-
Total systematic uncertainty	29	31	31	65
Total	42	41	41	94
Inferred value	80446	80423	80441	2174
χ^2 probability (in %)	70	58	67	61
weight 4q channel (in %)	7.1	22.0	21.6	45.7

Table 8.4: *Overview of the data results in both the LEP combined hadronic and semi-leptonic W^+W^- channels for different scenarios for the treatment of the Colour Reconnection induced systematic uncertainty. The uncertainty due to radiative corrections in the hadronic channel was equalized between the four LEP experiments, and fixed to the difference found between WandY and RacoonWW in this thesis.*

8.3.5 Comparison between LEP experiments

Figure 8.2 shows the inferred W mass values from the data of different LEP experiments. Results for different residual calibration treatments for the Colour Reconnection systematic

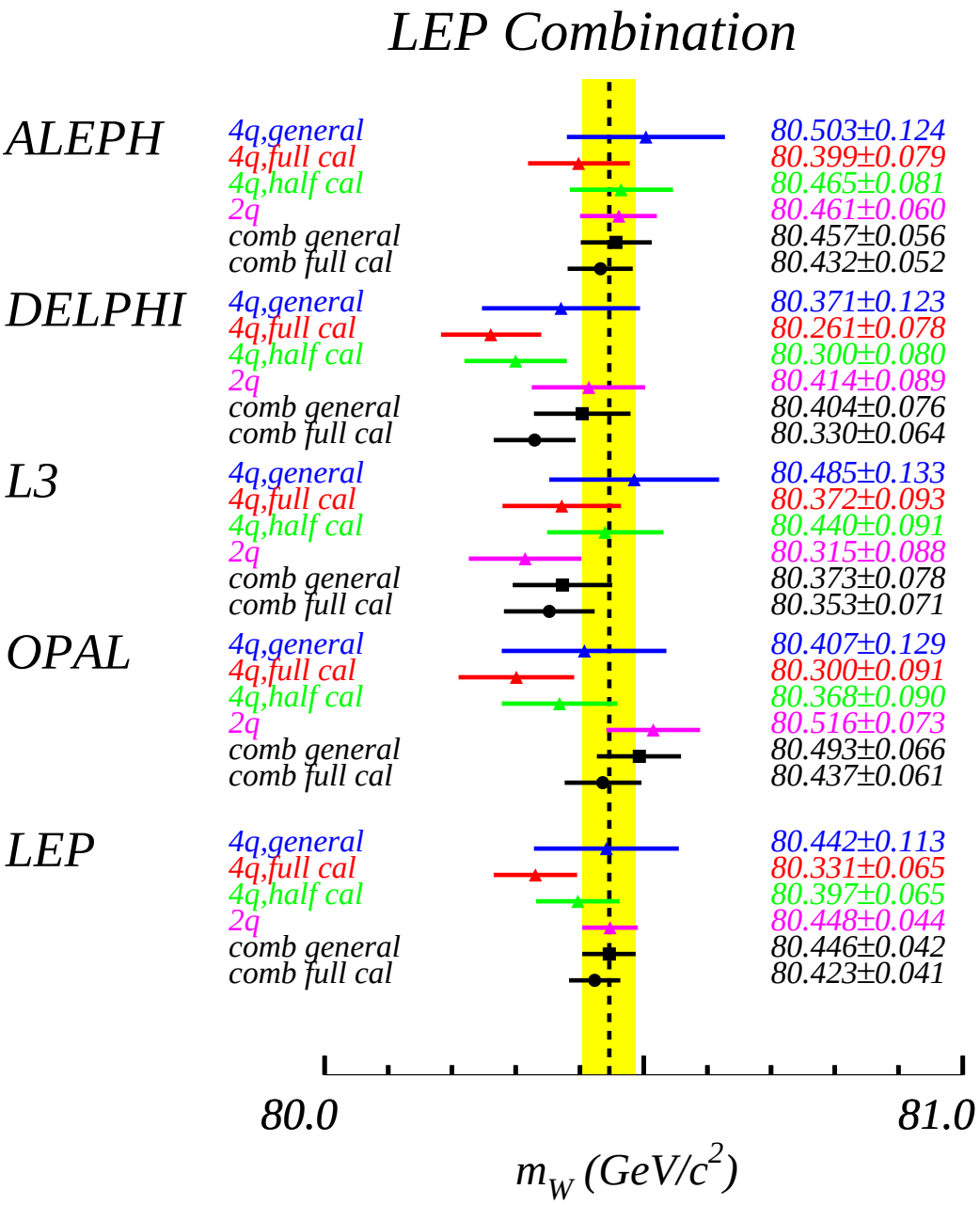

Figure 8.2: *Values of the W mass inferred from data samples collected by the different LEP experiments. The bars reflects the total uncertainty. Also the combined values are shown. The results denoted by '4q' and '2q' are inferred from respectively the fully hadronic and semi-leptonic W^+W^- decay channel. The different Colour Reconnection treatments are discussed and defined in the text.*

uncertainty were used. The uncertainty due to radiative corrections in the fully hadronic final state was equalized between all LEP experiments to the value obtained within this thesis for the difference between Wandy and RacoonWW (cfr. section 6.6). This figure illustrates visually the self consistency of the results between all LEP data sets, as reflected by the probability mentioned in Table 8.4.

8.4 Discussion and conclusions

The proposed treatments to reduce the Colour Reconnection uncertainty discussed in chapter 7 were executed in this chapter. The virtual likelihood arising from the feasibility study of a measurement of κ in the SK1 model was assumed to be a true likelihood reflecting the outcome of a true measurement. Whenever it becomes possible via these measurements to disfavor the ARIADNE and HERWIG models of Colour Reconnection to the extend that they can be discarded, it was shown that the total uncertainty of the LEP combined W mass measurement in the fully hadronic W^+W^- decay channel can be reduced from 110 to 59 MeV/c^2. Unarguably this reduction of about 46% is extremely important and can only be feasible when all LEP experiments perform a well scrutinized particle flow and differential W mass or $\Delta m_W(i,j)$ measurement. It has also a major impact on the LEP combined W mass from all W^+W^- decay channels, as the determination of the central value will use much better the statistical information.

It must however be noticed that the systematic uncertainty of the particle flow measurement could have been underestimated in [1]. The dominant uncertainty component was due to the modelization of the fragmentation and was studied by using three different models, namely PYTHIA, ARIADNE and HERWIG. The systematic uncertainty was assigned as the spread of the measured particle flow observable when using the various models. Because each of those fragmentation models are equally likely, a flat Bayesian prior should be assumed when quoting systematic uncertainties. Therefore a more correct evaluation of the systematic uncertainty is obtained when quoting the maximal difference between the observables estimated from the three models. Applying this procedure rather than the one used in [1] would lead to much larger uncertainties in the particle flow measurement. It turns out that the total uncertainty would be dominated by systematical rather than statistical components. This feature could alter the resulting likelihood $\mathcal{L}(\kappa)$ of the feasibility study performed in chapter 7 and also change the W mass and width combination determined in this chapter. Although this argument on the particle flow method, the concepts and conclusions of the studies presented in this thesis would remain valid after the proposed correction.

Chapter 9

Interpretation of the results

The results obtained on the W mass and width in this thesis and certainly their combined value with similar LEP measurements in other experiments and other decay channels, are extremely important for the interpretation of the Standard Model. As mentioned in chapter 1 those measurements, together with other direct measurements of electroweak parameters, constrain the predicted value of the mass of the yet undiscovered Higgs boson. Also the W mass and width values obtained from direct measurements can be compared with those inferred indirectly from the electroweak theory. Direct measurements in the two-dimensional plane of the W boson mass and the top quark mass, both highly sensitive to radiative corrections, can differentiate between the Standard Model and models beyond it. This chapter aims to summarize the state-of-art of the information contained in [1] together with the knowledge accumulated in this thesis.

9.1 Comparison of W boson resonance properties obtained from different WW decay channels at LEP2

Within the Standard Model, the leptonic decaying W bosons should have the same kinematic properties as those decaying hadronically. Therefore it is interesting to compare the inferred W mass and width from both decay channels. Because the measurements are dominated by systematic rather than statistical uncertainties, a possible difference could also indicate that some systematic uncertainties are wrongly estimated. Therefore when evaluating this difference, the systematic uncertainties arising from Colour Reconnection and Bose-Einstein Correlations in the fully hadronic decay channel are set to zero. The result is obtained from a fit where the imposed correlations are the same as those for the results given in chapter 8. The uncertainty due to radiative corrections in the fully hadronic final state is equalized between all LEP experiments to the value obtained within this thesis for the difference between WandY and RacoonWW (cfr. section 6.6). The columns denoted by 'general' in Table 9.1 summarize the central value and the uncertainty breakdown of this difference for the W mass and width without applying the residual calibrations for the Colour Reconnection treatment. It turns out that the W boson properties inferred from both decay channels are in extremely good agreement and also that the evaluated result is self consistent. This observation for the W mass is in contradiction with the likelihood obtained from the measurement of the

κ parameter within the SK1 model of Colour Reconnection (cfr. chapter 7). Although the limited statistical significance of this test, this inferred likelihood $\mathcal{L}(\kappa)$ disagrees with the LEP combined value of $\Delta m_W(4\mathrm{q} - 2\mathrm{q})$ by roughly 2 standard deviations. This can already be observed in the results quoted in the column denoted by 'full calibration' in Table 9.1. In the determination of these numbers the shift predicted by the SK1 model was applied on the central value of the data inferred values for the W mass in the hadronic channel, while the residual systematic uncertainties due to Colour Reconnection and Bose-Einstein Correlations were set to zero. Similar to the studies performed in chapter 8 the value of κ was taken from the feasibility study in chapter 7. When applying this residual calibration procedure, the value of $\Delta m_W(4\mathrm{q} - 2\mathrm{q})$ deviates significantly from zero. For completeness also the results from a residual calibration defined by the Colour Reconnection treatment denoted by 'half calibration' in chapter 8 are quoted in Table 9.1.

Source of uncertainty	general Δm_W MeV/c^2	full calibration Δm_W MeV/c^2	half calibration Δm_W MeV/c^2	general $\Delta\Gamma_W$ MeV/c^2
Detector	9	9	9	26
Fragmentation	17	17	17	28
Photonic	16	16	16	42
LEP beam energy	17	17	17	8
Others	3	3	3	17
Total systematic uncertainty	30	30	30	60
Total	49	49	49	153
Inferred value	10	-97	-33	-12
χ^2 probability (in %)	65	64	63	55

Table 9.1: *Overview of the data results for the difference $\Delta m_W(4q - 2q)$ of the W boson properties inferred in the LEP combined hadronic and semi-leptonic W^+W^- channels for different scenarios for the treatment of the Colour Reconnection induced systematic uncertainty.*

9.2 World average for W boson properties

The mass and width of the W boson was directly measured by the UA2 experiment [91] at CERN and from data collected by the CDF [92, 93] and D0 [94, 95] experiments at the Tevatron collider in Fermilab (Chicago, US). The W bosons were produced in $\mathrm{p\bar{p}}$ collisions and their leptonic decay was studied. The shape of the inclusive transverse mass spectrum contains information on the parameters of interest, therefore a maximum likelihood fit on this distribution was used to infer both the W boson mass and width. In Figure 9.1 the obtained values from the Run I of the Tevatron are compared and combined with the results from LEP2. The combined LEP2 result reflects the 'general' case without any residual calibrations in the fully hadronic channel. In fact the preliminary LEP2 result quoted in [1] was used

rather than the numbers presented in this thesis. They only differ by $\sim$1 MeV/c^2, mainly due to the DELPHI updated values evaluated in this thesis. A remarkable good agreement is observed between the results of both completely different methods applied in different physics collisions. When residual calibrations would have been applied to optimize the uncertainty due to Colour Reconnection, the agreement would still be good.

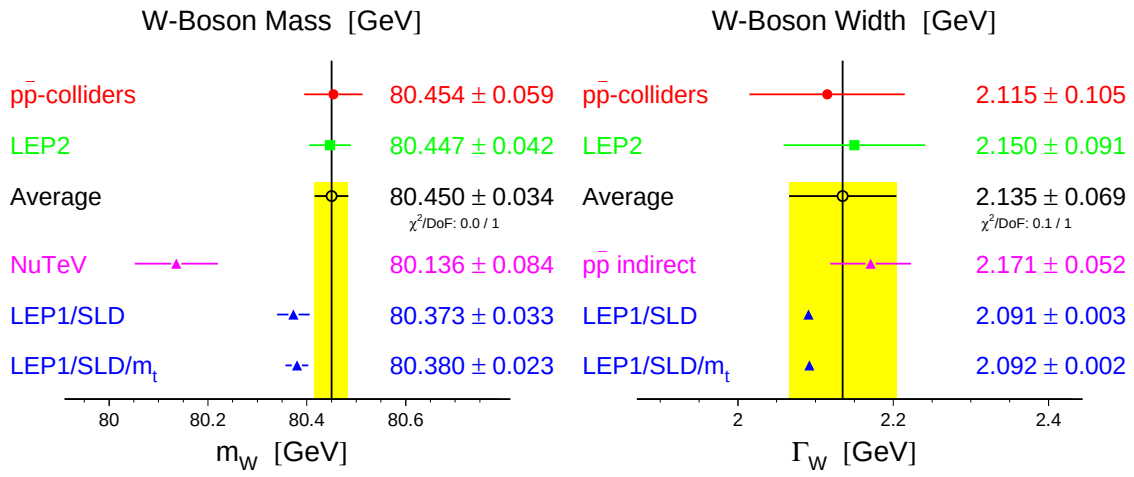

Figure 9.1: *Comparison of direct and indirect measured W boson properties [1].*

9.3 Compatibility within the Standard Model

The precise electroweak measurements performed by experiments can be used to test the validity of the Standard Model and, within its framework, to infer valuable information about its fundamental parameters (cfr. section 1.5). The bottom parts in Figure 9.1 indicate the results calculated indirectly via Standard Model equations. Separately shown is the recent measurement from the NuTeV Collaboration [16]. From the ratio of neutral to charged current cross-sections in neutrino-nucleon scattering, a precise measurement was extracted for $\sin^2\theta_W$, which can be directly related to m_W via the electroweak relation 1.14. A significant disagreement of about three standard deviations was found between this indirect W mass measurement and the world combined direct measurement. It was already mentioned in section 1.5 that this observation has a non-negligible effect on the probability for the data to be self consistent within the global electroweak fit. The NuTeV experiment took data exclusively in 1996 and 1997, hence investigations with increased statistics are not possible or are at least not planned in the nearby future.

Apart from the W boson also the top quark plays a crucial role when calculating radiative corrections in the Standard Model. The measurements of the mass of the top quark performed by the CDF [96] and D0 [97] experiments were combined to a value of m_t = 174.3 $\pm$ 5.1 GeV/c^2. The direct measurements of both the W boson and top quark mass are compared

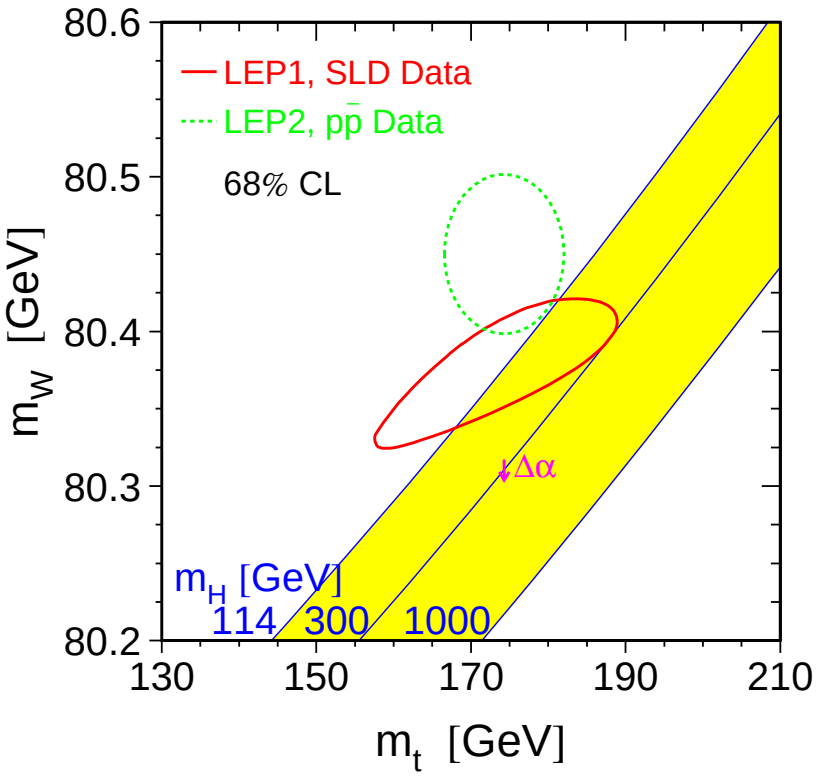

Figure 9.2: *Comparison of direct and indirect measured W boson and top quark mass, indicated by respectively the dashed and solid contours. In both cases the 68% CL contours are plotted. Also shown is the Standard Model relationship for the masses as a function of the Higgs boson mass. The arrow labeled* $\Delta\alpha$ *shows the variation of this relation if* $\alpha(m_Z^2)$ *is changed by one standard deviation. This variation gives an additional uncertainty to the Standard Model band shown in the fi gure.*

with their indirect evaluation in Figure 9.2. A reasonable agreement is found between the direct and indirect measurements and both of them prefer a low value of the Higgs mass. The proposed residual calibrations for the treatment of the large uncertainty due to Colour Reconnection would bring both results even closer to each other, as the inferred W mass would be about 30 MeV/c^2 lower than shown in Figure 9.2. This confirms in some sense the existence of the effect.

The uncertainty on the effective electromagnetic coupling $\alpha(m_Z^2)$ arises from the contribution of light quarks to the photon vacuum polarization, $\Delta\alpha^{(5)}_{had}(m_Z^2)$, as mentioned in Equation 1.18. These hadronic corrections can be related through dispersion integrals to the cross-section for hadron production in e^+e^- collisions in the centre-of-mass energy range below 5 GeV. They cannot be calculated from first principles and should be measured experimentally. New projects have been setup at the e^+e^- B-factories like BaBar and BELLE for a

much better measurement with less systematic uncertainties. However, there exists not one, but two measured values. The second one arises from τ decay data and differs from the first by more than two standard deviations [98]. This theoretical uncertainty on the hadronic contributions to $\alpha(m_Z^2)$ induces a noticeable effect for the indirect determination on the Higgs mass via global electroweak fits. It turns out that the difference between the e^+e^- determined and the τ-based evaluation translates into a shift of 16 GeV/c^2 on the Higgs mass value. This is the main theoretical uncertainty entering the blue band in Figure 9.3, which reflects the information one can infer on the Higgs boson mass from the electroweak measurements, assuming the Standard Model relations. The 95% CL upper limit on m_H is 193 GeV/c^2.

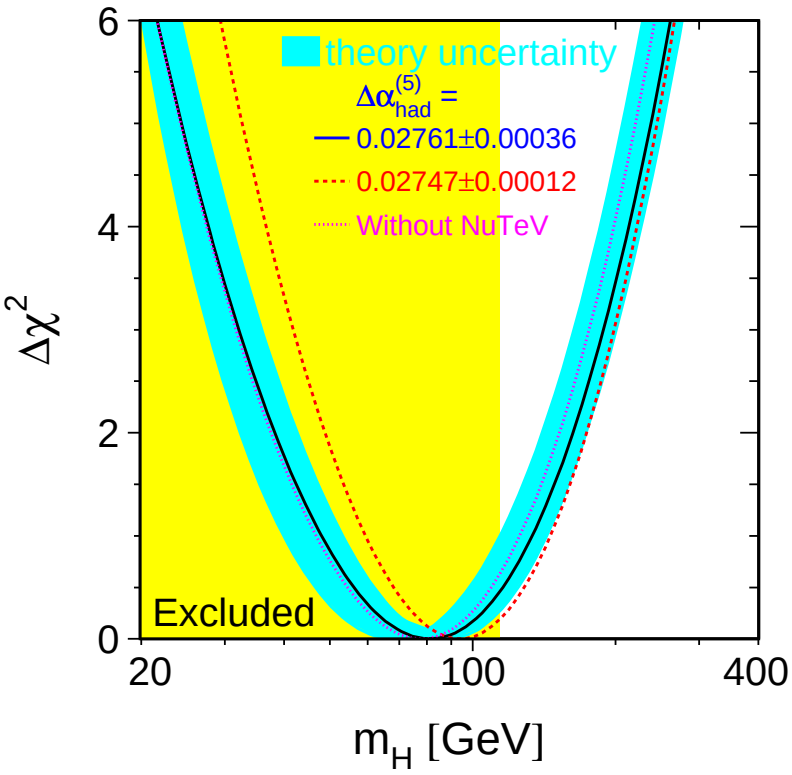

Figure 9.3: *The so-called 'blue band plot' illustrates the $\Delta\chi^2$ of the indirect fit to infer the mass of the Higgs boson. The line is the result of the fit using all data, while the band represents an estimate of the theoretical uncertainty due to missing higher order corrections. The vertical band shows the 95% CL exlusion limit on the Higgs boson mass from the direct search at LEP2. The dashed curve is the result obtained using the evaluation of $\Delta\alpha^{(5)}_{had}(m_Z^2)$ from reference [99].*

The contribution in the global fit for the Higgs boson mass of each individual measurement of an electroweak parameter or pseudo-observable related to those, is shown in Figure 9.4. The direct measurement of the W boson mass prefers a light Higgs boson with a

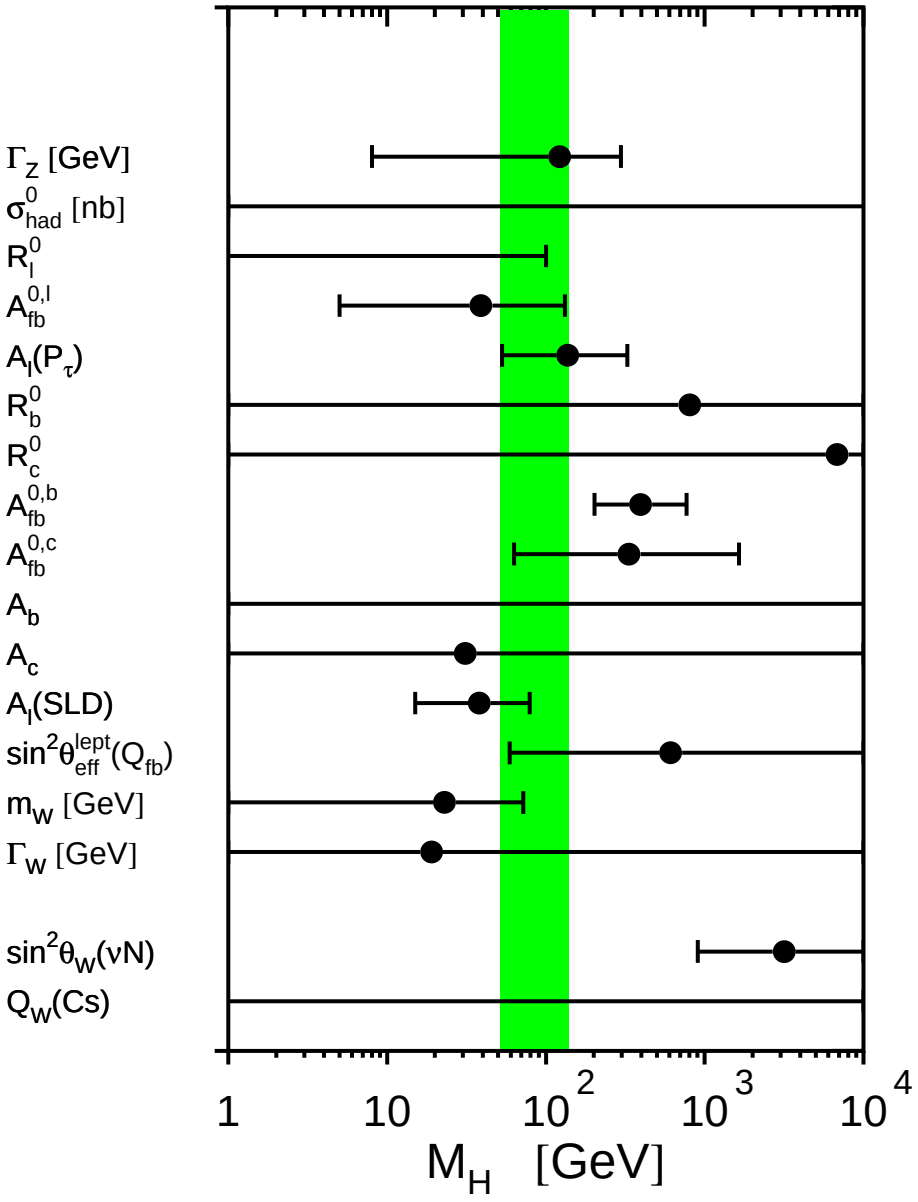

Figure 9.4: *Constraints on the mass of the Higgs boson from each pseudo-observable. The Higgs boson mass and its 68% CL uncertainty is obtained from a five-parameter Standard Model fit to the observable, constraining* $\Delta\alpha^{(5)}_{had}(m_Z^2) = 0.02761 \pm 0.00036$, $\alpha_s(m_Z^2) = 0.118 \pm 0.002$, $m_Z = 91.1875 \pm 0.0021$ *GeV/c*^{2} *and* $m_t = 174.3 \pm 5.1$ *GeV/c*^{2}. *Because of these four common constraints the resulting Higgs boson mass values cannot be combined at once. The shaded band denotes the overall constraint on its mass derived from all pseudo-observables including the above four Standard Model parameters.*

mass around 20 GeV/c^2, while the NuTeV results on $\sin^2\theta_W(\nu\mathrm{N})$ and the forward-backward asymmetry $A_{fb}^{0,b}$ measurement from LEP push its central value to higher values. The direct values of these last two measurements are significantly different from their indirect expectations, resulting in large pull shown in Figure 1.3.

9.4 Compatibility with models beyond the Standard Model

As discussed in section 1.7, the Standard Model is generally expected not to be the final theory about particle physics. Many experimentalists and theoreticians search for signals or models to extend this, up to now correct, phenomenological model. Besides these internal consistency checks of the Standard Model, the electroweak precision observables may be useful to distinguish between different candidates for alternative electroweak theories. In Figure 9.5 the Standard Model prediction of the W mass as a function of the top quark mass is compared with the prediction within the Minimal Supersymmetric extension of the Stan-

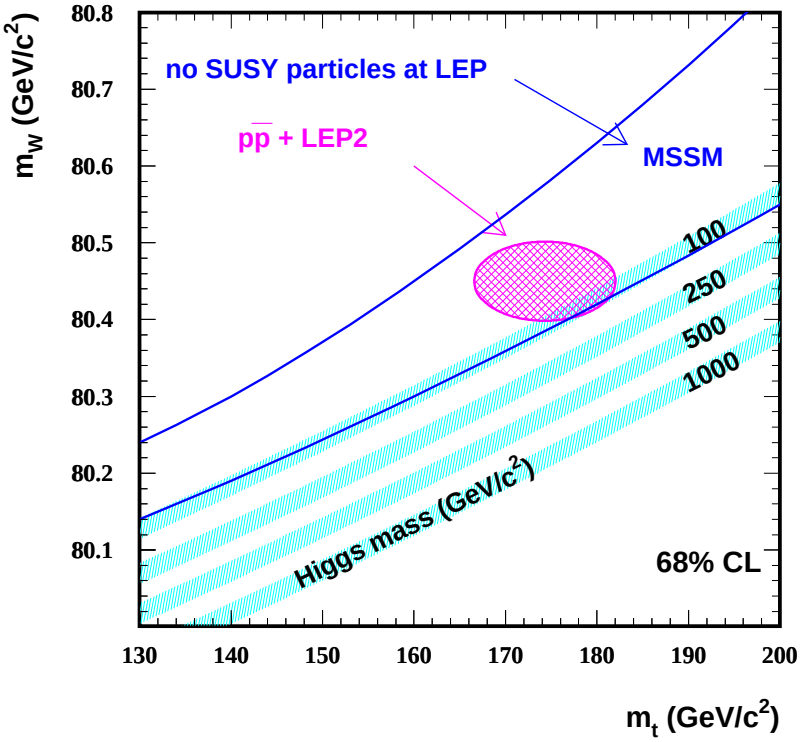

Figure 9.5: *Constraints in the two dimensional space of the W boson and top quark mass due to their direct measurements, together with the predictions for the Standard Model Higgs boson mass (ranging continuously from 100 to 1000 GeV/c^2) and the allowed phase-space for the MSSM.*

dard Model or MSSM. The calculations of the MSSM prediction are based on results quoted in [100]. The largest uncertainty within the Standard Model arises from the mass of the yet undiscovered Higgs boson, while in the MSSM this is not a free parameter. The uncertainty on the MSSM allowed phase-space originates from the unknown mass scales of supersymmetric particles. In the small overlap region between both models, the MSSM behaves like the Standard Model, because all supersymmetric particles are heavy and decouple from the electroweak precision observables. It can be seen that in the MSSM the mass of the lightest MSSM Higgs boson must be smaller than about 130 GeV/c^2 for m_t = 175 GeV/c^2 [19].

The world combined values of the direct top quark and W boson mass measurements certainly do not exclude the MSSM, but when in the future a Higgs boson is found, those measurements could differentiate between a Standard Model and a MSSM Higgs boson.

9.5 Outlook

Because the properties of the W boson occupy a crucial place in the verification of the Standard Model or theories beyond it, the research towards a more precise evaluation of those parameters will continue. At some LEP experiments there is still some work to be done before finalizing the W mass and width analyses. The proposals for the treatment of Colour Reconnection systematic uncertainties discussed in this thesis have still to be approved by all LEP Collaborations. Also the accumulation of the prior knowledge on the Colour Reconnection models with the measurements of the particle flow ratio and the $\Delta m_W(i,j)$-like observable is still ongoing. The expected uncertainty on the final LEP combined W mass and width could be slightly smaller than those quoted in the columns denoted by respectively 'full calibration' and 'general' in Table 8.4, because some experiments do not yet have preliminary results for the full LEP2 data set.

In the nearby future the CDF and D0 experiments will measure the mass and width of the W boson from their data collected during the Run II phase (2001-2005) of the Tevatron collider. From these analyses they expect to obtain a precision on the W mass of about 30 MeV/c^2 per experiment [101] giving a Tevatron combined uncertainty of about 25 MeV/c^2. For the top quark mass a final resolution of 2 to 3 GeV/c^2 is expected.

Next in line is the Large Hadron Collider or LHC which should, from 2007 onwards, produce pp collisions. Two multi-purpose detectors, CMS and ATLAS, will be built around the interaction points, and again from the transverse mass distribution of leptonic decaying W bosons an estimate can be made for the W boson mass and width. The target accuracy for the W mass is of the order of 15 MeV/c^2, which exceeds the precision of all previous measurements. The expected uncertainty to which they could infer the top quark mass is about 1 GeV/c^2. Both measurements would shrink the direct measured ellipse in Figures 9.2 and 9.5, but still the LEP results on the W mass would remain important as they are measured in a completely different physics environment with different systematic uncertainties.

Therefore the obtained results in this thesis will remain important until the data taking with a linear collider becomes possible. These proposed experiments could probably be ready to start data taking around 2012. Among them one find three projects : TESLA at DESY in Europe, NLC in the United States and JLC in Japan. This category of linear collider experiments could evaluate the top quark mass to a precision of about 40 MeV/c^2 from

a threshold scan, while the expected uncertainty for the W boson mass is about 6 MeV/c^2. Although these remarkable possible achievements exceed the precision of all previous measurements, one needs some precise knowledge on electroweak parameters for commissioning and designing these immense experiments. The human and financial efforts needed to accomplish these machines are so extreme that they will probably be unique and one has to take into account different discovery scenarios in the design of the experiments. Therefore the LEP results on the W mass still remain interesting during the design of the machine parameters, as they enter in many radiative corrections which can be used to exclude some of the allowed regions of phase-space for the Standard Model or theories beyond it.

Summary

This thesis presents the measurements of the W boson mass and width in the fully hadronic W^+W^- decay channel in e^+e^- collisions at LEP. A Bayesian convolution technique was applied to infer information about these main parameters characterizing the W boson resonance. The analysis was based in a frequentist way on Monte Carlo simulation of the physics and detector of interest. With a novel approach, related to Kalman filtering techniques, it was shown that the estimators made optimal use of the relevant statistical information content of the events. All relevant data sets collected by the DELPHI experiment were used and the work includes the complete study and evaluation of possible systematic uncertainties on the constructed estimators, yielding:

$$\begin{array}{rcrcrcl} m_{\mathrm{W}} & = & 80.371 & \pm & 0.053\,(\mathrm{stat}) & \pm & 0.111\,(\mathrm{syst}) \quad \mathrm{MeV/c^2} \\ \Gamma_{\mathrm{W}} & = & 2.192 & \pm & 0.107\,(\mathrm{stat}) & \pm & 0.134\,(\mathrm{syst}) \quad \mathrm{MeV/c^2} \end{array}$$

after combination. It turned out that the largest systematic uncertainty component arises from the possibility of Colour Reconnection between the two fragmenting W systems in the event and dominates the LEP combined statistical uncertainty of the W mass measurement in the fully hadronic decay channel by a factor 2 or 3. A novel method was proposed to extract information about this yet unknown or at least unclear effect. After applying this method on the DELPHI data together with the results from the particle flow method within DELPHI, it was found that some of the phenomenological models prefer a non-negligible amount of Colour Reconnection. For the SK1 model a value for κ of 1.96 was preferred with a 68% confidence interval of [0.66,4.56], which suggests the existence of the effect as a 2σ deviation from zero. With this prior knowledge a proposal and feasibility study was initiated for the LEP experiments to optimize their measurements of the W mass in this particular decay channel. The inferred information about Colour Reconnection models was optimally convoluted into the Bayesian m_W estimator by applying residual calibrations on its bias. A reduction of the total uncertainty by 45% could be envisaged for the LEP combination of this measurement, resulting in a preliminary value of :

$$m_{\mathrm{W}} = 80.337 \pm 0.030\,(\mathrm{stat}) \pm 0.051\,(\mathrm{syst}) \quad \mathrm{MeV/c^2}$$

rather than the less optimal value :

$$m_{\mathrm{W}} = 80.448 \pm 0.036\,(\mathrm{stat}) \pm 0.110\,(\mathrm{syst}) \quad \mathrm{MeV/c^2} \quad .$$

obtained without applying the residual calibrations proposed in this thesis. In the determination of the other systematic uncertainties original methods were designed or extended.

A global tuning of the PYTHIA model parameters describing the jet fragmentation and the LUBOEI model parameters describing the Bose-Einstein Correlations between identical bosons was proposed and performed. The predicted event shape, single and double particle distributions were compared with those obtained from the copious LEP1 hadronic Z^0 data. The results are interesting for the measurement of the strength of the Bose-Einstein Correlations between identical bosons arising from the decay of different W bosons in W^+W^- events. The method of the so-called Mixed Lorentz Boosted Z^0's was extended and it was verified that it can be utilized to estimate systematic uncertainties arising from the reconstruction or simulation of jets. Applying the method on both the W mass and width measurements did facilitate the evaluation of those systematic uncertainties.

The obtained results on the W mass will remain important until the data of a high energy linear collider becomes available. Probably one has to wait until the year 2014 for first results inferred from these data.

Appendix A

The Jackknife method

With the advent of fast computers useful statistical tools to estimate the uncertainties of fit parameters became popular. One of them is called the 'Jackknife' and was invented in 1956 by Quenouille and developed further by Tukey in 1957. The method can be used instead of the more recent bootstrap method, developed by Efron [102] in the late 1970's.

Starting from a sample of $\mathcal{N}$ measurements, the Jackknife begins by throwing out the first measurement, leaving a Jackknifed data set of $\mathcal{N}-1$ values. The statistical analysis is performed on the reduced sample, giving a measured value of a parameter m_i^{Jack}. The process is repeated for each measurement i in the sample, resulting in a set of parameter values $\{m_i^{\text{Jack}}|i=1,...,\mathcal{N}\}$. The standard uncertainty on the parameter, σ^2_{Jack}, estimated on the full sample of $\mathcal{N}$ measurements is given by the formula:

$$\sigma^2_{\text{Jack}} = \frac{\mathcal{N}-1}{\mathcal{N}} \cdot \sum_{i=1}^{\mathcal{N}} (m_i^{\text{Jack}} - m)^2 \tag{A.1}$$

where m is the result of inferring the parameter on the full sample. The advantage of using this method compared to other bootstrap techniques is that no knowledge is assumed about the underlying probability density function. The Jackknife method was used in this thesis to evaluate the statistical uncertainties on the difference in inferred m_W or Γ_W between correlated event samples.

Appendix B

Update of ALEPH results

The ALEPH experiment updated their results concerning the W mass measurement for the winter conferences 2003 [103]. They quote a significant shift in the central values compared to previous preliminary or published results [1]. This was explained by an incomplete simulation of the electromagnetic showers in their calorimeters initiated by low energetic neutral particles. For completeness of the thesis and not to confuse the reader too much by changing the main text, this appendix collects the update of some of the relevant tables and figures. All conclusions drawn in the chapter 7 and 8 of this thesis concerning the treatments of Colour Reconnection uncertainties via the feasibility study remain valid. It is mainly the LEP combined value of the W mass, as mentioned in Figure 8.2, which is changed from m_W = 80.446 $\pm$ 0.042 GeV/c^2 to m_W = 80.411 $\pm$ 0.043 GeV/c^2. This update brings the direct measurement of the W mass closer to the indirect measured one.

Source of uncertainty	general m_W MeV/c^2	full calibration m_W MeV/c^2	half calibration m_W MeV/c^2
Statistical uncertainty	35	28	30
Detector	10	11	10
Fragmentation	18	17	19
Photonic	12	12	12
LEP beam energy	17	17	17
Others	6	5	6
Bose-Einstein Correlations	14	14	14
Colour Reconnection	90	-	38
Colour Reconnection measurement	40	40	-
Total systematic uncertainty	104	52	51
Total	110	59	59
Inferred value	80420	80318	80390
χ^2 probability (in %)	53	51	51

Table B.1: *Update of Table 8.2. Overview of the data results in the LEP combined hadronic W^+W^- channel for different scenarios for the treatment of the Colour Reconnection induced systematic uncertainty.*

Source of uncertainty	general m_W MeV/c^2	full calibration m_W MeV/c^2	half calibration m_W MeV/c^2
Statistical uncertainty	29	24	25
Detector	14	13	13
Fragmentation	18	18	18
Photonic	8	9	9
LEP beam energy	17	17	17
Others	4	3	3
Bose-Einstein Correlations	1	4	4
Colour Reconnection	8	-	11
Colour Reconnection measurement	3	12	-
Total systematic uncertainty	31	32	32
Total	43	40	40
Inferred value	80414	80388	80409
χ^2 probability (in %)	76	66	75
weight 4q channel (in %)	8.6	29.0	28.8

Table B.2: *Update of Table 8.3. Overview of the data results in both the LEP combined hadronic and semi-leptonic W^+W^- channels for different scenarios for the treatment of the Colour Reconnection induced systematic uncertainty.*

Source of uncertainty	general m_W MeV/c^2	full calibration m_W MeV/c^2	half calibration m_W MeV/c^2
Statistical uncertainty	30	26	26
Detector	14	13	13
Fragmentation	18	18	18
Photonic	9	13	13
LEP beam energy	17	17	17
Others	4	3	4
Bose-Einstein Correlations	1	3	3
Colour Reconnection	6	-	9
Colour Reconnection measurement	3	9	-
Total systematic uncertainty	31	32	32
Total	43	41	41
Inferred value	80411	80391	80407
χ^2 probability (in %)	75	66	74
weight 4q channel (in %)	7.1	22.2	21.9

Table B.3: *Update of Table 8.4. Overview of the data results in both the LEP combined hadronic and semi-leptonic W^+W^- channels for different scenarios for the treatment of the Colour Reconnection induced systematic uncertainty. The uncertainty due to radiative corrections in the hadronic channel was equalized between the four LEP experiments, and fixed to the difference found between WandY and RacoonWW in this thesis.*

Source of uncertainty	general Δm_W MeV/c^2	full calibration Δm_W MeV/c^2	half calibration Δm_W MeV/c^2
Detector	12	12	12
Fragmentation	17	17	17
Photonic	16	16	16
LEP beam energy	17	17	17
Others	3	3	3
Total systematic uncertainty	32	32	32
Total	48	48	48
Inferred value	22	-81	-21
χ^2 probability (in %)	71	69	69

Table B.4: *Update of Table 9.1. Overview of the data results for the difference $\Delta m_W(4q-2q)$ of the W boson properties inferred in the LEP combined hadronic and semi-leptonic W^+W^- channels for different scenarios for the treatment of the Colour Reconnection induced systematic uncertainty.*

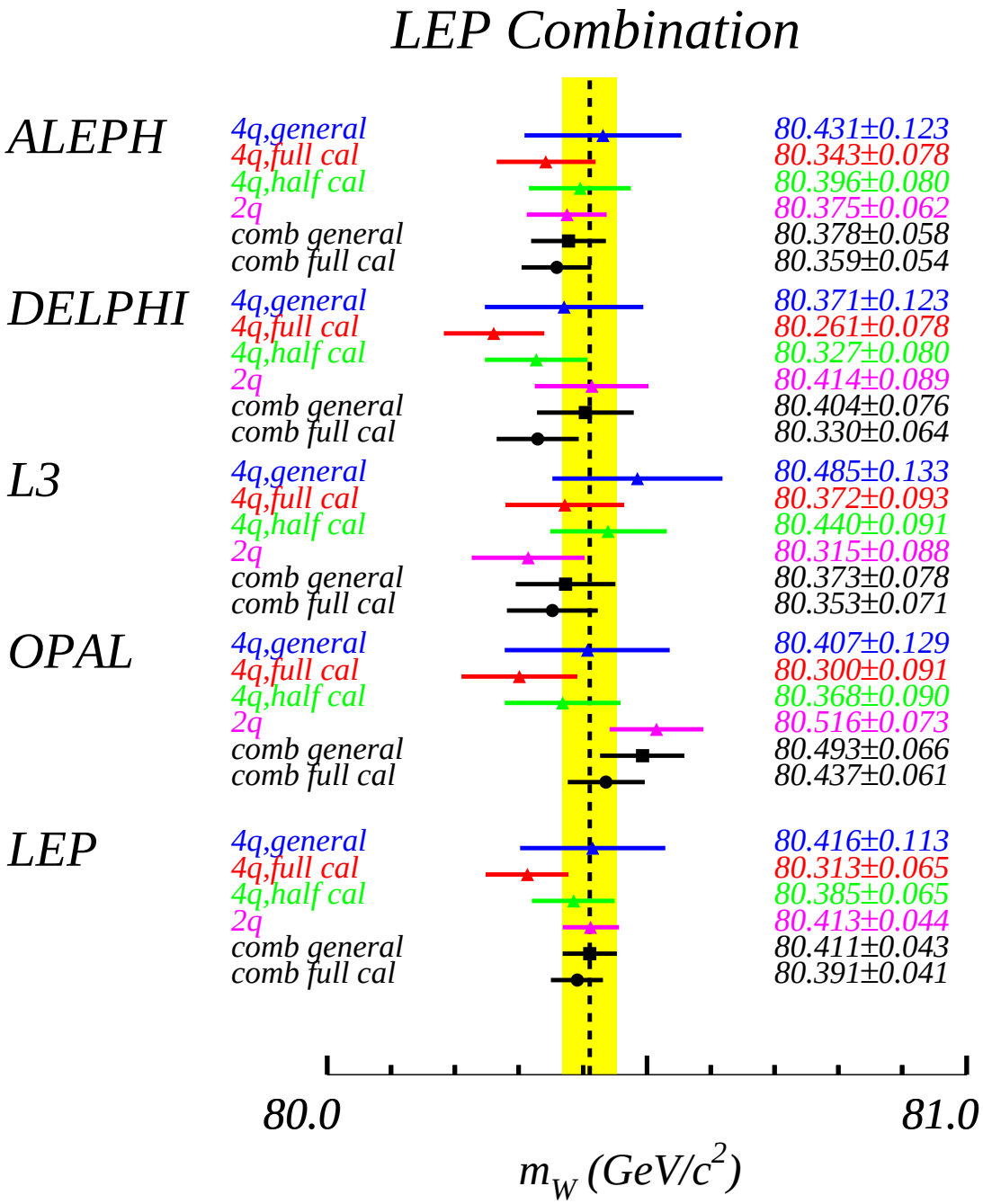

Figure B.1: *Update of Figure 8.2. Values of the W mass inferred from data samples collected by the different LEP experiments. The bars reflects the total uncertainty. Also the combined values are shown. The results denoted by '4q' and '2q' are inferred from respectively the fully hadronic and semi-leptonic W^+W^- decay channel. The different Colour Reconnection treatments are discussed and defined in the text.*

Bibliography

[1] The LEP and SLD Collaborations, *A combination of preliminary electroweak Measurements and Constraints on the Standard Model*, CERN-EP 2002-091 and hep-ex/0212036.

[2] The LEP Collaborations, *Search for the Standard Model Higgs boson at LEP in the year 2000*, contributed paper for ICHEP 2002 (Amsterdam).

[3] S. Weinberg, *The quantum theory of fields. Volume 1: Foundations*, Cambridge Univ. Press, 1995;
S. Weinberg, *The quantum theory of fields. Volume 2: Modern applications*, Cambridge Univ. Press, 1996.

[4] S.L. Glashow, *Partial-Symmetries of Weak Interactions*, Nucl. Phys. **B22**(1961) 579.

[5] A.Salam and J.C. Ward, *Electromagnetic and Weak Interaction*, Phys. Lett.**13**(1964) 168.

[6] S. Weinberg, *A model of Leptons*, Phys. Rev. Lett.**19**(1967) 1264.

[7] R. Brout and F. Englert, *Broken symmetry and the mass of gauge vector mesons*, Phys. Rev. Lett.**13**(1964) 321.

[8] P.W. Higgs, *Broken symmetries, massless particles and gauge fields*, Phys. Rev. Lett.**12**(1964) 132, Phys. Rev. Lett.**13**(1964) 508.

[9] M. Veltman, *Radiative Corrections to vector boson masses*, Phys. Lett. **B91**(1995) 95.

[10] G. 't Hooft, *Renormalization of Massless Yang-Mills Fields*, Nucl. Phys. **B33**(1971) 173;
G. 't Hooft, *Renormalizable Lagrangians for Massive Yang-Mills Fields*, Nucl. Phys. **B35**(1971) 167;
G. 't Hooft and M. Veltman, *Regularization and renormalization of gauge fields*, Nucl. Phys. **B44**(1972) 189.

[11] D.A.Ross and M. Veltman, *Neutral currents and the Higgs mechanism*, Nucl. Phys. **B95**(1975) 135.

[12] K. Hagiwara et al., *Review of Particle Physics*, Phys. Rev. **D66**(2002) 01001.

[13] G. Montagna, O. Nicrosini, G. Passarino, F. Piccinni and R. Pittau, *TOPAZ0 Version 4.0 : A version of a computer program for evaluation of de-convoluted and realistic observables at LEP1 and LEP2*, Nucl. Phys. **B401**(1993) 3, Comput. Phys. Commun.**76**(1993) 328 and hep-ph/9804211 (update).

[14] D. Bardin *et al.*, *ZFITTER Version 6.21 : A Semi-Analytical Program for Fermion Pair Production in e^+e^- Annihilation*, Comput. Phys. Commun.**133**(2001) 229 and hep-ph/9908433.

[15] W.M. Yao for CDF and D0 Collaborations, *Standard Model Higgs and Top Mass measurements at the Tevatron*, Proceedings of the American Physical Society Meeting, hep-ex/9903068.

[16] NuTeV Collaboration, *A Precise Determination of Electroweak Parameters in Neutrino-Nucleon Scattering*, Phys. Rev. Lett.**88**(2002) 091802 and hep-ex/0110059.

[17] G. Ross, *Grand Unified Theories*, Benjamin 1985.

[18] S. Weinberg, *The quantum theory of fields. Volume 3: Supersymmetry*, Cambridge Univ. Press, 2000.

[19] S.P. Martin, *A Supersymmetry Primer*, hep-ph/9709356.

[20] P. Fayet, *About the origins of the Supersymmetric Standard Model*, Nucl. Phys. Proc. Suppl. 101(2001)81 and hep-ph/0107228.

[21] R. Jackiw and K. Johnson, *Dynamical model of spontaneously broken gauge symmetries*, Phys. Rev. **D8**(1973) 2386;
S. Weinberg, *Implications of dynamical symmetry breaking*, Phys. Rev. **D13**(1976) 974.

[22] LEP Energy Working Group, *Evaluation of the LEP centre-of-mass energy above the W pair production threshold*, Eur. Phys. J. **C11**(1999) 573;
LEP Energy Working Group, *Evaluation of the LEP centre-of-mass energy for data taken in 1998*, LEP Energy working group note 99/01;
LEP Energy Working Group, *Evaluation of the LEP centre-of-mass energy for data taken in 1999*, LEP Energy working group note 00/01
LEP Energy Working Group, *Evaluation of the LEP centre-of-mass energy for data taken in 2000*, LEP Energy working group note 01/01.

[23] B. Dehning *et al.*, *Status of the LEP2 Spectrometer Project*, CERN-SL-2000-038-BI.

[24] C. Ainsley, *LEP2 Beam Energy Measurements using Radiative Return events*, Talk presented at the ICHEP 2002 Conference (Amsterdam).

[25] G. Wilkinson, *Status of the Energy Calibration*, Talk presented at the LEP Jamboree 6th of March 2003 (CERN).

[26] DELPHI Collaboration, *The DELPHI Detector at LEP*, Nucl. Instrum. Methods **A303**(1991) 233;
DELPHI Collaboration, *Performance of the DELPHI Detector*, Nucl. Instrum. Methods **A378**(1996) 57.

[27] R.L. Gluckstern, *Uncertainties in track momentum and direction due to multiple scattering and measurement errors*, Nucl. Instrum. Methods **A24**(1963) 381.

[28] DELPHI Collaboration, *DELPHI Data Analysis Program (DELANA) User's Guide*, DELPHI 89-44 PROG 137 (1989).

[29] M. Elsing *et al.*, *Changes in the track reconstruction to recover from the TPC sector 6 failure*, DELPHI 2001-004 TRACK 95.

[30] V. Bocci *et al.*, *Architecture and performance of the DELPHI trigger system*, Nucl. Instrum. Methods **A362**(1995) 361.

[31] V. Perevozchikov and N. Smirnov, *PHDST Package Description V.3 VZD — Viewer of Zebra Data for DELPHI User's Manual*, DELPHI 92-118 PROG 189.

[32] Tz. Spassov and N. Smirnov, SKELANA — Skeleton Analysis Program, 1995;
F. Cossutti *et al.*, *Improvements to SKELANA for Version 2.0*, DELPHI 99-175 PROG 239.

[33] DELPHI Collaboration, *DELPHI event generation and detector simulation - User Guide*, DELPHI 89-67 PROG 142 (1989).

[34] G. Altarelli, T. Sjostrand and F. Zwirner, *Workshop on Physics at LEP2 - Volume 1*, CERN-96-01-Vol-1 (1996).

[35] S. Jadach, G. Passarino and R. Pittau, *Reports of the Working Groups on Precision Calculations for LEP2 Physics*, CERN 2000-009 (2000).

[36] A. Denner, S. Dittmaier, M. Roth and D. Wackeroth, *Order α corrections to $e^+e^- \to WW \to$ 4 fermions (+γ)*, Nucl. Phys. **B560**(1999) 33, Nucl. Phys. **B587**(2000) 67, Phys. Lett. **B475**(2000) 127 and hep-ph/0101257.

[37] S. Jadach, W. Placzek, M. Skrzypek, B.F.L. Ward and Z. Was, *Gauge invariant YFS exponentiation of (un)stable WW production at and beyond CERN LEP2 energies*, Phys. Rev. **D54**(1996) 5434, Phys. Lett. **B417**(1998) 326, Phys. Rev. **D61**(2000) 113010 and Comput. Phys. Commun.**140**(2001) 432.

[38] E. Barberio, B. van Eijk and Z. Was, *PHOTOS : a universal Monte Carlo for QED radiative corrections in decays*, Comput. Phys. Commun.**66**(1991) 115, Comput. Phys. Commun.**79**(1994) 291.

[39] E. Accomando, A. Ballestrero and E. Maina, *WPHACT 2.0 : A fully massive Monte Carlo generator for four fermion physics at e^+e^- colliders*, hep-ph/0204052.

[40] A. Ballestrero, R. Chierici, F. Cossutti, E. Migliore, *Four-fermion simulation at LEP2 in DELPHI*, CERN-EP-2002-069, hep-ph/0210208, accepted by Comput. Phys. Commun.

[41] A.P. Chapovsky and V.A. Khoze, *Screened-Coulomb ansatz for the non-factorisable radiative corrections to the off-shell W^+W^- production*, Eur. Phys. J. **C9**(1999) 449.

[42] Y. Kurihara, J. Fujimoto, T. Munehisha and Y. Shimizu, *Test Of QEDPS - A Monte Carlo For The Hard Photon Distributions In e^+e^- Annihilation Process*, Progress of Theoretical Physics **96** (1996) 1223, KEK-Preprint-95-126 .

[43] S. Jadach, W. Placzek and B.F.L. Ward, *Gauge invariant YFS exponentiation of (un)stable Z-pair production at and beyond CERN LEP2 energies*, Phys. Rev. **D56**(1997) 6939.

[44] G. Passarino in Working Group Report *Four fermion production in e^+e^- collisions*, CERN-2000-009 and hep-ph/0005309.

[45] S. Jadach, B.F.L. Ward, Z. Was, *The precision Monte Carlo event generator KK for two-fermion final states in e^+e^- collisions*, Comput. Phys. Commun.**130**(2000) 260.

[46] G. Altarelli and G. Parisi, *Asymptotic freedom in parton language*, Nucl. Phys. **B126**(1977) 298.

[47] T. Sjöstrand, *High-Energy Physics event generation with PYTHIA 5.7 and JETSET 7.4*, Comput. Phys. Commun.**82**(1994) 74.

[48] G. Corcella *et al., HERWIG 6 : an event generator for Hadron Emission Reactions With Interfering Gluons (including supersymmetric processes)*, J. High Energy Phys. **01** (2001) 010.

[49] L. Lonnblad, *ARIADNE version 4 : a program for simulation of QCD-cascades implementing the colour dipole moment*, Comput. Phys. Commun.**71**(1992) 15.

[50] B. Anderson, *The Lund model*, Cambridge Univ. Press , 1998.

[51] L. Lönnblad, T. Sjöstrand, *Bose-Einstein effects and W mass determinations*, Phys. Lett. **B351**(1995) 293-301 .

[52] L. Lönnblad, T. Sjöstrand, *Modelling Bose-Einstein correlations at LEP2* , Eur. Phys. J. **C2**(1998) 165, hep-ph/9711460.

[53] DELPHI Collaboration, *Tuning and Test of Fragmentation Models Based on Identified Particles and Precision Event Shape Data*, Z. Phys. **C73**(1996) 11 .

[54] V. Kartvelishvili, R. Kvatadze, R. Moller, *Estimating the effects of Bose-Einstein correlations on the W mass measurement at LEP2*, Phys. Lett. **B408**(1997) 331.

[55] G. Gustafson, U. Pettersson and P.M. Zerwas, *Jet Final States in WW Pair Production and Colour Screening in the QCD Vacuum*, Phys. Lett. **B209**(1988) 90.

[56] N. Van Remortel, *Bose-Einstein Correlations in WW events*, Talk presented during the XXXVIIIth Rencontres de Moriond 2003 (to appear in the proceedings).

[57] T. Sjostrand and V.A. Khoze, *On colour Rearrangement in hadronic W^+W^- events*, Z. Phys. **C62**(1994) 281.

[58] G. Gustafson and J. Hakkinen, *Colour interference and confinement effects in W-pair production*, Lund preprint LU-TP 94-9.

[59] L. Lönnblad, *Reconnecting coloured dipoles*, Z. Phys. **C70**(1996) 107.

[60] G. Altarelli, T. Sjostrand, F. Zwirner, *Workshop on Physics at LEP2 - Volume 2*, CERN-96-01-Vol-2 (1996).

[61] J. D'Hondt, *W mass and Colour Reconnection at LEP*, proceedings for Rencontres de Moriond XXXVII (electroweak session), hep-ex/0205036.

[62] J. D'Hondt, *Colour Reconnection in WW events*, proceedings for the XXXII International Symposium on Multiparticle Dynamics (2002).

[63] JADE Collaboration, *Experimental studies on multijet production in e^+e^- annihilation at PETRA energies*, Z. Phys. **C33**(1986) 23.

[64] S. Catani, Y.L. Dokshitzer, M. Olsson, G. Turnock and B.R. Webber, *New clustering algorithm for multijet cross-sections in e^+e^- annihilations*, Phys. Lett. **B269**(1991) 432.

[65] J. D'Hondt, *Tuning at LEP*, Talk presented during the LEP WW Workshop (CERN 2000),
webpage http://lepewwg.web.cern.ch/LEPEWWG/lepww/ .

[66] F. Seemann, *Λ(1520)-Produktion in hadronischen Z-Zerfällen*, Diploma Thesis at the University of Wuppertal.

[67] J. D'Hondt, *Comparison of LEP tunings in 4-jet like background events*, Talk presented during the LEP WW Workshop (CERN 2001),
webpage http://lepewwg.web.cern.ch/LEPEWWG/lepww/ .

[68] DELPHI Collaboration, *W pair production cross-section and W branching fractions in e^+e^- interactions at 189 GeV*, Phys. Lett. **B479**(2000) 89.

[69] DELPHI Collaboration, *b-tagging in DELPHI at LEP*, submitted to Eur. Phys.J C, CERN-EP 2002-088.

[70] Y.L. Dokshitzer, G.D. Leder, S. Moretti and B.R. Webber, *Better Jet Clustering Algorithms*, J. High Energy Phys. **8** (1997) 1.

[71] L. Lonnblad, *ARCLUS - A new jet clustering algorithm inspired by the Colour Dipole Model*, Z. Phys. **C58**(1993) 471.

[72] J. D'Hondt and N.J. Kjær, *Exact optimization of likelihood analyses in a unified Bayesian-Frequentist Monte Carlo Framework : The 'K2-filter'*, contributed paper to 'Advanced Statistical Techniques in Particle Physics', Grey College, Durham, 18-22 March 2002.

[73] DELPHI Collaboration, *Measurement of the W-pair cross-section and of the W mass in e^+e^- interactions at 172 GeV*, Eur. Phys. J. **C2** (1998) 581;
N.J. Kjær and M. Mulders, *The ideogram technique for LEP2 analysis*, DELPHI 97-55 PHYS 705.

[74] P. Abreu *et al.*, *The estimation of the effective centre-of-mass energy in $q\bar{q}\gamma$ events from DELPHI*, Nucl. Instrum. Methods **A427**(1999) 487.

[75] G. D'Agostini, *Bayesian reasoning in high-energy physics : principles and applications*, CERN Report 99-03.

[76] M.G. Kendall and A. Stuart, *The advanced theory of statistics (volume 1-2-3)*, Charles Griffin & Company 1963.

[77] N.J. Kjær and M. Mulders, *Mixed Lorentz Boosted Z^0's*, CERN-OPEN/2001-026.

[78] S. Jadach *et al.*, *On theoretical uncertainties of the W boson mass measurement at LEP2*, Phys. Lett. **B523**(2001) 117.

[79] F. Cossutti, *Radiative corrections systematics on DELPHI semi-leptonic W mass measurement*, Talk presented during the LEP WW Workshop (CERN 2003),
webpage http://lepewwg.web.cern.ch/LEPEWWG/lepww/ .

[80] DELPHI Collaboration, *Measurement of the Mass and Width of the W Boson in e^+e^- Collisions at $\sqrt{s}$=189 GeV* Phys. Lett. **B511**(2001) 159.

[81] F.A. Berends, R. Pittau and R. Kleiss, *EXCALIBUR - A Monte Carlo program to evaluate all four fermion processes at LEP 200 and beyond*, Comput. Phys. Commun.**85**(1995) 437.

[82] J. D'Hondt, *W mass systematic uncertainties from FSI*, Talk presented during the LEP WW Workshop (Lisbon 2000),
webpage http://lepewwg.web.cern.ch/LEPEWWG/lepww/ .

[83] The LEP and SLD Collaborations, *A combination of preliminary electroweak Measurements and Constraints on the Standard Model*, CERN-EP 2001-098 and hep-ex/0112021.

[84] J. D'Hondt and N.J. Kjær, *Measurement of Colour Reconnection model parameters using m_W analyses*, contributed paper for ICHEP 2002, DELPHI 2002-048 CONF 582.

[85] Ahmimed Ouraou, private communication.

[86] P.Abreu *et al., Investigation of Colour Reconnection in WW pairs using particle flow*, contributed paper for EPS HEP 2001 (Budapest), DELPHI 2001-061 CONF 489.
P.Abreu *et al., Update of the Investigation of Colour Reconnection in WW pairs using particle flow*, contributed paper for ICHEP 2002 (Amsterdam), DELPHI 2002-047 CONF 581.

[87] L. Lyons, D. Gibaut and P. Clifford, *How to combine correlated estimates of a single physical quantity,* Nucl. Instrum. Methods **A270**(1988) 110.

[88] DELPHI Collaboration, *Measurement and interpretation of the W-pair cross-section in e^+e^- interactions at 161 GeV,* Phys. Lett. **B397**(158) 1997.

[89] Richard Hawkings and Elisabetta Barberio, private communication.

[90] D. Bloch *et al., Measurement of the mass and width of the W boson in e^+e^- collisions at $\sqrt{s}$ = 192-209 GeV*, contributed paper for ICHEP 2002 (Amsterdam).

[91] UA2 Collaboration, *An improved determination of the ratio of W and Z masses at the CERN $\overline{p}p$ collider,* Phys. Lett. **B276**(1992) 354.

[92] CDF Collaboration, *Measurement of the W boson mass with the Collider Detector at Fermilab*, Phys. Rev. **D64** (2001) 052001.

[93] CDF Collaboration, *Direct Measurement of the W Boson Width in $p\bar{p}$ Collisions at $\sqrt{s}$ = 1.8 TeV*, Phys. Rev. Lett. **85** (2000) 3347.

[94] D0 Collaboration, *A direct measurement of the W boson decay width*, Phys. Rev. **D66** (2002) 032008.

[95] D0 Collaboration, *Improved W boson mass measurement with the D0 detector*, Phys. Rev. **D66** (2002) 012001.

[96] CDF Collaboration, *Measurement of the Top Quark Mass with the Collider Detector at Fermilab,* Phys. Rev. Lett.**82**(1999) 271.

[97] D0 Collaboration, *Direct Measurement of Top Quark Mass by the D0 collaboration*, Phys. Rev. **D58** (1998) 052001.

[98] M. Davier, S. Eidelman, A. Höcker and Z. Zhang, *Confronting Spectral Functions from e^+e^- Annihilation and τ Decays: Consequences for the Muon Magnetic Moment*, hep-ph/0208177.

[99] J.F. De Trocóniz and F.J. Ynduráin, *Calculation of $\bar{\alpha}_{QED}$ on the Z,* Phys. Rev. **D65** (2002) 093002.

[100] P.H. Chankowski, A. Dabelstein, W. Hollik, C. Jünger and G. Weinglein, *Δr in the MSSM,* Phys. Lett. **B417**(1994) 101.

[101] G. Glenzinski, *Electroweak Prospects for Tevatron Run II*, Talk presented during the ICHEP 2002 conference (Amsterdam), hep-ex/0211038.

[102] B. Efron, *Computers and the Theory of Statistics*, SIAM Rev. **21**(1979)460.

[103] S. Jezequel, *ALEPH Physics Results*, Public talk presented during the LEP Jamboree (6th of March 2003).